Modelling Low-Density Flow in Hypersonic Impulse Facilities

Thesis by

Vincent Wheatley, B.E. (Hons)

Submitted for the Degree of

Masters of Engineering Science

Department of Mechanical Engineering

The University of Queensland

Brisbane, Australia

2001

(Submitted August 10, 2001)

Statement of Originality

The work presented in this thesis is, to the best of my knowledge and belief, original, except as acknowledged in the text. The material has not been submitted, either in whole or in part, for a degree at this or any other university.

Vincent Wheatley

Abstract

In the past decade there has been a resurgence of interest in rarefied, hypervelocity flows. This interest can be chiefly attributed to the increasing use of aerobraking maneuvers to save fuel on interplanetary missions [57]. The computational tool of choice to simulate the rarefied hypervelocity flows encountered by spacecraft during these maneuvers is the Direct Simulation Monte Carlo method (DSMC) [10]. In some cases, such as the Magellan probe's flight through the upper atmosphere of Venus, DSMC has produced anomalous results , which implies that experimental validation of DSMC for hypervelocity conditions should be undertaken.

Unfortunately, present experimental facilities that produce rarefied gas flows are not capable of generating flow speeds of the order of 10 km/s that are required to simulate the conditions encountered during an aerobraking maneuver. One possible method for generating rarefied hypervelocity flows is to modify an expansion tube [55]. A series of low density experiments have been carried out by Chiu [49] in the X1 expansion tube at the University of Queensland (UQ).

The purpose of this thesis was to assess whether a useful, rarefied test flow with a flow speed of the order of 10 km/s could be generated in X1. A major goal was to develop a CFD model of X1 that produces results that are in agreement with the experimental data of Chiu [49]. Once the accuracy of the CFD model had been established, more detailed information could be extracted from the simulation results than was available from the experimental data. Most importantly, it was possible to establish the variation of flow parameters across the proposed test flow, which determines whether or not the flow is suitable for experiments. As the flow through the majority of the facility is in the continuum regime, a compressible Navier-Stokes solver was used to simulate the flow. To determine the minimum model complexity required to accurately simulate the experimental conditions, viscous effects, chemisty modelling and non-ideal diaphragm dynamics were

progressively added to the computational model until the results were in reasonable agreement with the experimental data. Finite-rate chemistry modelling was implemented in a one-dimensional Lagrangian CFD code to enable the combined effects of non-ideal diaphragm dynamics and nonequilibrium chemistry to be explored.

At the low speed end of UQ's collection of impulse-flow facilities, is a small reflected-shock tunnel [7, 19]. The possibility of generating rarefied flow in the small shock tunnel (SST) is also explored in this thesis. While hypervelocity testing cannot be carried out in the SST because of its limited stagnation temperature, it will still produce a high Mach number rarefied flow. Essentially, the SST will provide a non-reacting reference flow for computational and experimental techniques to be applied to the flow in X1. Unlike X1 the SST does not have a free piston driver nor as many stages of gas processing so simulation techniques can be assessed at low densities without as many confounding influences. To assess whether a useful rarefied test flow can be generated in the SST, a computational study of the effects of low densities on the performance of the facility has been carried out. Key results include the effect of backpressure and low stagnation pressures on the nozzle starting process and the performance of the SST's contoured and conical nozzles. The outcome of this study was a recommended configuration for the facility and a set of operating conditions that are predicted to produce a useful, rarefied test flow.

Acknowledgements

First and foremost I must express my gratitude to my supervisor, Dr Peter Jacobs, for his thoughtful guidance, gentle encouragement, (almost) unlimited patience, and insight into all facets of this thesis. I tried to compile a mental list of everything I should thank him for, but my brain overloaded before I finished.

I also must thank my associate supervisor, Dr David Mee, particularly for our discussions on instrumentation and experimental oddities. This gratitude extends to the other members of the group involved with low-density testing in X1, Sam Chiu and Dr Michael Macrossan. Without the experiments Sam conducted, this thesis wouldn't have had an experimental leg to stand on and Dr Macrossan's insights and experience in the field of rarefied gas dynamics were invaluable.

I would like to thank my fellow members of the compressible CFD group, James Faddy, Richard Goozee, Dr Chris Craddock, Kevin Austin and Ben Stewart, who helped ensure that the stress of postgraduate life never got out of hand. On a different note, I must thank Dr Chris Craddock for his expertise on finite-rate chemistry, the operation of the Small Shock Tunnel, and how to best convert CAD drawings to postscript form.

The staff of the Mechanical Engineering Department were of great help during this thesis, particularly Steve Kimball, Barry Allsop, Tony Olds and the office staff. I would also like to thank the system manager of the pselab, Tony Keating, for his help.

The facilities provided by the University of Queensland's High Performance Computing Group were invaluable to this thesis. I would particularly like to thank Martin Nicholls for allowing me extra privileges when I had a deadline to meet.

I would like to acknowledge the financial support for this thesis provided by the Australian Research Council in the form of an Australian Postgraduate Award, and the Department of Mechanical Engineering in the form of the Departmental Top-up.

Thanks must also go to my family and friends for their encouragement and understanding. Finally, and most importantly, I would like to express my love and eternal gratitude to my fiancé Cindy, whose love and support kept me both sane (I think) and happy through my undergraduate degree and this thesis.

Vincent Wheatley

Contents

List of Figures

List of Tables

Nomenclature

a	: local sound speed, m/s
A	: area, m^2
a_n	: normal accommodation coefficient
a_t	: tangential accommodation coefficient
C^*	: $(\mu^* T_\infty)/(\mu_\infty T^*)$
c_f	: skin friction coefficient
c_p	: pressure coefficient
C_p	: coefficient of heat capacity (constant pressure), J/(kg.K)
C_v	: coefficient of heat capacity (constant volume), J/(kg.K)
CFL	: Courant-Friedrichs-Lewy number
D	: characteristic object size, m
D_{test}	: test section size, m
e	: specific internal energy, J/kg
E	: total specific energy of a gas, J/kg
f_i	: mass fraction of species i
F_{wall}	: shear friction force at a wall, N
F_{loss}	: effective body force due to losses, N
g	: one terrestrial gravity, m/s^3
G^o	: Gibb's free energy, J/kg
h	: specific enthalpy, J/kg
H	: molar enthalpy, J/mole
H_f^o	: molar enthalpy of formation, J/mole
K_{eq}	: equilibrium constant
k_b	: backward rate coefficient
k_f	: forward rate coefficient

k : coefficient of thermal conductivity, W/(m.K)

$K_{eq,r}$: Equilibrium constant for species r

Kn : Knudsen number

L : Reference length scale/plate length, m

m : mass, kg

M : Mach number

M : molecular weight, g/mole

MW : molecular weight, g/mole

NJ : number of reacting species and third bodies

NSP : number of reacting species

p : pressure

p_{pitot} : Pitot pressure, Pa

P : Bird's breakdown parameter

P_D : breakdown parameter based on D

PRF : pressure reduction factor

q : heat flux, W/m^2

r : radius, m

R^0 : universal gas constant, 8.31451 J/(mole.K)

R : gas constant, J/(kg.K)

Re : Reynolds number

R_N : Nose radius, m

S : speed ratio

St : Stanton number

t : time, s

δt : time step, s

δt_{chem} : chemistry time step, s

δt_{signal} : minimum time required for a wave to traverse a cell, s

$\delta t_{allowed}$: maximum allowable time step, s

t_{test} : test flow duration

T : temperature

u : velocity in x/axial direction, m/s

U : state vector

v : velocity in y/radial direction, m/s

V : volume, m^3

x : axial distance, m

X_i : mole fraction of species i

Z : ln(10^4/T)

Greek

α : reactant stoichiometric coefficient

β : product stoichiometric coefficient

δ : boundary layer thickness, m

γ : ratio of specific heats, C_p/C_v

γ_j : mole number

λ : mean free path

$\dot{\omega}$: mass rate of production of a species, g/(s m^3)

τ_c : mean free time

μ : coefficient of viscousity, Pa.s

ρ : density

χ : Cheng's rarefaction parameter

$\bar{\chi}$: Strong interaction parameter

Subscripts

∞ : freestream value

$*$: throat value

0 : stagnation value

3 : fully expanded driver gas value

4 : unexpanded driver gas value

av : average value

D : based on D

drv : driver value

$evac$: initial evacuated conditions in the test section/dump tank

e : nozzle exit value

eff : effective value

I : incident

i : species number

j : cell number

L : based on L

mix : property of a mixture

R : reflected

r : reaction number

res : reservoir value

s : post shock value

st : shock tube value

$test$: test section value

w : wall value

x : based on x

Superscripts

$*$: value at the characteristic temperature T^*

$normal$: value during normal density operation

o : molar value

$rarefied$: value during low-density operation

CHAPTER 1

Introduction

1.1 Practical Applications of Rarefied Hypervelocity Flows

In the past decade there has been a resurgence of interest in rarefied, hypervelocity flows. This interest can be chiefly attributed to two factors; the increasing use of aerobraking maneuvers to save fuel on interplanetary missions [57], and the fact that a greater understanding of rarefied hypervelocity flows is required to optimise the design of re-entry vehicles [29].

During an aerobraking maneuver a spacecraft flies through the upper atmosphere of a planet to decrease its angular momentum and hence alter its orbit. Aerobraking was pioneered by the Magellan probe in the upper atmosphere of Venus and has since been used on the Mars Pathfinder and Mars Global Surveyor missions. Aerobraking maneuvers were also planned for the failed Mars Climate Orbiter mission and, in the near future, aerobraking will be used to circularise the orbit of the Mars Surveyor 2001 spacecraft when it arrives at Mars.

As the Magellan probe flew through the upper atmosphere of Venus its flight speed was 9 km/s and the flow over the satellite was in the transitional regime between continuum and free-molecular flow. In this regime, the classical equations of continuum fluid dynamics no longer hold and computations based on these give inaccurate estimates of lift and drag. The tool of choice to simulate the flow becomes the Direct Simulation Monte Carlo method (DSMC) [10] where the motions and collisions of the gas molecules are simulated on a computer. However, during the last phase of Magellan's historic flight, the thruster firing sequence required to maintain the stability of the satellite indicated that the aerodynamic forces on the spacecraft differed from the values predicted by DSMC

(personal communication, D. F. Rault to M. N. Macrossan). In view of these anomalous results, an improved understanding of the aerodynamics of high-speed, rarefied flow encountered during aerobraking maneuvers is required [87].

To optimise the design of reusable space transportation vehicles, accurate predictions of the surface heating, temperature, and flow field quantities during re-entry are required so that the weight of the thermal protection system can be minimised to increase the payload capacity. Obtaining accurate predictions by computational fluid dynamics (CFD) methods requires accurate modelling of the flow field chemistry, gas-surface interaction, body and shock slip, as well as the thermochemical nature of the flow field [28]. Due to the extreme conditions encountered during re-entry, and the associated modelling difficulties, it becomes essential to calibrate the CFD codes used against experimental data for a wide range of flow conditions [29]. While some codes have proven to be accurate for the flows that can be obtained in present ground based test facilities, calibration for the high energy, rarefied hypervelocity flows encountered during re-entry has only been possible using relatively scarce flight data. Gupta, Moss and Price [29] compared results from DSMC and a number of continuum CFD codes with the flight data from the Japanese Orbital Re-entry Experiment (OREX) vehicle. While the flight data agreed quite well with the DSMC predictions for altitudes greater than 84 km, there were still significant discrepancies at altitudes of around 95 km (see Section 2.4 for more detail).

1.2 The Role of DSMC and the Need for Calibration

In general there is a lack of experimental data on the aerodynamics of rarefied gases in comparison with other areas of fluid dynamics and DSMC has assumed the role of surrogate for experiments [59]. Molecular collision models have been developed for DSMC that can involve exchange of energy between translational, rotational, vibrational and electronic energy modes, but the assumption of being near equilibrium conditions is often incorporated into the derivation of these models [10]. Aerobraking maneuvers and re-entry present extreme conditions where collision models can be expected to be severely tested, it is very important that the accuracy of DSMC be assessed in these conditions. To emphasize the importance of having accurate collision models, Figure 1.1 shows the effect of surface collision parameters known as accommodation coefficients on heat transfer

to a sharp cone with a 45^0 half angle [48]. A comparison is made between experimentally measured and computed heat transfer values for varying Knudsen number, which is a measure of the degree of rarefaction of the flow. DSMC results for several different values of the normal and tangential accommodation coefficients (a_n and a_t respectively) are shown. Examination of Figure 1.1 reveals that there are significant discrepancies between the measured and computed values and that inaccuracy in the accommodation coefficients produces large errors in the predicted heat transfer.

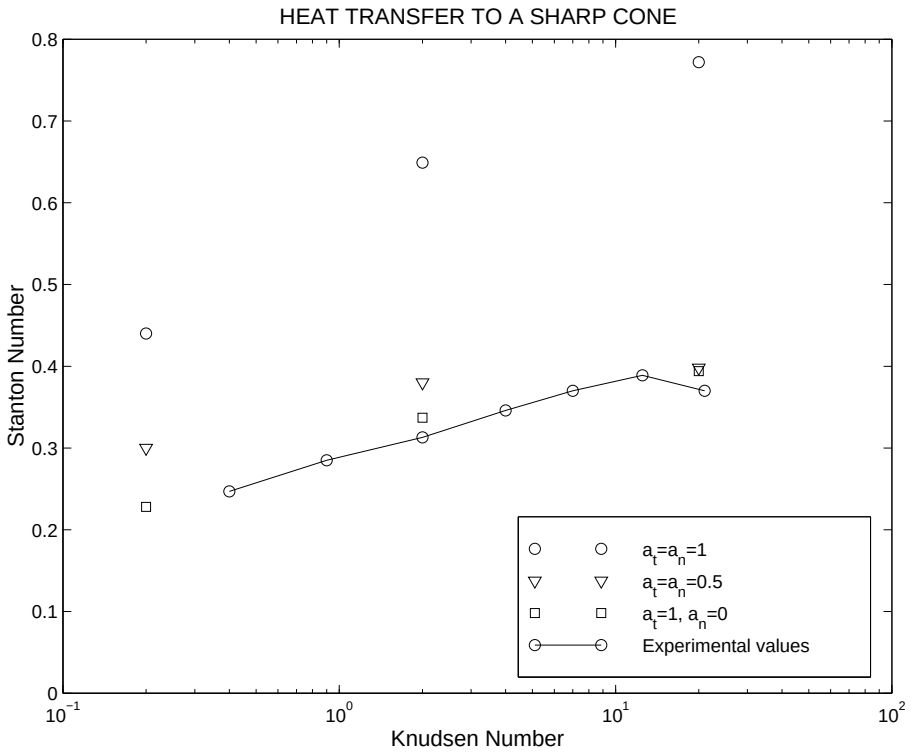

Figure 1.1: Sharp cone heat transfer values from reference [48] for a flow of helium with a stagnation temperature of 293 K.

Note that although the flow conditions in Lord's experiments were hypersonic (at around 1.5 km/s), they are still well below the "hypervelocity" conditions encountered during an aerobraking maneuver or re-entry, which are the concern of this thesis. However, from Lord's results, it can be extrapolated that if the estimates of collision parameters such as accommodation coefficients are inaccurate for hypervelocity flow, then there is little hope of correctly predicting the aerodynamic characteristics of a spacecraft using DSMC. To remedy this situation an experimental validation of DSMC for hypervelocity conditions should be undertaken. This thesis will take a step towards the provision of rarefied hypervelocity flow in a wind tunnel test facility.

1.3 Developing Rarefied Hypervelocity Facilities

A review of the capabilities of both past and present hypersonic low density wind tunnels is presented in Section 2.1. Unfortunately, present experimental facilities that produce rarefied gas flows (such as the DLR Göttingen continuous operation Hypersonic Vacuum Wind Tunnel [21] and the SR3 low density facility [1]) are limited to stagnation temperatures of around 2500 K and hence test speeds of under 2.5 km/s. Thus, they are incapable of producing the hypervelocity conditions required to assess DSMC as desired. A flow speed of the order of 10 km/s is required to simulate the conditions encountered during an aerobraking maneuver.

One possible method for generating rarefied hypervelocity flows is to modify an expansion tube [55]. In 1998 there was a pilot study into the development of a rarefied hypervelocity test facility using the X1 expansion tube at the University of Queensland [87]. In the pilot study rarefied flow was generated by operating the tube at low densities and then expanding the flow into the dump tank via a conical nozzle attached to the exit of the tube. This generated a flow of argon in the transitional regime at 8.8 km/s with a test flow duration of 60 μs. A 50 mm diameter central core flow was produced with a Pitot pressure variation of 30%. Unfortunately these spanwise variations make the flow unsuitable for most experiments where a nominally uniform core flow is required. Another problem identified in the pilot study was the unacceptably large amount of time-variation in the experimental data. In addition to this there were found to be significant differences between the experimental data and the results from a CFD simulation, pointing to inadequacies in the simulation technique (This will be further discussed in Chapter 5).

To continue the study into developing a rarefied hypervelocity test facility, a new series of experiments has been conducted by Chiu [49] using a free jet to expand a flow of nitrogen into the dump tank. The results of these experiments (see Chapter 5) consist of Pitot pressure histories at discrete locations throughout the dump tank and static pressure histories at several points along the expansion tube from which shock speeds can be calculated. While this data is extremely useful, a great deal more information on the flow field is required before meaningful testing can be carried out in the facility. This information could be obtained from an accurate CFD model of the flow through the facility.

A major goal of this thesis is to develop a CFD model of X1 that produces results

that are in agreement with the experimental data of Chiu [49]. Once the accuracy of the CFD model has been established, more detailed information can be extracted from the simulation data than is available from the experimental data. Most importantly, it is possible to establish the variation of flow parameters across the proposed test flow which determines whether or not the flow is suitable for experiments. The divergence of the core flow can also be determined along with the degree of rarefaction of the flow. The final CFD model can also be used to predict the performance of X1 at different operating conditions. This would enable the establishment of a tentative range of rarefied flows that can be produced in X1.

At the low speed end of the University of Queensland's collection of impulse-flow facilities is a small reflected-shock tunnel [7, 19]. The possibility of generating rarefied flow in the small shock tunnel (SST) is also explored in this thesis. The flow generated in the SST is non-reacting due to the moderate stagnation temperature of around 2000 K. This is well below the temperature at which a significant level of nitrogen dissociation occurs. As a result of the moderate stagnation temperature, the test flow speed in the SST is limited to about 2 km/s. While hypervelocity testing cannot be carried out in the SST, it will still produce a high Mach number rarefied flow. Essentially, the SST will provide a non-reacting reference flow for computational and experimental techniques to be applied to the flow in X1. Unlike X1 the SST does not have a free piston driver nor as many stages of gas processing so simulation techniques can be assessed at low densities without as many confounding influences. The lack of chemical reactions and a free piston driver in the SST lead to a situation where the flow through the facility is inherently much "cleaner" than that through X1. This allows the performance of instrumentation at low densities to be evaluated in the absence of high levels of flow noise. Inadequacies in the instrumentation can then be more easily identified as noise and drift in the measured signals will be primarily due to the instrumentation itself. Also, producing rarefied flow in the SST is beneficial simply because it expands the range of experimental testing that can be carried out at the University of Queensland.

1.4 Outline of Thesis

The primary objective of this thesis was to develop accurate computational models of the flow in hypersonic impulse facilities when operated at conditions designed to produce a rarefied test flow. The major contributions that were made by this thesis are as follows:

- It was established what degree of rarefaction must be produced in an impulse facility for non-continuum effects to be observed on a suitable model placed in the test flow;
- Experiments were defined that could be carried out in the impulse facilities at UQ where the effects of rarefaction are important, allowing the surface interaction parameters used in DSMC to be tested;
- The details of the flow in the SST when operated at pressures an order of magnitude lower than normal were studied;
- It was established why previous attempts to produce rarefied flow in the SST have failed and a set of operating conditions that produce a useful low-density test flow were devised;
- The computational modelling of the X1 expansion tube was investigated and it was established what aspects of the flow processes need to be modelled to produce reliable estimates of the real conditions;
- These techniques were applied to flow in the real facility both to validate the methods and to provide detailed flow field information for experimentalists;
- Finite-rate chemistry modelling was implemented in a one-dimensional Lagrangian CFD code;

The research behind these contributions is described in detail in the remainder of this thesis. To guide the reader, a breakdown of the purpose and contents of the following chapters is provided below.

Chapter 2 In the first section of this chapter, a review of the capabilities of past and contemporary low-density hypersonic wind tunnels is presented. The purposes of this review are to survey the techniques by which rarefied hypersonic flows have

been produced, and to assess whether existing facilities are capable of producing test flows that simulate the conditions encountered during an aerobraking maneuver. In the second section, a number of parameters that quantify the degree of rarefaction of a flow are discussed, and a target value is set for the degree of test flow rarefaction in the SST. The next section is comprised of a brief overview of the computational techniques used to simulate rarefied hypersonic flows and, finally, some rarefaction effects on the surface parameters of two model types are presented. The purpose is to aid in designing suitable experiments to be conducted in the impulse facilities at UQ.

Chapter 3 The possibility of generating rarefied flow in the Small Shock Tunnel is explored in this chapter. First, a description of the SST is presented, where the flow processes that generate the test flow for normal density operation are discussed in some detail. Following this, analytical calculations of the fill conditions required to produce the target level of test flow rarefaction are presented. Numerical simulations were used to assess whether these fill conditions produce a useful rarefied test flow when either a contoured nozzle or a conical nozzle is installed. Further simulations were used to refine the fill conditions and investigate the flow processes that occur in the facility during low-density operation. The details and results of the numerical models are presented in this chapter. The chapter concludes with recommendations of the configuration and fill conditions that should be used to produce a rarefied test flow in the SST, and a useful experiment that could be carried out in the new flow conditions.

Chapter 4 The purpose of this chapter is to present the details of the X1 expansion tube and the low-density experiments of Chiu [49] that were used in the development and validation of an accurate CFD model of the flow through X1, which is discussed in full detail in Chapter 5. The chapter begins with a description of the X1 expansion tube, where the flow processes that generate the test flow are discussed in some detail. The operating conditions used during Chiu's study are then presented. Following this, the instrumentation used during low-density operation is described, and samples of the recorded data are presented. Finally, techniques used to interpret the experimental data are discussed.

Chapter 5 In this chapter, a series of computational approaches are presented, which have been applied to simulate the flow through X1 during low-density operation. The aim of these simulations was to produce a CFD model of the flow through X1 that reproduces the experimental data described in Chapter 4. The chapter starts with a discussion of some details associated with modelling X1, including the CFD code that was used. Also included in the first section are calculations of the inflow conditions for the initial simulations, a brief investigation of some unusual features in the experimental data, and the computational grid definition. In the next two sections, results of the initial simulations of the flow through X1's acceleration tube and dump tank are presented. The initial simulations were run for the two extremes of flow chemistry; equilibrium and frozen flow. The results of the simulations are compared with experimental data and the flow processes that affect the test flow are discussed. Following this, non-ideal rupture dynamics are discussed. Two models for non-ideal diaphragm rupture are presented and their effects on the flow field are compared for both equilibrium and finite rate flow chemistry. This was made possible by the finite-rate chemistry modelling implemented in the Lagrangian CFD code, L1D, as part of this thesis (see Appendix A). The validity of assuming that the flow chemistry was either in equilibrium or frozen could also be determined from results presented in this section. One of the non-ideal diaphragm rupture models was then incorporated into the full two-dimensional model of the acceleration tube and dump tank. The results obtained from running this model are the topic of the next section. The chapter concludes with a discussion of the flow processes that need to be computationally modelled in order to produce reliable estimates of the real conditions in the facility.

Chapter 6 The final chapter of this thesis contains a summary of the results obtained throughout the course of this thesis, and the conclusions that were drawn from them. Recommendations are made regarding: how the SST should be operated; what flow processes must be modelled to successfully simulate the flow in impulse facilities; and what further computational and experimental work should be undertaken on the topic of this thesis.

CHAPTER 2

Literature Review

This chapter is divided into four sections. In the first section, a review of the capabilities of past and contemporary low-density hypersonic wind tunnels is presented. The purposes of this review are (1) to assess whether existing facilities are capable of producing test flows that simulate the conditions encountered during an aerobraking maneuver, and (2) to survey the techniques by which rarefied hypersonic flows have been produced. Some of these techniques may be applied to the production of rarefied flow in the impulse facilities at the University of Queensland (UQ).

In the second section, the parameters that measure the degree of rarefaction of a flow are discussed. A target value is set for the degree of rarefaction of the test flow in the Small Shock Tunnel (SST). The third section is comprised of a brief overview of the computational techniques used to simulate rarefied hypersonic flows. This was included to clarify some of the results presented in the fourth section, in which some effects of rarefaction on measurable quantities are reviewed. Rarefaction effects on the surface parameters measured on both flat plates with sharp leading edges and blunt bodies in rarefied hypersonic flows are presented. The purpose is to aid in designing suitable experiments to be conducted in the impulse facilities at UQ.

2.1 Low-Density Hypersonic Wind Tunnels

By the early 1960s the low-density wind tunnel had become an important laboratory device for investigating the behavior of high speed, low density gas flows. The initial design, development, construction and instrumentation of the low density wind tunnel began in 1946 at the NACA Ames Laboratory (Ames) and the University of California (UC), Berkeley [82]. These designs were later duplicated or modified by several other research groups such as the University of Toronto Institute for Aerophysics (UTIA), the Armament Research and Development Establishment (ARDE) at Fort Halstead, England, Laboratoire Mediterraneen de Recherches Thermodynamique (LMRT) at Nice and the University of Southern California (USC), Los Angeles.

Various aspects of the design and operation of these early wind tunnels were presented by Stalder [79]. The facilities were designed to operate continuously, with the goal of producing free-molecular test flows. The majority of the tunnels were driven by vacuum pumps without any heating of the air supply. This limited the test section Mach numbers achievable in most of the facilities to values below 6 in order to prevent air condensing in the test section [79]. One effort to remedy this was made by the Ames group. The Ames low-density wind tunnel had two test sections. One with an unheated air supply and one using air heated in a zirconia pebble-bed heater. The pebble-bed heater was capable of producing air stream stagnation temperatures of up to 2500 K, which corresponds to conditions obtained at a flight Mach number of 7 [79].

The static pressures in the test sections of these facilities ranged from below 0.001 torr in the LMRT tunnel to 0.1 torr in the Ames tunnel. Nozzles were designed to produce exit Mach numbers ranging between 2.0 and 8.0 for the noted test pressures [82]. To achieve Mach numbers higher than this and with a test section static temperature high enough to prevent liquefaction, the stagnation temperature of the gas had to be significantly increased above the levels that could be achieved in the facilities mentioned thus far.

Despite the fact that the early continuous operation tunnels were capable of producing test flows with Mach numbers up to 8.0, in 1960 Wittliff and Wilson [89] noted that experimental low density data were relatively rare for Mach numbers greater than 6. It was felt that the shock tunnel could be a useful tool for obtaining data in this flow regime, so a program of low density studies was undertaken at Cornell Aeronautical Laboratory, Inc.

(CAL), utilizing the 11 by 15-inch hypersonic shock tunnel. Impulsive facilities such as shock tunnels are particularly useful for producing high speed flow as the high stagnation temperatures required to prevent liquefaction can be achieved without the expensive gas heating systems and wall cooling systems that would be required in a facility that operates continuously [85]. The name of the 11 by 15-inch hypersonic shock tunnel describes the size of its test section. The tunnel consisted of a high pressure driver, a driven tube and a three stage hypersonic nozzle. The nozzle consisted of a convergent-divergent first stage, a flow turning section, and a straight walled divergent nozzle. The convergent portion of the first stage had an area ratio of 19:1, which is sufficient to reflect the incident shock and hence nearly stagnate the gas behind the reflected shock. The contoured divergent section of the first stage then expanded the gas to produce uniform flow at approximately Mach 4. The flow turning section of the nozzle served to remove diaphragm particles from the air stream. The third stage was a straight walled nozzle with a 15^0 included angle that further expanded the flow before it entered the test section. The tunnel was operated at tailored conditions using air as the test gas with either a helium or hydrogen driver. As this thesis is concerned with modelling hypervelocity facilities, only the operating conditions that produce the highest velocities will be discussed here. For the 11 by 15-inch shock tunnel, the highest velocities were achieved using an ambient temperature hydrogen driver. The range of flow conditions that Wittliff and Wilson [89] produced using such a driver are listed in Table 2.1.

The author believes this shock tunnel was the first rarefied hypersonic impulse facility. To allow the performance of this facility to be compared to its successors, the parameters that best characterise the performance of rarefied hypersonic facilities must be identified. As the focus of this thesis is on hypervelocity facilities, the flow speed is clearly a parameter that must be identified for each previous facility to establish whether or not rarefied hypervelocity flow has already been generated in a ground based facility. The degree of rarefaction of the flow can be universally characterised by the free-stream mean free path. This is preferred as it depends only on the flow conditions as opposed to parameters such as the Knudsen number that are dependent on the characteristic scale of the models tested in the facilities. The stagnation temperature of the test flow is also important because it determines whether high temperature effects such as finite-rate chemistry and radiative heating have been simulated.

A program of experimental research into hypersonic low density flow fields was continued at CAL through the use of two larger impulse facilities; the 6-foot shock tunnel and the 48-inch hypersonic shock tunnel [85, 84]. Low density flows ranging from near continuum to near free-molecular were produced in these facilities to investigate the validity of the rarefied flow theories available at the time, and to obtain data to guide future theoretical investigations. The CAL 6-foot and 48-inch shock tunnels were both conventional shock tunnels utilizing the tailored-interface principal of operation. As with the 11 by 15-inch hypersonic shock tunnel, the names of the tunnels pertain to the size of their test sections. The 48-inch hypersonic shock tunnel was used to produce the higher density, lower Mach number flows at CAL and consequently is of less relevance to this thesis than the 6-foot tunnel and will not be discussed further here. The 6-foot shock tunnel was designed to produce reservoir pressures of 2.5 to 200 MPa and reservoir temperatures of 4000 to 8000 K. However the low density investigations of [85] were made with a nominal reservoir temperature of 4000 K, and over a reservoir pressure range of 2.5 to 45 MPa. The driver used was heated to 675 K and consisted of a mixture of two parts of hydrogen and one part of helium. Tailored operation was achieved by generating a shock with a Mach number of around 6.25, which produced a reservoir temperature of approximately 4000 K behind the reflected shock. This reservoir temperature was selected to provide a test section static temperature high enough to prevent liquefaction and to ensure that the thermochemical nonequilibrium effects in the nozzle would be small [85]. The range of flow conditions generated in the 6-foot shock tunnel for the low density studies of Vidal and Wittliff are shown in Table 2.1. It was noted that for the lowest density tests (i.e. $Re_\infty/L = 14600\,m^{-1}$), the nozzle wall boundary layers become very large resulting in a usable inviscid core flow around 150 mm in diameter. For the higher density tests a uniform core flow with a diameter of over 900 mm was produced.

Around the same time as the low density experiments began at CAL, a 24-inch diameter shock tube was constructed at the AVCO-Everett Research Laboratory (AERL) for chemical kinetics studies at conditions encountered during high altitude hypersonic flight [47]. To avoid the use of a large diaphragm, the shock tube is driven by a 127 mm diameter high pressure section, which is coupled to the 0.61 m diameter low pressure section by a 1.2 m long transition section located immediately downstream of the diaphragm. Observations were made though a window located 13.7 m from the diaphragm. The high

pressure driver gas for the shock tube was provided by the products of combustion of a hydrogen-nitrogen-oxygen mixture. After combustion the mixture had a pressure of approximately 1.4 MPa, which was sufficient to rupture the 2.5 mm thick copper diaphragm separating the high and low pressure sections. After the diaphragm ruptures, a shock propagates into the low pressure section compressing and accelerating the sample gas that initially fills the low pressure section. The test flow is comprised of the shock heated sample gas between the shock and the contact surface between the sample and the driver gas. This results in a test time defined by the distance between the shock and the contact surface when the shock reaches the observation window. The initial driver gas composition and sample gas pressure were varied to produce shock speeds between 5 and 8 km/s. An approximate range of test conditions that could be produced in this facility using air as the sample gas at 0.068 Pa and a varied initial composition of the drive mixture is shown in Table 2.1. These conditions were calculated from the shock speeds and fill pressures presented in reference [47] by iteratively solving the Rankine-Hugoniot equations for the equilibrium conditions behind the shock.

At present, rarefied hypersonic wind tunnel testing is chiefly carried out in six facilities; the V1G and V2G Hypersonic Vacuum Wind Tunnels and the V3G High Vacuum Wind Tunnel at the DLR Göttingen, Germany, the SR3 low density wind tunnel at the Laboratoire d'Aerothermique, France, the Oxford Low Density Wind Tunnel at Oxford University, England, and the LENS (CALSPAN) facility in the USA.

The DLR Göttingen continuous operation Hypersonic Vacuum Wind Tunnel with test sections V1G and V2G simulates Mach and Reynolds numbers at high altitudes from 70 to 120 km [21]. Different altitudes or gas densities are simulated using conical nozzles and by varying the stagnation pressure. The gas can be heated to 2600 K to avoid condensation and to perform heat transfer measurements. During operation the constant stagnation pressures are maintained by compressors and the low densities in the test sections are maintained by a vacuum pumping system. The High Vacuum Wind Tunnel V3G is especially suited for investigating satellite aerodynamics, studying gas surface interactions, and for simulating flow processes in a high-vacuum environment. It extends the operating range of the facility towards higher altitudes and lower densities using a sonic orifice free jet expansion to produce the test flow. Free molecular flow can be achieved in V3G. The facility was originally built in 1965, then modified in 1968 before being

upgraded in 1992. The combined operating range of the tunnels is shown in Table 2.1.

The SR3 low density facility is a classical open-jet wind tunnel and is described in detail in reference [1]. As with the wind tunnels at DLR, the SR3 operates continuously. To produce hypersonic test flows a supply of compressed nitrogen is heated to avoid the risk of condensation then expanded through a conical nozzle into a large vacuum chamber. The chamber is continuously evacuated by one of two sets of vacuum pumps. The range of hypersonic working conditions in SR3 is given in Table 2.1.

Facility		CAL 11 by 15"	CAL 6'	AVCO	DLR	SR3
p_0 (kPa)	min	353	2500	N/A	0.5	17.3
	max	5890	45000	N/A	25000	12000
T_0 (K)		3200	3230	∼14600	300	800
		3700	4050	∼24600	2600	1300
u_∞ (m/s)		2740	∼2500	4660	∼730	∼1200
		3050	∼2800	7633	∼2300	∼1600
M_∞		8.4	13.5	3.5	6.0	6.8
		10.3	24.0	4.3	25.0	21.1
Re_∞/L (m^{-1})		22100	14600	590	400	35500
		134000	543000	1278	5×10^6	668000
λ_∞ (mm)		0.13	0.05	6.89	0.01	N/A
		0.58	2.30	10.20	50.00	N/A
D_{test} (m)		0.28 by 0.38	1.82 (square)	0.61	0.25,0.4 & 1.3	2.0
t_{test} (μs)		3500	≥300	50-30	continuous	continuous

Table 2.1: Range of hypersonic low density conditions in the CAL 11 by 15-inch hypersonic shock tunnel using hydrogen driver gas [89], the CAL 6-foot shock tunnel [85], the AVCO-Everett Research Laboratories 24-inch shock tube using air initially at 0.068 Pa (calculated from the shock speeds and fill conditions provided) [47], the V1G, V2G and V3G Vacuum Wind Tunnels at DLR Göttingen [21] and the SR3 Low Density Wind Tunnel [1]. ∼ indicates an approximate value calculated by the author assuming a calorically perfect gas. N/A indicates that the data was not available.

The Oxford Low Density Wind Tunnel is a suck-down wind tunnel. The test gas is drawn from the atmosphere by continuously evacuating the facility, hence its stagnation pressure is nominally limited to 100 kPa [61], rendering it incapable of producing flow with as high a Mach number as those in SR3.

Details on the LENS (CALSPAN) facility are not currently available to the author so its operation will not be reviewed here.

The range of flow conditions that can be experimentally produced in the facilities listed here is extensive, spanning the transition regime from continuum to rarefied flow

at Mach numbers of up to 25. However, of the facilities listed here, only the AVCO-Everett 24-inch shock tube was capable of generating rarefied hypervelocity flow with a free-stream velocity of the order of 10 km/s. Unfortunately, the fact that the test flow in this facility was comprised of the gas immediately behind the primary shock resulted in the test flow having a static temperature of 4165-5230 K. Due to these high static temperatures the Mach number of the test flow was limited to values below 4.5, well below the levels needed to fully simulate the conditions encountered during aerobraking maneuvers. The older facilities such as the CAL 6-foot shock tunnel were capable of producing rarefied flows with stagnation temperatures over 4000 K and flow speeds of around 3.5 km/s. Unfortunately, the stagnation temperatures of present facilities are limited to values below 2600 K. This has resulted in a paucity of experimental data on rarefied hypervelocity flows [87].

One possible method for generating rarefied hypervelocity flows is to modify an expansion tube [55]. In 1998 there was a pilot study into the development of a rarefied hypervelocity test facility using the X1 expansion tube at the University of Queensland [87]. In the pilot study rarefied flow was generated by operating the tube at low densities and then expanding the flow into the dump tank via a conical nozzle attached to the exit of the tube. This generated a flow of argon in the transitional regime at 8.8 km/s with a test flow duration of 60 μs. A 50 mm diameter central core flow was produced with a Pitot pressure variation of 30%. Unfortunately these spanwise variations made the flow unusable for most experiments where a nominally uniform core flow is required. Another problem identified in the pilot study was the unacceptably large amount of time-variation in the experimental data. In addition to this there were found to be significant differences between the experimental data and the results from a CFD simulation, pointing to inadequacies in the simulation technique. Chapter 5 examines the issues involved in the simulation of flows within the pilot facility.

To continue the study into producing rarefied hypervelocity flow in X1, a new series of experiments has been conducted by Chiu [49] using a free jet to expand a flow of Nitrogen into the dump tank. The details of these experiments can be found Chapter 4.

2.2 Conditions for Rarefied Flow

Before entering into a detailed discussion of the parameters used to define the degree of rarefaction of an expanding hypersonic flow, the more basic question, "What is rarefied flow?", is worth exploring. Historically, the basic parameter used to define the flow regime has been the Knudsen number [32],

$$Kn = \frac{\lambda}{L} ,$$

where λ is the mean-free path in a gas and L is the reference flow scale. A flow is considered to be in the continuum regime when its Knudsen number tends to zero. In the continuum regime, the microscopic structure of the gas can be disregarded; the flow can be studied by considering only its macroscopic properties such as density, velocity and temperature. When the Knudsen number of a flow tends to infinity, it is considered to be in the free-molecular flow regime. In this regime, the gas dynamics are governed by molecular collisions with body surfaces. Intermolecular collisions do not need to be considered.

A transitional regime exists between the continuum and free-molecular flow regimes. In this flow regime both gas-surface and intermolecular collisions play an important role. In answer to the question posed at the beginning of this section, a flow is considered rarefied if it is in either the transitional or free-molecular regime (i.e. the microscopic structure of the gas is important). Viscous effects and strong thermal non-equilibrium of the flow (a non-Maxwellian velocity distribution function) are important features of rarefied hypersonic flows. In addition to this, thermal and chemical relaxation lengths become comparable to, or greater than, the reference length scale of the flow, and the difference between the translational, rotational and vibrational temperatures becomes a determining factor in the gas dynamics [32]

It has been argued that the continuum description of an expanding flow is no longer valid when a variable known as the breakdown parameter, P, is greater than 0.04 [10]. The breakdown parameter is defined here as,

$$P = \frac{\sqrt{\pi}}{2} S \frac{\lambda}{\rho} \left| \frac{\partial \rho}{\partial x} \right| \tag{2.1}$$

where ρ is density and S is the speed ratio, $u/(2RT)^{0.5}$. Physically, this parameter corresponds to the ratio of the mean time between molecular collisions, τ_c, and the time taken for the flow to traverse a length scale based on the macroscopic gradient of density, $\rho^{-1}|\partial\rho/\partial x|$. In any region of an expanding flow where the breakdown parameter is greater than 0.04, it is probable that the Navier-Stokes equations with no slip boundary conditions will give an inaccurate description of the flow.

For flow over an object, the importance of rarefaction is indicated by the ratio of the collision time, τ_c, to the characteristic flow time about the object. For an object with a characteristic size of D, the characteristic flow time is given by D/u, where u is the characteristic speed of the flow [50]. The resultant ratio is equal to the breakdown parameter with the characteristic size of the object replacing the length scale based on macroscopic flow gradients and can be expressed as,

$$\frac{\tau_c}{D/u} = \frac{\sqrt{\pi}}{2} KnS \tag{2.2}$$

where Kn is the Knudsen number, λ/D, which is the parameter most commonly used in experimental studies to indicate the degree of flow rarefaction. It is convenient to drop the constant term, which is approximately unity, and define the breakdown parameter based on object size as,

$$P_D = KnS = \frac{\lambda}{D}\frac{u}{\sqrt{2RT}} \,. \tag{2.3}$$

The critical value of $P = 0.04$ identified by Bird corresponds to only 25 collisions occurring over the characteristic length scale. It is reasonable to assume that a value of $P_D = 0.04$ would indicate the onset of transitional regime flow when an object of characteristic size D is placed in the flow [87]. The mean free path can be related to viscosity by,

$$\lambda = \frac{2\mu}{\rho\sqrt{8RT/\pi}} \,. \tag{2.4}$$

Substituting this expression for λ into equation 2.3 allows P_D to be expressed in terms of more familiar gas dynamics parameters; the Mach number, M, and the Reynolds number, $Re_D = \rho u D/\mu$, as

$$P_D = \frac{\sqrt{\pi}\gamma M^2}{2Re_D} \,. \tag{2.5}$$

As the objective of producing low density flow in the SST is to observe non-continuum

effects in the flow over models rather than in the undisturbed flow structure, the aim of this work becomes to produce a flow in a small shock tunnel with P_D of the order of 0.04 for a suitable model.

A merged shock boundary layer would be expected to dominate the flow around any model placed in the low-density test flow. A parameter derived directly from merged shock-boundary layer theory, which has been frequently used to correlate experimental data (e.g. [85]), is Cheng's rarefaction parameter [15],

$$\chi = \frac{p_\infty D}{\mu_\infty u_\infty C^*} \,. \tag{2.6}$$

Here the subscript ∞ denotes the freesteam value and,

$$C^* = \frac{\mu^* T_\infty}{\mu_\infty T^*} \,, \tag{2.7}$$

where μ^* is the viscosity evaluated at the characteristic temperature, T^*, which is given by,

$$T^* = \frac{T_s + T_w}{2},$$

where T_s is the temperature behind the shock and T_w is the temperature of the model wall. Cheng's rarefaction parameter can also be expressed as,

$$\chi = \frac{Re_D}{\gamma M^2 C^*} = \left(2Kn_\infty S_\infty C^*/\sqrt{\pi}\right)^{-1} \,, \tag{2.8}$$

hence it is related to the freestream breakdown parameter with a slight modification to account for the difference between freestream conditions and typical conditions in the merged shock-boundary layer [49]. For a Mach 7 nitrogen test flow in the SST, the freestream temperature is around 180 K. The temperature behind a bow shock in front of a blunt model can be approximated by the total temperature of the flow, which is around 1950 K. Assuming the wall temperature of the model is 296 K, a characteristic temperature of 1123 K was calculated. At the characteristic and freesteam temperatures, the viscosity of nitrogen from the Sutherland expression is 1.1784×10^{-5} Pa.s and 4.2825×10^{-5} Pa.s respectively. Substituting these values into the equation 2.7, C^* was calculated to be 0.58. Comparing equations 2.3 and 2.8, and accounting for C^* being of

the order of unity, it can be seen that [49],

$$P_D \approx \chi^{-1} \, .$$

This indicates that the target value of the freestream breakdown parameter, $P_D = 0.04$, corresponds to Cheng's rarefaction parameter, χ, having a value of 25.

2.3 Simulation Techniques for Rarefied Hypersonic Flows

In the discussion of measurable rarefaction effects (presented in Section 2.4), a number of the computational techniques used to simulate rarefied flows are mentioned. Developing a rarefied hypervelocity test facility to experimentally assess one such technique, the direct simulation Monte Carlo method (DSMC), was one of the motivations for this thesis. The purpose of this section is to briefly describe the computational techniques used to simulate rarefied hypersonic flows. The extension of continuum techniques to rarefied hypersonic flows is discussed first, followed by an overview of DSMC.

2.3.1 Extending Continuum Techniques to Rarefied Hypersonic Flows

Rarefaction effects are generally incorporated into continuum simulation techniques through alteration of the shock and surface boundary conditions [18]. By their nature, continuum approaches cannot accurately predict the variation of flow properties within a few mean free paths of a surface, the gas in this region comprises what is known as the Knudsen layer. For continuum flow, the mean free path tends to zero, resulting in property changes in the Knudsen layer being insignificant to the overall flow. This allows the accurate assumption that the tangential velocity of fluid at the surface of a body is zero, and that the fluid temperature at the surface is equal to that of the body. These two assumptions are commonly referred to as no-slip boundary conditions. However, for Knudsen numbers greater than 0.03 [4], the variation of tangential velocity and temperature in the Knudsen layer become significant to the overall flow. Surface boundary conditions simulating the effects of the temperature jump and tangential velocity slip in the Knudsen layer are based on first order considerations derived from kinetic theory [18]. Analytical expressions for the effective slip boundary conditions have been formulated by numerous researchers including Shidlovskiy [73], Cercignani and Tironi [13], and Hendricks [31]. Chrusciel, Lewis and Sugimura [18] presented expressions for the surface temperature and tangential velocity jump that were used in continuum calculations of rarefied hypersonic flow over spherical nosetip. Their results are among those reviewed in Section 2.4.

Just as with the inviscid shock layer of classical theory, the concept of a thin shock layer may be applied to the viscous, heat conducting region between the shock and the surface of a blunt or non-slender body, provided the density level in the layer is much

higher than that in the freestream [16]. Viscous formulations of the gas dynamic equations based on such thin shock-layer approximations are referred to as viscous shock layer theory. Computational approaches based on viscous shock layer theory are referred to as VSL simulations. VSL simulations were used extensively in the literature surveyed in Section 2.4. Two different boundary conditions may be applied at the shock; viscous modified Rankine-Hugoniot relations and inviscid shock relations [16]. Due to its resemblance to body slip terms, the change in the shock boundary condition when the viscous modified Rankine-Hugoniot relations are used is often called "shock slip". The modified shock boundary condition includes corrections to the tangential velocity and total enthalpy. Cheng [16] noted that a shock capturing Navier-Stokes solution of the flow field should provide the shock slips correctly, even when the structure of the shock is not physically correct on the basis of kinetic theory. Jain and Adimurthy [41] went further than this, stating that several investigations on the problem of rarefied hypersonic flow in the stagnation region of a blunt body indicated that Navier-Stokes analysis may be valid far beyond the limits imposed by theoretical considerations.

2.3.2 The Direct Simulation Monte Carlo Method

The basic concepts of DSMC and its numerical procedure are described in Bird's monograph [10]. An excellent review of recent advances in the method is included in Ivanov and Gimelshein's review of computational hypersonic rarefied flows [32]. In this section, only a brief overview of DSMC is presented, which is chiefly taken from reference [58].

In DSMC, the real gas is modelled by thousands of simulated molecules in a computer. The velocity components, internal states and positions of these molecules are stored by the computer and are modified over time as the molecules concurrently undergo representative intermolecular collisions and boundary interactions in the simulated physical space. The core feature of DSMC is that the intermolecular collisions are considered on a probabilistic rather than a deterministic basis. All simulations are of an unsteady nature and the time parameter in the simulations may be identified with physical time. When a steady flow problem is to be solved, the solution is the asymptotic limit of unsteady flow. DSMC simulations are initiated from states that can be specified exactly, such as a vacuum or uniform equilibrium flow. As a consequence of this, initial estimates of the flow field are not required and the method does not involve any iterative procedures. The simulated physical

space is divided into a network of computational cells to facilitate the selection potential collision pairs and the sampling of macroscopic flow properties. While the method can take advantage of any flow symmetries to reduce the size of the computational domain and the number of position co-ordinates that need to be stored for each simulated molecule, collisions are always treated as three-dimensional phenomena. Boundary conditions are specified by a set of parameters that govern how each simulated molecule interacts with the boundary, rather than by a distribution function. All procedures may be specified in such a manner that the computational time is directly proportional to the number of molecules included in the simulation [58].

2.4 Measurable Effects of Flow Rarefaction

The objective of low-density testing in the small shock tunnel (SST) and the X1 expansion tube would be to assess the accuracy of CFD predictions (both continuum and DSMC) of the flow about a model, in the presence of rarefaction effects. To enable this, the flow rarefaction must have a significant effect on a measurable quantity such as heat transfer, surface pressure, skin friction or drag. As the low-density flow generated in the SST will be near continuum (see Section 3.4), the effect of flow rarefaction on a parameter is defined as the fractional departure from a continuum prediction of its value. This can be determined by comparing the continuum prediction with either experimental data or a DSMC prediction. For some conditions, the difference between a DSMC prediction of a quantity and its continuum value could be due, in part, to inaccuracies in the DSMC simulation technique. If this is the case, it would still be desirable to conduct experiments at conditions where this occurs to provide data that would aid in resolving inadequacies in the simulation technique.

To aid in designing suitable experiments to conduct in the SST and X1, a number of measurable rarefaction effects that have been observed in the literature are reviewed in the following sections. The review focuses on the surface quantities observed on two simple model types (flat plates with sharp leading edges and axisymmetric blunt bodies) during low-density hypersonic testing. In many of the studies reviewed, multiple flow conditions were used. Where this was the case, the results included in the review are those obtained from the flow conditions closest to those expected in the SST. No attempt has been made to convert the data to a common set of parameters. Some of the literature reviewed did not contain sufficient infomation for this to be attempted.

Data on other model types in rarefied hypersonic flow is also available in the literature. For example: Koshmarov [44] measured the overall heat transfer to sharp cones in low-density supersonic flow and compared the results to continuum predictions. The effect of flow rarefaction on heat transfer to cylinders placed transverse to a hypersonic flow has been studied by a number of authors [89, 85, 74]. Shimada [74] also studied the effect of flow rarefaction on the skin friction and pressure distributions about a transverse cylinder.

2.4.1 Rarefied Hypersonic Flow about a Flat Plate

An early experimental study of hypersonic low-density flow over a flat plate was conducted by Vidal and Wittliff [85] using the hypersonic shock tunnels at CAL, which were described in Section 2.1. The heat transfer and surface pressure distributions along the plate were experimentally measured for a broad range of freestream conditions. The heat transfer data was presented in the non-dimensional from, $M_\infty^3 St$, where St is the Stanton number, which is defined as,

$$St = \frac{q}{\rho_\infty u_\infty (h_0 - h_w)} \ ,$$

where q is the heat flux and h is enthalpy. This was plotted against the viscous interaction parameter,

$$\bar{\chi} = M_\infty^3 \sqrt{C/Re_x},$$

where C is the Chapman-Rubesin constant that relates viscosity to temperature and,

$$Re_x = \frac{\rho_\infty u_\infty x}{\mu_\infty} \ ,$$

where x is the streamwise distance from the leading edge of the plate. The experimental data were compared to the strong interaction theory of Cheng [15]. For the freestream conditions; $M_\infty = 13.5$, $Re_\infty/L = 82700$ (L is the length of the plate) and $\lambda_\infty = 0.254\,\text{mm}$ (λ is the mean free path), the experimental $M_\infty^3 St$ values differ significantly from strong interaction theory for $\bar{\chi} \geq 40$. In this region, which is close to the leading edge, the experimental values are overestimated by strong interaction theory, which predicts an exponential rise in heat transfer as x decreases. For the less rarefied freestream conditions; $M_\infty = 14.1$, $Re_\infty/L = 216,500$ and $\lambda_\infty = 0.1\,\text{mm}$, the experimental values diverge from strong interaction theory near $\bar{\chi} = 50$. So the region of non-continuum flow near the leading edge of a flat plate becomes smaller as the degree of flow rarefaction (measured here by λ_∞) decreases. At the less rarefied condition, strong interaction theory underpredicts the value of $M_\infty^3 St$ at $\bar{\chi} = 50$ by around 12.5%. Experimental values of p/p_∞ were also plotted against $\bar{\chi}$ and compared with the distribution predicted by the strong interaction theory of Cheng [15]. The experimental values fell below the predicted levels at all values of $\bar{\chi}$, with a greater deviation from continuum

theory near the leading edge. The work of Vidal and Wittliff [85] was continued by Vidal and Bartz [84], who measured $M_\infty^3 St$ and p/p_∞ distributions along flat plates at angles of attack in hypersonic low-density flow.

Shimada [74] used a Navier-Stokes solver, with both slip and no-slip boundary conditions, and DSMC to predict the flow field over a flat plate for $M_\infty = 7$ and Re_L ranging from 100 to 5000. Two different slip boundary conditions were used in the simulations, one of which was derived in Simada's paper [74]. Distributions of the pressure coefficient, c_p, the skin friction coefficient, c_f, and the Stanton number were plotted against $\sqrt{Re_x}/M$, which is inversely proportional to an estimate of the local Knudsen number, Kn_x, based on the laminar boundary layer thickness (see Section 2.2 for discussion on various rarefaction parameters). When plotted in this form, the profiles from each computational approach did not vary much for the different values of Re_L. For all Re_L, the differences in the profiles from four computational approaches became significant for $\sqrt{Re_x}/M \leq 3$. For the case where $Re_L = 5000$, a value of $\sqrt{Re_x}/M$ of 3 corresponds to $x/L = 0.1$. For $\sqrt{Re_x}/M = 0.2$ ($x/L = 0.04$ for $Re_L = 5000$), the differences between the DSMC and Navier-Stokes (all boundary conditions) predictions of c_p, c_f and St were around 16%, 10% and 20% respectively, with the Navier-Stokes predictions being greater for all three quantities. The effect of the slip boundary conditions was to prevent the exponential increase of the quantities close to the leading edge, however the predictions were still not consistent with the DSMC results.

Up to date computational techniques and experimental data were brought together by Lengrand, Allegre, Chpoun and Raffin [46], who compared experimental St and surface pressure (p) distributions along a flat plate with predictions from DSMC and a Navier-Stokes solver. The experiments were performed in the SR3 low density wind tunnel described in Section 2.1 using a 0.1 m long flat plate with a sharp leading edge. Results for the two test conditions listed in Table 2.2 were presented in reference [46]. Both

Condition	M_∞	T_∞ (K)	u_∞ (m/s)	λ_∞ (mm)	Re_L
1	20.2	13.6	1500	2.35	1131
2	20	13.6	1502	0.785	3351

Table 2.2: Test conditions from reference [46].

St and p were plotted against x/λ_∞. Reproductions of these plots for the test condition

with $\lambda_\infty = 2.35\,\text{mm}$ are shown in Figure 2.1 with the DSMC predictions omitted for clarity. From this plot it can be seen that the distributions of p diverge for $x/\lambda_\infty < 20$

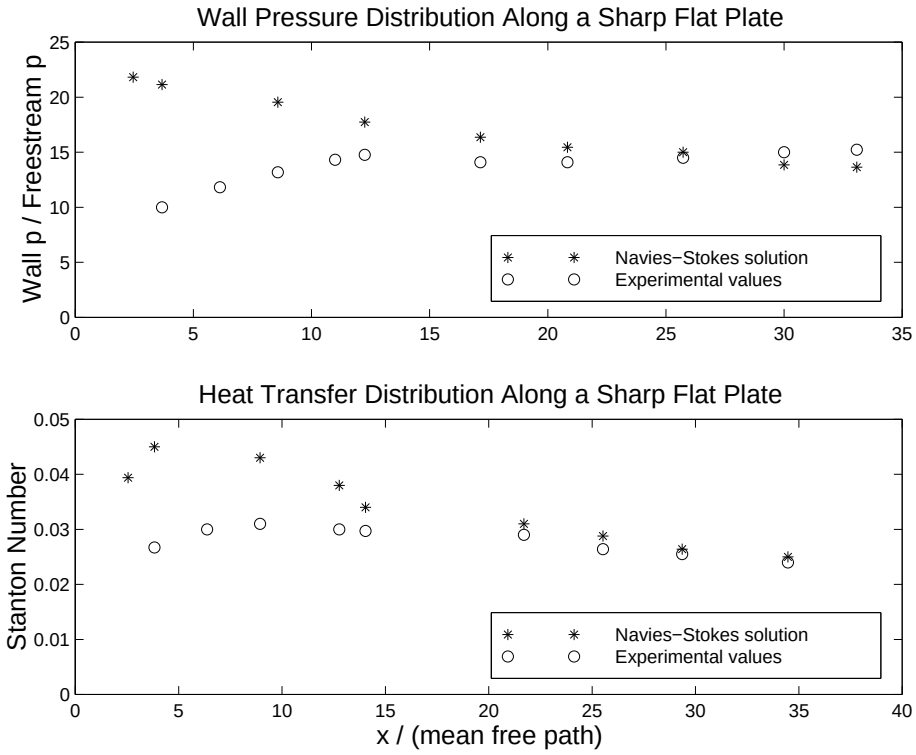

Figure 2.1: Experimental and computed distributions of Stanton number (St) and surface pressure (p) along a flat plate in rarefied hypersonic flow from reference [46].

while the distributions of St diverge for $x/\lambda_\infty < 30$. Taking the non-continuum region near the leading edge to end at $x/\lambda_\infty = 25$, the corresponding value of $\sqrt{Re_x}/M$ is around 1.3. This is of the same order as the value where Shimada's [74] continuum and DSMC results converge. For the second test condition with $\lambda_\infty = 0.785\,mm$, the experimental and Navier-Stokes distributions of p diverge for $x/\lambda_\infty < 80$, while there are significant differences between the distributions of St for all x/λ_∞ considered. At $x = 25\lambda_\infty$ the Navier-Stokes prediction of St is around 20% higher than the experimental value. The experiments and simulations were repeated for a flat plate at a 10^0 angle of attack. The non-continuum effects were found to be weaker on the inclined plate, with the Navier-Stokes prediction of the heat transfer distribution being slightly lower than the experimental values along the entire plate.

2.4.2 Rarefied Hypersonic Flow about a Blunt Body

An early experimental study of hypersonic low-density flow over a blunt body was conducted by Vidal and Wittliff [85] using the hypersonic shock tunnels at CAL, which were described in Section 2.1. The models used in this study were hemisphere cylinders with an assortment of nose radii. Stagnation point heat transfer and the heat transfer distribution around the nose were experimentally measured for a broad range of freestream conditions. The stagnation point Stanton number was plotted against Cheng's rarefaction parameter, χ [15], which is discussed in Section 2.2. The experimental values were compared to the theoretical predictions of Cheng [15]. For $\chi = 10$ and a nose radius (R_N) of 6.35 mm, the measured stagnation point Stanton number was around 17% lower than the theoretical prediction. The Stanton number distribution around the nose was non-dimensionalised by the stagnation point Stanton number and compared to the theoretical distribution of Lees [45]. Agreement between the two distributions was good except at 45^0 from the stagnation point, where the theory was high by around 17%, and at 90^0, where the theoretical distribution tended to zero but a value of around 0.75 was measured. It was also found that the measured distribution did not change significantly as the freestream Knudsen number, Kn_∞, was varied from 0.01 to 0.1.

Jain and Adimurthy [41] used a Navier-Stokes solver, with and without slip boundary conditions, to simulate the flow in the stagnation region of a sphere in hypersonic low-density flow. The values of the stagnation point heat transfer obtained from their simulations were plotted against χ and compared with the experimental data of, amongst others, Vidal and Wittliff [85]. The values predicted using the Navier-Stokes solver were around 20% lower than the experimental values of reference [85] for $\chi = 10$. At this value of χ, there was no visible difference between the Navier-Stokes values predicted with and without slip boundary conditions. It is interesting to note that while there was a significant difference between the continuum prediction and the data of reference [85], for which the stagnation temperature was around 2000 K (equal to that in the SST), other data from experiments with stagnation temperatures of around 1000 K were in agreement to within $\pm$1% of the continuum prediction at $\chi = 10$.

Comparative flow field calculations for rarefied hypersonic flow over a highly cooled spherical nosetip were made by Chrusciel, Lewis and Sugimura [18] to isolate slip-flow

effects at the body surface and the influence of a relatively thick shock transition region, which are the first departures from continuum theory that occur as the degree of flow rarefaction is increased. Comparisons were made between continuum viscous shock-layer (VSL) results incorporating various slip boundary conditions and results obtained from a kinetic theory Monte-Carlo code described in reference [86]. The simulations were run with $M_\infty = 26$, $T_w/T_\infty = 2$ and $\lambda_\infty/R_N = 0.24$ and 0.75. From the results of these simulations it was concluded that viscous effects in the shock transition region significantly affect the entire flow field, and that the continuum results without body slip significantly underpredict the temperature and velocity profiles near the surface over the aft portion of the nosetip but considerably overpredict the heat transfer and skin friction. For the case with $\lambda_\infty/R_N = 0.24$, the stagnation point heat transfer predicted using VSL with only "shock-slip" was 18% greater than the value from the Monte-Carlo simulation.

More recently, Moss, Cuda and Simmonds [58] have quantified the effects of rarefaction on hypersonic flow over a blunt cone with a hemispherical nose by comparing DSMC and VSL results for freestream Knudsen numbers ($Kn_\infty = \lambda_\infty/R_N$), ranging from a continuum value of 0.001 to a transitional value of 0.156. VSL simulations were run both with and without slip boundary conditions. The blunt cone that was the subject of the majority of the simulations had a nose radius of 0.0254 m and a half angle of 5^0. For the results shown here, the flow speed was set to a re-entry velocity of 7.5 km/s and the wall temperature of the cone was taken to be 1000 K. Figure 2.2 shows the predicted variation of stagnation point Stanton number and drag coefficient with Knudsen number from both DSMC and VSL simulations. From Figure 2.2 it can be seen that St diverges from the continuum prediction for $Kn_\infty \geq 0.036$. At $Kn_\infty = 0.036$ VSL overpredicts the stagnation point heat transfer by approximately 17%. On the other hand, there is very little difference between the continuum and DSMC predictions of the drag coefficient at $Kn_\infty = 0.036$, indicating that it is not as sensitive to flow rarefaction.

In 1997, Gupta, Moss and Price [29] presented results from a VSL analysis of the re-entry flow field around the forebody of the Japanese Orbital Re-entry Experiment (OREX) vehicle. This vehicle is a 50^0 spherically blunted cone with a nose radius of 1.35 m and a base diameter of 3.4 m. Calculations were performed for the OREX trajectory for an altitude range of 105 to 48.4 km. A series of VSL calculations were made with different non-continuum effects (slip and thermal non-equilibrium) included to assess their importance

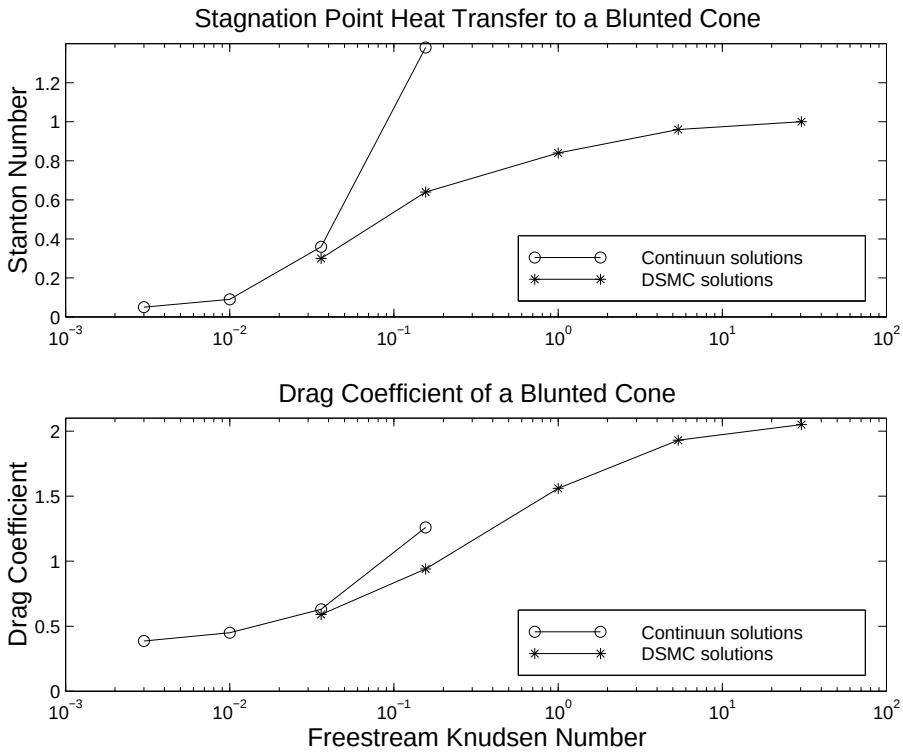

Figure 2.2: Predicted variation of blunt cone stagnation point Stanton number (St) and drag coefficient (c_d) with Knudsen number from both DSMC and VSL simulations from reference [58].

at different altitudes. It was found that at altitudes greater than 84 km, both slip boundary conditions and two-temperature thermochemical modelling were required to accurately predict the heat transfer rates inferred from flight data. The VSL predictions of stagnation point heat flux were compared to flight data and DSMC results over much of the OREX trajectory. At an altitude of 92.8 km, where $M_\infty = 26.96$ and $Kn_\infty = 0.0086$, the stagnation point heat flux inferred from the flight data was approximately 80 kW/m^3, while a value of around 95 kW/m^3 was calculated using DSMC and VSL with a two-temperature model and slip boundary conditions. For the other VSL calculations, a stagnation point heat flux of around 120 kW/m^3 was obtained at this altitude. These results emphasise once again that continuum approaches significantly overpredict the stagnation point heat transfer to a blunt body in rarefied hypersonic flow, and also indicate some inaccuracies in the DSMC calculations.

CHAPTER 3

Producing Rarefied Flow in a Small Reflected-Shock Tunnel

The University of Queensland's collection of impulse-flow facilities includes a small reflected-shock tunnel [7, 19]. The flow generated in the Small Shock Tunnel (SST) is non-reacting because the stagnation temperature is limited to the moderate value of 2500 K, which also limits the test flow speed to around 2 km/s. While hypervelocity flows cannot be realised in the SST, it is still desirable to operate the facility at rarefied conditions in order to provide a high Mach number, non-reacting reference flow for computational and experimental techniques to be applied to the flow in the X1 expansion tube. Unlike X1 (see Chapter 4 for details), the SST does not have a free piston driver nor as many stages of gas processing so simulation techniques can be assessed at low densities without as many confounding influences. The lack of chemical reactions and a free piston driver in the SST also allows the performance of instrumentation at low densities to be evaluated in the absence of high levels of flow noise. In addition to this, producing rarefied flow in the SST is beneficial simply because it expands the range of experimental testing that can be carried out at the University of Queensland.

The possibility of generating rarefied flow in the Small Shock Tunnel is explored in this chapter. First, a description of the SST is presented, where the flow processes that generate the test flow for normal density operation are discussed in some detail. Following this, analytical calculations of the fill conditions required to produce the target level of test flow rarefaction are presented. Numerical simulations were used to assess whether these fill conditions produce a useful rarefied test flow when either a contoured nozzle or a conical nozzle is installed. Further simulations were used to refine the fill conditions and investigate the flow processes that occur in the facility during low density operation. The

details and results of the numerical models are presented in this chapter. The chapter concludes with a recommendation of the configuration and fill conditions that should be used to produce a rarefied test flow in the SST and an experiment that could be conducted in the new test flow conditions.

3.1 The Small Shock Tunnel

The Small Shock Tunnel facility (SST) at the University of Queensland is a reflected shock tunnel with a fixed-length high pressure driver [7, 20]. At present it is primarily used for laser optics and the investigation of problems associated with larger reflected shock tunnels. It is a relatively low enthalpy facility, operating up to a maximum enthalpy of approximately 3 MJ/kg with a room-temperature helium driver. Total temperatures in the nozzle supply region are limited to 2500 K resulting in minimal chemical and thermal non-equilibrium effects, making analysis of the test flows relatively simple.

The layout of the SST is illustrated in Figure 3.1. The tunnel consists of a high pressure cylinder that initially contains the driver gas, a lower pressure cylinder referred to as the shock tube in which the test gas is initially contained, a nozzle, a test section, and a dump tank. The driver and shock tube are separated by an aluminium diaphragm known

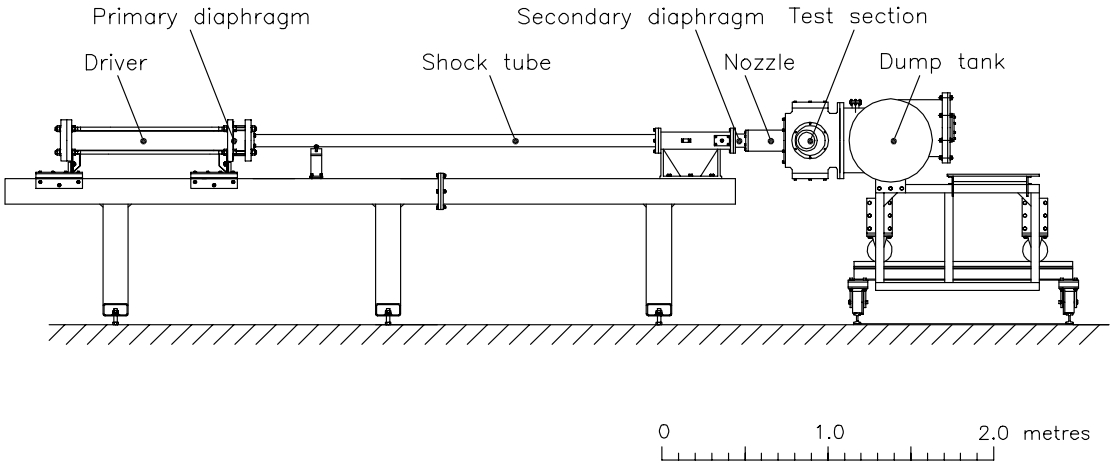

Figure 3.1: Layout of the Small Shock Tunnel (Figure 5.1 from [19]).

as the "primary" diaphragm. This can be ruptured with the aid of a pneumatic piercing mechanism contained within the driver tube. For normal density operation the driver tube is typically filled with bottled high pressure helium or nitrogen to a maximum pressure of 6 MPa absolute, the shock tube is filled with test gas to a pressure of the order of 20 kPa absolute. When the primary diaphragm is ruptured, the high pressure driver gas expands into the shock tube and generates a shock wave which rapidly compresses the low pressure test gas. This shock wave, which is referred to as the primary shock, propagates along the length of the shock tube compressing and accelerating the test gas. This process is illustrated via the distance-time ($x-t$) wave diagram in Figure 3.2 along with the other

processes that occur in the SST.

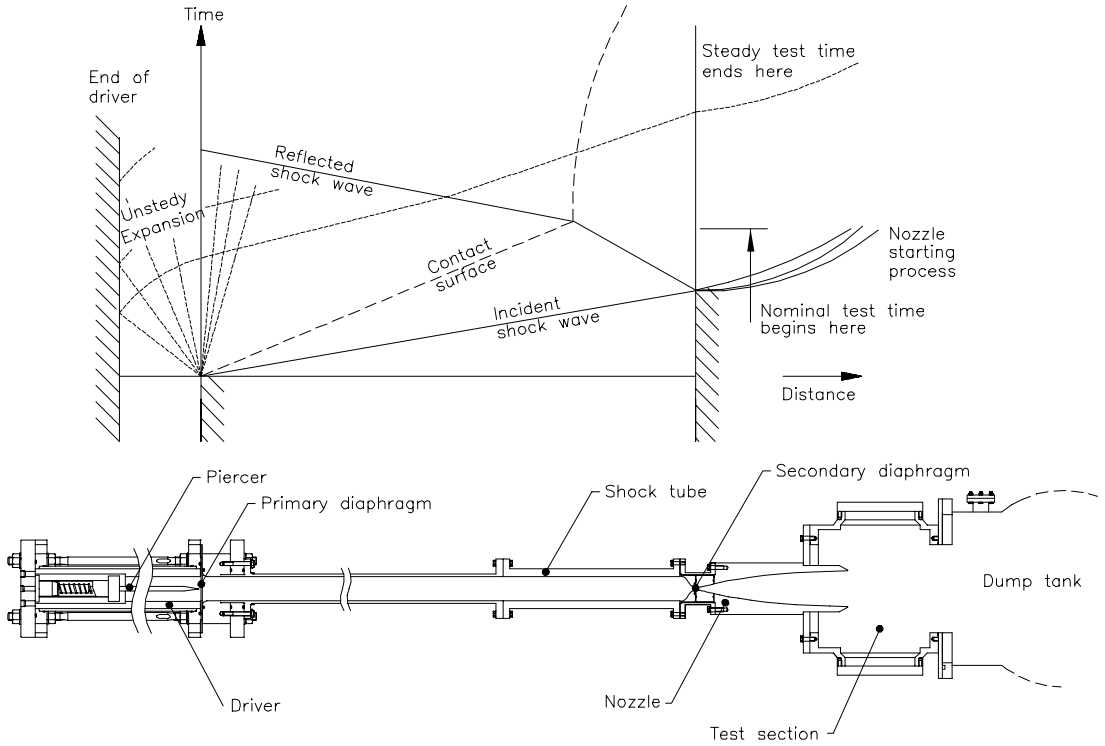

Figure 3.2: Wave diagram of the shock and expansion processes that produce the test flow in the SST (Figure 5.2 from [19]).

The primary shock reflects off the nozzle contraction region where a cellophane or thin plastic secondary diaphragm is placed. The shock reflected from the secondary diaphragm generates nominally stagnated high pressure and high temperature gas. This high pressure gas ruptures the secondary diaphragm and then expands through the nozzle into the test section and dump tank. For normal density operation the test section and dump tank are both evacuated to a pressure less than 400 Pa prior to conducting a test in the tunnel. The beginning of test flow is signified by the termination of the nozzle starting process and the establishment of a steady expansion into the test section. The nozzle starting process will be discussed in more detail after the flow processes that occur within the shock tube have been discussed.

While the test gas expands through the nozzle into the test section, the reflected shock wave travels back up the shock tube and passes through the interface between the driver and test gas. If no further shocks or expansion waves are produced when the shock interacts with the interface, conditions in the tunnel are said to be “tailored” [90]. Tailored conditions are characterized by a steady nozzle supply pressure and an interface that slowly

moves towards the nozzle throat as the gas in the nozzle supply region flows through into the test section (as illustrated in the top part of Figure 3.2).

In theory, the test time in a reflected shock tunnel operating at tailored conditions is limited by the propagation of expansion waves into the test section provided the supply of test gas has not been exhausted. Ignoring contamination, waves that limit the test time emanate from the unsteady expansion of the driver gas and are reflected from the end of the driver as can be seen from Figure 3.2. In practice, the useful test time may have terminated well before these theoretical limits. Various studies have shown that complex interactions between the boundary layer in the shock tube and the reflected shock can reduce the ideal test time through contamination of the test gas slug with driver gas [22, 80]. Bifurcation of the reflected shock into two oblique shock waves within the boundary layer can cause driver gas to "jet" along the wall and subsequently contaminate the nozzle supply region [80]. This is the reason why an 'under-tailored' mode of operation is often preferred. In this mode, the interaction of the reflected shock and the contact surface generates expansion waves that propagate into the nozzle supply region. The nozzle supply pressure subsequently decreases with time, however, the contact surface moves upstream away from the nozzle thereby delaying the arrival of the driver gas and increasing the test time. On the other hand, "over-tailored", or "equilibrium interface", operation produces a series of reflected shock waves which result in an increasing pressure in the nozzle supply region, but a shorter test period before driver gas contamination occurs.

A typical SST nozzle supply pressure history measured by Craddock [19] is shown in Figure 3.3 for tailored conditions with helium driving a nitrogen test gas. The transducer used to record the nozzle supply pressure history was located 68 mm upstream of the nozzle contraction. The time scale has been referenced to the arrival time of the primary shock. Shortly after the initial shock passes the pressure transducer, the reflected shock passes in the opposite direction followed by a gradual increase in pressure to a maximum, then a slow decay. Close inspection of the increase in pressure due to the reflected shock shows that the pressure increase is stepped. This stepped increase in pressure suggests that the reflected shock is bifurcated into two oblique shock waves within the boundary layer containing a separation bubble. The gradual increase in pressure after the passage of the bifurcated reflected shock is possibly a result of a pseudo-shock train set up by the bifurcated reflected shock. This shock train would slowly decelerate the driver gas and

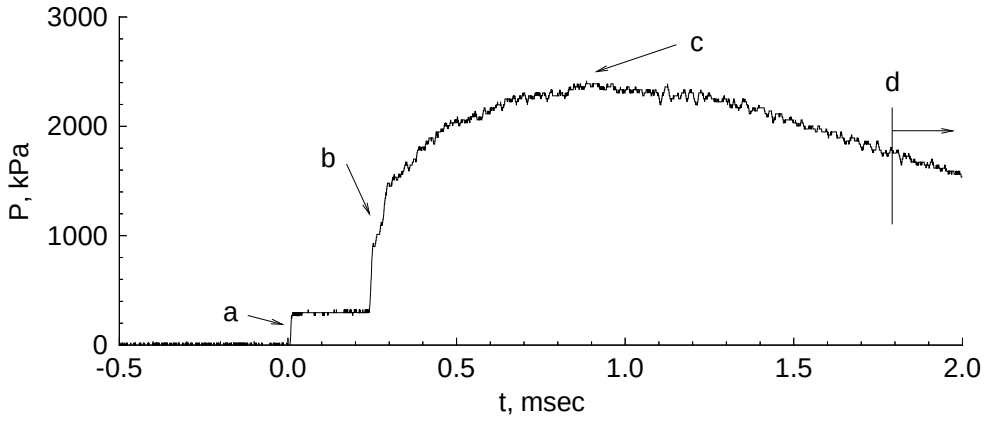

Figure 3.3: Typical history of the nozzle supply pressure showing the principal events: (a) arrival of the incident shock; (b) reflected shock; (c) establishment of equilibrium pressure; (d) driver gas contamination (Figure 5.3 from [19]).

cause the test gas pressure to increase. Eventually the drainage of the test gas through the nozzle causes the pressure to decay.

The test gas drains through the nozzle throat and into the divergent part of the nozzle once the initial shock has reflected off the end of the shock tube and caused the light secondary diaphragm to rupture. The initial flow of the test gas through the nozzle forms a series of unsteady shocks and expansions as it moves down the nozzle. This process, known as nozzle starting, can significantly reduce the available test time for pulse facilities where the test time is of the same order as the nozzle starting time. A quantitative understanding of the starting process can be gained from the experimental and analytical studies of Amann [2] and Smith [77] which were briefly summarised by Craddock [19] whose summary is repeated in the following paragraph.

> The rupture of the light secondary diaphragm causes a shock to form (labelled [a] in Fig. 3.4), which travels down the nozzle accelerating the low pressure gas already in the nozzle. Upstream of the shock is a contact surface (labelled [b]), which separates the test gas and the accelerated gas originally in the nozzle. The diverging walls of the nozzle slow the shock down, however, the test gas behind it is expanded to a high Mach number. This differential causes an upstream-facing shock (labelled [c]) to be formed which moves upstream relative to the mean fluid velocity, but has a net downstream motion due to the high fluid velocity. Between the upstream-facing shock and the

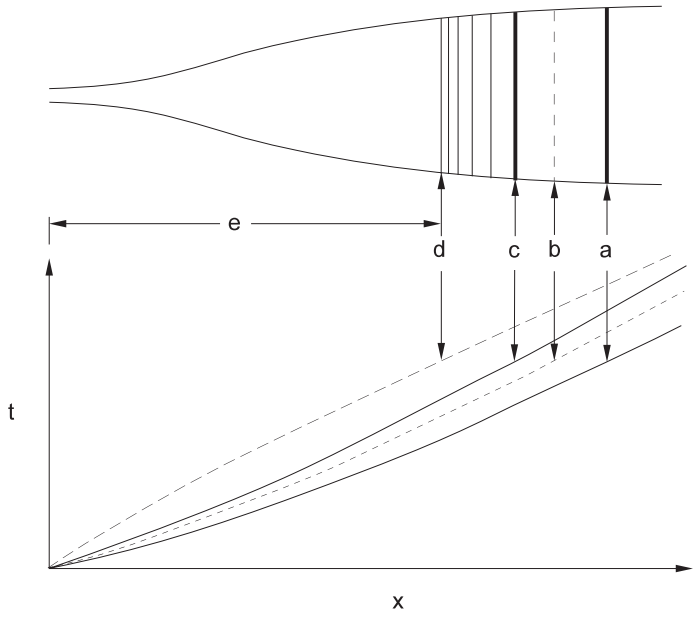

Figure 3.4: Quasi-one-dimensional representation of the nozzle starting process in both the physical and x-t plane [77]. Labelled features are: [a] primary shock; [b] contact surface; [c] upstream facing shock; [d] upstream head of unsteady expansion; [e] steady expansion (Figure 5.4 from [19]).

steady expansion generated at the nozzle throat (labelled [e]), is an unsteady expansion ([c] to [d]), which also has a net motion downstream with velocity $u - a$. All of these waves eventually move out of the nozzle and into the test section after which time the test time begins. The time from the passage of the initial shock through the test section to the arrival of the steady expansion flow is largely a function of the nozzle geometry and Mach number of the flow. Smith [77] noted that the starting time can be reduced for a given Mach number nozzle by increasing the nozzle expansion angle and reducing the size of the throat. Relatively large initial pressures in the nozzle prior to the arrival of the starting waves can also increase the nozzle starting time, however, this only becomes a concern for high stagnation temperature flows ($>$ 3500K) [77, 26, 34] because the available test time is correspondingly short.

The time required to establish a steady expansion within the nozzle is also governed by the attachment and stabilisation of the wall boundary layer. For long, high Mach number nozzles, the boundary layer on the nozzle wall is typically very thick and can take an appreciable amount of time to attach even after the starting waves have moved through the nozzle [19]. Operating at low densities will make this problem worse. A careful

investigation of the nozzle starting process is necessary when assessing the viability of producing a rarefied test flow in the SST.

This discussion on the flow processes that occur within the SST during normal density operation provides a background for assessing the viability of using the facility to produce rarefied test flows. For low-density operation of the SST, the same basic flow processes will occur with each process altered to some degree by low-density effects, such as thicker boundary layers in the shock tube and nozzle.

3.2 Analytical Calculation of Required Operating Conditions

As part of an undergraduate thesis, an attempt was made to generate rarefied flow in the SST by arbitrarily reducing the fill pressures from the normal operating pressures to values of 325 kPa in the driver and 3 kPa in the shock tube [6]. No effort was made to determine whether these fill conditions would produce test flows in which significant rarefaction effects could be measured on models placed in the test section. The logical first step towards producing rarefied flow in the SST is estimate what fill conditions will produce a test flow with a P_D value of 0.04, so that the flow over a model of characteristic size D will be in the transitional regime.

The conditions in the test flow can be approximated analytically by examining the one-dimensional approximations of the processes that occur within the tunnel. Operation of the tunnel begins when the primary diaphragm is ruptured causing the primary shock to propagate down the shock tube. The conditions behind the primary shock can be found by solving what is known as the Riemann problem (see e.g. [25]). The Riemann problem is to determine what occurs when interaction is allowed between two uniform slugs of gas, known as the left and right states, which have different properties. In this case the left and right states correspond to the fill conditions in the driver and shock tube respectively. The solution of the Riemann problem depends on the ratio of the left and right pressures, not their absolute values [25]. Ideally, this implies that if the ratio of the pressure in the driver to the pressure in the shock tube is maintained when the fill pressures are decreased, then the Mach number of the primary shock, and hence the temperature and flow speed behind it, will be unchanged. The next process that occurs in the ideal case is the reflection of the primary shock from the convergent section of the nozzle. For an ideal gas the Mach number of reflected shock, M_R, is found by solving,

$$\frac{M_R}{M_R^2-1} = \frac{M_I}{M_I^2-1}\sqrt{1+\frac{2(\gamma-1)}{(\gamma+1)^2}(M_I^2-1)\left(\gamma+\frac{1}{M_I^2}\right)},$$

where M_I is the Mach number of the incident shock (see e.g. [5]). It can be seen from this expression that as Mach number of the primary shock is not altered by the uniform scaling of the fill pressures, then M_R will also be unaffected. Also, for an ideal gas the

ratio of properties across a shock are a function of the shock Mach number and γ only. The point of the above argument is that if the pressures are uniformly scaled, gas behind the reflected shock will be stagnated as in the normal case, resulting in tailored operation. The nozzle supply temperature, T_{res}, which is the temperature behind the reflected shock will also be identical to the value produced during normal operation.

For adiabatic, isentropic flow through the nozzle, the Mach number at the nozzle exit plane, M_e, is a function of the ratio of the exit area of the nozzle, A_e, to the throat area, A_*, as can be seen from the following relation governing isentropic nozzle flow;

$$\left(\frac{A_e}{A_*}\right)^2 = \frac{1}{M_e^2}\left[\frac{2}{\gamma+1}\left(1+\frac{\gamma-1}{2}M_e^2\right)\right]^{\frac{\gamma+1}{\gamma-1}} . \tag{3.1}$$

For supersonic flow at the nozzle exit, both the total temperature and pressure are constant so the temperature and pressure at the nozzle exit, T_e and p_e, can be calculated using the Mach number relations,

$$\frac{T_{res}}{T_e} = 1+\frac{\gamma-1}{2}M_e^2 \tag{3.2}$$

$$\frac{p_{res}}{p_e} = \left(\frac{T_{res}}{T_e}\right)^{\frac{\gamma}{\gamma-1}} . \tag{3.3}$$

The density at the nozzle exit, ρ_e, can readily be calculated using the ideal gas law. These relations indicate that, for ideal operation of the SST, the temperatures, Mach numbers and pressure ratios within the facility remain unchanged when the fill pressures throughout the facility are uniformly scaled down. This allows the conditions produced during low density operation to be estimated from the normal operating conditions. When the fill pressures are reduced by a factor, which will referred to from here on as the pressure reduction factor (PRF), the pressure in any region can be estimated by dividing the normal operating pressure in that region by the PRF. This also applies to the density in any region because the temperature is unchanged so the density will also be scaled by the PRF.

The fill and nozzle supply conditions from reference [7] for normal, tailored operation of the SST with a helium driver and nitrogen test gas are shown in Table 3.1. The conditions in the test section are approximated as being equal to the conditions at the nozzle exit plane for these quasi-one-dimensional calculations. The temperature and pressure at the nozzle exit plane are found from the nozzle supply conditions given in Table 3.1

Driver gas	helium
Driver fill pressure, p_{drv}	3.25 MPa
Driver fill Temperature, T_{drv}	296 K
Test gas	nitrogen
Shock tube fill pressure, p_{st}	16.5 kPa
Driver fill Temperature, T_{st}	296 K
Initial test section/dump tank pressure, p_{evac}	400 Pa
Initial test section/dump tank Temperature, T_{evac}	296 K
Nozzle supply temperature, T_{res} (computional)	1920 K
Nozzle supply pressure, p_{res} (experimental)	2.0 MPa

Table 3.1: SST operating conditions from reference [7].

using equations 3.2 and 3.3. In these equations the exit Mach number, M_e, is set to the value that the nozzle was designed to produce, 7, rather than the higher value that would be obtained by solving equation 3.1. The reason for this is that the nozzle wall boundary layers significantly decrease the effective exit area of the nozzle, and consequently the exit Mach number, hence the higher Mach number would be unrealistic. The breakdown parameter, P_D, for normal operation is then calculated using equation 2.5. A characteristic dimension, D, of 10 mm was chosen for the calculation of the breakdown parameter as in references [6] and [49]. The nozzle exit conditions calculated using this procedure are shown in Table 3.2.

T_e	177.8 K
p_e	483.1 Pa
ρ_e	9.155×10^{-3} kg/m^3
Re_D	1.345×10^{4}
P_D	4.519×10^{-3}

Table 3.2: Analytically estimated nozzle exit conditions for normal density operation of the SST.

Substituting $Re_D = \rho u D/\mu$ into equation 2.5, then using the ideal gas law to express density as p/RT yields,

$$P_D = \frac{\sqrt{\pi}\gamma M^2}{2}\frac{RT}{puD} .$$

Let the superscripts $rarefied$ and $normal$ denote the conditions in the SST during low and normal density operation respectively. As the temperature and velocity are ideally unchanged for the two operating conditions, it can be seen that at the nozzle exit plane,

$$\frac{P_D^{rarefied}}{P_D^{normal}} = \frac{p_e^{normal}}{p_e^{rarefied}} = PRF . \tag{3.4}$$

Setting $P_D^{rarefied}$ to the target value of 0.04 identified in the previous chapter, and using the P_D value for normal operation from Table 3.2, a PRF value of 8.85 was calculated from equation 3.4. This indicates that if the fill pressures in the SST are uniformly decreased by a factor of approximately 10, then the breakdown parameter in resultant test flow should approach the target value of 0.04.

3.3 Numerical Simulations

To further assess the possibility of producing rarefied flow in the SST, two-dimensional effects that were neglected in the previous section must be investigated. Boundary layer growth along the nozzle wall and the nozzle starting process are the two items most likely to affect the performance of the tunnel at low densities. The reason for this is that boundary layer thickness increases as the flow tends toward lower densities. This can be readily seen by examining the analyical estimate for the thickness, δ, of a laminar boundary layer on a flat plate (see e.g. [24]):

$$\delta = \frac{5x}{Re_x^{0.5}} \propto \frac{1}{\sqrt{\rho}} ,$$

where x is the distance from the boundary layer origin. The densities towards the exit of the nozzle are orders of magnitude lower than in other portions of the facility, so it is here that the thicker boundary layers will be most significant. To investigate their effect in this region, along with the nozzle starting process, the SST nozzles and test section have been modelled axisymmetrically using the compressible Navier-Stokes solver, Mb_cns [38]. These models are also used to investigate the effect of the initial pressure in the test section (p_{evac}) on the nozzle starting process and the test flow. This needs to be investigated due to the difficulty in evacuating the test section and dump tank to pressures below the usual value of 400 Pa because of air leaks into the facility and the limited capacity of the vacuum pump.

3.3.1 Mach 7 Contoured Nozzle Simulations

The Mach 7 contoured nozzle was modelled first as it produces parallel flow in the test section during normal operation, which is ideal for experimental research. This nozzle would be most useful if it functions at low densities because, in addition to parallel flow being ideal for experiments, the lack of gradients in the resultant core flow leads to small values of the breakdown parameter, P, which imply that the core flow will not be subject to non-continuum effects.

The computational model, *m7ndt* (for Mach 7 nozzle and dump tank), extends from the nozzle throat to the entrance of the dump tank and is based on the overall geometry shown in Figure 3.5. The geometric definition of the computational model is contained in the simulation's input parameter file, *m7ndt.sit*, which is included in Appendix B. The

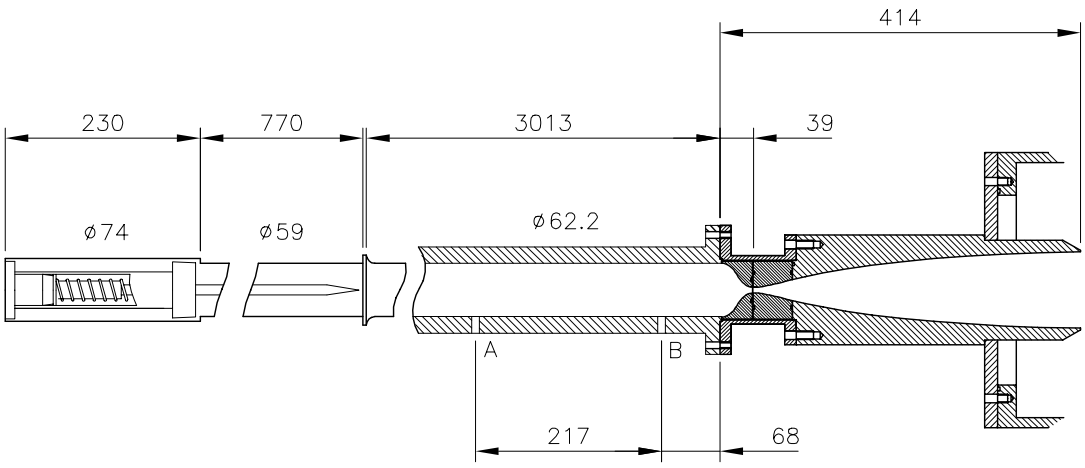

Figure 3.5: SST Mach 7 contoured nozzle and test section (Figure 6.6 from [19]).

entrance to the dump tank is modelled as a supersonic outflow boundary condition in the simulation; this assumes that the pressure in the dumptank does not reach a level high enough to significantly affect the test flow within the simulation time. The nozzle is modelled from the throat onwards to allow a supersonic inflow boundary condition to be set. Boundary layer growth in the contraction, which is not included in the model, is expected to be negligible due to the short length of this section (39 mm) and the relatively low speeds and high densities upstream of the throat. The computational grid for the nozzle has 70 cells in the cross-flow direction and 280 cells in the axial direction. The cells are radially clustered towards the wall, as can be seen in Figure 3.6, in order to adequately capture the boundary layer growth.

The cells in the nozzle and test section are initially filled with room temperature nitrogen. The pressure of this fill gas is varied between simulations to establish what level of evacuation is required for the nozzle to start properly and produce a uniform test flow. The inflow temperature and pressure at the nozzle throat are calculated from the nozzle supply conditions in Table 3.1 and the PRF using the following relations that assume a perfect gas and a throat Mach number of 1.0:

$$\frac{T_{res}}{T_*} = \frac{\gamma - 1}{2}$$

$$\frac{p_{res}}{p_*} = PRF \left(\frac{\gamma - 1}{2} \right)^{\frac{\gamma}{\gamma - 1}}$$

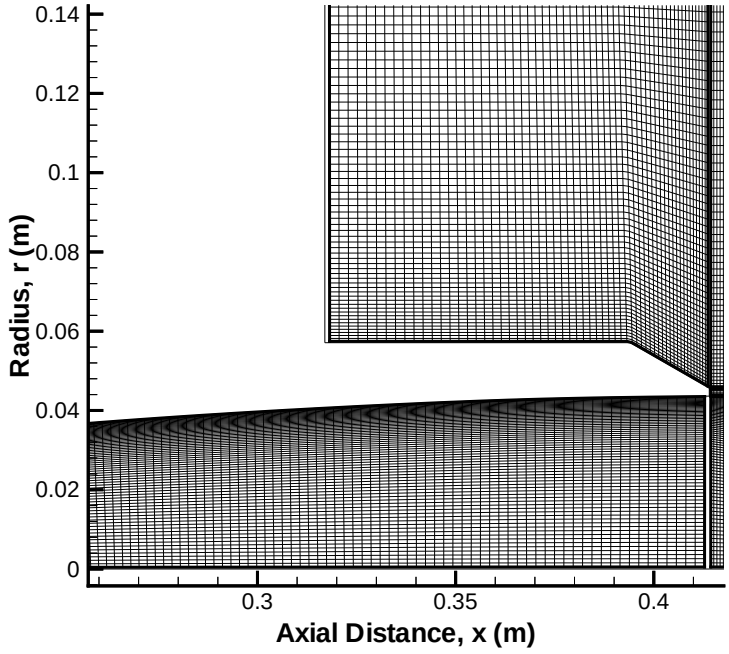

Figure 3.6: Sample of the mesh for the Mach 7 contoured nozzle numerical model.

The flow speed at the throat, which is equal to the sound speed, is then calculated using,

$$u_* = a_* = \sqrt{\gamma R T_*} \, .$$

The simulations were initiated at the rupture of the secondary diaphragm (located at the nozzle throat) and were terminated 1 ms after the rupture, allowing the entire nozzle starting process and expected test time to be simulated.

The initial simulation of the contoured nozzle and test section used a PRF of 10 and a fill pressure of 200 Pa (≈1.5 torr). This relatively high value of p_{evac} was tried because it can be readily achieved with the vacuum pump attached to the SST. The evolution of the flow field over the simulation time is shown in Figure 3.7. It can be seen from the first frame of Figure 3.7 that, as the starting waves move through the nozzle, the boundary layer is separated from the nozzle wall in the region of the contact surface. The next frame shows the flow field as the starting waves are exiting the nozzle. The relatively high initial pressure in the nozzle has caused the boundary layer to detach from the nozzle wall for the majority of its length. The strong oblique shock waves caused by the boundary layer separation can clearly be seen in the final three frames of Figure 3.7 along with the shear

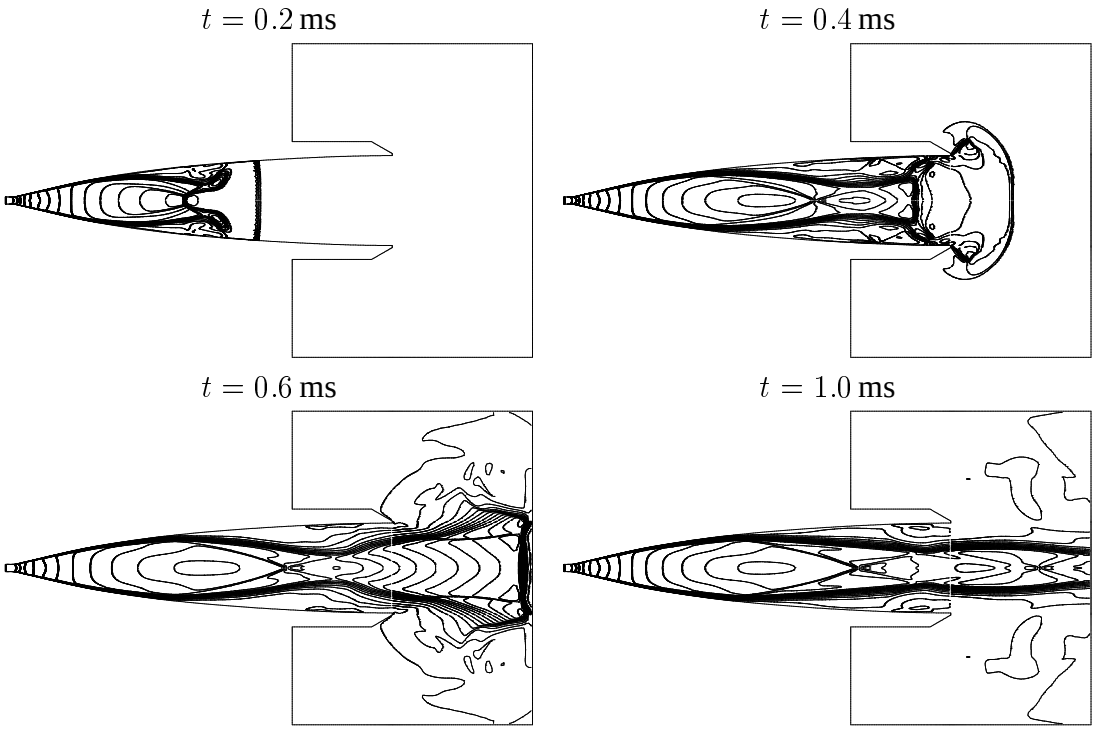

Figure 3.7: Mach number contours showing the evolution of the flow field in the SST Mach 7 contoured nozzle and test section for PRF = 10 and p_{evac} = 200 Pa. Time, t, is the time after secondary diaphragm rupture.

layer between the expanded test gas and the relatively stagnant gas within the separation bubble. The final frame was generated 1 ms after diaphragm rupture, by this time the flow field has become reasonably steady. While the boundary layer is attached over a greater length of the nozzle wall than earlier, the oblique shock structure remains intact, which prevents the nozzle from producing a usable test flow.

For the second simulation p_{evac} was reduced to 133 Pa (≈1 torr). The flow structure that evolved was qualitatively very similar to that computed in the first simulation with p_{evac} = 200 Pa. This can be seen by comparing the last frame of Figure 3.7 with Figure 3.8, which shows the computed Mach number contours from the second simulation at 1 ms after diaphragm rupture. It is apparent that the backpressure in the nozzle and test section, p_{evac}, must be significantly decreased to allow the nozzle to start properly.

To establish whether the contoured nozzle can produce a useful test flow for a PRF of 10, p_{evac} was reduced 33 Pa (≈0.25 torr) for the third simulation. The evolution of the flow field over the simulation time is shown in Figure 3.9. It can be seen from the first frame of Figure 3.9 that, as with the previous simulations, the boundary layer is separated

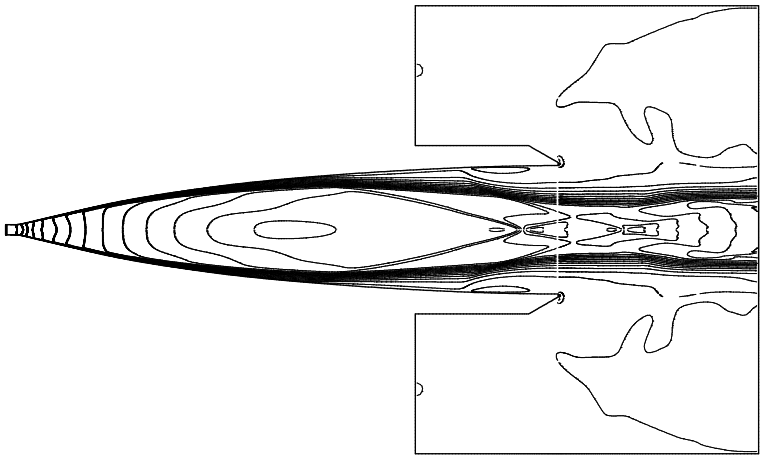

Figure 3.8: Mach number contours showing the flow field in the SST Mach 7 contoured nozzle and test section 1 ms after secondary diaphragm rupture for PRF = 10 and p_{evac} = 133 Pa .

from the nozzle wall near the location of the contact surface. However, the separation distance is visibly smaller than in the case with p_{evac} = 200 Pa. By the time of the third frame, at t = 0.6 ms, the boundary layer is attached over almost the entire length of the nozzle, and a reasonably uniform core flow has been established. It can be seen from the final frame Figure 3.9 that the nozzle has started properly with the backpressure of 33 Pa used in the third simulation; the boundary layer is completely attached and the core flow at the nozzle exit is devoid of strong waves. The flow exiting the nozzle is "under-expanded", meaning that the static pressure of the flow is greater than the backpressure in the test section. The pressure of the core flow is reduced to the backpressure across an expansion fan centered on the nozzle exit, which can be seen in the final two frames of Figure 3.9.

A study by Smith [77] indicated that for normal densities and stagnation temperatures up to 3500 K, initial pressures in a shock tunnel nozzle of up to the steady static pressure of the core flow can be tolerated without any loss of test time. To investigate whether this criteria still holds for the low density flows of interest here, a simulation was run with a backpressure of 50 Pa, which is slightly lower than the 56.85 Pa steady core flow pressure computed in the third simulation. The evolution of the flow field for the simulation with p_{evac}=50 Pa is shown in Figure 3.10. From this figure it can be seen that the boundary layer is detached near the nozzle exit throughout the simulation time. This causes weak oblique compression waves to form near the nozzle exit, which can be seen in the final two frames of Figure 3.10. At the nozzle exit plane, these compression waves cause a rise

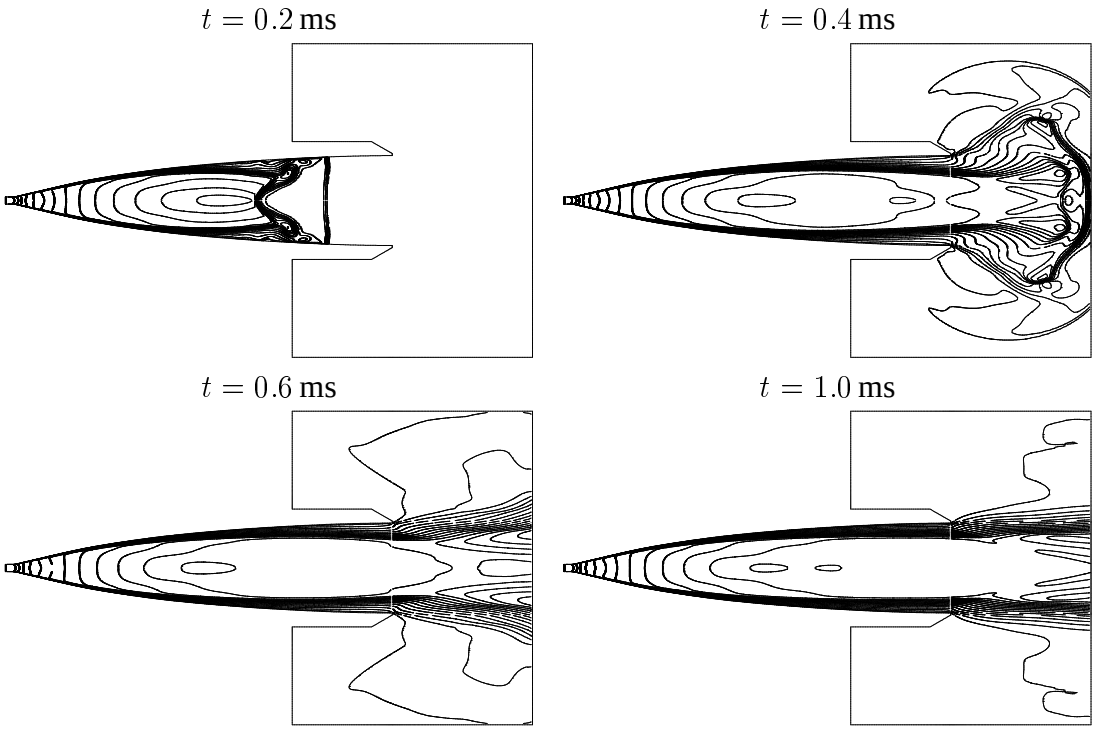

Figure 3.9: Mach number contours showing the evolution of the flow field in the SST Mach 7 contoured nozzle and test section for PRF = 10 and p_{evac} = 33 Pa. Time, t, is the time after secondary diaphragm rupture.

in Pitot pressure at a radius of approximately 25 mm. This can be seen in Figure 3.11, which compares the nozzle exit Pitot pressure profiles from three different simulations. It appears that the backpressure used in this simulation is slightly too high to allow the nozzle to operate ideally even though the flow is under-expanded. This indicates that the previously mentioned criteria of Smith [77] does not hold for the low densities used here, and that for the Mach 7 contoured nozzle to operate properly at these low densities, the flow must be significantly under-expanded (i.e. $p_{evac} \approx 33$ Pa for $PRF = 10$).

ρ_{test}	1.07×10^{-3} kg/m^3
u_{test}	1863 m/s
p_{test}	56.85 Pa
T_{test}	179.6 K
$p_{pitot,test}$	3429 Pa
M_{test}	6.82
Re_{test}/L	1.689×10^5
$P_{D,test}$	0.03416
λ_{test}	0.0713 mm

Table 3.3: Nominal test conditions 10 mm from the Mach 7 contoured nozzle exit plane for p_{evac} = 33 Pa and PRF = 10.

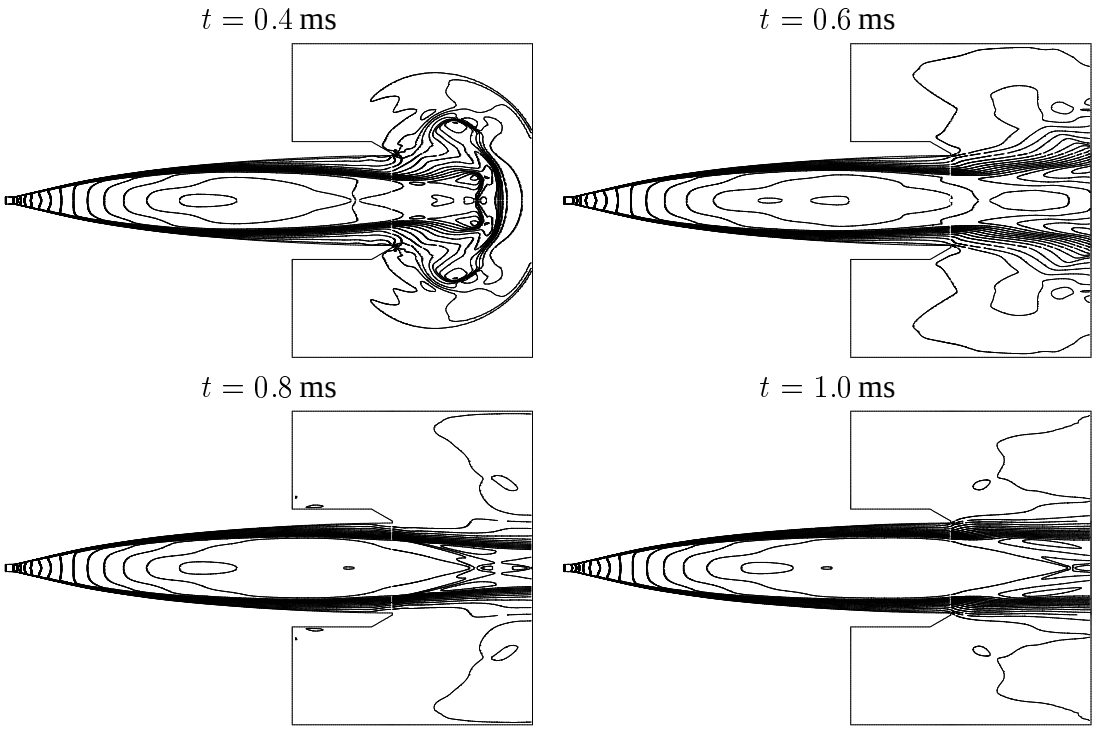

Figure 3.10: Mach number contours showing the evolution of the flow field in the SST Mach 7 contoured nozzle and test section for PRF = 10 and p_{evac} = 50 Pa. Time, t, is the time after secondary diaphragm rupture.

For tests in the SST utilizing optical measurement techniques, models are typically located 10 mm downstream of the nozzle exit plane [52]. For the fill conditions that were found to produce a useful test flow (p_{evac} = 33 Pa and PRF = 10), the computed profiles of some important flow properties at the model location are shown in Figure 3.12. From these profiles it can be seen that the core flow produced by the Mach 7 contoured nozzle has a radius of approximately 27 mm. The nominal test conditions were taken to be those at a radius of 20 mm and are given in Table 3.3. The P_D value of 0.034 in the test flow is 14.6% lower than the target value of 0.04. To achieve the target P_D value, the PRF would have to be increased, which would result in a corresponding decrease in the static pressure of the test flow. For the contoured nozzle to operate properly for such a condition, p_{evac} would have to be decreased below 33 Pa. As this cannot be achieved with the vacuum pump currently attached to the SST, simulations of the contoured nozzle for higher PRF values have not been carried out. Instead it was decided to investigate the performance of the facility's Mach 7 conical nozzle at low densities.

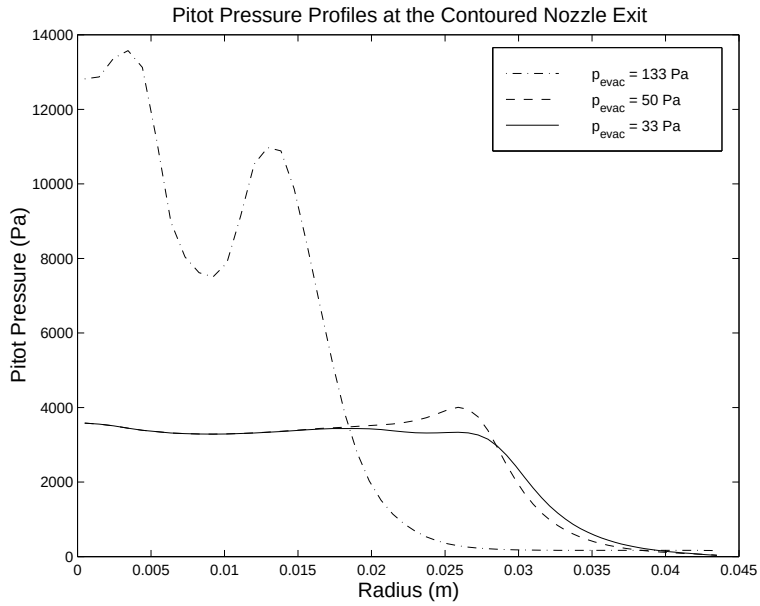

Figure 3.11: Computed Pitot pressure profiles across the exit of the SST Mach 7 contoured nozzle 1 ms after secondary diaphragm rupture for PRF = 10 and p_{evac} = 133 Pa, 50 Pa and 33 Pa.

3.3.2 Mach 7 Conical Nozzle Simulations

The SST is also equipped with a conical nozzle that nominally produces Mach 7 flow. Figure 3.13 shows the Mach 7 conical nozzle installed in the SST. While this nozzle produces a slightly divergent test flow, its overall length is approximately half that of the contoured nozzle, leading to a significant reduction in the boundary layer thickness at its exit plane. The conical nozzle has strong favourable pressure gradients along its entire length while, in contrast, the flow straightening part of the contoured nozzle involves some turning-related recompression of the gas. It was hoped that this, along with the reduction in the effect of the nozzle wall boundary layer, would allow the conical nozzle to operate effectively for a value of p_{evac} greater than 33 Pa. To investigate this, the Mach 7 conical nozzle was numerically modelled in the same manner as the contoured nozzle. The computational model, *m7coni_ndt* (for Mach 7 conical nozzle and dump tank), extends from the nozzle throat to the entrance of the dump tank and is based on the overall geometry shown in Figure 3.13. The exact geometry of the model is contained in the simulation's input parameter file, *m7coni_ndt.sit*, which is included in Appendix B. The supersonic inflow and outflow boundary conditions from the contoured nozzle simulations were also used in the conical nozzle simulations. The computational grid for the nozzle has 70 cells in the cross-flow direction and 280 cells in the axial direction.

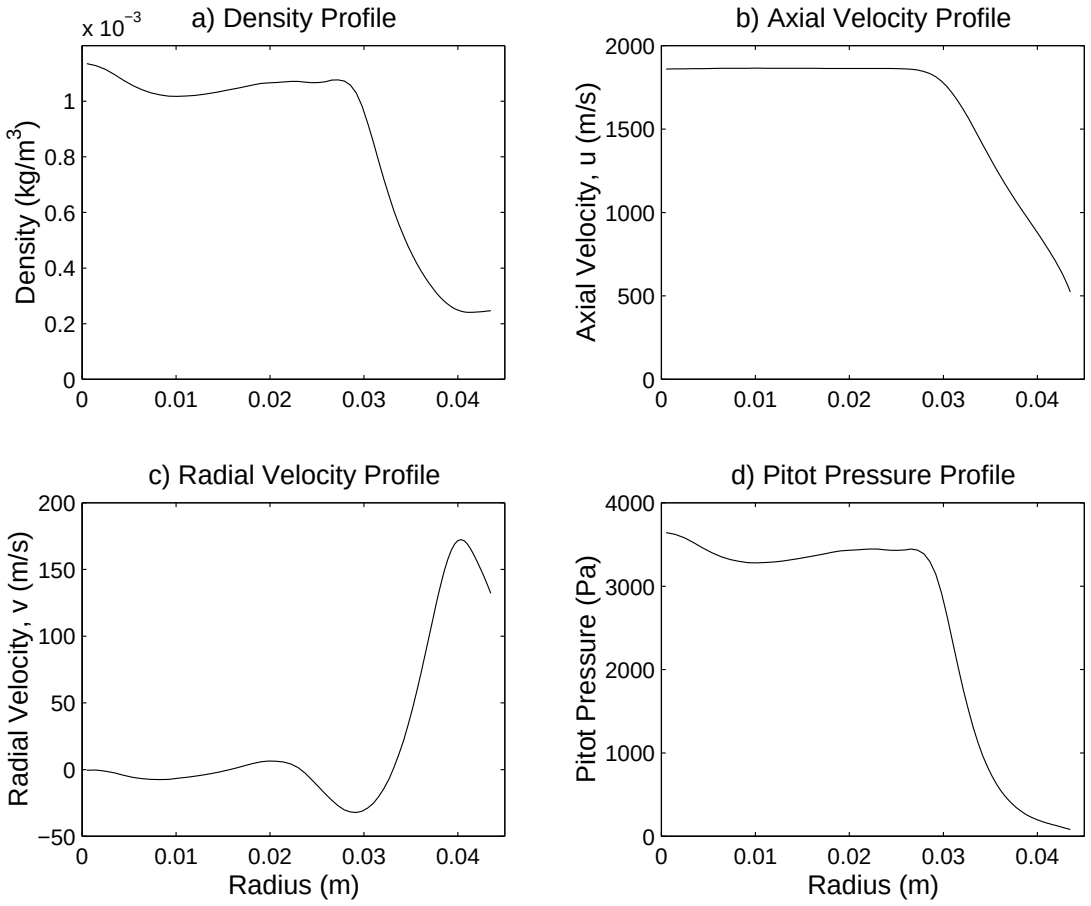

Figure 3.12: Computed profiles of density, axial velocity, radial velocity and Pitot pressure 10 mm from the SST Mach 7 contoured nozzle exit plane 1 ms after secondary diaphragm rupture for PRF = 10 and p_{evac} = 33 Pa.

As with the contoured nozzle, the first simulation of the conical nozzle was run with PRF = 10 and p_{evac} = 200 Pa. For these conditions, the conical nozzle performed in a similar manner to the contoured nozzle when a backpressure of 50 Pa was used; the boundary layer remained unattached near the nozzle exit for the entire simulation time. The backpressure, p_{evac}, was reduced to 133 Pa (1 torr) for the next simulation. Contour plots of Mach number from this simulation are presented in Figure 3.14. These show the evolution of the flow field during the simulation time. From Figure 3.14 it can be seen that the boundary layer rapidly becomes attached along the whole length of the nozzle wall despite the fact that the core flow is overexpanded. A clean test flow is present upstream of the oblique compression wave that raises the pressure of the core flow to the backpressure. As expected, the conical nozzle is capable of operating properly in the presence of a much higher backpressure (four times higher in this case) than the contoured nozzle.

Computed profiles of some important properties across the test flow at the model

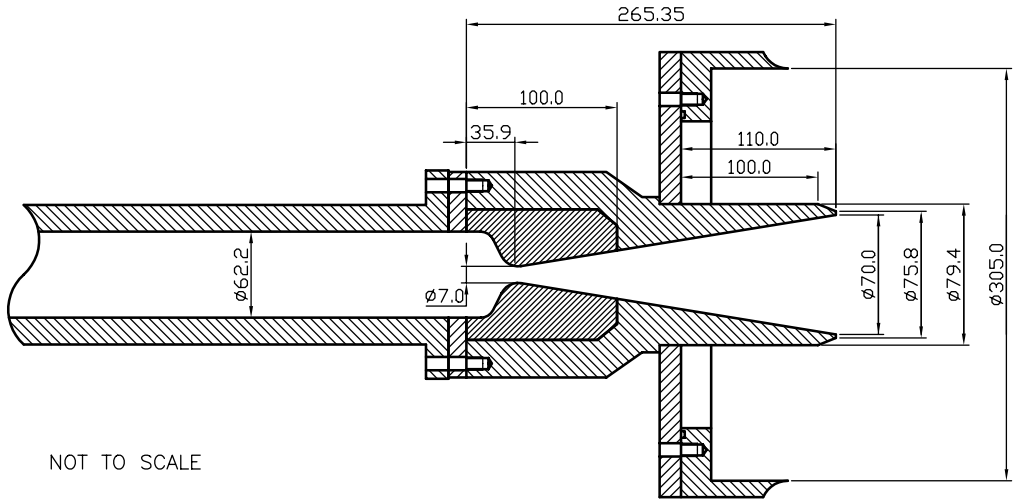

Figure 3.13: SST Mach 7 conical nozzle and test section.

location (10 mm downstream of the nozzle exit plane) are shown in Figure 3.15. From these profiles it can be seen that the core flow produced by the Mach 7 conical nozzle for a PRF of 10 has a radius of approximately 25 mm. The nominal test conditions were taken to be those at a radius of 10 mm and are given in Table 3.4. From Figure 3.15 it can be seen that the nozzle has performed very well with regard to producing a uniform test flow; the profiles of density, axial velocity and Pitot pressure are quite flat within the core flow. The radial velocity profile shows that the flow angularity does become significant towards the edge of the test flow, which is the major drawback of using a conical nozzle. The test flow Mach number of 6.565 is lower than the design value of 7 due to the thick boundary layer reducing the effective exit area of the nozzle. As the flow has not been expanded as much as was anticipated in Section 3.2, the P_D value of 0.02835 in the test flow is lower than the target value of 0.04. To achieve the target P_D value, the PRF must be increased to around 15.

ρ_{test}	1.269×10^{-3} kg/m^3
u_{test}	1855 m/s
p_{test}	72.43 Pa
T_{test}	192.3 K
$p_{pitot,test}$	4053 Pa
M_{test}	6.565
Re_{test}/L	1.886×10^{5}
$P_{D,test}$	0.02835
λ_{test}	0.0516 mm

Table 3.4: Nominal test conditions 10 mm from the Mach 7 conical nozzle exit plane for p_{evac} = 133 Pa and PRF = 10.

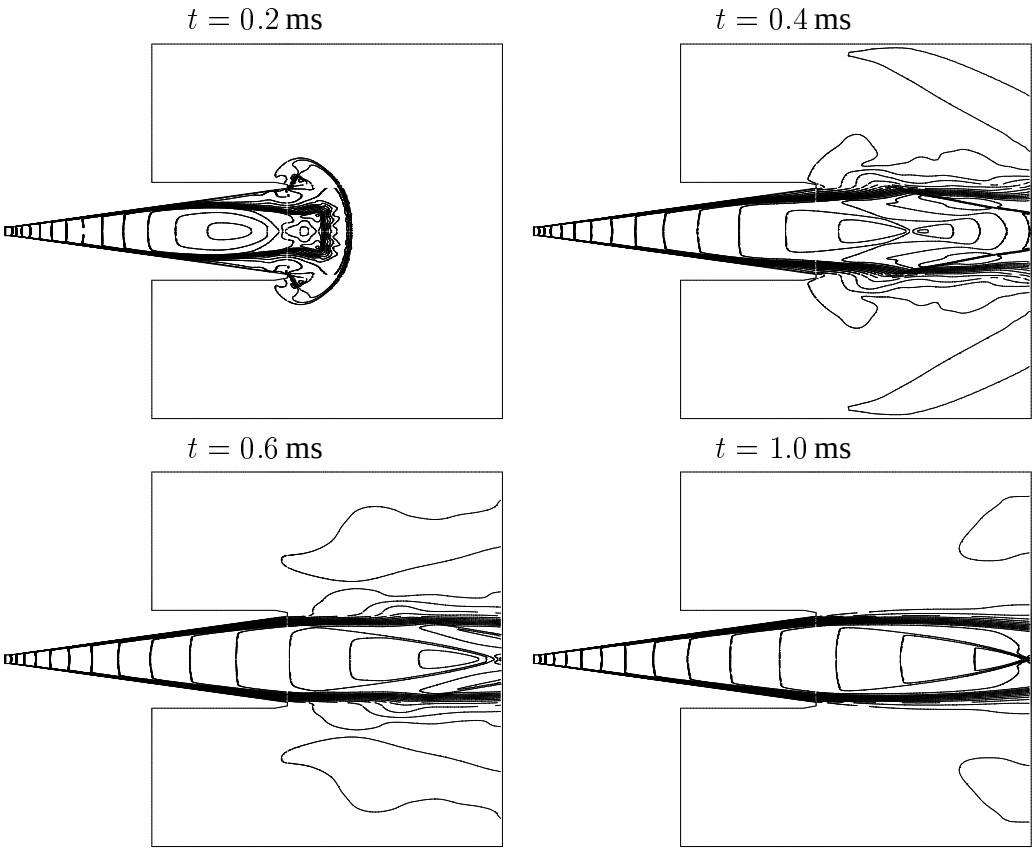

Figure 3.14: Mach number contours showing the evolution of the flow field in the SST Mach 7 conical nozzle and test section for PRF = 10 and p_{evac} = 133 Pa. Time, t, is the time after secondary diaphragm rupture.

For the next simulation the PRF was increased to 15 and p_{evac} was decreased to 67 Pa (0.5 torr). Contour plots of Mach number from this simulation are presented in Figure 3.16. As before, these show the evolution of the flow field during the simulation time. From Figure 3.16 it can be seen that the boundary layer rapidly becomes attached along the whole length of the nozzle wall as in the case with PRF =10. The core flow is overexpanded and an oblique shock has formed to compress it to the backpressure. A clean test flow is present upstream of the oblique shock.

Computed profiles of some important properties across the test flow at the model location (10 mm downstream of the nozzle exit plane) are shown in Figure 3.17. From these profiles it can be seen that the thicker boundary layers present when PRF = 15 have reduced the radius of the core flow to approximately 23 mm. The nominal test conditions were again taken to be those at a radius of 10 mm and are given in Table 3.4. As for the case with a PRF of 10, the conical nozzle has performed well with regard to producing a

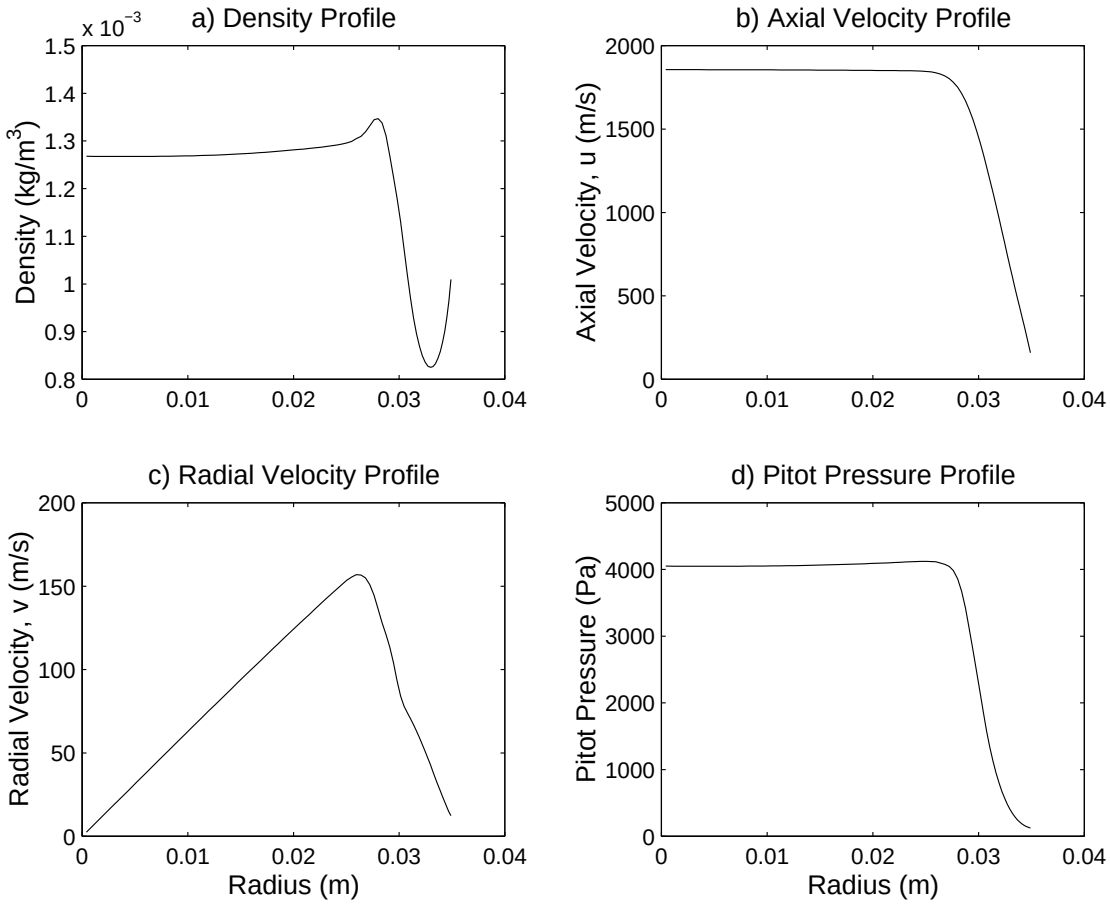

Figure 3.15: Computed profiles of density, axial velocity, radial velocity and Pitot pressure 10 mm from the SST Mach 7 conical nozzle exit plane 1 ms after secondary diaphragm rupture for PRF = 10 and p_{evac} = 133 Pa.

uniform test flow; the greatest deviations from the nominal values of density, axial velocity and Pitot pressure across the test flow are only 2%, 0.5% and 1.5% respectively. The radial velocity profile shows that the flow angularity becomes more significant towards the edge of the test flow. At the edge of the test flow at a radius of 23 mm, the radial velocity of 137 m/s corresponds to a flow angularity of 4.2^0. The P_D target value of 0.04 has been achieved precisely, leading to the tentative conclusion that the fill conditions used in this simulation (PRF = 15 and p_{evac} = 67 Pa) will produce a test flow suitable for experiments in which the effects of rarefaction are important.

Before it can be concluded that a suitable operating condition has been established, it must be checked whether the continuum approach used to simulate the flow in the SST was valid. To enable this, a contour plot of the breakdown parameter, P, in the conical nozzle and test section has been produced for the proposed test conditions (see Figure 3.18). It can be seen that the critical value of 0.04 is exceeded only in very narrow

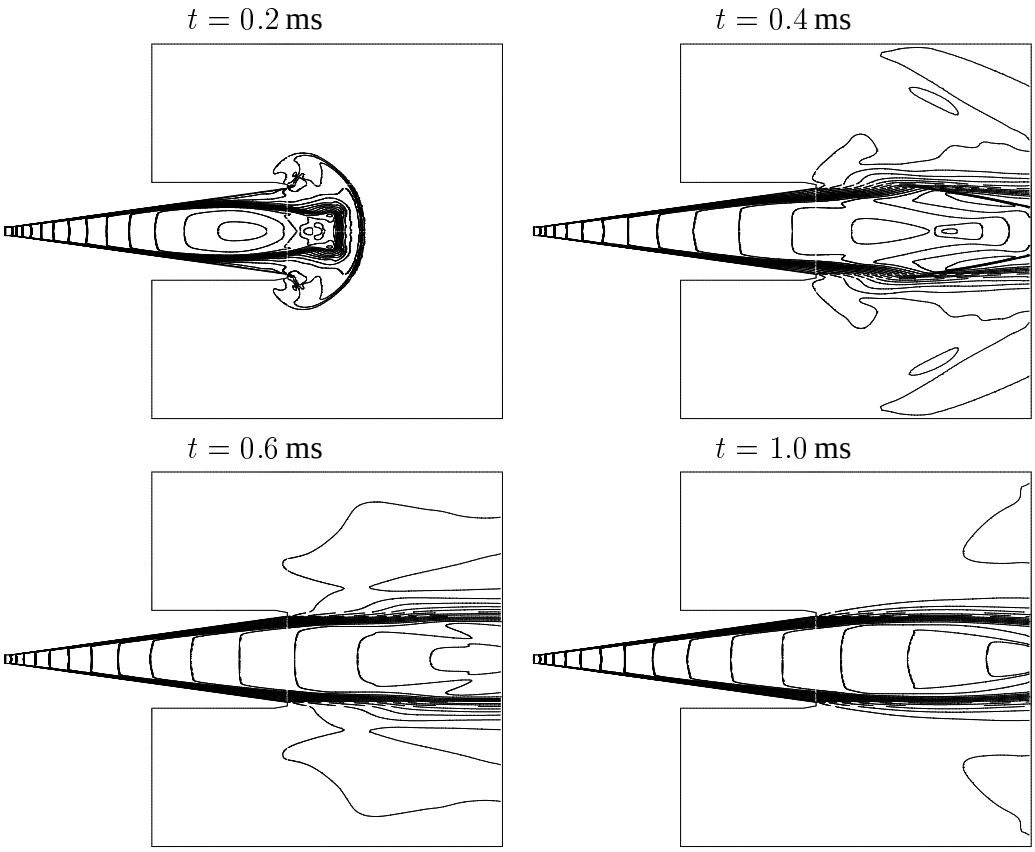

Figure 3.16: Mach number contours showing the evolution of the flow field in the SST Mach 7 conical nozzle and test section for PRF = 15 and p_{evac} = 67 Pa. Time, t, is the time after secondary diaphragm rupture.

regions within the shear layer and the oblique shock attached to the nozzle exit where the flow is always in thermal non-equilibrium no matter what the degree of freestream rarefaction. It has been established that shock capturing Navier-Stokes solvers accurately predict the flow field around shocks even when the predicted structure of the shock is not physically correct on a kinetic theory basis [16]. From this it appears that the compressible Navier-Stokes solver, Mb_cns, can be used with reasonable confidence to simulate the flow through the SST during low-density operation.

Figure 3.19 shows contours of P_D based on a characteristic model size of 10 mm at t = 1 ms. This plot shows that if testing at a slightly higher degree of rarefaction is desired, it can be accomplished merely by positioning the model further from the nozzle exit plane. For example if a test P_D of 0.05 is required, the model should be located approximately 42 mm from the nozzle exit plane. However, the variation of flow properties in the axial direction also makes the test flow unsuitable for experiments using models with large

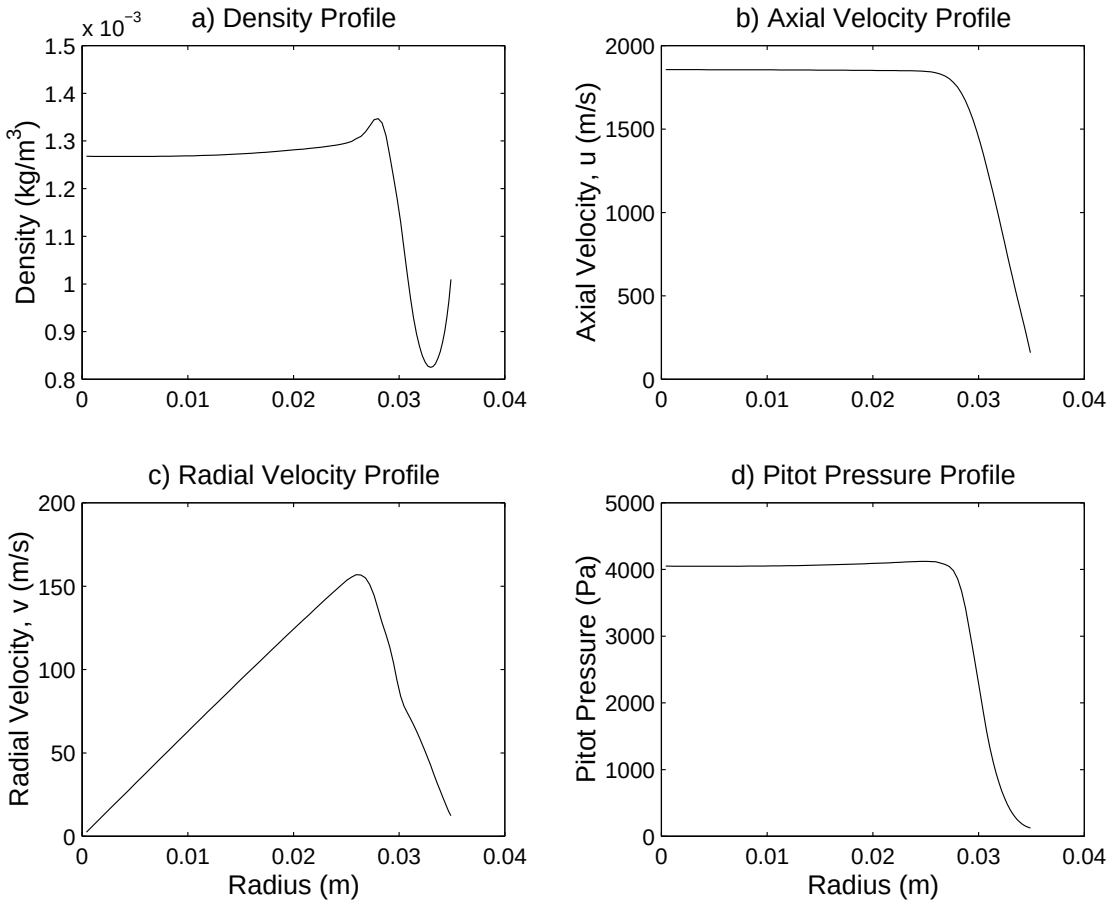

Figure 3.17: Computed profiles of density, axial velocity, radial velocity and Pitot pressure 10 mm from the SST Mach 7 conical nozzle exit plane 1 ms after secondary diaphragm rupture for $PRF = 15$ and $p_{evac} = 67$ Pa.

axial lengths, such as flat plates.

ρ_{test}	8.948×10^{-4} kg/m^3
u_{test}	1853 m/s
p_{test}	52.25 Pa
T_{test}	192.7 K
$p_{pitot,test}$	2851 Pa
M_{test}	6.482
Re_{test}/L	1.303×10^5
$P_{D,test}$	0.04001
λ_{test}	0.0737 mm

Table 3.5: Nominal test conditions 10 mm from the Mach 7 conical nozzle exit plane for p_{evac} = 67 Pa and PRF = 15.

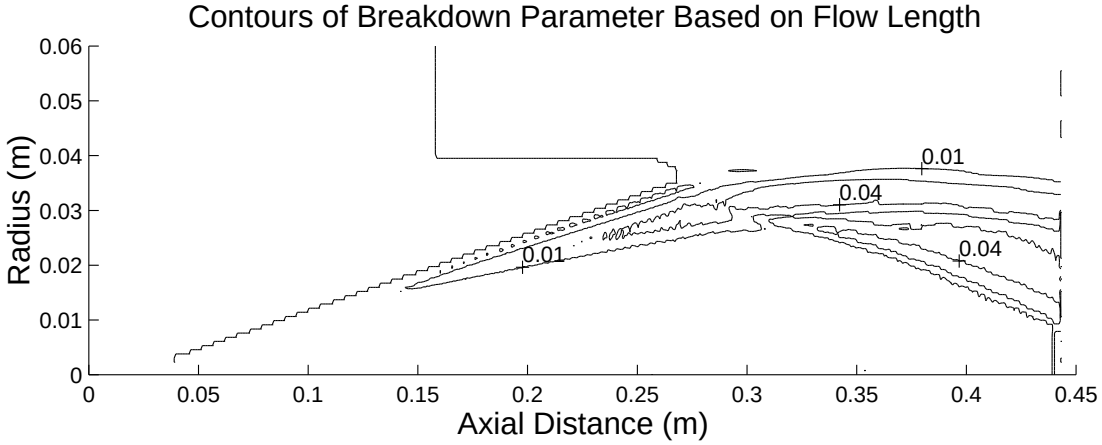

Figure 3.18: Contours of the breakdown parameter, P, in the SST Mach 7 conical nozzle and test section 1 ms after secondary diaphragm rupture for PRF = 15 and p_{evac} = 67 Pa.

3.3.3 Simulation of the Entire SST

To investigate whether a useful test flow will still be established when the variations in the nozzle supply pressure are accounted for, a computational model of the entire SST has been constructed. The computational domain of the model, *m7coni_full*, includes the driver, shock tube, Mach 7 conical nozzle and the test section. The computational grid for the conical nozzle and test section is the same as for *m7coni_ndt*. The computational grid for the shock tube and driver has 1580 cells in the streamwise direction and 70 cells in the cross-stream direction. As before, the cells are radially clustered towards the wall to help resolve the boundary layer. The details of the model geometry and discretisation can be found in the simulation's input parameter file, *m7coni_full.sit*, which is included in Appendix B. As with the final simulation of the conical nozzle and test section, *m7coni_full* was run with $PRF = 15$ and $p_{evac} = 67$ Pa. The cells in the driver section were initially filled with room temperature helium at 216.7 kPa and those in the shock tube were filled

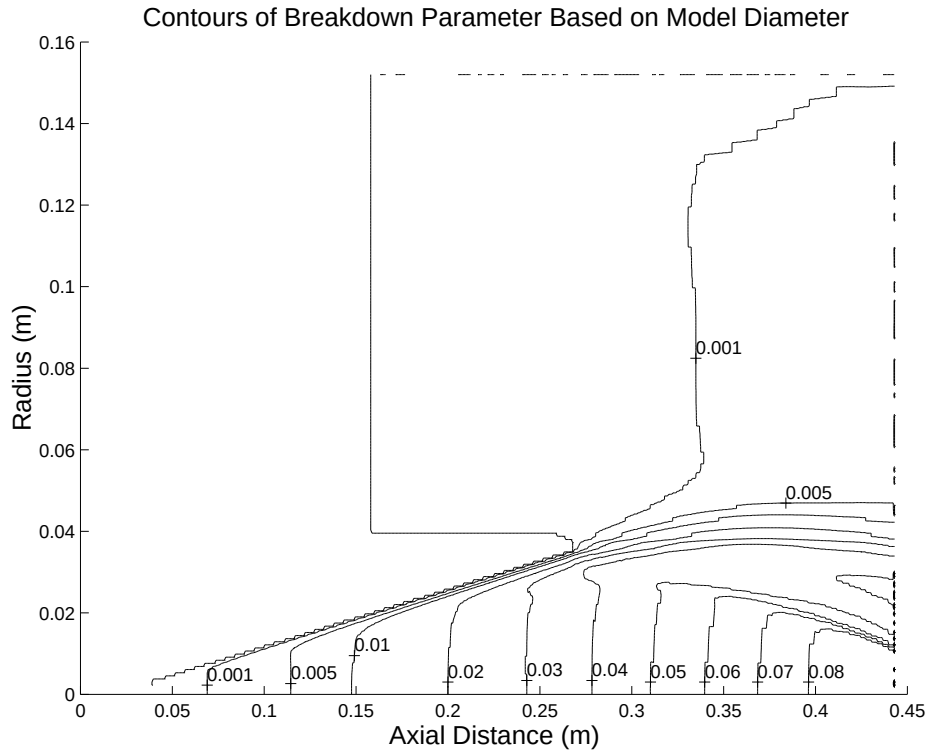

Figure 3.19: Contours of the breakdown parameter based, P_D, based on a model size of 10 mm in the SST Mach 7 conical nozzle and test section 1 ms after secondary diaphragm rupture for $PRF = 15$ and $p_{evac} = 67$ Pa.

with room temperature nitrogen at 2 kPa. The simulation was initiated with the rupture of the primary diaphragm and terminated when it was estabished whether the nozzle had started properly. Due to the time constraints on this thesis, the simulation could not be run long enough to yield a prediction of the test time. Figure 3.20 shows contour plots of Mach number at four instants after the rupture of the secondary diaphragm. These show the evolution of the flow field in the test section. It can be seen from Figure 3.20 that the conical nozzle still starts rapidly and produces a reasonably uniform test flow even with the variation in nozzle supply pressure that occurs when the entire operating cycle of the SST is simulated. However, the test flow is much "noisier" than in the simulations with constant throat conditions. This is because the bifurcated reflected shock and the separated flow behind it [22] generate large variations in the flow properties across the shock tube, which result in additional waves being generated within the nozzle.

3.3.4 Simulation of a Previous Attempt to Produce Rarefied Flow in the SST

It was mentioned in Section 3.2 that an attempt to experimentally generate rarefied flow in the SST has already been made as part of an undergraduate thesis [6]. This was done by reducing the fill pressures to values of 325 kPa in the driver and 3 kPa in the shock tube. The Mach 7 contoured nozzle was used and the test section and dump tank were pumped down to around 400 Pa. Pitot pressure time histories were recorded at a series of radii across the nozzle exit plane. A number of problems were observed in the experimental data that were not adequately explained:

- The flow was very unsteady at most radii.
- There were large differences in the measured pitot pressures between shots.
- At times when a uniform core flow was present, it had a diameter of around 18 mm compared to the 87.2 mm exit diameter of the nozzle.
- High pitot pressures were observed in the region outside the uniform core while at still greater radii the pitot pressures dropped to a very low level.

A simulation has been run using the experimental fill conditions in order to ascertain whether these problems are consistent with the effects of having a relatively high value of p_{evac} that were observed in the computational results presented earlier in this section.

First, the flow in the SST was simulated one-dimensionally to determine whether the fill conditions used in the experimental study resulted in tailored operation. A Lagrangian CFD code, L1d [33], was used to perform the simulation. L1d has been shown to simulate the gas dynamics of shock tunnels with reasonably accuracy [36, 40]. The computational domain of the simulation was based on the dimensions of the SST shown in Figure 3.5. The gas states of the computational cells that modelled the driver, test gas and dump tank fill gas were initially set to the experimental fill conditions listed in Table 3.6. Both the nitrogen test gas and the helium driver were modelled as being calorically perfect gases. The simulation, which contained 510 cells, was initiated at the rupture of the primary diaphragm and was terminated after 3.5 ms of simulation time had elapsed.

Figure 3.21 shows an $x-t$ wave diagram generated from the results of the simulation. From this figure it can be seen that when the reflected shock intersects the contact surface, the contact surface is not brought to rest, rather it begins to travel upstream. This indicates that the fill conditions used in the experiments of reference [6] result in "under-tailored" operation. As the conditions are under-tailored, the nozzle supply pressure will decay over time. To account for this, the shock reflection process had to be included in the two-dimensional simulation of the facility.

As before, Mb_cns was used to perform the simulation of the SST operating with the experimental fill conditions. For this simulation, the computational domain includes the last 1.5 m of the shock tube, the Mach 7 contoured nozzle and the test section. The initial conditions for the simulation were set so that the primary shock was effectively located 0.5 m from the contraction to allow for some boundary layer development in the shock tube. This was done by setting the gas states in the cells upstream of the shock location to the post shock conditions from the L1d simulation, which are shown in Table 3.6 along with the fill conditions. Downstream of the shock location the cellular gas states were set to the shock tube fill conditions while the cells in the nozzle and test section were initialised to the evacuated state listed in Table 3.6. The same computational mesh was used as for corresponding sections in the other Mb_cns simulations. 2 ms of simulation time elapsed before the simulation was terminated.

Driver gas	helium
Driver fill pressure, p_{drv}	325 kPa
Driver fill Temperature, T_{drv}	296 K
Test gas	nitrogen
Shock tube fill pressure, p_{st}	3.0 kPa
Driver fill Temperature, T_{st}	296 K
Initial test section/dump tank pressure, p_{evac}	400 Pa
Initial test section/dump tank Temperature, T_{evac}	296 K
Primary shock speed (from L1d simulation)	1.203 km/s
Post shock axial velocity (from L1d simulation)	916.98 m/s
Post shock temperature (from L1d simulation)	952.57 K
Post shock pressure (from L1d simulation)	40.639 kPa

Table 3.6: SST fill conditions from reference [6].

Figure 3.22 shows Mach number contours at three instants during the "test time" proposed by Attwood, which begins approximately 1 ms after the initial shock exits the nozzle and lasts around 0.5 ms. Clearly the nozzle has failed to start; as in the first simulation

presented in Section 3.3, the high initial pressure has caused nozzle boundary layer to separate, and produced strong oblique shock waves within the nozzle. Despite being processed by the oblique shock waves within the nozzle, the flow exiting the nozzle is still "overexpanded", meaning its static pressure is lower than the backpressure in the test section. The flow is compressed to the backpressure via an oblique shock at the nozzle exit, which can be seen clearly in Figure 3.22. The unsteady nature of the flow, which Attwood observed experimentally, can also be seen in this figure through the changing locations and angles of the oblique shock waves. A possible cause of this is that the shock structure is sensitive to the inflow conditions at the nozzle throat, which vary during the test time because the tunnel was operated at undertailored conditions. Figure 3.23 shows a comparison of Attwood's experimental data with the computed nozzle exit Pitot pressure profile at t = 1.64 ms. After examining the contour plots shown in Figure 3.22, the flow processes behind the features of the experimental Pitot profile can be readily identified: The high Pitot pressures at a radius of around 15 mm confirm the presence of the oblique shock wave at the nozzle exit, while the low values at radii greater than 25 mm are caused by the relatively stagnant gas between the shear layer and the nozzle wall.

The flow features observed in the experimental data of reference [6] have been adequately predicted using the simulation techniques outlined in this chapter. There are some discrepancies between the experimental and computed nozzle exit Pitot pressure profiles; the positions of the oblique shock wave and shear layer are slightly different. This is to be expected as the flow is unsteady and Attwood observed significant variation in the measured Pitot pressures between tests. The likely cause of the variation between tests is that the initial pressure in the nozzle and test section, p_{evac}, was not carefully controlled. The position of the shear layer and the oblique shock waves are sensitive to the value of p_{evac}, hence small variations in this parameter could significantly alter the Pitot pressure measured at a given radius. These results clearly indicate that to produce a useful rarefied test flow in the SST, p_{evac} must be strictly controlled and decreased to a level significantly lower than that used previously in order for the nozzle to start. The results also demonstrate that the simulation techniques outlined in this chapter can predict the mechanisms that can cause attempts to produce a rarefied test flow to fail.

3.4 Conclusion: Recommended Operating Conditions and Tests

The results presented in this chapter indicate that to produce a uniform, high Mach number test flow in the SST with $P_D \approx 0.04$, the Mach 7 conical nozzle should be used along with the fill conditions specified in Table 3.7. Note that the pumping capacity of the facility must be increased in order to achieve the recommended initial pressure in the test section. The test conditions predicted to result from operating the facility as specified are also listed in Table 3.7.

Driver gas	helium
Driver fill pressure, p_{drv}	216.7 kPa
Driver fill Temperature, T_{drv}	296 K
Test gas	nitrogen
Shock tube fill pressure, p_{st}	2.0 kPa
Driver fill Temperature, T_{st}	296 K
Initial test section/dump tank pressure, p_{evac}	67 Pa
Initial test section/dump tank Temperature, T_{evac}	296 K
Nominal test flow density, ρ_{test}	8.948×10^{-4} kg/m^3
Nominal test velocity, u_{test}	1853 m/s
Nominal test static pressure, p_{test}	52.25 Pa
Nominal test static temperature, T_{test}	192.7 K
Nominal test Pitot pressure, $p_{pitot,test}$	2851 Pa
Nominal test Mach number, M_{test}	6.482
Nominal test Reynolds number, Re_{test}/L	1.303×10^{5}
Nominal test breakdown parameter, $P_{D,test}$	0.04001
Nominal test mean free path, λ_{test}	0.0832×10^{-3} mm

Table 3.7: Recommended SST fill conditions and predicted test conditions.

3.4.1 Possible Experiments

In this section, an experiment is described that could be conducted in the low-density test flow that would be generated in the SST if the recommended operating conditions are adopted. Its key feature is that the rarefaction of the flow should have a significant effect on the quantity measured during the experiment. This would allow both continuum codes with slip boundary conditions and DSMC to be experimentally validated against a new set of experimental data.

In designing a possible experiment, the first factor considered was the type of model

to be tested. The model selected must have its surface parameters measurably altered by the rarefaction of the test flow. Rarefaction effects on the surface parameters of two model types were reviewed in Section 2.4. These were flat plates with sharp leading edges and axisymmetric blunt bodies. The low-density test flow in the SST is predicted to have significant gradients in the axial direction, making it unsuitable for testing models with large axial lengths, such as flat plates. The test flow is also axisymmetric in nature, making an axisymmetric model a logical choice. Axisymmetric blunt bodies are of interest to researchers in the field of rarefied gas dynamics as they are representative of the shapes of aeroshells, which are commonly exposed to rarefied hypersonic flows in reality. For these reasons, the model type suggested for low-density testing in the SST is an axisymmetric body in the form of a spherically blunted cone.

The next element of the experimental design considered was the parameter to be measured. Surface parameters such as heat transfer, skin friction, surface pressure and drag are easier to measure than quantities such as the shock standoff distance, which is why they were the focus of the review presented in Section 2.4. For low-density testing in the SST, it would be convenient to utilize transducer types that are already used in shock tunnel testing at UQ. This effectively rules out skin friction and surface pressure as possible measured quantities as the size of the transducers presently used is of the order of 10 mm, which is too large to install on the spherically blunted nose of a model small enough to be tested in the SST. While pressure tappings could be used to overcome the problem of the size of the pressure transducers, the resultant increase in response time makes them impractical for this application. Heat transfer measurements in the shock tunnels at UQ are presently made using thin film gauges. The sensing element of these gauges has dimensions of around 0.2 mm by 1 mm, which is small enough to be mounted on the nose a reasonably small model. The thin film gauges are accurate to within $\pm$10% and are used to measure heat fluxes from the order of 1 kW to several MegaWatts (personal communication, D. J. Mee). Overall drag is measured at UQ by mounting models on the front of a bar gauge similar to that described in Section 4.3. Using this arrangement the overall drag in the streamwise direction can readily be measured to within $\pm$10% (personal communication, D. J. Mee). A draw back of this arrangement is that around 150 μs after the flow arrives at the gauge location, the initial stress waves have reflected from the downstream end of the gauge and begin to interfere with the measurement. In theory, deconvolution

can be used to resolve this problem but this has not yet been attempted for the gauges discussed here. To choose between heat transfer and drag as the suggested measured variable, the results of Moss, Cuda and Simmonds [58] were considered (see Section 2.4 for details). Their plots of stagnation point heat transfer and drag on a spherically blunted cone versus freestream Knudsen number showed that the stagnation point heat transfer is significantly more sensitive to the flow rarefaction. For this reason it is suggested that the stagnation point heat transfer should be measured during low-density testing of blunt bodies in the SST.

Once an appropriate model type and measured variable for low-density tests in the SST had been determined, all that remained was to size the radius of the nose, R_N, such that the effect of rarefaction would be measurable. As the heat transfer measured using the thin film gauges used at UQ is only accurate to within $\pm$10%, the rarefaction effect on the heat transfer must be greater than 10%. The stagnation point heat transfers measured by Vidal and Wittliff [85] were around 20% lower than the Navier-Stokes predictions of reference [41] and the strong interaction theory of Cheng [15] for $\chi = 10$ based on nose radius. By using the approximate relationship, $\chi \approx P_D^{-1}$, and setting the characteristic dimension, D, to be equal to R_N, it was calculated that a nose radius of 4 mm would be required to achieve $\chi \approx 10$ for the test conditions predicted in the SST. The data on the stagnation point heat flux to the OREX vehicle presented in reference [29] indicated that at an altitude of 92.8 km, a continuum prediction of the heat flux overpredicted the value inferred from the flight data by almost 19%. For the OREX vehicle at this altitude $u_\infty = 7456$ m/s, $Kn_\infty = 0.0086$ and $S = 21.1$ from which P_D based on nose radius was calculated to be 0.19. To achieve this value in the test flow predicted in the SST, the nose radius of the model would have to be 2.1 mm, which is considerably smaller than the value calculated earlier. One of the reasons for this is that the flow speed of around 2 km/s in Vidal and Wittliff's experiments was much lower than the OREX vehicle's flight speed of around 7.5 km/s. Greater freestream velocities produce a larger density increase across the bow shock and a correspondingly greater decrease in the rarefaction of the gas in the shock layer. The result of this appears to be that for higher freestream velocities, a greater degree of freestream rarefaction is required before measurable deviations in surface parameters occur. As the predicted test speed in the SST is close to that used in Vidal and Wittliff's experiments, it is expected that non-continuum effects will be observed at a similar degree

of freestream rarefaction. From this discussion, it appears that if the nose radius of the model to be tested in the SST is set to 3 mm, then the rarefaction of the flow should cause a continuum approach to overpredict the stagnation point heat transfer by more than 10%.

In summary, it is recommended that a spherically blunted cone with a nose radius of 3 mm be tested in the SST when operated at the conditions given in Table 3.7. During these tests, it is recommended that the stagnation point heat flux be measured with one of the thin film gauges currently in use at UQ. It is hoped that the rarefaction of the test flow will cause the stagnation point heat flux to measurably deviate from its continuum value by more than 10%.

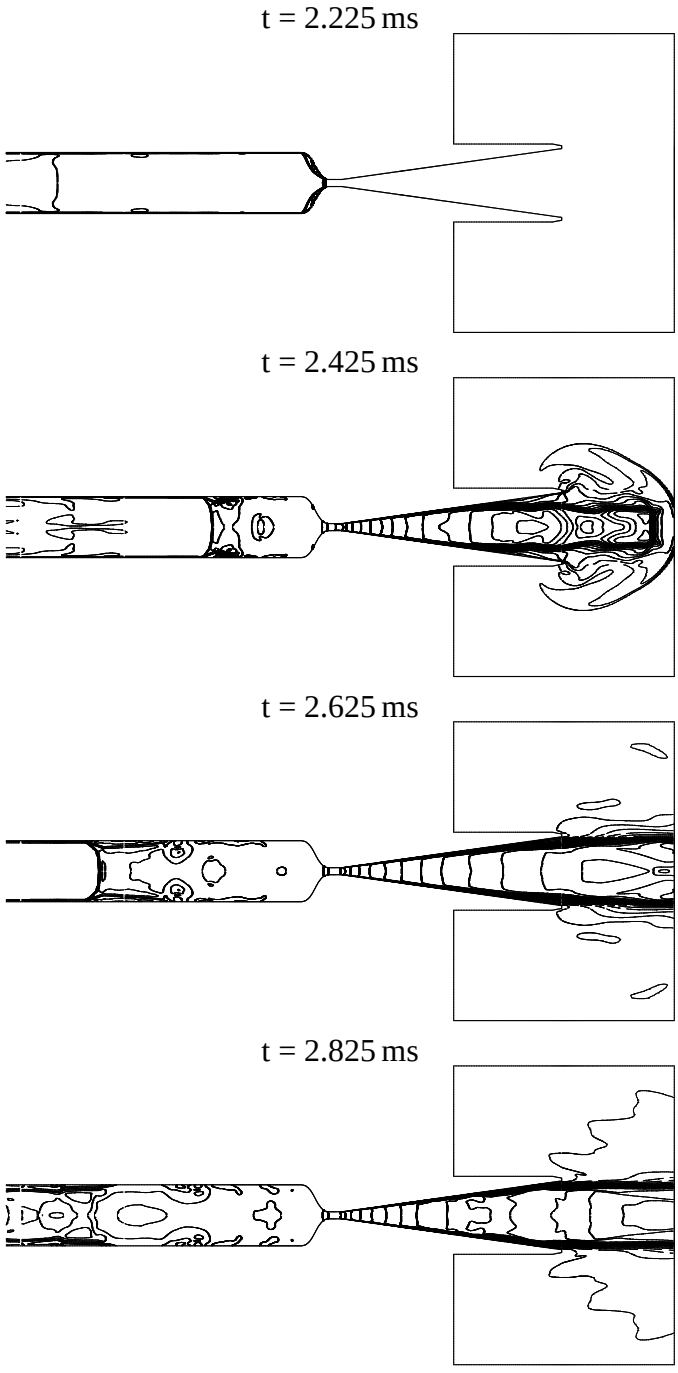

Figure 3.20: Mach number contours showing the evolution of the flow field in the SST Mach 7 conical nozzle and test section from the simulation of the entire SST. Time, t, is the time after primary diaphragm rupture.

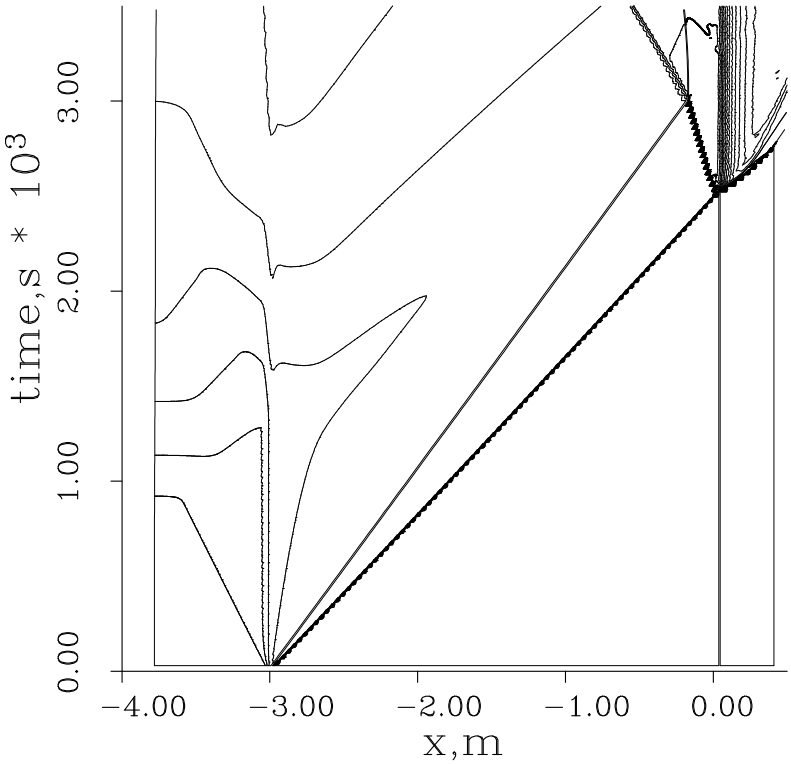

Figure 3.21: $x - t$ wave diagram of the showing the flow processes that occur in the SST when operating at the experimental conditions of Attwood [6].

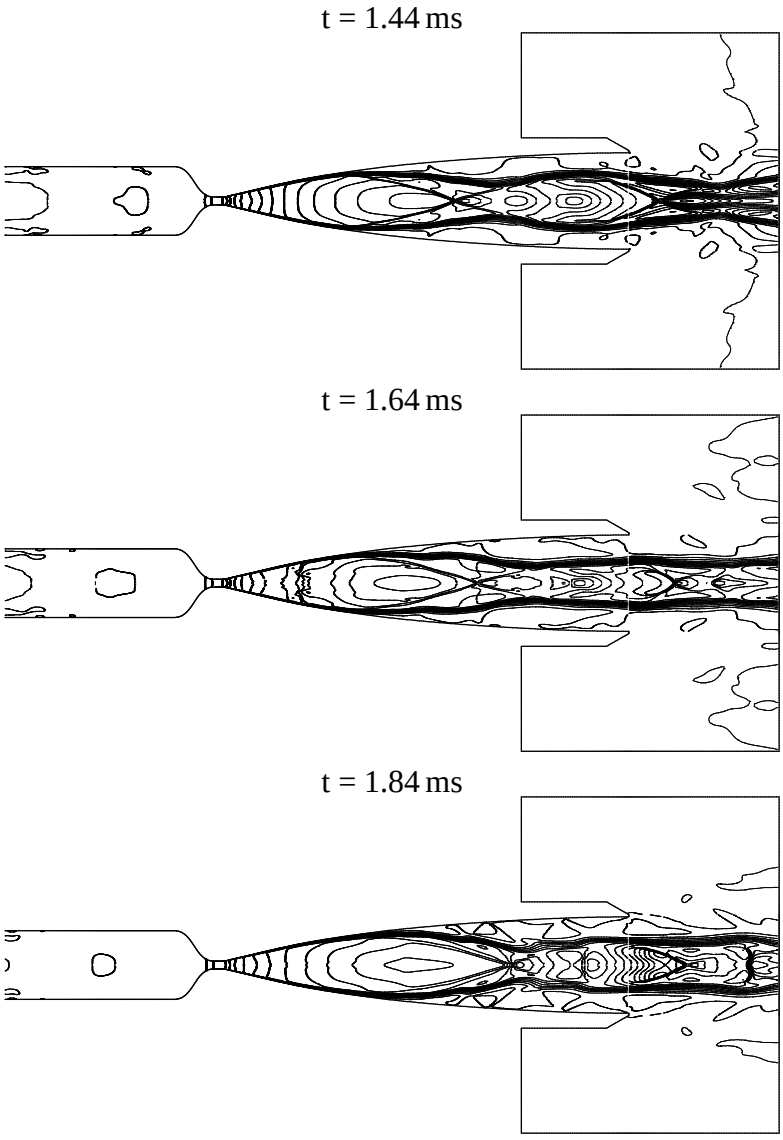

Figure 3.22: Mach number contours showing the evolution of the flow field in the SST Mach 7 contoured nozzle and test section for the conditions listed in Table 3.6. Time, t, is the time after the initialisation of the simulation.

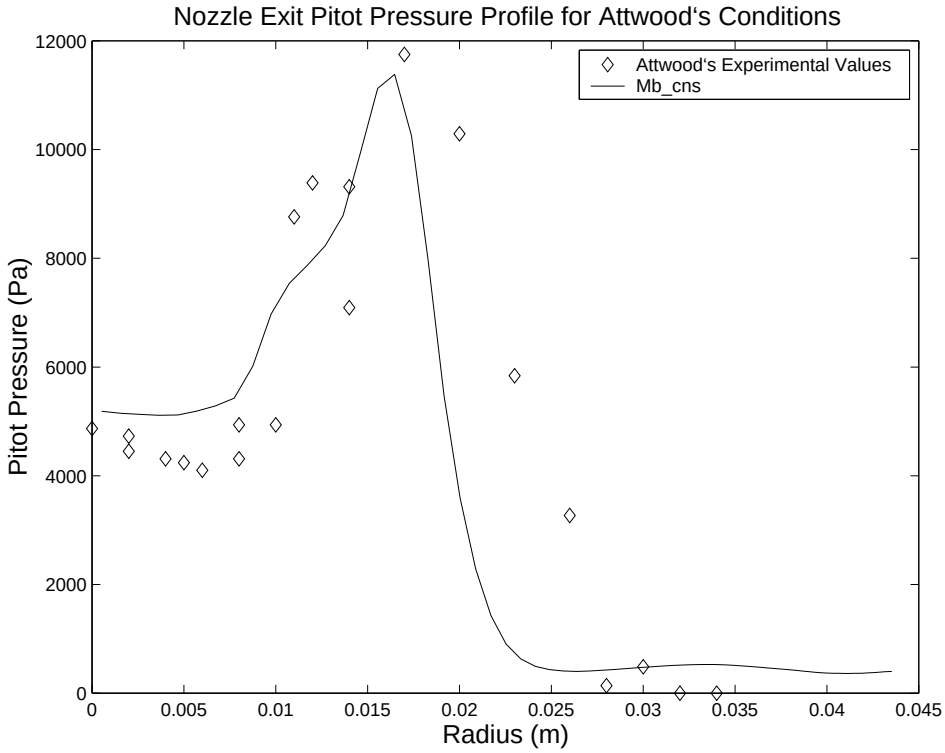

Figure 3.23: Computed and experimental nozzle exit Pitot pressure profiles. Computed values were taken 1.2 ms after diaphragm rupture. Experimental values are from Attwood [6].

CHAPTER 4

Producing Rarefied Hypervelocity Flow in the X1 Expansion Tube

A review of facilities capable of producing high speed, rarefied flows is presented in Section 2.1. This review revealed that present facilities are limited to stagnation temperatures of under 2600 K and hence flow speeds of around 2 km/s. It was noted in Section 1.2 that experimental testing of DSMC is required for the rarefied hypervelocity conditions encountered during an aerobraking maneuver. To simulate these conditions, flow speeds of the order of 10 km/s, which cannot be attained in present low-density facilities, are required. The possibility of modifying an expansion tube to produce a rarefied hypervelocity flow was first investigated by Wendt et al [87]. In this pilot study, a rarefied test flow was generated by operating the X1 expansion tube at UQ with reduced fill pressures, then expanding the flow exiting the tube into the dump tank via a conical nozzle. The result of this was an 8.8 km/s flow of argon in the transitional regime. Unfortunately, cross-stream and temporal variations made the flow unsuitable for experiments. The effort to utilize X1 as a rarefied hypervelocity test facility has been continued, with a greater degree of success, by Chiu and his co-workers [49]. The purpose of this chapter is to present the details of the X1 expansion tube and the experiments of Chiu that were used in the development and validation of an accurate CFD model of the flow through X1, which is discussed in full detail in Chapter 5. The chapter begins with a description of the X1 expansion tube, where the flow processes that generate the test flow are discussed in some detail. The operating conditions used during Chiu's study are then presented. Following this, the instrumentation used during low-density operation is described, and samples of the recorded data are presented. Finally, techniques used to interpret the experimental data are discussed.

4.1 The X1 Expansion Tube

The X1 expansion tube at the University of Queensland is a small scale, free piston-driven expansion tube [66]. X1 was the first expansion tube to be driven by a free piston driver. Superorbital flows (flight speed above 8 km/s or total enthalpy over 30 MJ/kg [23]) with test speeds of up to 15 km/s can be produced in X1.

The layout of X1 when configured with a single driver is shown in Figure 4.1. The facility consists of the following components: A high pressure cylinder called the compression tube, which initially contains the driver gas and the 3.4 kg free piston. An annular reservoir that stores the compressed air used to drive the free piston. A lower pressure cylinder referred to as the shock tube, which initially contains the test gas. A cylinder referred to as the acceleration tube, which is initially filled with very low pressure acceleration gas. Finally, a large dump tank/test section with a volume of 0.15 m^3 which is also initially filled with low pressure acceleration gas. The geometries of sections used in the experiments of reference [49] are shown in Table 4.1.

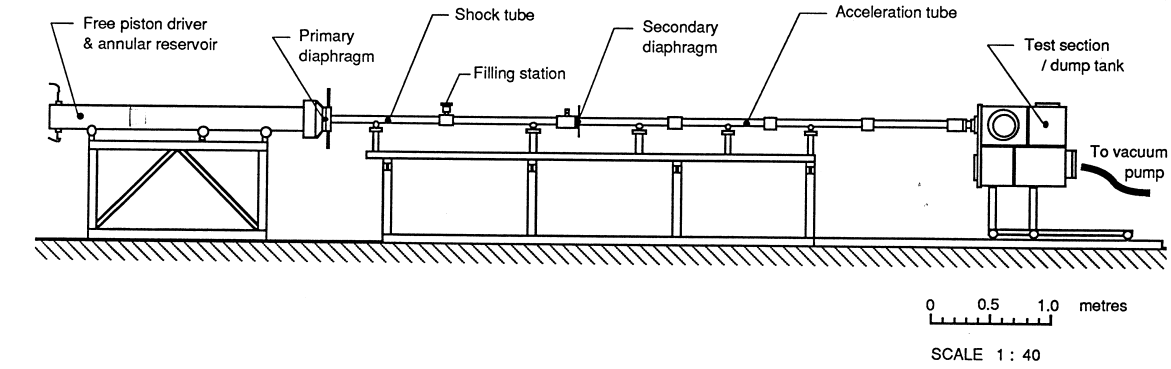

Figure 4.1: Layout of the X1 expansion tube (Figure 1 from [49]).

Section	Length (m)	Internal Diameter (mm)
Compression tube	2.30	100
Shock tube	2.09	38.1
Acceleration tube	2.91	38.1

Table 4.1: X1 section dimensions when configured with a single driver.

The driver and shock tube are separated by a steel diaphragm known as the “primary” diaphragm. During operation of the facility, the compressed air in the annular reservoir

propels the free piston down the compression tube, compressing the driver gas. At some point, the pressure of the driver gas exceeds the burst pressure of the primary diaphragm, causing it to rupture. The high pressure driver gas then expands into the shock tube and generates a shock wave that rapidly compresses the low pressure test gas. This shock wave, which is referred to as the primary shock, propagates along the length of the shock tube compressing and accelerating the test gas. This process is illustrated via the distance-time ($x - t$) wave diagram in Figure 4.2 along with the other processes that occur in X1.

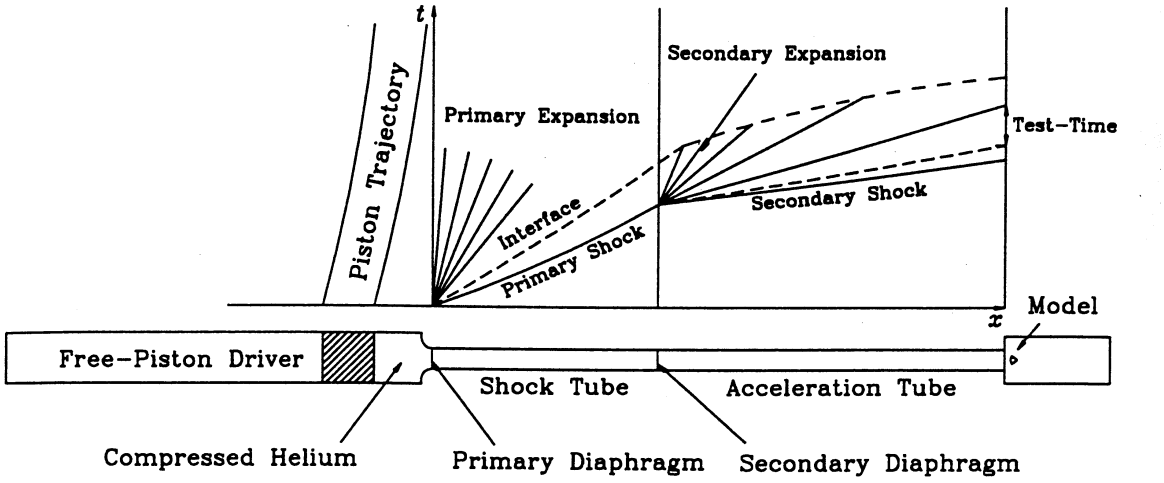

Figure 4.2: Ideal wave diagram of the shock and expansion processes that produce the test flow in X1 (Figure 1.2 from [23]).

Upon reaching the end of the shock tube, the primary shock ruptures the light plastic "secondary" diaphragm, which initially separates the test gas from the acceleration gas. For ideal expansion tube operation, the secondary diaphragm is assumed to be massless and to rupture instantaneously, as illustrated in Figure 4.2. The compressed test gas is then processed by an unsteady expansion and begins to expand into the acceleration tube generating the "secondary" shock, which compresses and accelerates the low pressure acceleration gas. The unsteady expansion that propagates upstream through the test gas (downstream in the laboratory reference frame as expansion waves travel at velocity $u - a$ and the shock compressed test gas is supersonic) serves to expand it to the desired test conditions. The test flow begins with the passage of the contact surface between the acceleration gas and the test gas past the model location. The test flow at the model location is terminated by one of the following two events; the arrival of the tail of the

unsteady expansion, or the arrival of the disturbance caused by the reflection of the head of the expansion off the contact surface between the driver and the test gas.

4.2 Low-Density Operating Conditions

To generate a rarefied hypervelocity test flow in X1, Chiu and his co-workers used low initial fill pressures in the shock and acceleration tubes, the resultant test flow in the acceleration tube was then further expanded via a free jet into the dump tank. As usual, helium was used as the driver gas and, at the recommendation of the author, nitrogen was used as the test and acceleration gases to simplify CFD simulations of the test flow. The set of nominal fill conditions used in the experiments of reference [49] are given in Table 4.2.

Section	Fill Pressure	Gas
Compression tube	536 torr (71443 Pa)	He
Shock tube	14.5 torr (1932.7 Pa)	N_2
Acceleration tube/dump tank	15 Pa	N_2

Table 4.2: Nominal fill conditions for X1 used in the experiments of reference [49].

The materials, thicknesses and approximate burst pressures of the diaphragms used during low density testing in X1 are listed in Table 4.3.

Diaphragm	Material	Thickness	Static Burst Pressure
Primary	Steel	0.55 mm	$\approx$19.25 MPa
Secondary	Polyethylene	9 μm	$\approx$20 kPa

Table 4.3: Diaphragms used during low density testing in X1.

4.3 Low-Density Instrumentation

During low-density operation of X1, the flow field in the dump tank was surveyed using bar gauges specifically designed for the experiments of reference [49]. These bar gauges were used to give fast response Pitot pressure measurements in the impulsively starting flow. Surveys of the radial Pitot pressure distribution were made at six axial locations between 25 and 340 mm from the exit of the acceleration tube.

Bar gauges were used in preference to conventional Pitot probes with piezoelectric pressure transducers due to the poor response of such probes in low-density, short duration flows [49]. It is the shielding in front of the PCB pressure transducer that causes a conventional Pitot probe to have a poor response in such flows. The shielding is necessary to protect the pressure transducer from erosion caused by diaphragm fragments travelling with the flow at high speeds. The bar gauges used during low density operation of X1 are shown in Figure 4.3. They are a modified form of the conventional bar gauge. To improve

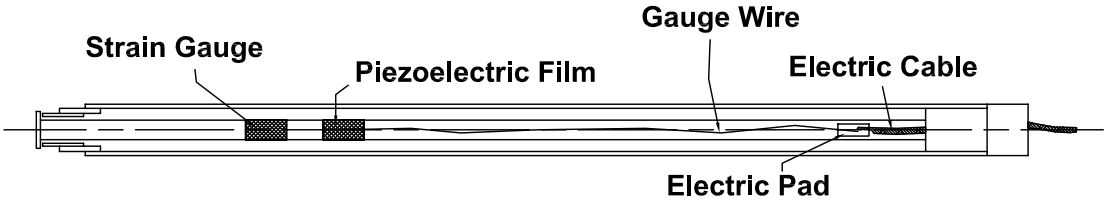

Figure 4.3: Bar gauge design for low-density, impulsively starting flows (Figure 2 from [49]).

the aerodynamic shielding of the bar and the survivability of the gauge, a steel disc of 9 mm diameter and 1 mm thickness was attached to the front of each bar. Although the addition of the disc slows the response of the bar gauge, its rise time is still only around 5 μs [49].

Two types of strain sensing elements were used in the bar gauges during the program of low-density testing in X1; piezoelectric polymer films [76] and semiconductor strain gauges (Kulite type ACP-120-300). Piezoelectric film with an axial length of 10 mm was wrapped around each bar with its most sensitive axis aligned with the bar axis. Two strain gauges were mounted on opposite sides of each bar in a bending compensation arrangement allowing the axial strain in the bar to be measured. The strain gauge amplifier had a rise time of 1 μs. It was noted during the experiments that the signals from the piezoelectric film gauges drifted during some tests. The signals from the semiconductor strain gauges did not show this effect.

The calibration of the bar gauges using PCB impact hammers (type 086-C04 and 086-D80) is described in reference [49]. The accuracy of this calibration was estimated to be $\pm$5%. The calibration of the bar gauges was then checked by placing bar gauges in a known flow produced by a shock tube. This was done because the average pressure over the surface of the disc on the front of the bar gauge differs from the Pitot pressure of the flow: A curved bow shock forms in front of the gauge, causing the pressure on the disc to

vary from close to the Pitot pressure at the center, to lower values near the edge of the disc. From the shock tube tests, the overall uncertainty in the measured disc average pressure was estimated to be $\pm 7\%$ for average pressures of the same order as those at the exit of the expansion tube. Away from the exit of the tube in the expansion tube tests, the Pitot pressure drops to as low as 3% of value at the exit and the uncertainty in the bar gauge measurements increases. At the most distant locations included in the flow field survey, the uncertainty in the disc average pressure was estimated to increase to a maximum of $\pm 15\%$ [49].

During the low-density experiments in X1, a large spike in the signal from the strain sensing devices was recorded upon arrival of the flow at the bar gauge locations. The spike duration was typically around 10 μs and was attributed to ionization of the flow as it is stagnated by the front of the bar gauge [49]. The spike was separated from the pressure signal by positioning the strain sensing devices on the bar such that the spike has subsided by the time the stress waves generated by the flow arrive at the transducer locations.

Static wall pressure was monitored at a number of locations along the expansion tube using commercially available PCB piezoelectric transducers (111, 112 and 113 series) [62]. These transducers have a diameter of 5.5 mm and a response time of between 1 and 2 μs. The transducers were mounted flush to the tube wall to minimise the response time. The manufacturer's calibration factors were used to convert the recorded voltages to pressures. The designations, locations (distances from the acceleration tube exit), sensitivities, types and serial numbers of the active static pressure transducers in X1's shock tube and acceleration tube are given in Table 4.4. The static pressure traces from these transducers are used to calculate the primary and secondary shock speeds.

4.4 Low-Density Experimental Data

For each low density test in X1, the static pressures along the tube were recorded at the transducer locations given in Table 4.4 and bar gauge pressures were recorded at up to three discrete locations in the dump tank. The data acquired during shot S5_157 (see Chiu's report [17] for the full set of experimental data) is presented here as an example of the data obtained during a typical test. The shock speeds and fill pressures from shot S5_157 were used in the development of the CFD models presented in Chapter 5. For

Transducer	Location (mm)	Sensitivity (V/kPa)	Serial Number	Transducer Type
ST1	3585	1.508×10^{-4}	8487	111A22
ST2	3410	1.670×10^{-2}	15290	112A22
ST3	3233	1.460×10^{-4}	9533	111A22
AT1	2718	7.304×10^{-3}	14534	112A21
AT3	2018	1.500×10^{-2}	15292	112A22
AT5	1076	7.562×10^{-3}	14536	112A21
AT7	376	4.120×10^{-3}	9569	113A21
AT8	120	1.624×10^{-2}	10633	112A22

Table 4.4: Designations, locations (distances to the left of the acceleration tube exit), sensitivities, types and serial numbers of active static pressure transducers in X1.

shot S5_157, the fill pressures were equal to the nominal fill pressures given in Table 4.2. The static pressure histories measured during shot S5_157 by the transducers in the shock tube are shown in Figure 4.4. The primary shock speed was calculated to be 5240 m/s

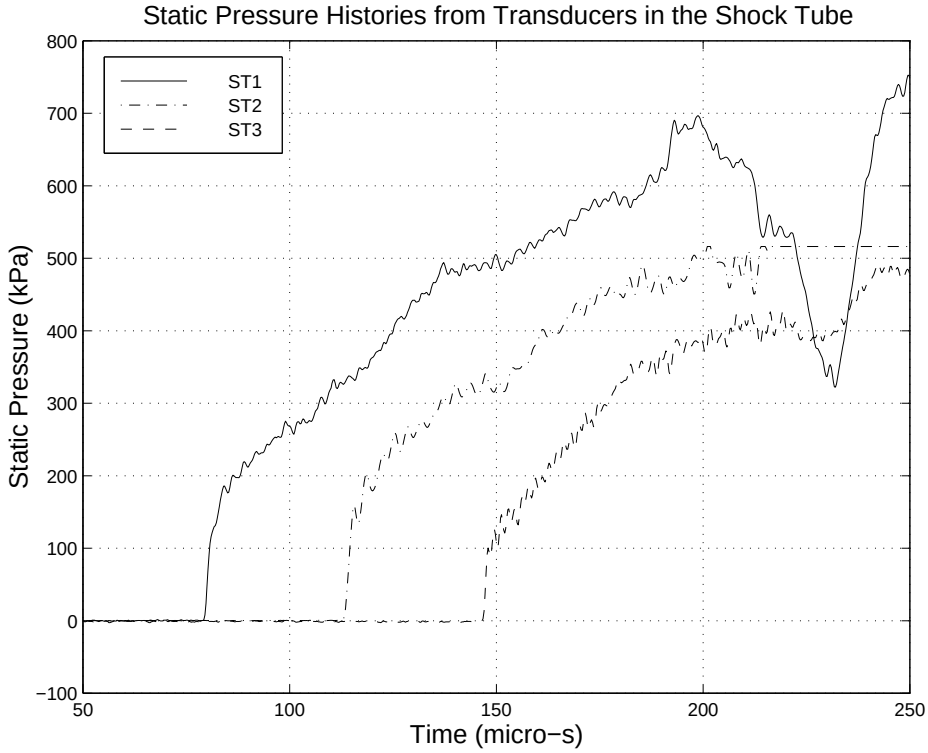

Figure 4.4: Measured static pressure traces from transducers in the shock tube during shot S5_157.

from the shock arrival times at the transducer locations. The static pressure histories from four of the transducers in the acceleration tube are shown in Figure 4.5. It can be seen that, prior to the arrival of the shock, the pressure indicated by the transducers is non-zero in some cases and shows some drift in some cases. This is associated with

the acceleration sensitivity of the pressure transducers. These effects are most obvious in the low pressure traces near the exit of the acceleration tube. The transducers are indicating pressures near the lower limit of their range in these traces e.g. transducer AT7 indicates about 10 kPa for shot S5_157 but the PCB type 113A21 pressure transducer has a calibrated range of 0.345 to 1330 kPa. The reason the gauges are operated near the low end of their range is that they need to be able to withstand the higher pressures in the expansion tube associated with the passage of the driver gas down the tube. The acceleration effects can be minimised with attention to their mountings in the tube. This was done in the present experiments and the drifts shown in Figure 4.5 are the smallest that could be achieved with the current transducers. The speed of the secondary shock near the

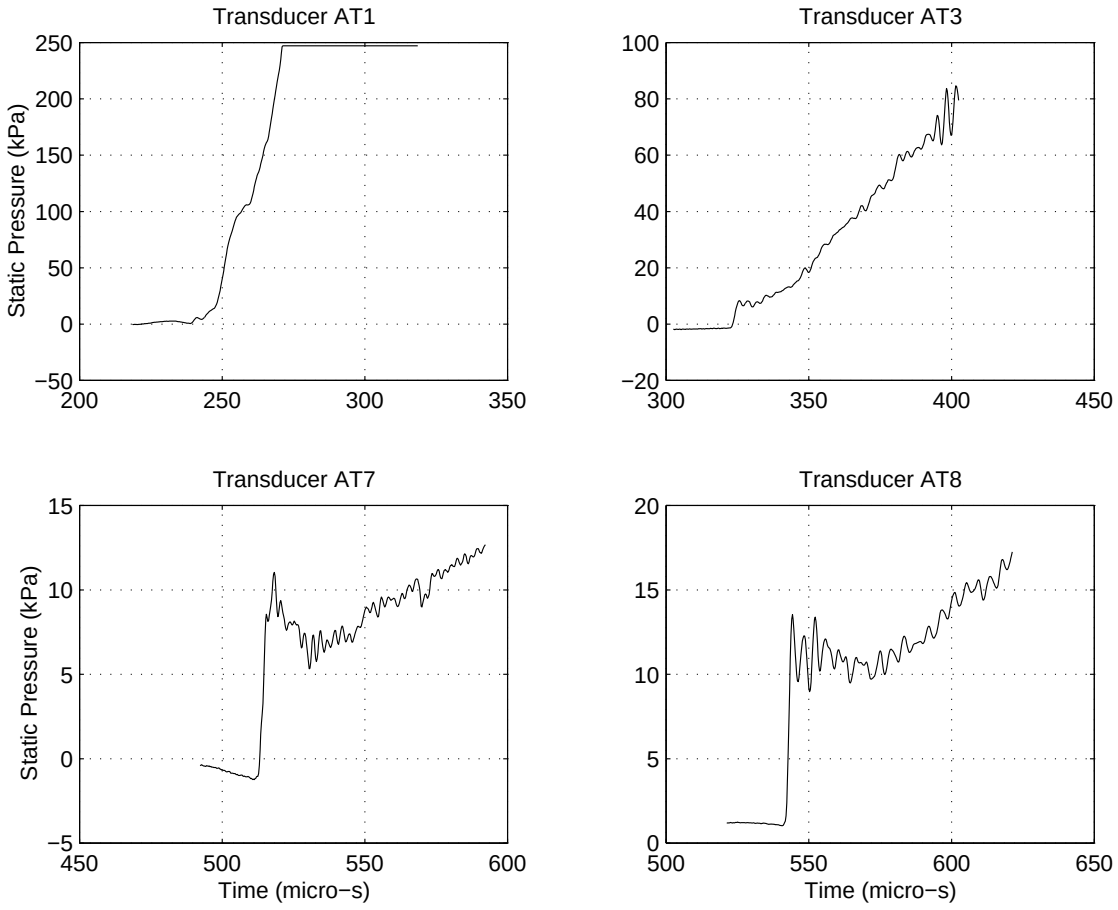

Figure 4.5: Measured static pressure traces from transducers in the acceleration tube during shot S5_157.

exit of the acceleration tube was calculated to be 8980 m/s from the difference between the shock arrival times at transducers AT7 and AT8. The estimated uncertainty in the measured shock speeds is $\pm 1\%$. During shot S5_157, three bar gauge pressure histories were recorded at an axial distance of 125 mm from the acceleration tube exit. These are

shown in Figure 4.6. The histories were recorded on the centerline and at a radius of 28 mm, both above and below the centerline. The noise caused by the ionization of the flow when it first impacts on the bar gauges can be seen in the histories shown in Figure 4.6 at a time of around 350 μs. To account for variations from the nominal conditions,

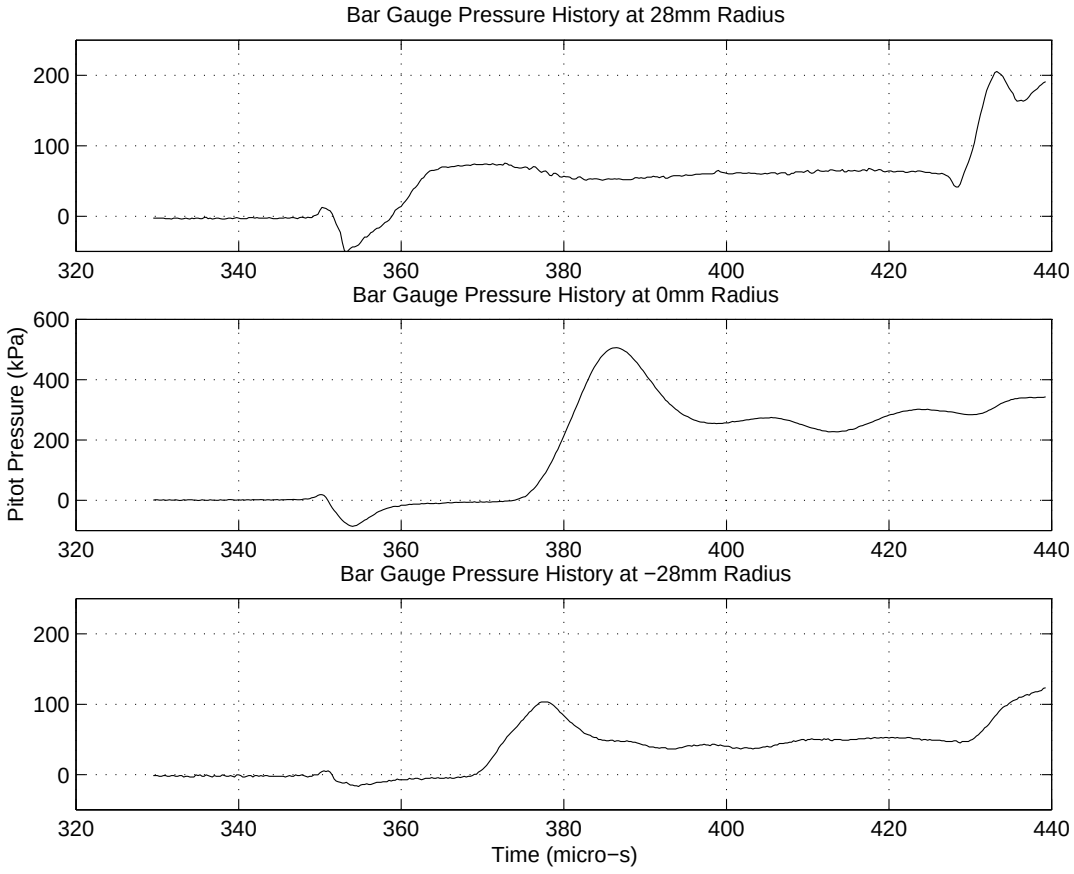

Figure 4.6: Measured bar gauge pressure histories from shot S5_157 at 125 mm from the acceleration tube exit.

the bar gauge pressure histories from each shot were normalised by an estimate of the test gas Pitot pressure at the exit of the acceleration tube, $P_{pitot,e}$, for that particular shot [49]. Estimates of the test gas Pitot pressure at the exit plane of the acceleration tube were calculated using the TUBE program [60]. TUBE computes the state of the test flow from the fill conditions and experimentally measured shock speeds assuming inviscid, one-dimensional flow in chemical equilibrium. Further details of the code can be found in reference [60]. The nominal value of the Pitot pressure at the acceleration tube exit was computed to be 627 kPa [49]. This value was used to normalise the CFD results presented in Chapter 5. The uncertainty in the calculated Pitot pressure is dominated by the $\pm$1% uncertainty in the secondary shock speed and was estimated to be $\pm$10%.

The results of the flow field survey at all six axial locations and nine different radii are given in Table 4.5 (refer to Chiu's report [17] for the full data set) and are plotted in Figure 4.7. The tabulated values, $(P_{bar}/P_{pitot,e})_{av}$, are the nominally steady bar gauge pressures of the test gas, which have been normalised by the estimated Pitot pressure at the acceleration tube exit and averaged over a number of tests. From the tabulated results, it can be seen that a core of high Pitot pressure flow exists near the centerline until 175 to 225 mm from the tube exit. At 225 mm the Pitot pressure is uniform to within experimental uncertainty [49]. Even at this distance, the strong axial gradient of Pitot pressure near the centerline renders the flow unsuitable for testing models with large axial lengths. From the Pitot pressure histories, it was determined that a nominally steady test time of 50 μs is available 225 mm from the acceleration tube exit.

Axial distance (mm)	25	75	125	175	225	340
$\left(\frac{P_{bar}}{P_{pitot,e}}\right)_{av}$ $r = 28$		0.02	0.10	0.15	0.10	0.03
$\left(\frac{P_{bar}}{P_{pitot,e}}\right)_{av}$ $r = 19$			0.20	0.11	0.09	
$\left(\frac{P_{bar}}{P_{pitot,e}}\right)_{av}$ $r = 14$	0.61	0.33	0.25	0.16	0.11	
$\left(\frac{P_{bar}}{P_{pitot,e}}\right)_{av}$ $r = 9$		0.55	0.29	0.17	0.10	
$\left(\frac{P_{bar}}{P_{pitot,e}}\right)_{av}$ $r = 0$	0.95	0.72	0.54	0.20	0.10	0.03
$\left(\frac{P_{bar}}{P_{pitot,e}}\right)_{av}$ $r = -9$	0.82	0.58	0.31	0.16	0.10	
$\left(\frac{P_{bar}}{P_{pitot,e}}\right)_{av}$ $r = -14$	0.63	0.34	0.23	0.15	0.10	
$\left(\frac{P_{bar}}{P_{pitot,e}}\right)_{av}$ $r = -19$			0.18	0.14	0.10	
$\left(\frac{P_{bar}}{P_{pitot,e}}\right)_{av}$ $r = -28$		0.02	0.11	0.11	0.10	0.03

Table 4.5: Results of the low-density flow field survey of X1's dump tank. Tabulated values are normalised, average bar gauge pressures. r is the radius from the tunnel axis in mm.

4.5 Data Analysis Techniques

It was mentioned in Section 4.3 that the pressure measured using the bar gauges differs from the Pitot pressure due to the pressure variation over the face of the disc attached to the front of the bar gauge. CFD simulations of nitrogen impacting on a disc normal to the flow were run to determine the pressure distribution on the face of the disc [49]. Both continuum (Mb_cns) and DSMC codes [11] were used. From these simulations, it was determined that the ratio of the average pressure on the disc to the Pitot pressure varies

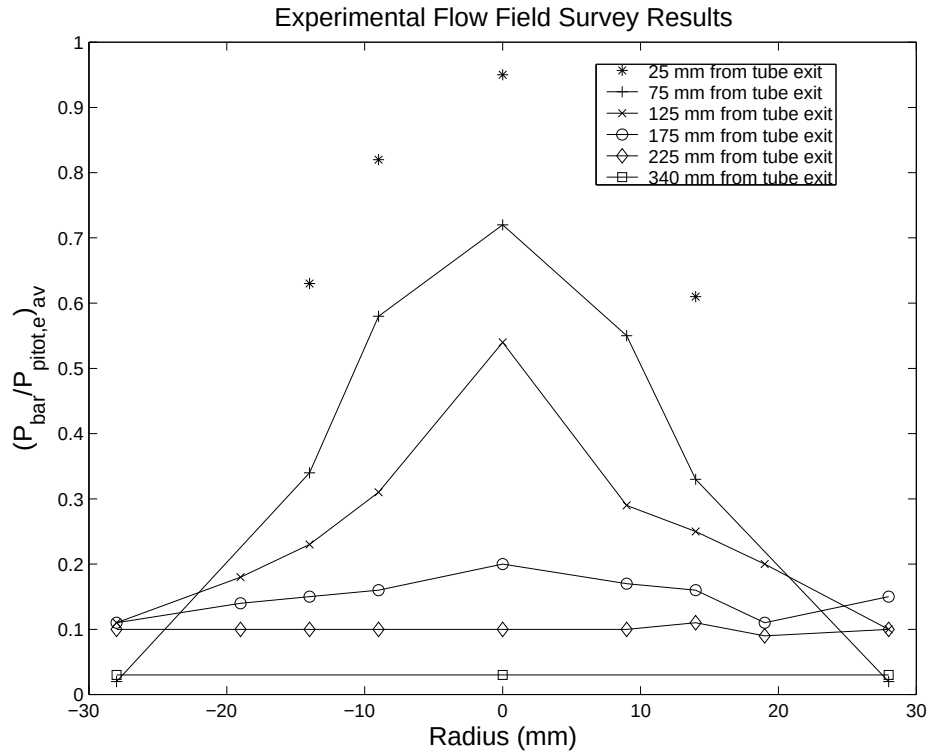

Figure 4.7: Experimentally determined profiles of normalised, average bar gauge pressure at several axial locations in X1's dump tank.

from around 0.9 or less for continuum flow, to around 0.95, depending on the Knudsen number. In reference [49], it was recommended that Pitot pressures computed using a continuum CFD code should be multiplied by a factor of 0.93 for comparison with the bar gauge pressures. This approach has been used in Chapter 5.

CHAPTER 5

Simulating Low-Density Hypervelocity Flow in the X1 Expansion Tube

In this chapter, a series of computational approaches are presented, which have been applied to simulate the flow in X1 during low-density operation. The aim of these simulations was to produce a CFD model of X1 that reproduces the static and Pitot pressures measured in the experimental investigation described in Chapter 4, which should ensure that the computational model is accurate. Once the accuracy of the model has been established, a wealth of information can be extracted from the CFD results that is not available from the experimental data. Most importantly, it is possible to establish the variation of flow parameters across the proposed test flow which determines whether or not the flow is suitable for experiments. The divergence of the core flow can also be determined along with the degree of rarefaction of the flow. The final CFD model can also be used to predict the performance of X1 at different operating conditions. This would enable the establishment of a tentative range of rarefied flows that can be produced in X1. The range of test conditions that can be produced is of great interest to researchers who are likely to utilise the facility. Those investigating the accuracy of DSMC will require a large range of test conditions to thoroughly assess the computational technique for varying degrees of rarefaction at hypervelocity conditions. Other researchers may use the facility to experimentally determine the aerodynamic characteristics of re-entry capsules or interplanetary spacecraft that will undertake aerobraking maneuvers.

Section 5.1 begins with a discussion of some details associated with modelling X1, including the CFD code that was used. Also included in this section are calculations of the inflow conditions for the initial simulations. Approximate driver conditions are calculated to enable unusual experimental results in the shock tube to be investigated via a one-

dimensional simulation. The final modelling detail discussed is the computational grid definition. In the next two sections, results of the initial simulations of the acceleration tube and dump tank are presented. The initial simulations were run for the two extremes of flow chemistry; equilibrium and frozen flow. The results of the simulations are compared with experimental data and the flow processes that generate the test flow are discussed in some detail. In Section 5.4, non-ideal diaphragm rupture dynamics are discussed. Two models for non-ideal diaphragm rupture are presented and their effects on the flow field are compared for both equilibrium and finite-rate flow chemistry. This was made possible by the chemistry modelling implemented in the Lagrangian CFD code, L1D (The finite-rate chemistry modelling was implemented as part of this thesis and is described in Appendix A). The validity of assuming that the flow chemistry was either in equilibrium or frozen could also be determined from results presented in this section. One of the non-ideal diaphragm rupture models (the “holding time” model) was then incorporated into the full axisymmetric model of the acceleration tube and dump tank. The results obtained from running this model are the topic of Section 5.5. The best estimate of the flow field in the dump tank obtained from the CFD models is included in this section. The chapter concludes with a discussion of the flow processes that must be computationally modelled in order to produce reliable estimates of the conditions in X1 when operated at low densities.

5.1 X1 Modelling Details

For the operating conditions specified in Chapter 4, it was expected that the flow through the majority of X1 would be in the continuum regime. The flow should only become rarefied as it expands into the dump tank. One exception to this is that the gas within the shock waves present in the facility would not be in thermal equilibrium. However, it has long been established [16] that this small nonequilibrium region does not seriously affect the accuracy of continuum CFD results in the remainder of the flow field. The assumption of continuum flow will be assessed in a later section by examining the degree of rarefaction throughout the facility. In regions where the density is high enough for the gas to be considered a continuum, particle based methods such as DSMC are extremely inefficient due to the large number of particles and the high collision rate required to properly simulate the gas dynamics. As a result of this, it is most efficient to initially use a continuum CFD code to model the flow through the facility. The accuracy of the continuum results can then be assessed in regions where the continuum hypothesis breaks down to identify whether a different simulation technique is required in these regions.

To model the hypervelocity flow through X1 it is convenient to use a shock capturing CFD code that solves the compressible equations of gas dynamics. It was shown in the analysis of flow through the SST (see Chapter 3) that the effects of boundary layers are highly significant for low-density flow thus viscous effects must be modelled by the CFD code chosen. The high shock speeds present in X1 cause the shock processed gas to have a very high static temperature, around 8000 K in some cases. This may result in parts of the flow having high levels of dissociation and some ionisation that need to be modelled. One code that has all of the required features is Mb_cns [38]. Mb_cns is a multi-block compressible Navier-Stokes solver with shock capturing capability and a variety of gas models including nitrogen in chemical equilibrium. The code is parallelised allowing it to run on several processors simultaneously thus producing solutions far more rapidly than a conventional serial code. Mb_cns has the additional advantage that it was developed by Peter Jacobs, an academic within the Department of Mechanical Engineering at the University of Queensland, so the source code along with his expertise were available when it was desired to incorporate additional features in the code. Mb_cns is described in detail in reference [38].

An attempt was made to simulate rarefied flow in X1 using Mb_cns in an earlier study [87]. The simulation domain used in this study consisted of a conical nozzle attached to the exit of the acceleration tube and the dump tank. There were significant discrepancies between the CFD results and the experimental data to come out of the study. It was suggested that the errors in the CFD results could be attributed to the fact that the acceleration tube was not included in the CFD simulation, hence the effect of the boundary layer that grows along the acceleration tube wall was neglected. To remedy this, both the acceleration tube and the dump tank were included in the models of the facility presented here.

As a shock travels down the acceleration tube, a boundary layer grows in the flow behind it. As this boundary layer is swept out of the end of the tube, it will have a significant influence on the flow field in the dump tank during the test time. A boundary layer also grows behind the primary shock as it travels down the shock tube. It is thought that this boundary layer will have little effect on the test flow for two reasons: First, the flow in the shock tube has a much higher density and lower velocity than that in the acceleration tube resulting in a much thinner boundary layer. Second, when the primary shock arrives at the secondary diaphragm, the gas that will comprise the test flow is located immediately behind the primary shock where a boundary layer has only just begun to grow. The thicker boundary layers further upstream of the secondary diaphragm should have little influence on the test gas as it is expanded down the acceleration tube. The net result of this is that the cross-stream variation in the test gas as it exits the acceleration tube is chiefly due to two-dimensional effects in the acceleration tube. This implies that only the acceleration tube and dump tank must be modelled two-dimensionally provided an inflow condition at the secondary diaphragm station can be accurately determined from either experimental data or a one-dimensional code such as L1d [39]. The calculation of the state of the gas flowing into the model of the acceleration tube (inflow condition) is discussed further in Section 5.1.1.

In all simulations X1 is modelled as being axisymmetric. This poses a slight problem, as the dump tank is actually a rectangular prism as can be seen from Figure 4.1. The dump tank has been modelled as a cylinder with a radius equal to the minimum distance from the centerline to one of the dump tank walls. This is the distance from the centerline to the top wall, which is 147.5 mm. It will be shown later in this chapter that the simulation

time expires before any waves reflected from the modelled dump tank wall encroach on the test flow, so this approximation should not effect the estimate of the test conditions. The modelled geometry of the end of the acceleration tube and the dump tank is shown in Figure 5.1. In the simulations, the length of the acceleration tube was taken to be 2.91 m.

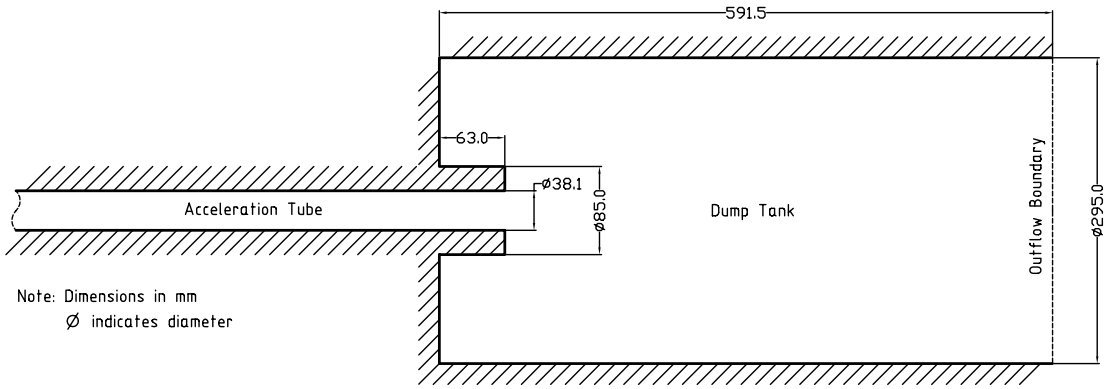

Figure 5.1: Modelled geometry of the end of X1's acceleration tube and dump tank.

5.1.1 Inflow Condition Calculation

As the Mb_cns model of the X1 is truncated upstream of the secondary diaphragm, an acceleration tube inflow condition must be determined for the simulation to proceed. The modelled inflow conditions must closely approximate the state of the gas that flows into the acceleration tube in the actual facility.

It is possible to make a purely analytical estimation of the performance of an expansion tube, and hence the acceleration tube inflow condition, based on the facility dimensions, fill states and the expected driver performance. Such an analysis was carried out by Trimpi [83] for dissociating air assuming ideal diaphragm rupture. However, experimental investigations have revealed that this approach is inaccurate [42, 75]. Neely [60] cites viscous effects on the flow, due to the low quiescent gas pressures in the shock and acceleration tubes, as the primary source of the inadequacies of such analytical predictive techniques. He goes on to state that one technique to minimise this complication, and any non-ideal driver effects, is to use the shock speeds observed during operation of the expansion tube to calculate the shock strengths in the test and acceleration gas. This approach of using experimentally observed shock speeds is adopted here to calculate the state of the gas flowing into the acceleration tube, which is initially taken to be the conditions behind the primary shock as it arrives at the secondary diaphragm. Using the

conditions behind the primary shock as our inflow conditions assumes that the secondary diaphragm operates ideally. This implies that when the primary shock arrives, the diaphragm material is instantly removed from the flow path so that a reflected shock is not generated. The effects of non-ideal diaphragm rupture are examined in Section 5.4. The conditions behind the primary shock are calculated from the fill conditions in the shock tube and the experimentally measured primary shock speed using the computational tool, Shock1D (available from www.mech.uq.edu.au/staff/jacobs/home/mb_cns.tar.gz). This code determines the post shock conditions by iteratively solving the Rankine-Hugoniot relations using the secant method. The state variables such as temperature, pressure and specific internal energy are recovered from the conserved variables, mass, momentum and energy using a model of nitrogen in chemical equilibrium. This gas model accounts for high temperature effects such as dissociation and ionization that significantly effect the post shock state. Figure 5.2 shows sample static pressure measurements at three locations

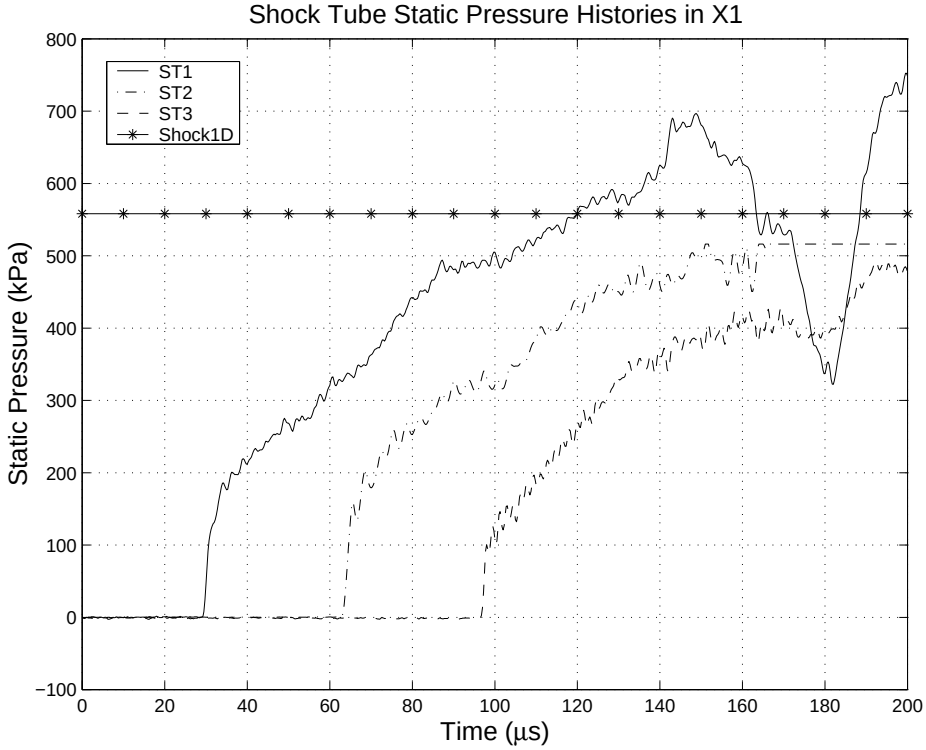

Figure 5.2: Measured static pressure traces from the shock tube in X1 during test S5_157 and the post shock pressure from Shock1D.

along the shock tube in X1 (see Chapter 4 for instrumentation details) along with the static pressure level behind the primary shock computed using Shock1D. Note that the signal from transducer ST2 becomes saturated before any steady level is reached and that the

recorded traces terminate before the arrival of the unsteady expansion at the transducer locations. It can be seen from Figure 5.2 that the measured static pressures upstream of the secondary diaphragm do not reach the calculated post shock pressure level until approximately 100 μs after the arrival of the primary shock. After this rise time has elapsed there is reasonable agreement between the measured pressure levels and the values computed from the observed shock speed.

Three factors that may contribute to the slow pressure rise behind the primary shock are; non-ideal rupture of the primary diaphragm, piston dynamics and the geometry of the compression tube. Non-ideal primary diaphragm rupture is likely to be the major cause as the duration of the pressure rise, approximately 100 μs, is of the same order as the opening time of the diaphragm and it is expected that pressure waves will be generated as the diaphragm opens [68]. The internal geometry of the X1 compression tube is shown in Figure 5.3. Upon rupture of the primary diaphragm, an unsteady expansion travels back into the driver gas. When the expansion propagates into the larger diameter section of the compression tube, compression waves form which travel downstream, gradually raising the pressure in the shock tube above the level behind the primary shock. To investigate the magnitude of this effect, the driver and shock tube have been computationally modelled using the Lagrangian one-dimensional CFD code, L1D [39] (See Appendix A for details of this code). In order to do this, the conditions in the driver had to be estimated as follows.

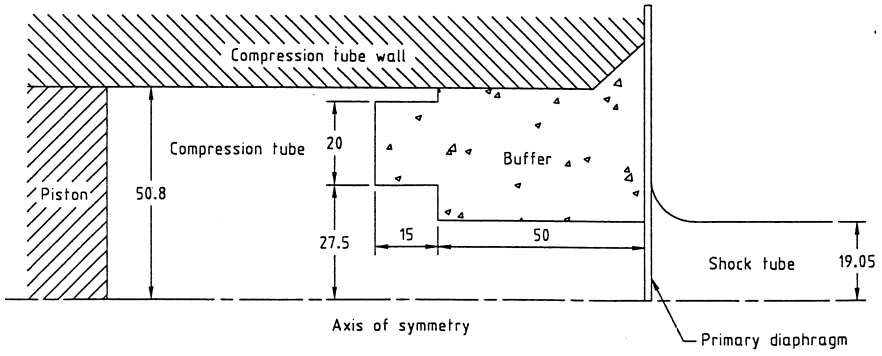

Figure 5.3: X1 driver geometry. Dimensions are in millimeters (Figure 5.3 from reference [43]).

5.1.2 Driver Condition Calculation

The bulk temperature the of the piston compressed driver gas can be estimated from the measured primary shock speed and the burst pressure of the primary diaphragm [23]. For this analysis it is assumed that the driver gas expands to the pressure behind the primary shock and the speed of the interface between the driver and test gas. Shock1D is used to calculate the conditions behind the primary shock from the observed shock speed (see Chapter 4 for experimental details), assuming that the test gas is nitrogen in chemical equilibrium. The speed of the interface is set to be the speed of the test gas behind the primary shock, while the pressure of the compressed driver gas is set to the burst pressure of the primary diaphragm. Due to the presence of the buffer, there is no area change between the driver and the shock tube in the immediate vicinity of the diaphragm. Assuming that the expansion of the driver gas after diaphragm rupture is ideal, the sound speed in the driver can be calculated using,

$$a_4 = \frac{\gamma - 1}{2} u_3 \left(1 - \left(\frac{p_3}{p_4} \right)^{\frac{\gamma-1}{2\gamma}} \right)^{-1} , \tag{5.1}$$

where the subscript 4 refers to the unexpanded driver gas and 3 refers to the fully expanded driver gas immediately behind the interface. The helium driver is assumed to be an ideal gas with γ = 1.667 and R = 2077 J/(kg.K). The bulk temperature in the driver can then be found using,

$$T_4 = \frac{a_4^2}{\gamma R} . \tag{5.2}$$

In the L1D simulation of X1's driver and shock tube, the piston face forms the left boundary of the computational domain and is assumed to remain stationary at the position it occupies when the diaphragm ruptures. The location of the piston face at diaphragm rupture can be calculated from the volume of the compressed driver gas, which is found using,

$$V_4 = \frac{m_{drv} T_4 R}{p_4} , \tag{5.3}$$

where m_{drv} is the mass of the driver gas. If the leaks around the piston are neglected, m_{drv} can be calculated from the compression tube fill conditions and the initial piston position using the ideal gas law. The parameters calculated using Shock1D and equations 5.1 to 5.3 are shown in Table 5.1 along with the fill conditions, initial driver volume and

the measured primary shock speed.

Driver gas	helium
Driver fill pressure, p_{drv}	71.44 kPa
Driver fill Temperature, T_{drv}	296 K
Initial driver volume	0.0182 m^3
Driver gas mass, m_{drv}	0.0021 kg
Test gas	nitrogen
Shock tube fill pressure, p_{st}	1932.0 Pa
Driver fill Temperature, T_{st}	296 K
Measured primary shock speed, $U_{primary}$	5244 m/s
Post shock flow speed, u_3 (Shock1D)	4748 m/s
Post shock static pressure, p_3 (Shock1D)	548.58 kPa
Driver bulk temperature, T_4 (computed)	2792.5 K
Primary diaphragm burst pressure, p_4	19.25 MPa
Piston face position at rupture	0.13 m

Table 5.1: X1 driver and shock tube conditions.

5.1.3 Effects of the Driver Area Variation

As mentioned earlier, the X1 driver and shock tube have been modelled one-dimensionally using L1D to assess the effect of the area variation in the driver on the static pressures in the shock tube. The computational domain for the L1D simulation extends from the piston face to the secondary diaphragm. The gas states of the computational cells in the driver were initially set to the bulk driver conditions shown in Table 5.1 while the gas states of the cells in the shock tube were initialised to the shock tube fill conditions. A total of 500 cells were used in the simulation. The computed static pressure histories at the transducer locations in the shock tube are shown in Figure 5.4. The effect of compression waves generated when the unsteady expansion traverses the area change in the driver section can be seen in this figure; a pressure increase is produced behind the primary shock as expected. However, the pressure rise is small compared with that across the primary shock. One can conclude that the area change in the driver is not the cause of the gradual pressure rise observed in the experimental data.

Even though we haven't identified the cause of the gradual pressure rise in the shock tube, we shall return to the issues of simulating the flow in the acceleration tube using a fixed set of post-shock conditions, obtained shortly before the shock arrives at the secondary diaphragm.

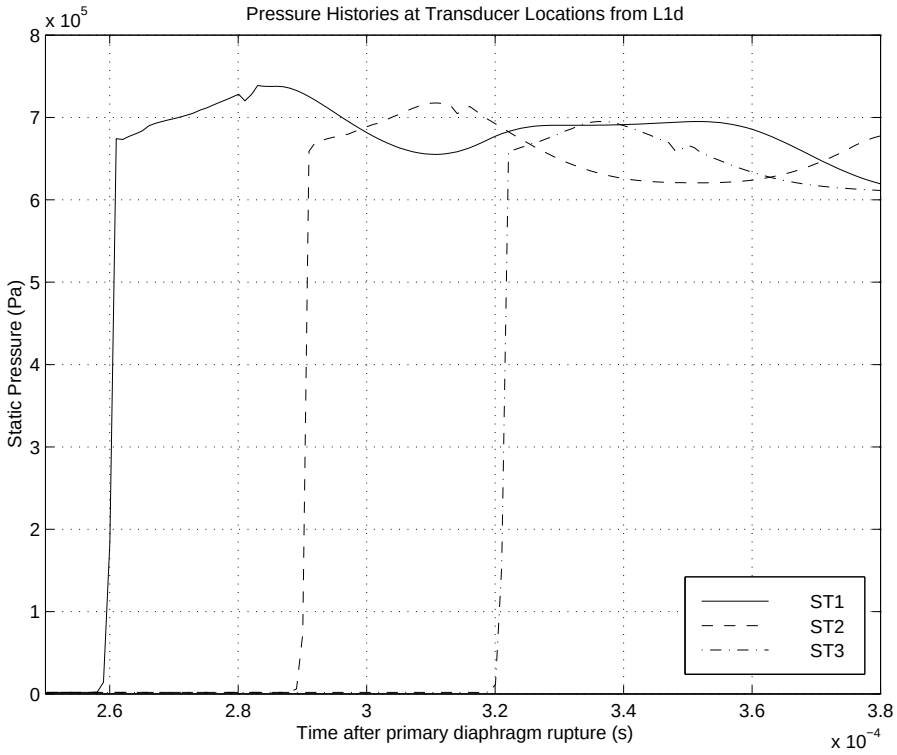

Figure 5.4: X1 shock tube static pressure histories computed using L1D.

5.1.4 Grid Definition

The initial axisymmetric computational models of X1's acceleration tube and dump tank, *x1rn2eq* and *x1rn2froz* (for X1 with a rarefied nitrogen test flow and equilibrium/frozen chemistry), are based on the geometry shown in Figure 5.1. For convenience, let us define the co-ordinate x as being the axial distance from the exit of the acceleration tube, and the co-ordinate r as being the radial distance from the axis of the acceleration tube. The computational models extend from the secondary diaphragm station at $x = -2.91\,\mathrm{m}$ to a plane part way along the dump tank at $x = 0.5285\,\mathrm{m}$. At the secondary diaphragm location, the inflow condition discussed in Section 5.1.1 is set. The other end of the computational domain is modelled as a supersonic outflow boundary. This assumes that waves do not reflect off the downstream end wall of the dump tank and affect the flow within the simulation time. The results shown in later sections will show that this assumption is valid; at the termination of the simulations the secondary shock is just exiting the computational domain. The computational grid for the acceleration tube has 3900 cells in the axial direction and 30 cells in the cross-flow direction. The cells are radially clustered towards the wall in order to adequately capture the boundary layer growth. This can be seen in Figure 5.5, which shows a sample of the computational grid near the exit of the

acceleration tube. For the most part, the computational grid for the dump tank has 300

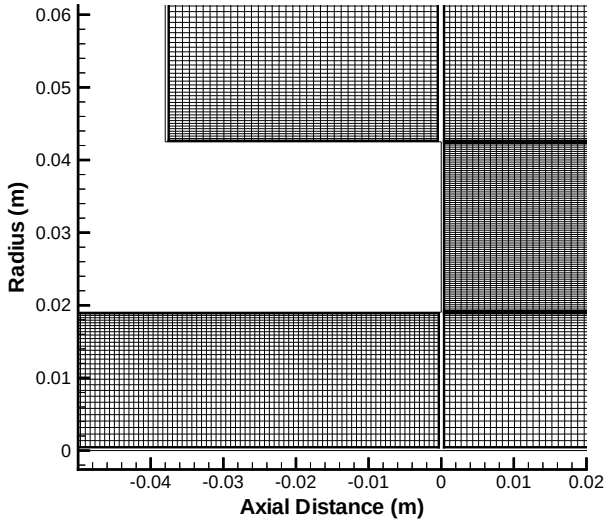

Figure 5.5: Sample of the computational grid for *x1rn2eq* and *x1rn2froz* at the entrance of the dump tank.

cells in the axial direction and 210 cells in the cross-flow direction. The computational grid for the initial simulations is composed of a total of 184,000 cells. The exact geometry of the initial computational model is contained in the simulation's input parameter file, *x1rn2eq.sit* (see Appendix B), which also includes the discretisation of each block in the model. Note that the input parameter file for *x1rn2froz* is the same as for *x1rn2eq* other than the chemistry model being altered. For this reason, only *x1rn2eq.sit* is included in the appendices. The cells in the model are initially filled with ambient temperature nitrogen with a pressure of 15 Pa.

The computational grid for the simulations presented in this chapter was arrived at after a number of simulations were run on coarser grids, in which some of the flow features did not appear to be adequately resolved. By refining the grid to the current level, the flow features around the shocks and contact surfaces were sharpened, but the overall solution did not vary much. This indicates that the results presented in this chapter are not sensitive to grid resolution. Typical simulations run on the grid presented in this section required approximately 100 days of CPU time to solve on an SGI Origin 2000 supercomputer. The physical time taken to run the simulations was considerably less than this, around 30 days, as the simulations were run in parallel on up to 8 processors.

5.2 Initial Simulation with Equilibrium Chemistry

The initial axisymmetric simulations of X1 operating at low densities were run for the two extremes of flow chemistry; equilibrium and frozen flow. The results of the simulation with frozen gas chemistry, *x1rn2froz* (for X1 with rarefied N_2 test gas and frozen chemistry), are presented in the next section (5.3). For the initial simulation with equilibrium gas chemistry, *x1rn2eq* (for X1 with rarefied N_2 test gas and equilibrium chemistry), the equilibrium nitrogen model of reference [69] is used. The species included in this equilibrium model are molecular (N_2), atomic (N) and ionized (N^+) Nitrogen, and electrons (e^-). The results of the initial equilibrium nitrogen simulation are presented in this section.

In order to accurately simulate the test flow in the dump tank, the flow through the acceleration tube must first be modelled correctly. To assess whether this has been achieved, the computed static pressure histories at four transducer locations along the acceleration tube have been compared with the experimental pressure histories from these transducers. Figure 5.6 shows a comparison between the computed pressure histories from the equilibrium nitrogen simulation and the raw experimental data. As the distance from the secondary diaphragm station increases, the difference between the computed and experimental shock arrival times at the transducer locations grows larger. For this simulation, the shock speed at the end of the acceleration tube (calculated from the shock arrival times at transducers AT7 and AT8) was found to be 4.46% greater than the experimental value of 9062 m/s. A possible cause of this discrepancy is that the assumption of equilibrium chemistry is not accurate; the validity of assuming the flow is in chemical equilibrium is explored in Section 5.4. Another possibility is the effect of the gradual pressure rise behind the primary shock (see Figure 5.2). In calculating the inflow condition for the Mb_cns simulations, it was assumed that the primary shock instantaneously raises the pressure of the test gas to the level calculated using Shock1D. The secondary shock then results from the discontinuity between the inflow gas and the fill gas in the acceleration tube. It is likely that this will produce a faster secondary shock than that driven by the lower pressures measured immediately behind the primary shock.

To enable easier comparison of the computed and experimental pressure traces, the time scales of the experimental histories were shifted to align the shock arrival times

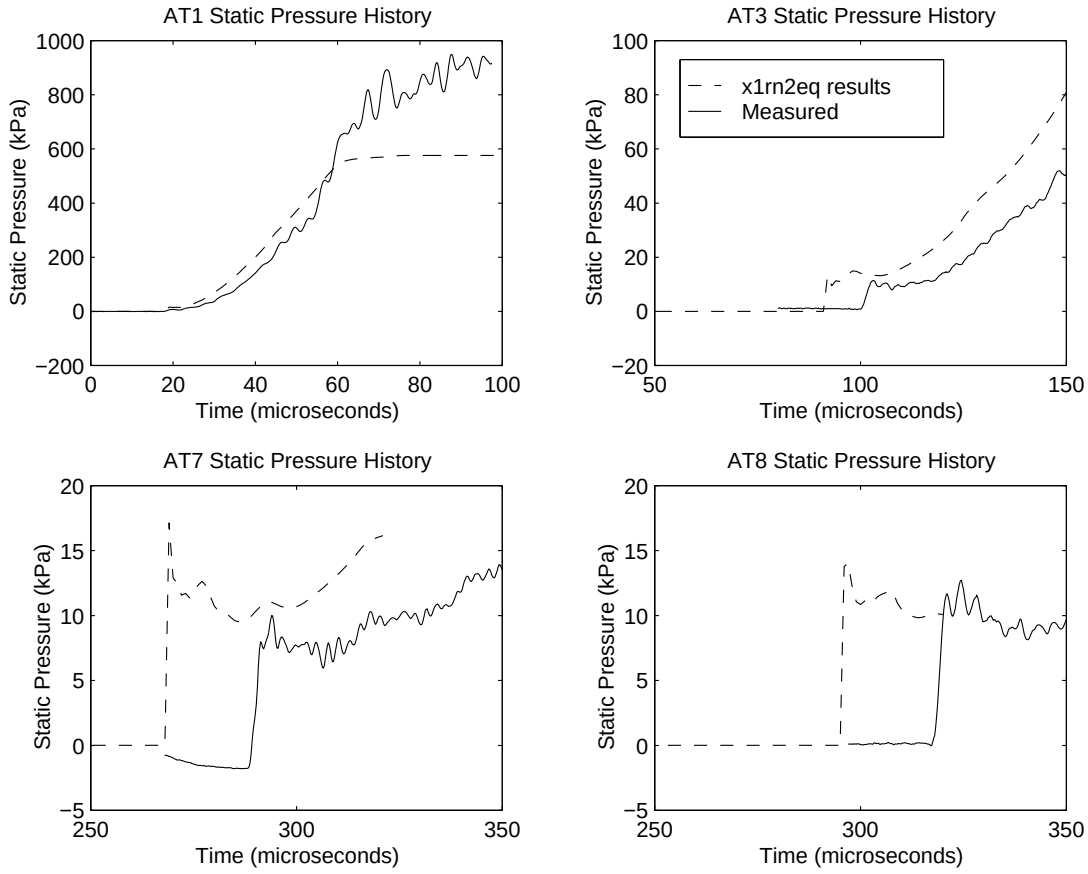

Figure 5.6: Computed and raw experimental static pressure histories in the acceleration tube of X1 at transducer locations AT1 (x = -2.718 m), AT3 (x = -2.018 m), AT7 (x = -0.376 m) and AT8 (x = -0.120 m). Computed values are from *x1rn2eq*. Experimental traces are from shot S7_26.

with those of the computed histories. Some of the experimental traces were also shifted vertically to compensate for the non-zero readings prior to the arrival of the shock, this is fair because it is believed that the drift seen is associated with the acceleration sensitivity of the pressure transducers, as discussed in Section 4.4. The aligned pressure histories are shown in Figure 5.7. It can be seen that there is very good agreement between the shape of the computational and experimental traces with a couple of exceptions: At transducer AT1 the experimental pressure continues to rise after the computed history has leveled off. At transducer AT3 it can be seen that the pressure gradient in the latter part of the expansion is greater in the computed history. The high experimental pressures at AT1 may be caused by a shock reflected from the secondary diaphragm. This possibility is explored in Section 5.5. The pressure gradient in the later part of the simulated expansion may be greater than that measured experimentally because of the unmodelled effects of piston motion. The agreement between magnitudes of the computed and experimentally

measured pressure histories is also very good.

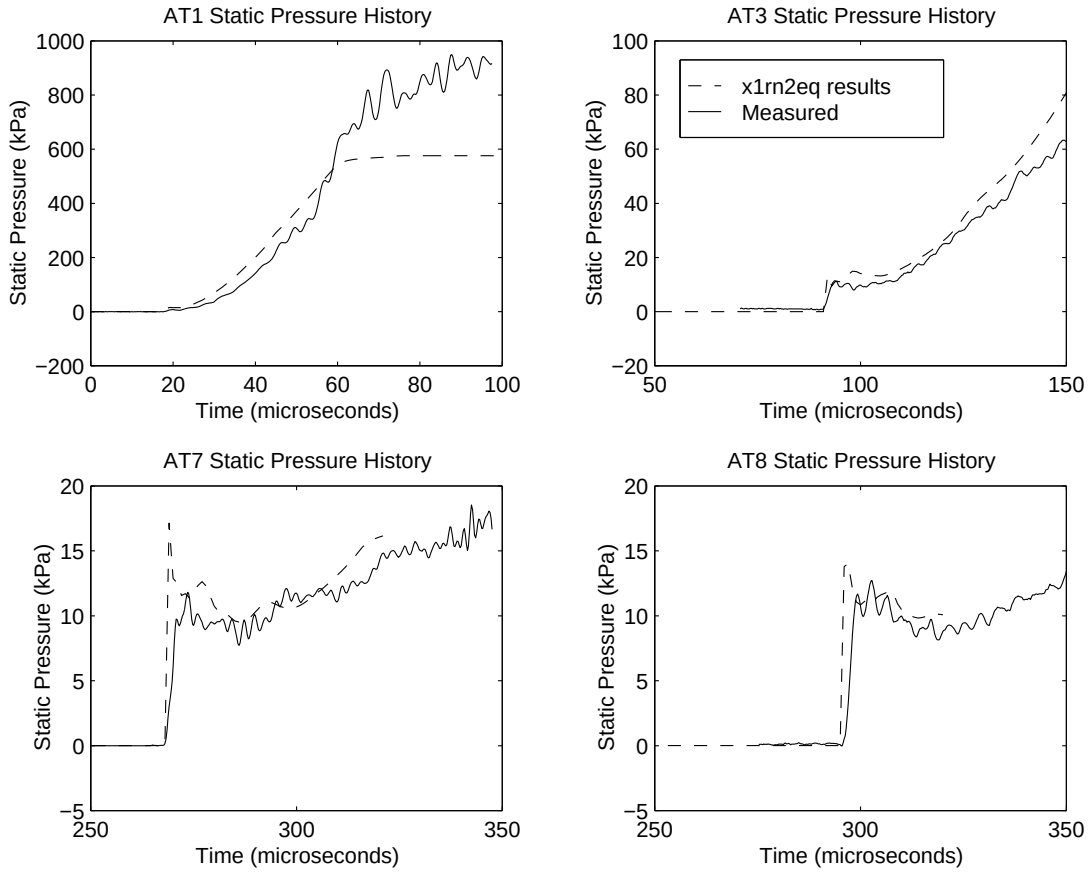

Figure 5.7: Aligned computed and experimental static pressure histories in the acceleration tube of X1 at transducer locations AT1 (x = -2.718 m), AT3 (x = -2.018 m), AT7 (x = -0.376 m) and AT8 (x = -0.120 m). Computed values are from *x1rn2eq*. Experimental values are from shot S7_26.

Now that it has been established that the simulation is in reasonable agreement with the experimental data within the acceleration tube, the results in the dump tank can be examined. The highest quality experimental bar gauge pressure data was measured with resistive strain gauges attached to the sensing bars (see Chapter 4 for details). One such bar gauge pressure history is compared to the values from the equilibrium simulation in Figure 5.8. As discussed in Section 4.4, both histories have been normalised by an estimate of the Pitot pressure at the acceleration tube exit from the TUBE program [60]. The Pitot pressure history from the CFD simulation has been multiplied by a factor of 0.93 to compensate for the difference between the measured bar gauge pressure and the Pitot pressure (see Section 4.5 for more details). The time-scale of the experimental history has been altered so that the shock arrival times coincides with that from the simulation results, this is to compensate for the error in the computed shock speed (4.46%) that

was identified earlier. The overall trends in bar gauge pressure after the arrival of the secondary shock (at $t \approx 330\ \mu$s) are in reasonable agreement. However, the sharp spike in Pitot pressure immediately following the arrival of the secondary shock in the simulated history is smeared over a much longer time period in the experimental trace. This is partially due to the response time of the bar gauage. From Figure 5.8 it can be seen that the simulation, *x1rn2eq*, has overestimated the steady Pitot pressure of the test flow by approximately 25% at that particular location.

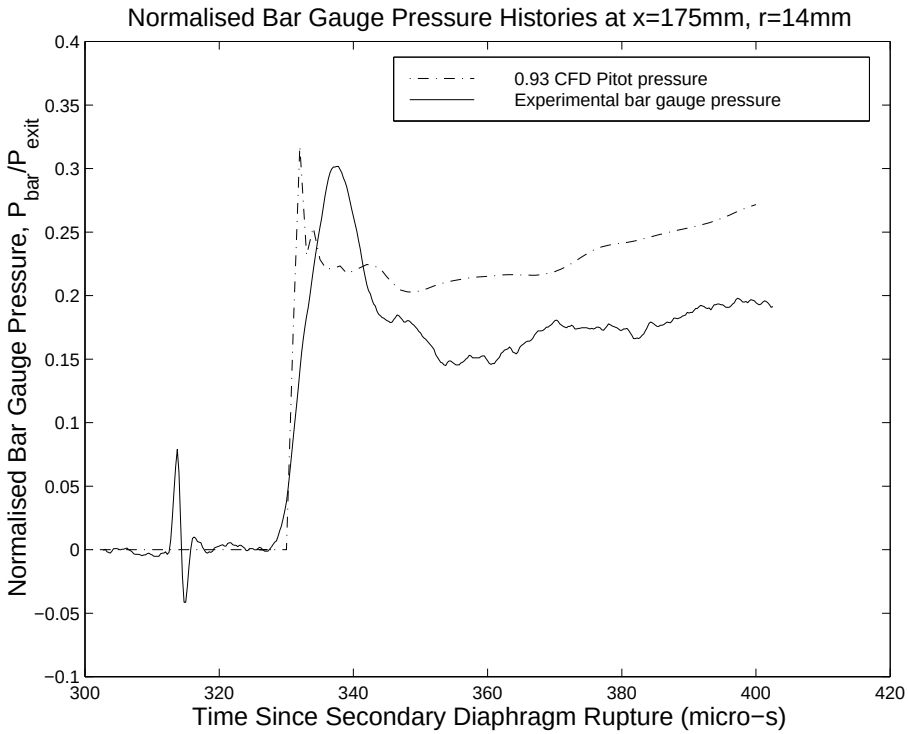

Figure 5.8: Normalised bar gauge pressure histories in the X1 dump tank 175 mm from acceleration tube exit at a radius of 14 mm. Computed values are from *x1rn2eq*.

The major flow processes that occur in the dump tank can be identified in the simulated pitot pressure history shown in Figure 5.8. The initial pressure jump (at $t \approx 330\,\mu$s) in the simulated history is due to the arrival of the secondary shock that compresses the acceleration gas. The contact surface between the shock processed acceleration gas and the test gas (secondary contact surface) arrives around 4 μs later. A gradual increase in pitot pressure begins later in the history; this signifies the arrival of the unsteady expansion at the transducer location. There are several features in the pitot pressure histories that cannot be attributed to the major flow processes mentioned thus far. The most visible of these features are the spikes in Pitot pressure that occur immediately after the arrival of

the secondary shock and the contact surface. To gain insight into the flow processes that cause the spikes, a series of contour plots showing the evolution of the flow field in the dump tank are shown in Figure 5.9.

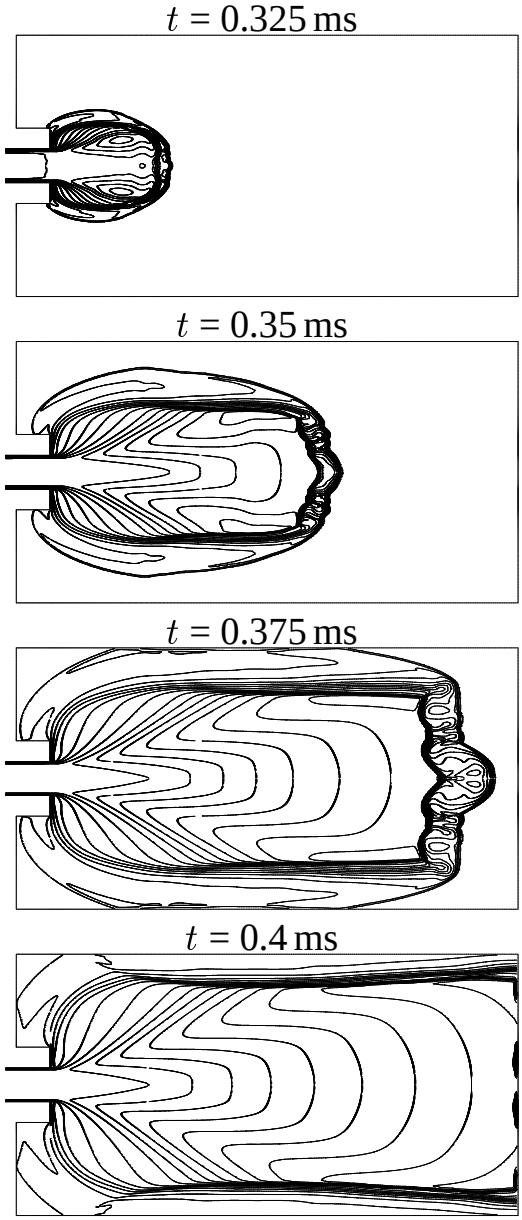

Figure 5.9: Contour plots of Mach number showing the evolution of the flow field in the dump tank for the simulation, x1rn2eq. t is the time since secondary diaphragm rupture.

The initial pressure spike is due to the starting process of the free-jet, which is analogous to the nozzle starting process described in Section 3.1. As the secondary shock travels into the dump tank the area of the shock surface increases, which causes the shock to decelerate. When the nitrogen in the dump tank is processed by this shock, its Mach number is lower than that of the gas that was originally in the acceleration tube, which

has been expanded to a high Mach number. An upstream facing shock forms to process the gas originating from the acceleration tube, reducing its velocity to that behind the secondary shock. A contact surface is present between the two shocks and it separates the gas originating from the acceleration tube and from the dump tank.

A second, longer duration spike in the computed Pitot pressure history occurs immediately after the secondary contact surface arrives at the transducer location. The phenomena suspected of causing this feature was observed by Jacobs in previous expansion tube simulations [37]. As the secondary shock and contact surface near the end of the acceleration tube, the distance separating them remains essentially constant. This is because the mass flow rate of acceleration gas through the secondary shock is balanced by the mass flow rate of gas bleeding into the boundary layer, so that the mass of gas between the shock and contact surface remains constant [54]. The acceleration gas bleeding into the boundary layer tends to accumulate just upstream of the secondary contact surface forming a large bulge in the boundary layer [37]. The bulge can clearly be seen in Figure 5.10, which shows the computed temperature contours in the acceleration tube 300 μs after secondary diaphragm rupture. At this time the secondary contact surface is located

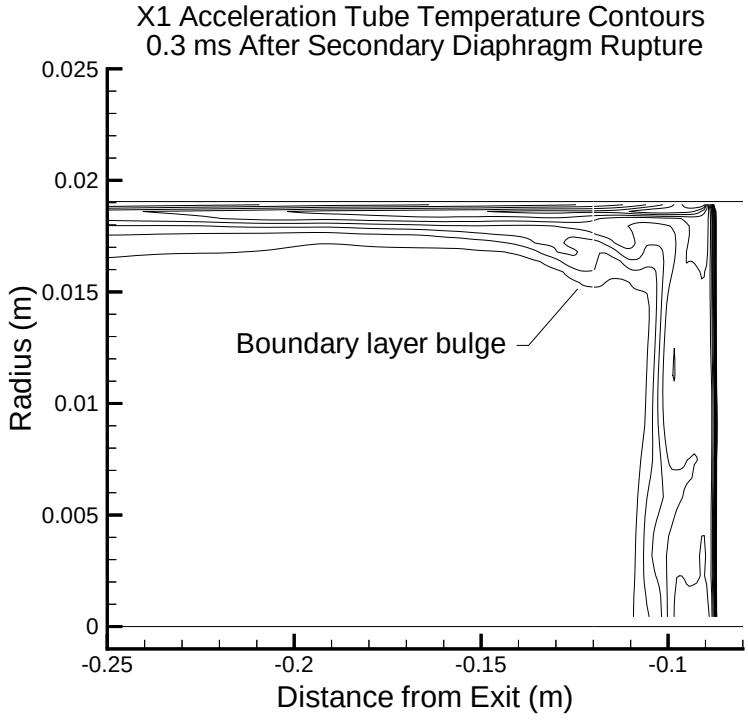

Figure 5.10: Computed temperature contours showing the boundary layer bulge in X1's acceleration tube at $t = 300$ μs.

at $x = -0.105\,\text{m}$ and the peak of the boundary layer bulge is at $x = -0.12\,\text{m}$. A series of radial Pitot pressure profiles at axial locations throughout the region of the bulge are shown in Figure 5.11. While the details of the flow processes in this region have not

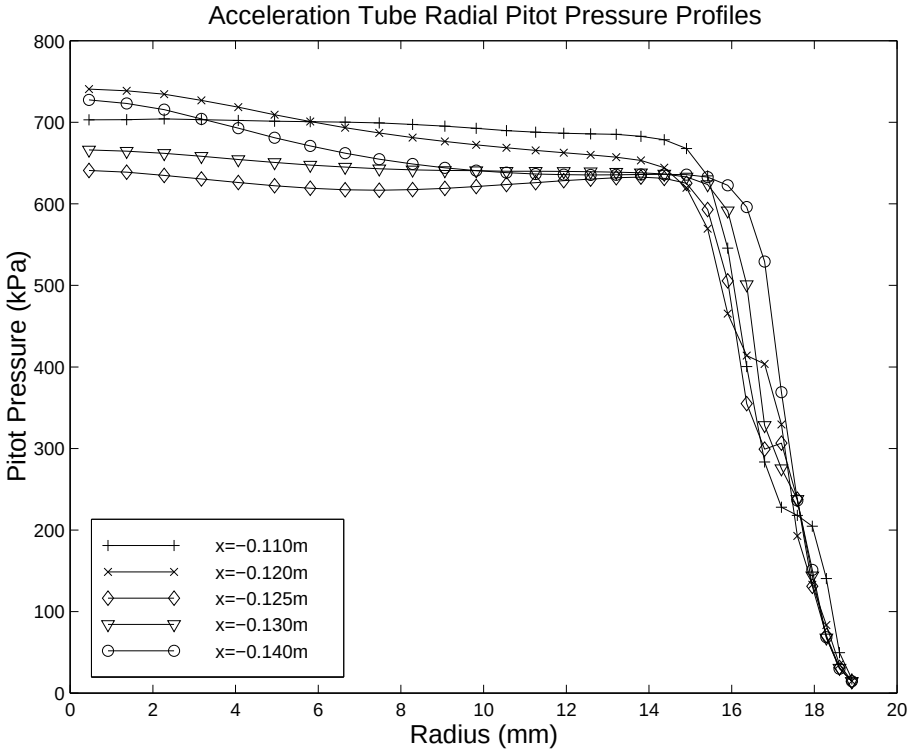

Figure 5.11: Radial profiles of P_{pitot} at axial locations in the region of the boundary layer bulge in X1's acceleration tube at $t = 300\ \mu$s.

been resolved, their effect on the Pitot pressure is apparent. At $x = -0.11\,\text{m}$, just behind the contact surface, the Pitot pressure profile is fairly uniform outside of the boundary layer. At $x = -0.12\,\text{m}$, the location of the peak of the boundary layer bulge, the profile becomes slightly peaked, with the pitot pressure at the centerline exceeding its value at $x = -0.11\,\text{m}$. At $x = -0.125\,\text{m}$ the boundary layer bulge has begun to thin and the Pitot pressure has dropped significantly across the entire tube. The Pitot pressure near the centerline then rises gradually as the distance from the peak of the bulge increases. At $x = -0.14\,\text{m}$, which is beyond the tail of the bulge, the Pitot pressure at the centerline has increased back to its original value. The Pitot pressure near the centerline follows the same trends as those observed behind the contact surface in the computed Pitot pressure history in the dump tank. It appears that the variation in Pitot pressure behind the contact surface in the dump tank is a result of the Pitot pressure variation near the acceleration tube centerline in the region of the boundary layer bulge.

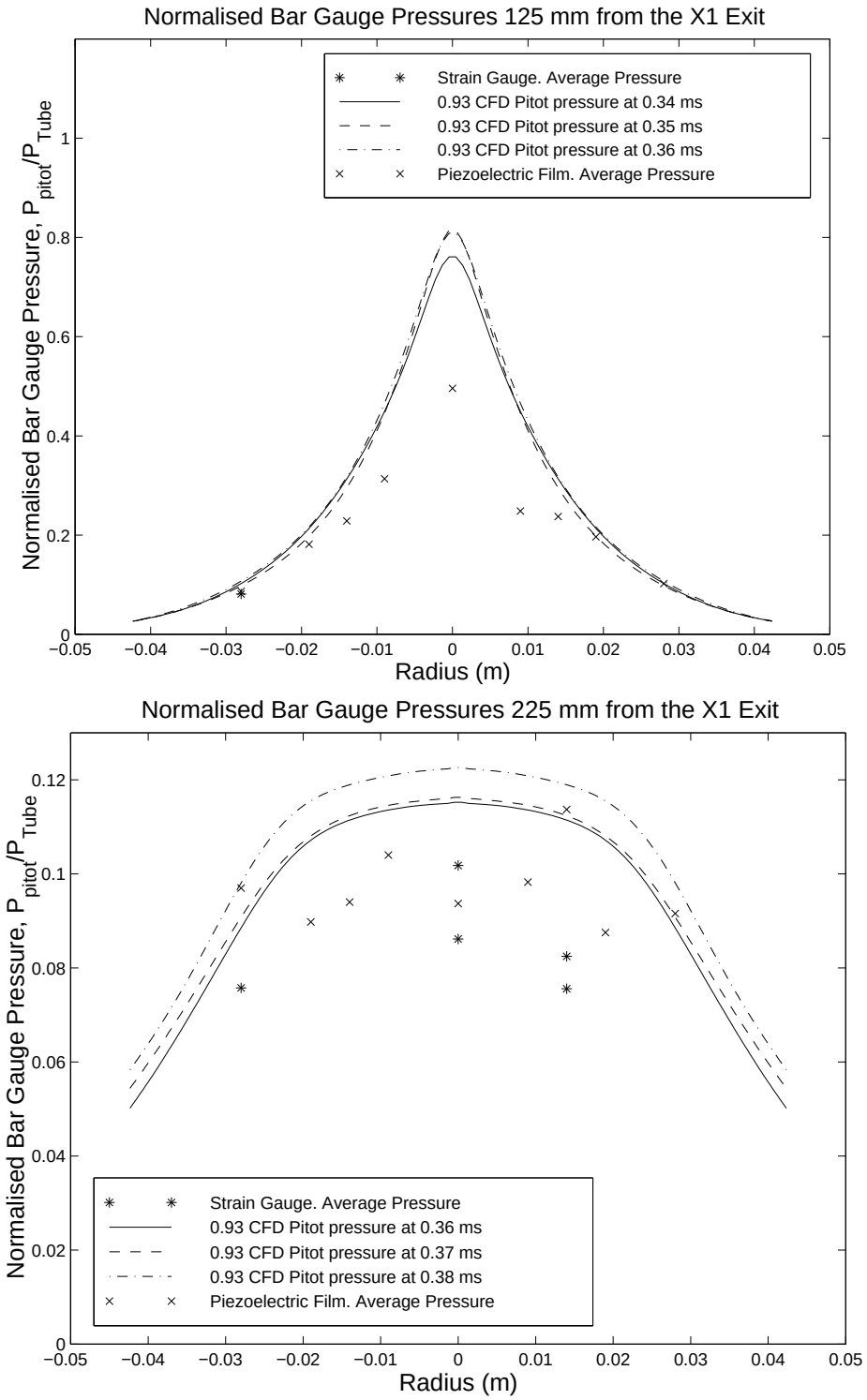

Figure 5.12: Normalised bar gauge pressure profiles in the X1 dump tank at 125 and 225 mm from acceleration tube exit during the passage of the test gas. Computed values are from *x1rn2eq*.

Figure 5.12 shows a comparison of the computed and experimental bar gauge pressure profiles during the passage of the test flow at $x = 125$ mm and $x = 225$ mm. From the profiles at $x = 125$ mm, it can be seen that the width of the high Pitot pressure core of the flow has been computed with reasonable accuracy. The results of an Eulerian simulation of the flow in X1's dump tank were presented in reference [49] where the effects of the boundary layers in the acceleration tube were neglected and the width of the core flow was significantly larger than that inferred from the experimental bar gauge pressure profiles. This indicates that the boundary layers at the end of the acceleration tube have a significant effect on the structure of the test flow. The profiles at $x = 125$ mm also show that the computed Pitot pressures from *x1rn2eq* at radii greater than 14 mm are in good agreement with the experimental data. However, the profiles at this location and at the nominal test location at $x = 225$ mm both show that the equilibrium simulation has significantly overestimated the Pitot pressure near the centerline.

In Section 5.1 it was stated that the validity of using a continuum CFD code (such as Mb_cns) to simulate the low-density flow through X1 must be assessed. This was done by evaluating Bird's breakdown parameter, P (see Section 2.2 for details), throughout the facility. It has been argued that the continuum description of the flow is no longer valid when the value of P exceeds 0.04 [10]. At the instant considered (350 μs), the breakdown parameter only exceeds 0.04 within the free jet into the dump tank. The computed contours of P in this region are shown in Figure 5.13. It can be seen that the core of the test flow is in the continuum regime as P is well below 0.04 near the centerline. The high values of P in the flow that has expanded around the corner at the acceleration tube exit indicate that this region of the flow will be subject to fairly strong non-continuum effects; the characteristic temperatures of the three thermal velocity components will be significantly different. It is expected that the flow in this region will not greatly affect the properties of the test flow near the centerline. The only other regions where the critical value of P is exceeded are within the shocks. However, as discussed in Section 5.1, the accuracy of shock capturing Navier-Stokes solvers is not compromised by the non-continuum effects that occur within shocks. From this data it appears that the accuracy of the estimated core flow conditions from Mb_cns should not be severely affected by non-continuum effects. It is important to note that the goal of this project is to produce a test flow where the breakdown parameter based on model size, P_D, is of the order of

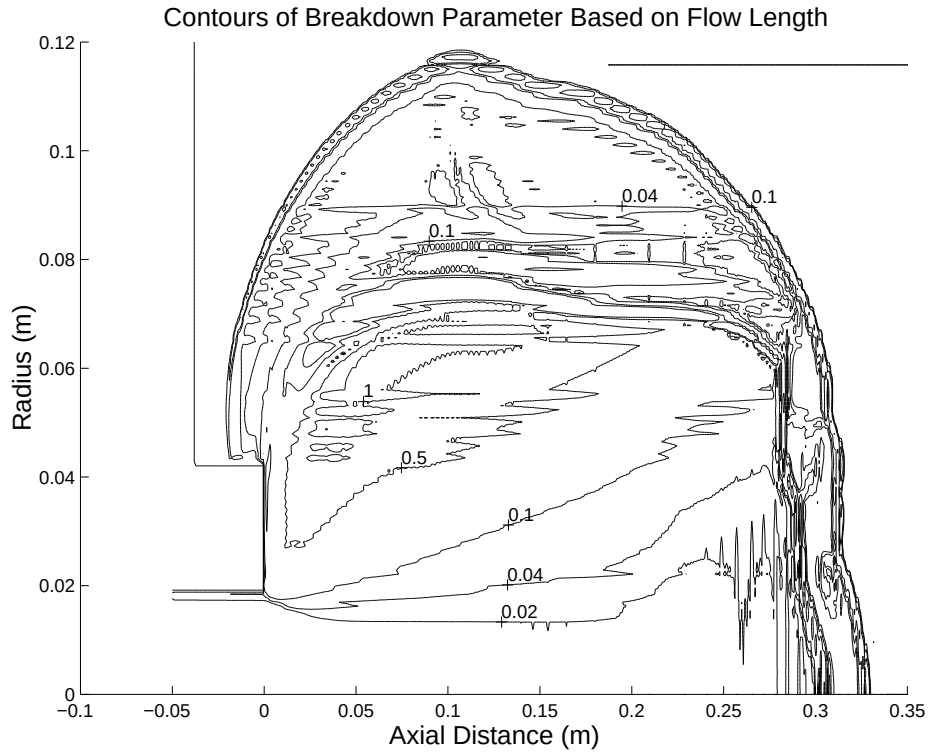

Figure 5.13: Computed contours of the breakdown parameter, P, based on the macroscopic gradient of density at $t = 350$ μs.

0.04. The value of P (the breakdown parameter based on macroscopic flow gradients) being less than 0.04 in the core flow does not compromise this goal as the size of the model should be considerably less than the length scale based on the macroscopic flow gradients. The reason for this is that for most experiments it is desirable for the flow over the model to be approximately uniform, which requires the flow gradients to be small in comparison to the model size.

In summary, there are two main problems with the results of the equilibrium simulation, *x1rn2eq*; the shock speed is slightly too high and, more importantly, the pitot pressures computed near the centerline in the dump tank are too large. One possible explanation for this is that the flow through the acceleration tube is frozen, which means that the flow expands too rapidly for chemical reactions to take place and significantly alter the composition of the gas. As the gas flowing into the acceleration has a high level of dissociation, freezing the chemistry should reduce the sensible energy of the flow down the tube by preventing the release of chemical energy into the flow via recombination. It was thought that this would result in lower shock speeds and Pitot pressures.

5.3 Initial Simulation with Frozen Chemistry

To simulate frozen flow in the acceleration tube and dump tank using Mb_cns, the pressure, temperature and velocity of the inflow gas at the secondary diaphragm station were taken to be the equilibrium values presented in Section 5.1.1. The flow through the remainder of the facility was then modelled as being a calorically perfect gas with $\gamma = 1.4$. This prevents the chemical energy tied up in the dissociated component of the inflow gas from re-entering the flow via recombination. This mimics the effect of frozen gas chemistry although the values of γ, R, C_p and C_v will be incorrect. The results from a simulation using this technique, *x1rn2froz*, are presented in this section.

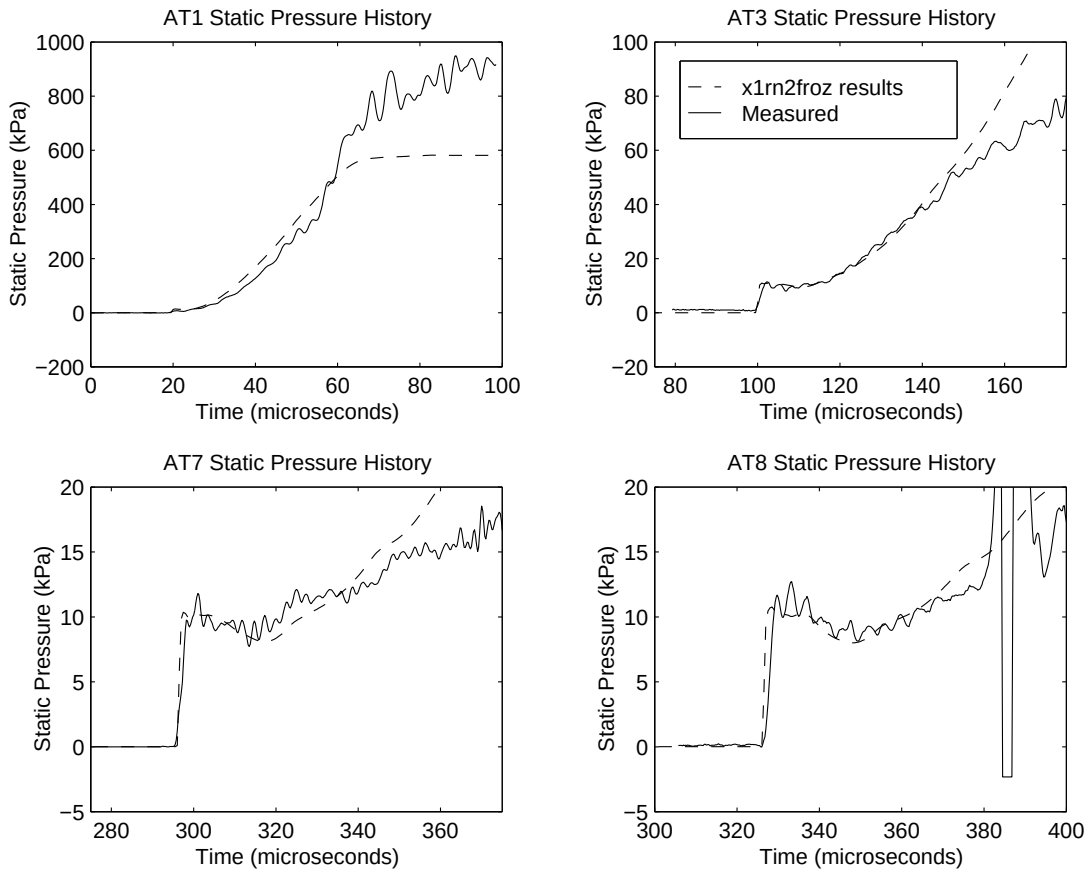

Figure 5.14: Aligned computed and experimental static pressure histories in the acceleration tube of X1 at transducer locations AT1 (x = -2.718 m), AT3 (x = -2.018 m), AT7 (x = -0.376 m) and AT8 (x = -0.120 m). Computed values are from *x1rn2froz*. Experimental values are from shot S7_26.

Figure 5.14 shows a comparison between the computed pressure histories from *x1rn2froz* and experimental data that has been aligned as in Section 5.2. For this simulation, the shock speed at the end of the acceleration tube (calculated from the shock arrival times at

transducers AT7 and AT8) was found to be 6.19% lower than the experimental value of 9062 m/s. So, as expected, freezing the flow chemistry results in a significant reduction in the shock speed. It can be seen that the agreement between shape of the computational and experimental traces is as good as in the results from the equilibrium simulation, *x1rn2eq* (see Figure 5.7). The two discrepancies that were observed in the results of *x1rn2eq* are still present. The agreement between magnitudes of the initial portions of the computed and experimentally measured static pressure histories is even better than in the results of *x1rn2eq*: The combination of the lower computed shock speed and the perfect gas model has lowered the pressures between the secondary shock and the contact surface so that they are in agreement with the experimental level.

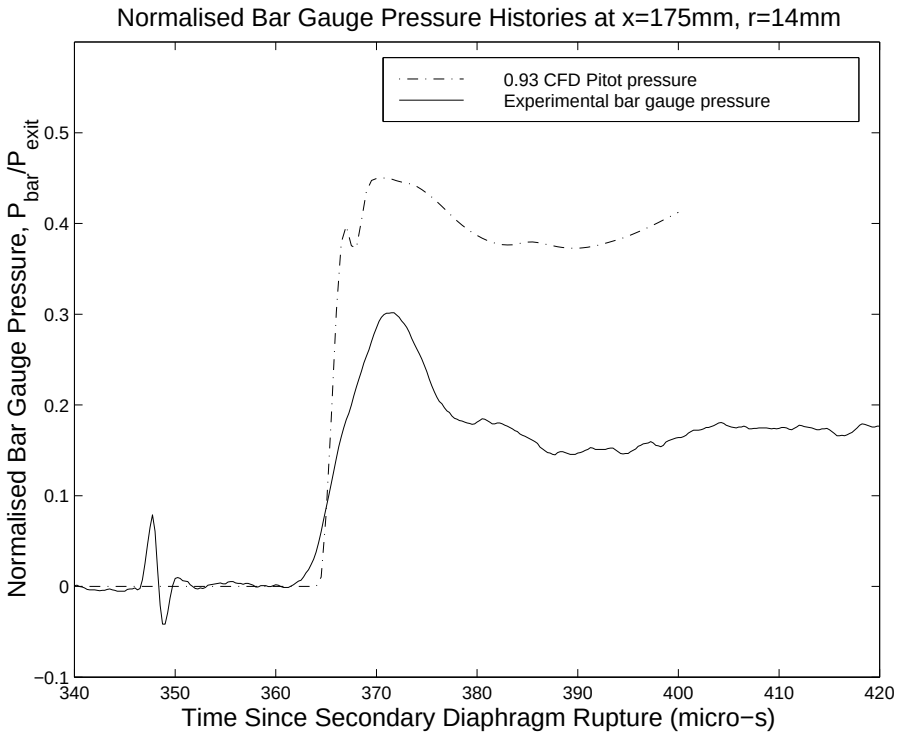

Figure 5.15: Normalised bar gauge pressure histories in the X1 dump tank 175 mm from acceleration tube exit at a radius of 14 mm. Computed values are from *x1rn2froz*.

As in the previous section, the computed Pitot pressure history at the point ($x = 175\,\text{mm}$, $r = 14\,\text{mm}$) is compared to a bar gauge pressure history measured using the strain gauges mounted on the sensing bar at this location. The results of the frozen simulation and the experimental history are shown in Figure 5.15, normalised and aligned as in the previous section. From Figure 5.15, it can be seen that while the agreement between the shape of the two histories is quite good, the Pitot pressures from the frozen simulation

are much higher than the measured bar gauge pressures. The nominally steady bar gauge pressure of the test flow from the frozen simulation is almost double the experimental level at this particular location. It is known that the errors in the computed velocities are reasonably small as the shock speed is underestimated by 6.19%. This implies that the high pitot pressure are due to a large overestimation of the density. The high density values result from the fact that the temperature of frozen test flows is generally lower than for those in equilibrium, due to the higher level of dissociation. The overestimation of Pitot pressures by the simulation with frozen chemistry can be confirmed by examining Figure 5.16. This figure shows a comparison of the computed Pitot pressure profiles during the passage of the test flow at $x = 175$ mm, and the nominally steady measured bar gauge pressure levels at this location. The error in the CFD profiles is very large around the centerline, indicating that a frozen gas composition is not a valid chemistry model for simulating the flow through X1 when operated at low-density conditions. It is apparent that the Pitot pressures in the facility are being reduced by some unmodelled mechanism.

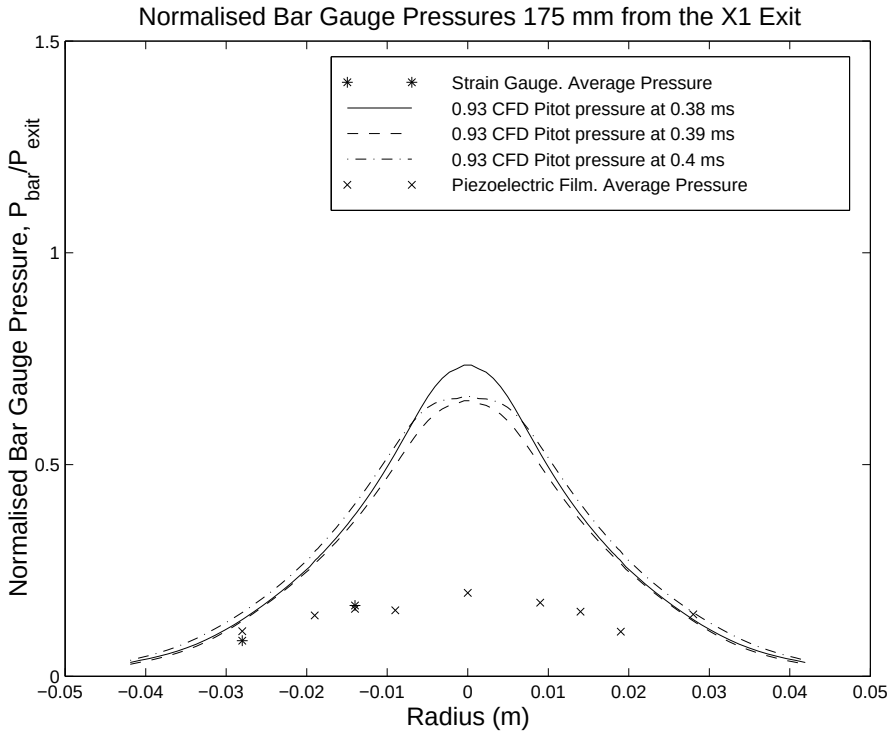

Figure 5.16: Normalised bar gauge pressure profiles in the X1 dump tank 175 mm from acceleration tube exit during the passage of the test gas. Computed values are from *x1rn2froz*.

5.4 Non-Ideal Diaphragm Rupture and Chemistry

It was noted in the previous section that an unmodelled mechanism was decreasing the total pressure of the flow through X1. One such mechanism that has been omitted from the computational models thus far is the diaphragm rupture process. An assumption of ideal diaphragm operation was made in Section 5.1.1, and this requires the diaphragm material to be instantaneously removed from the flow path upon the impact of the primary shock. This results in the behaviour illustrated in the wave diagram shown in Figure 5.17(a). Of particular note is that the primary shock is not reflected. However, experiments by Shinn and Miller [75] with helium test gas have shown that the shock reflected from a diaphragm maintains sufficient strength to travel over 110 mm upstream into the oncoming test gas even for the thinnest practical diaphragm (3.18 μm polyester film). The test gas originates from the vicinity of the secondary diaphragm hence a portion of it will be processed by the reflected shock and experience the resultant loss in total pressure and increase in entropy. In addition to this, the temperature rise behind the reflected shock may be sufficient to produce a level of dissociation that can only be eliminated by recombination in the unsteady expansion that follows secondary diaphragm rupture. Neely [60] noted that for air as the test gas, the severity of the expansion may cause effective freezing of the composition, leading to a nonequilibrium test flow.

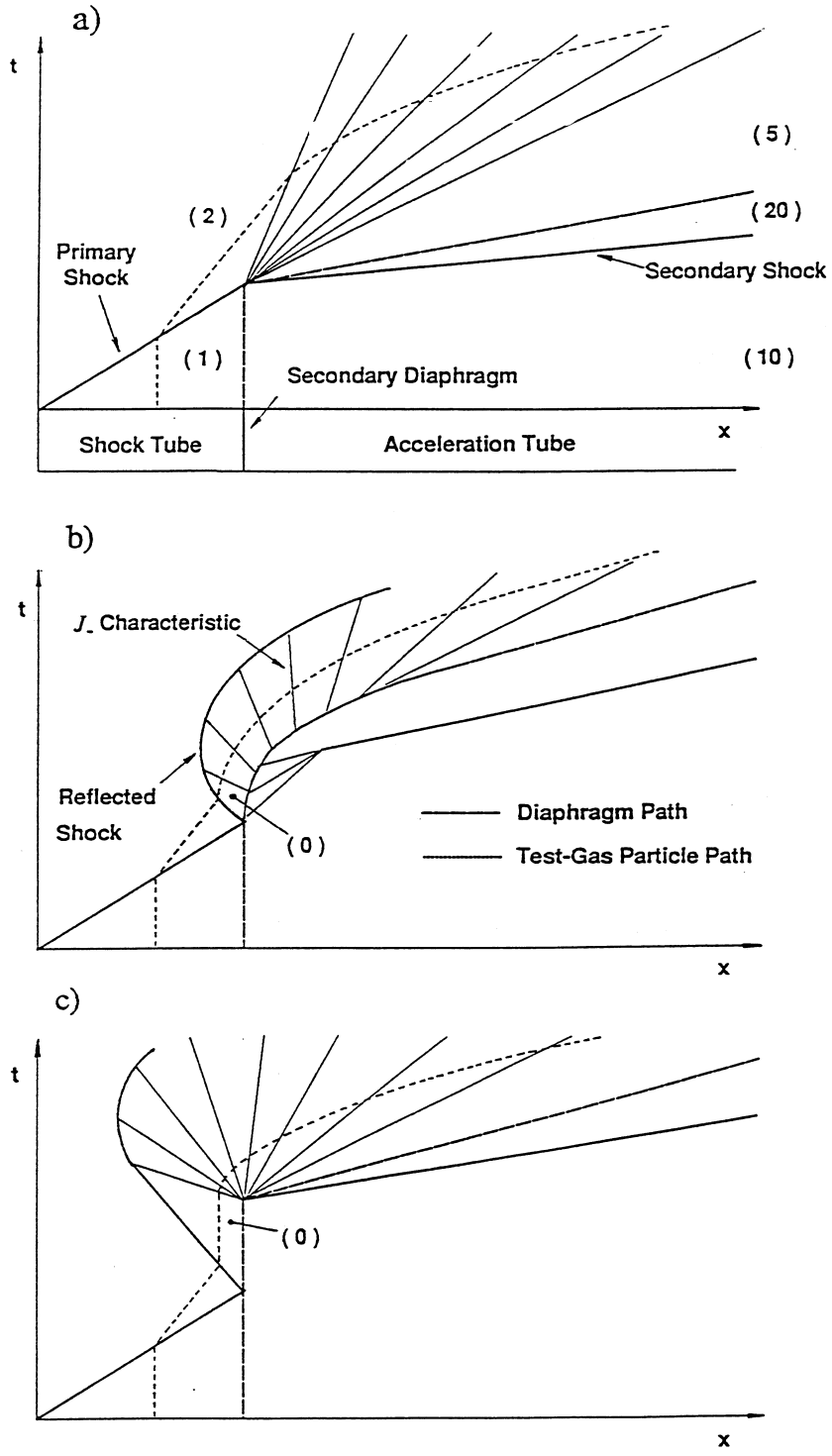

Figure 5.17: $x - t$ wave diagrams for secondary diaphragm rupture models; a) ideal diaphragm operation, b) inertial diaphragm model and, c) holding time model. Figure 2.10 from reference [8].

The manner in which the secondary diaphragm ruptures will effect both the strength of the reflected shock and the rate of expansion of the test gas. Operation of the X1 has shown that the light (secondary) diaphragm is sheared around its circumference by the shock processed test gas. This leaves the detached diaphragm material, which may be solid or vapourised, to travel with the flow [60]. The behaviour of the detached diaphragm material in the flow is unclear, but it is known that shock speeds observed in the acceleration tube could not be generated unless the diaphragm ceases to act as an obstacle to the flow within approximately one tube diameter of the diaphragm station. It has been suggested that fragmentation of the diaphragm may allow the test gas to leak past the diaphragm material [60]. A detailed computational study of diaphragm rupture processes was carried out by Petrie-Repar [67] using a axisymmetric Euler solver that featured adaptive meshing and time variant boundary conditions. Using this CFD code both the fragmentation and inertia of the light diaphragm could be modelled. Unfortunately, the Eulerian nature of the Petrie's code renders it unsuitable for modelling complete facilities where viscous effects are important. However, two simple, one-dimensional models have been developed to account for some of the effects of non-ideal diaphragm rupture without requiring the use of a specialised CFD code.

The planar, "diaphragm inertia" model for light diaphragm rupture was proposed by Morgan and Stalker [56]. In this model it is assumed that the diaphragm is sheared cleanly around its periphery upon the impact of the primary shock, it then remains intact and planar as it is accelerated by the pressure field. The inertia of the diaphragm material is assumed to be the sole source of resistance to its motion. The diaphragm material is removed from the flow path approximately one tube diameter downstream of the diaphragm station to account for its eventual fragmentation and the leakage of the test flow past it.

A second one-dimensional model for non-ideal diaphragm rupture was used by Wilson [88]. In this model the inertia of the diaphragm is represented by having the diaphragm remain intact after the impact of the primary shock for a specified "holding time". After this time the diaphragm is instantaneously removed from the flow path without further affecting the flow.

The differences in the wave processes caused by diaphragm inertia and holding time models can be seen by examining the Figure 5.17. The motion of the diaphragm in the diaphragm inertia model relieves the pressure behind the reflected shock so that it weakens

over time (see Figure 5.17(b)). This lowers the temperature of the test gas and hence the initial dissociation level. Additionally, the diaphragm inertia limits the initial expansion rate allowing effective recombination to occur [8]. For the holding time model (see Figure 5.17(c)), a fully stagnant region is formed behind the reflected shock. A centered unsteady expansion then forms when the diaphragm instantaneously ruptures at the expiration of the holding time. The strength of the reflected shock is not attenuated until the head of the expansion intersects it, leading to a significantly higher initial level of dissociation than for the diaphragm inertia model. Due to the strength of the reflected shock and the instantaneous rupture of the diaphragm, the initial expansion rate is also greater for the holding time model, leading to stronger nonequilibrium effects in the expanding test gas. The combination of these two effects indicates that the degree of test gas dissociation will be overestimated by the holding time model.

The effects of the diaphragm rupture models on the nonequilibrium flow composition in an expansion tube has been studied previously by Bakos and Morgan [9]. In their study, the nonequilibrium flow composition was found by first computing pressure-time histories for a number of test particles, then using a finite-rate chemistry package to calculate the composition time histories. The pressure time histories for the test particles were calculated both analytically, assuming a perfect gas, and numerically with equilibrium chemistry. This analysis assumes that the flow processes that occur in the expansion tube are decoupled from the effects of nonequilibrium chemistry, which may not be the case. The implementation of finite-rate chemistry modelling in the Lagrangian one-dimensional code, L1D (see Appendix A for details), enables the direct comparison of the effects of the two diaphragm rupture models on the flow chemistry in X1, with the gas dynamics and chemistry properly coupled. To achieve this, both the holding time and diaphragm inertia models were included in a set of L1D simulations of the flow through X1's shock tube and acceleration tube.

The diaphragm inertia model was implemented in an L1D simulation, *x1inert_dia*, by modelling the sheared diaphragm as a light piston. A 9 μm thick polyethylene secondary diaphragm was used in the low-density shots in X1. The density of polyethylene is around 2300 kg/m^3, resulting in the 19.05 mm radius diaphragm having a mass of 2.36×10^{-5} kg. The computational domain of the simulation extends from the entrance of the shock tube, at x = -5.0 m, to the exit of the acceleration tube at x = 0.0 m. The

2.36×10^{-5} kg piston that represents the sheared diaphragm material was initially located at the secondary diaphragm station, at x = -2.91 m. The gas in the shock tube was divided into 500 Lagrangian cells. The cells were clustered towards the diaphragm location to maintain reasonably small cell sizes when the gas near the diaphragm is rapidly expanded. The strength of the clustering along with the other simulation parameters can be obtained from the simulation's input parameter file, *x1inert_dia.Lp*, which is included in Appendix B. The initial state of gas in the shock tube was set to the conditions behind the primary shock, which are listed in Table 5.1. This effectively initiates the simulation upon the impact of the primary shock on the secondary diaphragm. The gas in the acceleration tube was discretised into 500 uniform cells, its initial state was that of room temperature nitrogen at 15 Pa. The simulation was allowed to run for 25 μs, by this time the diaphragm had travelled around 50 mm from its initial location, which is slightly more than one tube diameter. The simulation was then halted and the diaphragm removed from the flow, as required by the diaphragm inertia model. The simulation was then restarted without the diaphragm present and allowed to run until 200 μs after the rupture of the secondary diaphragm. Viscous effects were omitted to avoid confounding influences.

Roberts, Kendall and Morgan [72] calculated effective holding times for a number of light diaphragms used in expansion tube. This was done by constructing an $x - t$ wave diagram from heat flux signals recorded in the region of the diaphragm, extrapolating to determine the delay between the impact of the primary shock and the time at which the secondary shock is transmitted into the acceleration tube. For a planar 13 μm polyethylene diaphragm (similar to the 9 μm polyethylene diaphragm used during low-density testing in X1), the holding time was found to be of the order of 10 μs over a range of pressures behind the primary shock that includes value encountered during low-density testing in X1. For this reason a holding time of 10 μs was adopted here. The holding time model was implemented in an L1D simulation, *x1ht*, by first running a simulation in which the primary shock reflected from a solid wall. This initial simulation was run for a holding time of 10 μs following the reflection of the primary shock. The reflected shock was found to travel 8.45 mm upstream within the 10 μs period. The computed state of the stagnant gas behind the reflected shock is given in Table 5.2. The simulation including the holding time model was then formulated by dividing the flow into three gas slugs: The first gas slug extended from the entrance of the shock tube at x = -5.0 m to the location of

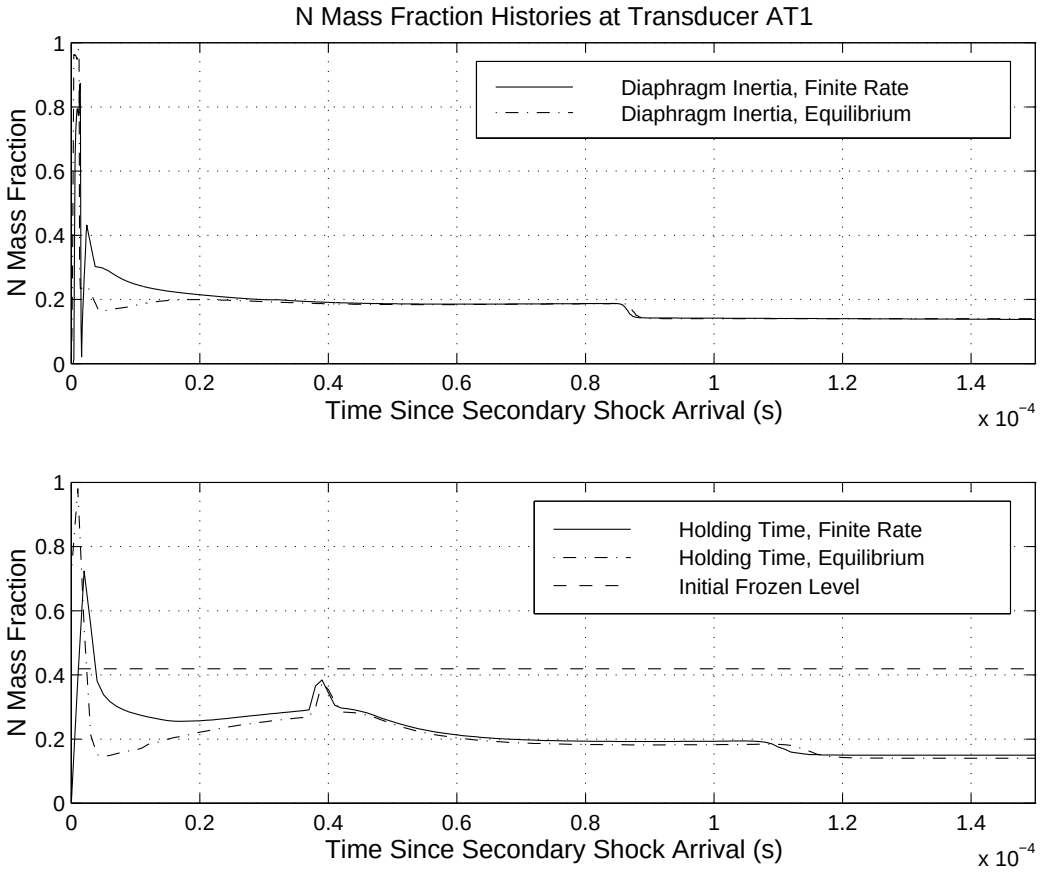

Figure 5.18: N mass fraction histories at AT1 from *x1inert_dia* and *x1ht* using both finite-rate and equilibrium chemisty.

the reflected shock at x = -2.91845 m, and contained gas with the conditions behind the primary shock given in Table 5.1. The second gas slug extended from the reflected shock location to the secondary diaphragm station at x = -2.91 m, and contained gas with the conditions behind the reflected shock given in Table 5.2. The final gas slug extended from the secondary diaphragm station to the acceleration tube exit at x = 0.0 m, and contained ambient temperature nitrogen at 15 Pa. When this simulation was initiated, there was no barrier to prevent the gas behind the reflected shock from suddenly expanding into the acceleration tube, thus simulating the instantaneous rupture of the secondary diaphragm after a 10 μs holding time. Each of the three gas slugs was discretised into 250 Lagrangian cells. The simulation was terminated 200 μs after the rupture of the secondary diaphragm. As in the simulation including the diaphragm inertia model, viscous effects were not modelled.

Figure 5.18 shows a comparison of the atomic nitrogen mass fraction (f_N) time histories computed using the two different diaphragm rupture models with finite-rate chem-

Post reflected shock static pressure	6826.4 kPa
Post reflected shock static temperature	10284 K
Post reflected shock N_2 mass fraction	0.5807
Post reflected shock N mass fraction	0.4189
Post reflected shock N^+ mass fraction	3.807×10^{-4}
Post reflected shock e^- mass fraction	1.492×10^{-8}

Table 5.2: Stagnant equilibrium conditions behind the shock reflected from the secondary diaphragm in X1.

istry. Simulations were also run with equilibrium chemistry so that the departure from equilibrium in different parts of the flow could be assessed. The time histories were recorded at the location of transducer AT1 at x = -2.718 m. The time, t, on the horizontal axis is the time since the arrival of the secondary shock. Unfortunately, L1D produces erroneous values at the intersection of blocks due to some unresolved problem with the numerics (personal communication, P. A. Jacobs). These spurious values are visible in the f_N histories at $t = 2\,\mu$s in the results of the diaphragm inertia simulations and at $t = 40\,\mu$s in the results of the holding time simulations. While these values are non-physical, they do not effect the remainder of the flow field and can be disregarded (personal communication, P. A. Jacobs). In the period just after the arrival of the contact surface, around $t = 3\,\mu$s, the flow is highly nonequilibrium. The departure from equilibrium is greater for the holding time simulation due to the higher initial expansion rate. As t increases, the flow passing the transducer location has been processed by a smaller portion of the expansion, hence the equilibrium value of f_N increases. The value of f_N does not increase much in the equilibrium diaphragm inertia simulation because the reflected shock is being continuously weakened, hence f_N of the gas prior to expansion is lower than in the holding time simulation. The effects of reflected shock attenuation are not seen in the holding time simulation until after $t = 40\,\mu$s. At this time, the gas flowing past the transducer location has been processed by the reflected shock after the head of the expansion has intersected it (see Figure 5.17(c) for a graphical representation). The weakening of the reflected shock lowers the dissociation level behind it, which causes the gradual decrease in the value of f_N between $t = 3\,\mu$s and the time at which the reflected shock passes the transducer location. The delayed attenuation of the reflected shock in the holding time simulation allows it to travel further upstream, this results in the reflected shock being swept past AT1 at a later time than in the diaphragm inertia simulation. From Figure 5.18, it can be concluded

that the main difference in the flow chemistry resulting from the use of the two diaphragm rupture models, is the greater level of dissociation present in the gas expanded prior to the attenuation of the reflected shock in the holding time simulation.

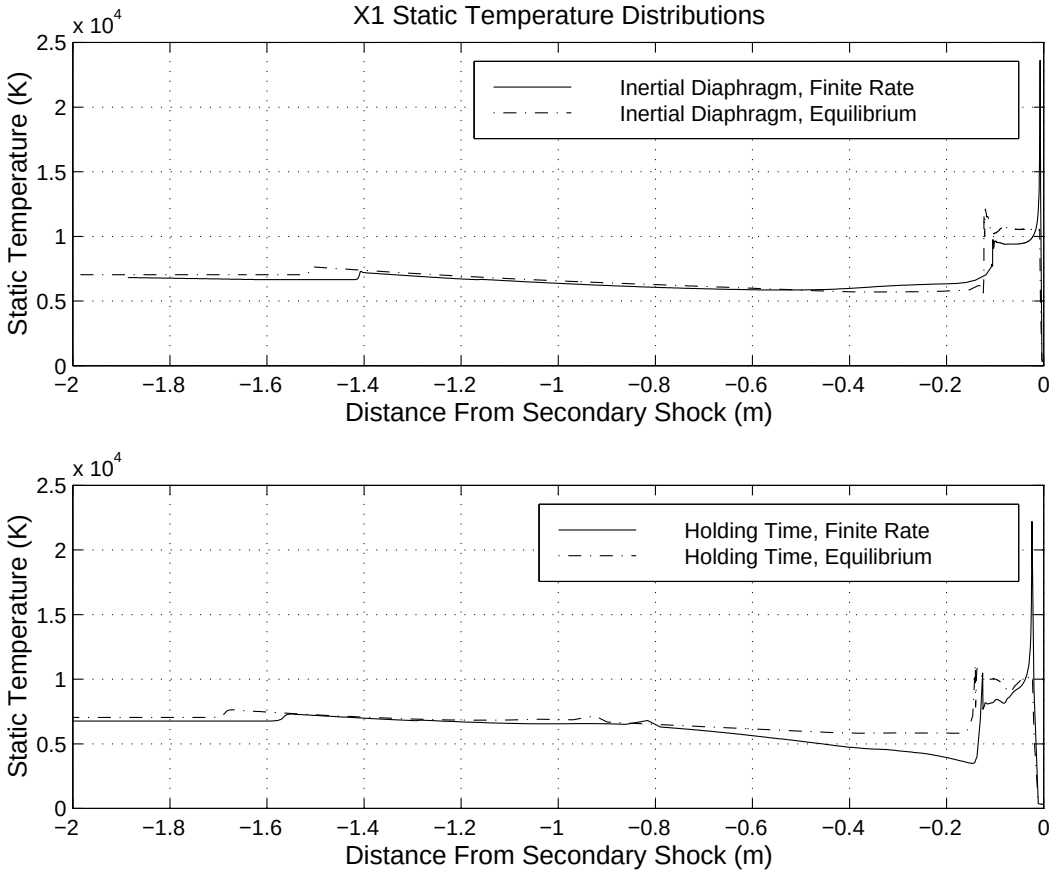

Figure 5.19: Temperature distributions 200 μs after secondary diaphragm rupture from *x1inert_dia* and *x1ht* using both finite-rate and equilibrium chemisty.

By comparing the finite-rate and equilibrium f_N histories for each rupture model simulation, the importance of nonequilibrium effects can be assessed. It can be seen from Figure 5.18 that for the holding time simulation, the departure from equilibrium is significant for approximately 40 μs following the arrival of the secondary shock. It is interesting to note that despite the large initial deviation from equilibrium, the nonequilibrium flow chemistry is only better approximated by the frozen dissociation level for a 10 μs period following the passage of the shock. For the diaphragm inertia simulation, the flow chemistry approaches to within 5% of equilibrium only 20 μs after the arrival of the secondary shock. The greater significance of nonequilibrium effects in the holding time simulation is further exemplified by the temperature distributions 200 μs after diaphragm rupture, which are shown in Figure 5.19. The distributions shown in this figure have been shifted

to align the shock positions; this was necessary to compensate for the unequal wave speeds that result from the different chemistry models. For the holding time simulation, the temperature of the test gas upstream of the contact surface is lower than the equilibrium level owing to the fact that f_N has not yet increased to the equilibrium level. The agreement between the temperature distributions for the diaphragm inertia models is very good. The difference between the two distributions upstream of the reflected shock is due to the different equilibrium states predicted by the finite-rate and fast equilibrium chemistry models (see Appendix A for details). The temperatures just upstream of the contact surface are higher for the simulation with finite-rate chemistry, which is the opposite of what was expected. A possible explanation for this is that the gas in this region has recombined to some extent, releasing chemical energy into the flow that was frozen during the expansion process, hence raising the temperature above the level from equilibrium simulation. Coincidentally, the temperature distribution from the equilibrium holding time simulation is in reasonable agreement with the results of the diaphragm inertia simulation, as can be seen from Figure 5.20.

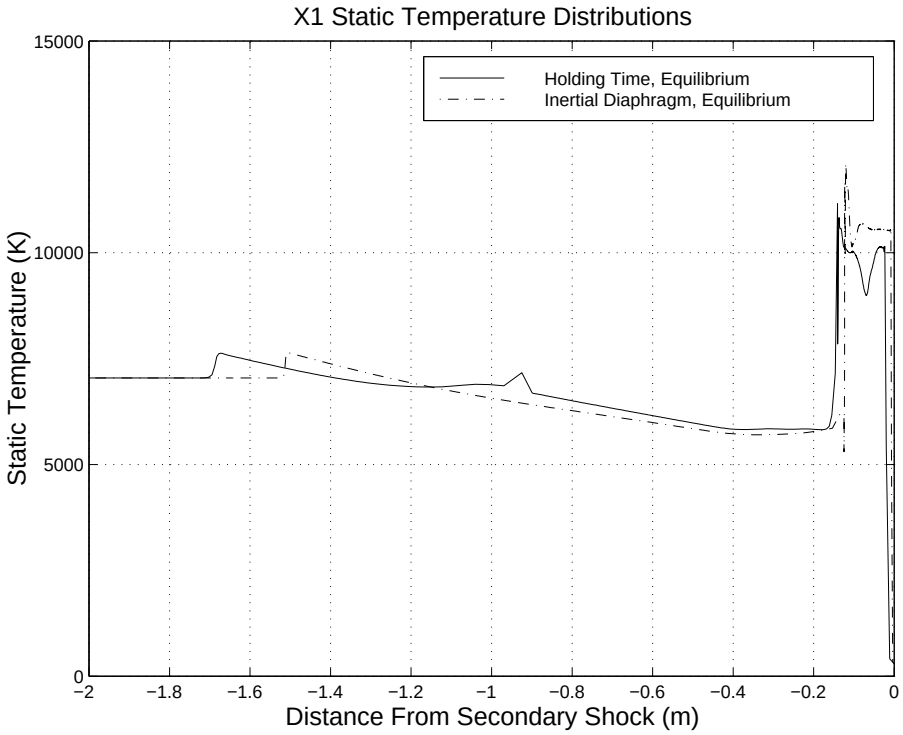

Figure 5.20: A comparison of the equilibrium temperature distributions 200 μs after secondary diaphragm rupture from *x1inert_dia* and *x1ht*.

In summary, use of the holding time model for diaphragm rupture along with finite-

rate chemistry results in a higher dissociation level of the initial portion of the expanded test gas than for the more realistic diaphragm inertia model. It was also determined that the departure from equilibrium of the test flow is much greater when the holding time model is used. These results are in agreement with the conclusions of Bakos and Morgan [9]. At least one new conclusion that can be drawn from the results presented in this section; for the low-density operating conditions presently used in X1, the flow conditions towards the end of the tube predicted using the holding time model with equilibrium chemistry are in reasonable agreement with those computed using the diaphragm inertia model with either finite-rate or equilibrium chemistry. In Section 5.3, it was observed that the results of the two-dimensional simulation with equilibrium chemistry agreed more closely with experimental data than those of the corresponding simulation with approximate frozen chemistry. This observation is supported by the results presented in this section; for both diaphragm rupture models, the flow composition calculated using the finite-rate chemistry model is more closely approximated by the equilibrium composition than by the frozen one.

5.5 Axisymmetric Simulation with the Holding-Time Model

To investigate whether the experimental conditions in X1 could be better simulated with the inclusion of a non-ideal diaphragm rupture model, the holding time model described in the previous section was incorporated into an Mb_cns simulation. The holding time model was used because the more realistic diaphragm inertia model cannot be easily implemented in a non-Lagrangian CFD code such as Mb_cns. Equilibrium chemistry modelling was used in preference to a frozen composition[1], as it was shown in the previous section that this provides a solution in reasonable agreement with that computed using finite-rate chemistry modelling.

To implement the holding time model in the Mb_cns simulation, *x1rn2srhr*, two extra blocks were added to the computational grid described in Section 5.1.4. The first extra block extends from a location in the shock tube at x = -3.11 m (x is the horizontal distance from the exit of the acceleration tube) to the location of the shock reflected from the secondary diaphragm at the expiration of the holding time. In Section 5.4 the reflected shock was calculated to be at x = -2.91845 m, after a 10 μs holding time has expired. The first extra block initially contains gas with the conditions behind the primary shock given in Table 5.1. The second extra block extends from the reflected shock location to the secondary diaphragm station at x = -2.91 m, and initially contains gas with the conditions behind the reflected shock given in Table 5.2. When this simulation was initiated, there was no barrier to prevent the gas behind the reflected shock from suddenly expanding into the acceleration tube, thus simulating the instantaneous rupture of the secondary diaphragm after a 10 μs holding time. Details of the discretisation of two extra blocks can be found along with other details in the simulation's input parameter file *x1rn2srhr.sit*, which is included in Appendix B.

To assess whether the flow through the acceleration tube has been modelled correctly, Figure 5.21 shows a comparison of the computed static pressure histories at four transducer locations along the acceleration tube and the experimental pressure histories from these transducers. The experimental data has been shifted in the same manner as in Sections 5.2 and 5.3. For the simulation incoporating the holding time model, the computed shock speed was found to be 8.1% greater than the experimental value of 9062 m/s. A

[1]Finite-rate chemistry modelling has not been implemented in Mb_cns to date.

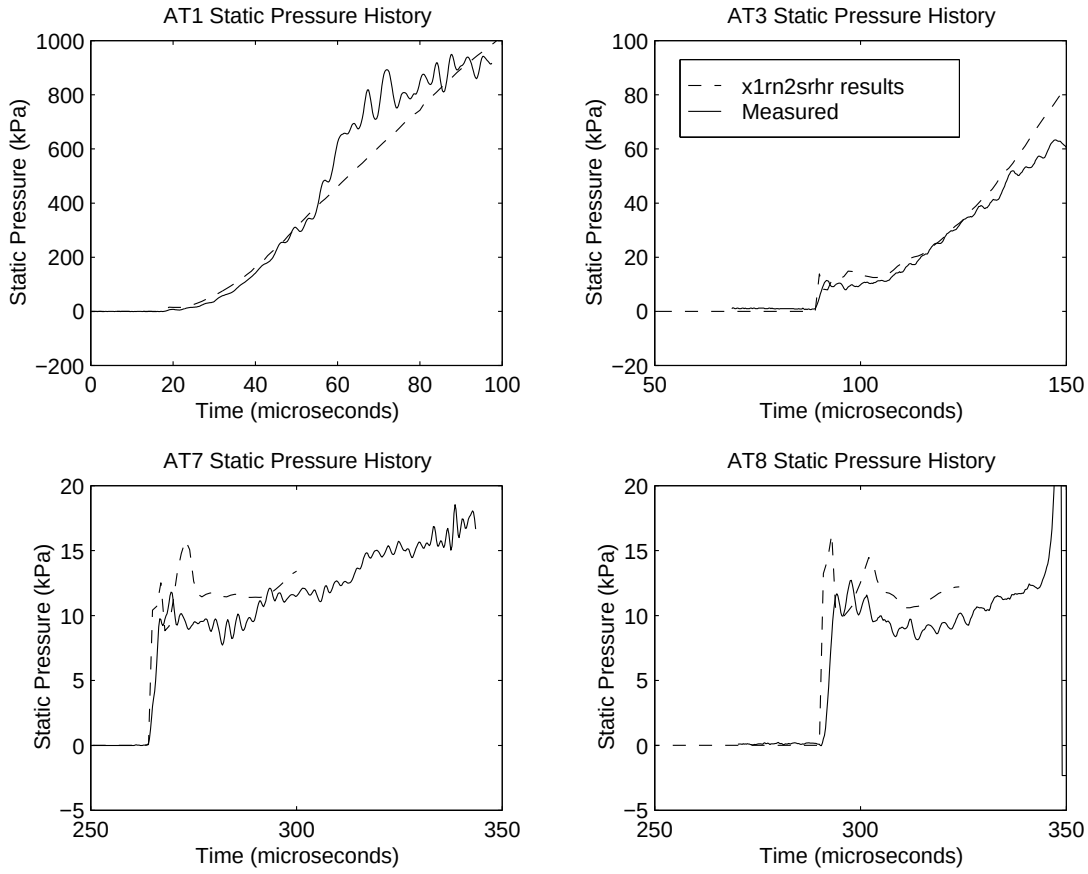

Figure 5.21: Aligned computed and experimental static pressure histories in the acceleration tube of X1 at transducer locations AT1 (x = -2.718 m), AT3 (x = -2.018 m), AT7 (x = -0.376 m) and AT8 (x = -0.120 m). Computed values are from *x1rn2srhr*. Experimental values are from shot S7_26.

possible cause of this is the effect of the gradual pressure rise behind the primary shock (see Figure 5.2). It can be seen that again there is very good agreement between the shape of the computational and experimental traces, with one exception: At transducer AT3, it can be seen that the pressure gradient in the latter part of the expansion is greater in the computed history. As mentioned in Section 5.2, the pressure gradient in the latter part of the simulated expansion may be greater than that measured experimentally because of the unmodelled effects of piston motion. In the results of the simulations without the holding time model, it was seen that at transducer AT1 the experimental pressure continued to rise after the computed history had leveled off. This problem has now been resolved by the inclusion of the holding time model, confirming that a reflected shock is generated during the rupture of the secondary diaphragm. The agreement between magnitudes of the computed and experimentally measured pressure histories is also quite good, the higher pressures behind the shock are caused by the overestimate of the shock speed.

Now that it has been established that the simulation is in reasonable agreement with the experimental data within the acceleration tube, the results in the dump tank can be examined. Figure 5.22 shows a comparison of the computed and experimental bar gauge pressure histories 175 mm from the exit of the acceleration tube at a radius of 14 mm. It

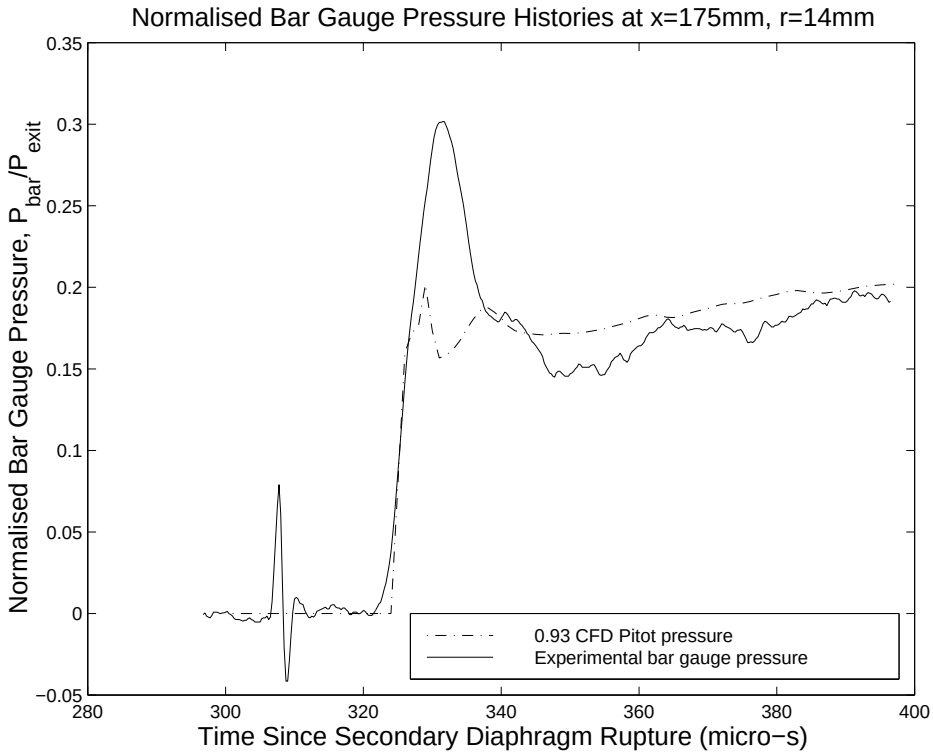

Figure 5.22: Noramised bar gauge pressure histories 175 mm from the exit of the acceleration tube at a radius of 14 mm. Computed values are from *x1rn2srhr*.

can be seen that the agreement between the nominally steady levels of the two histories is quite good, however, in this case the magnitude of the Pitot pressure spike due to the reverse shock is far greater in the experimental history. In Figure 5.23 a number of Mach number contour plots are presented that show the evolution of the flow field in the dump tank. At the time of the last frame of this figure, $t = 0.34$ ms, the test flow has just arrived at the nominal test location at $x = 225$ mm.

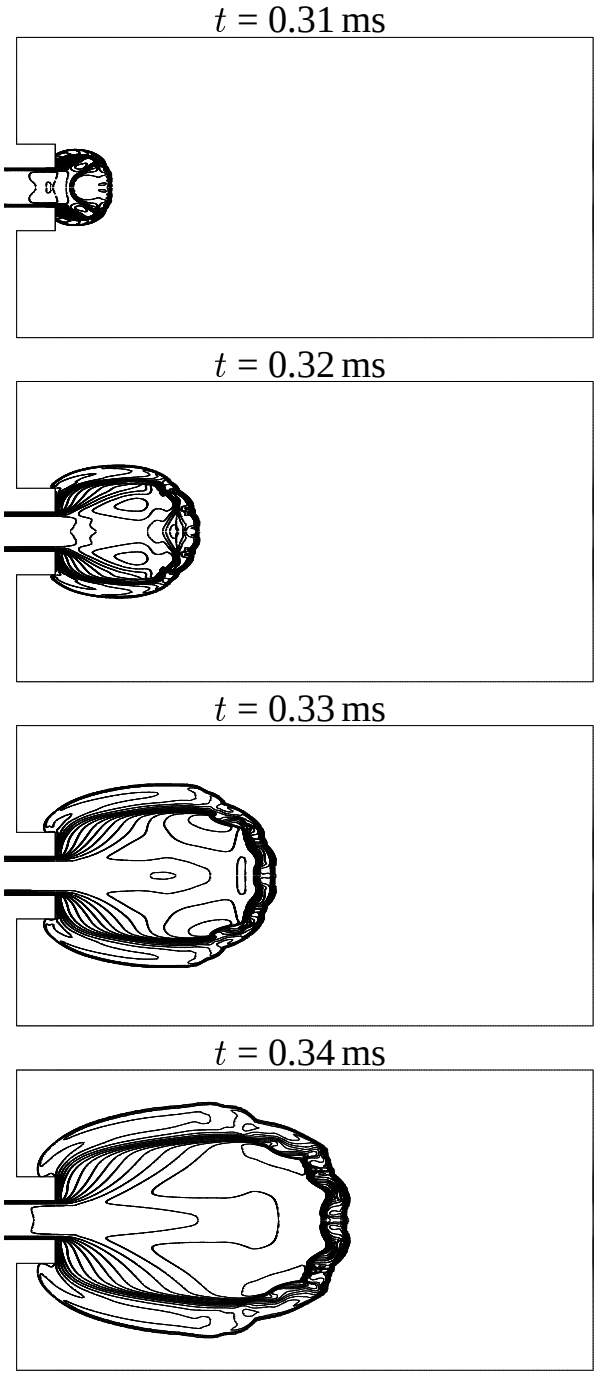

Figure 5.23: Contour plots of Mach number showing the evolution of the flow field in the dump tank for the simulation, *x1rn2srhr*. t is the time since secondary diaphragm rupture.

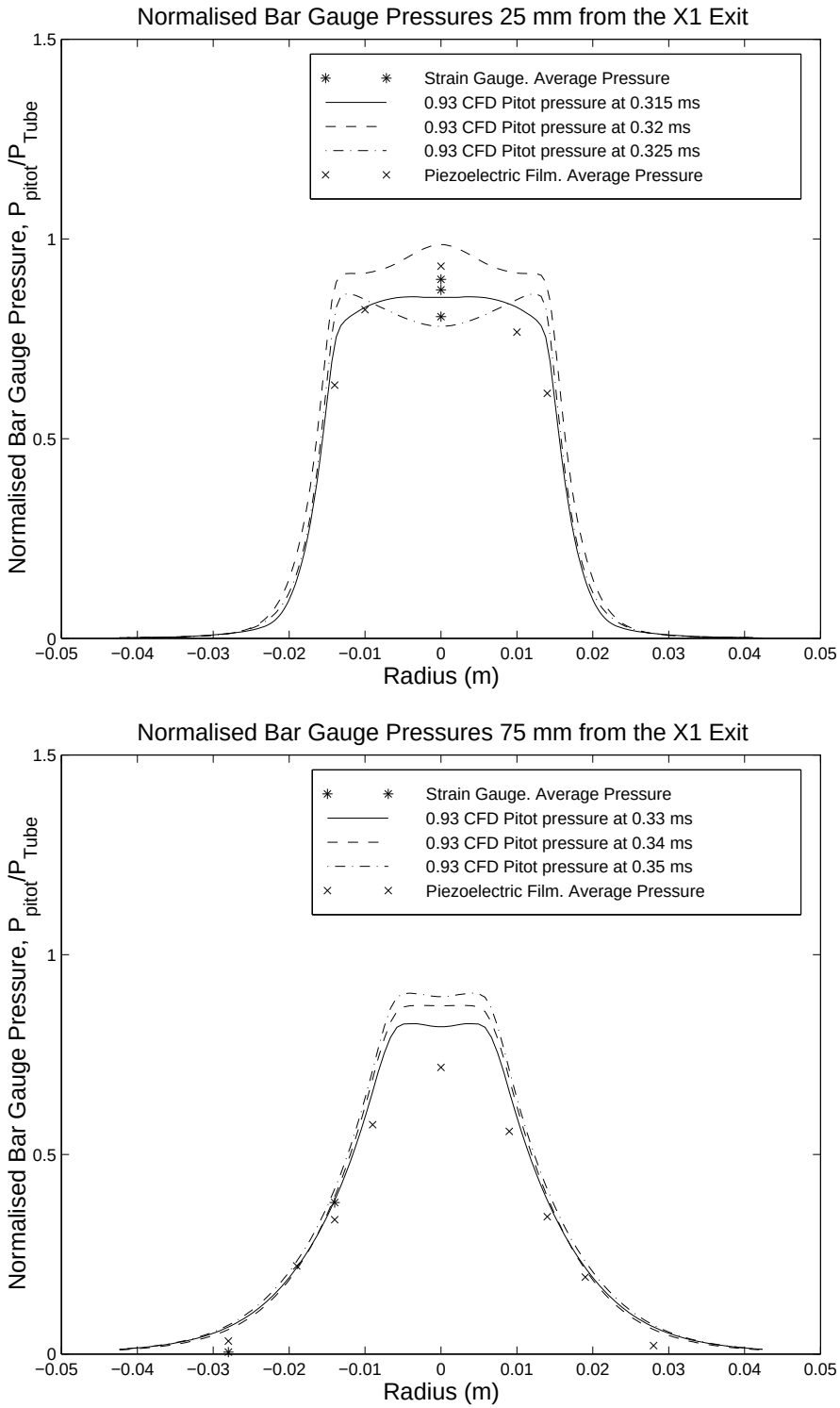

Figure 5.24: Normalised bar gauge pressure profiles in the X1 dump tank at 25 and 75 mm from acceleration tube exit during the passage of the test gas. Computed values are from *x1rn2srhr*.

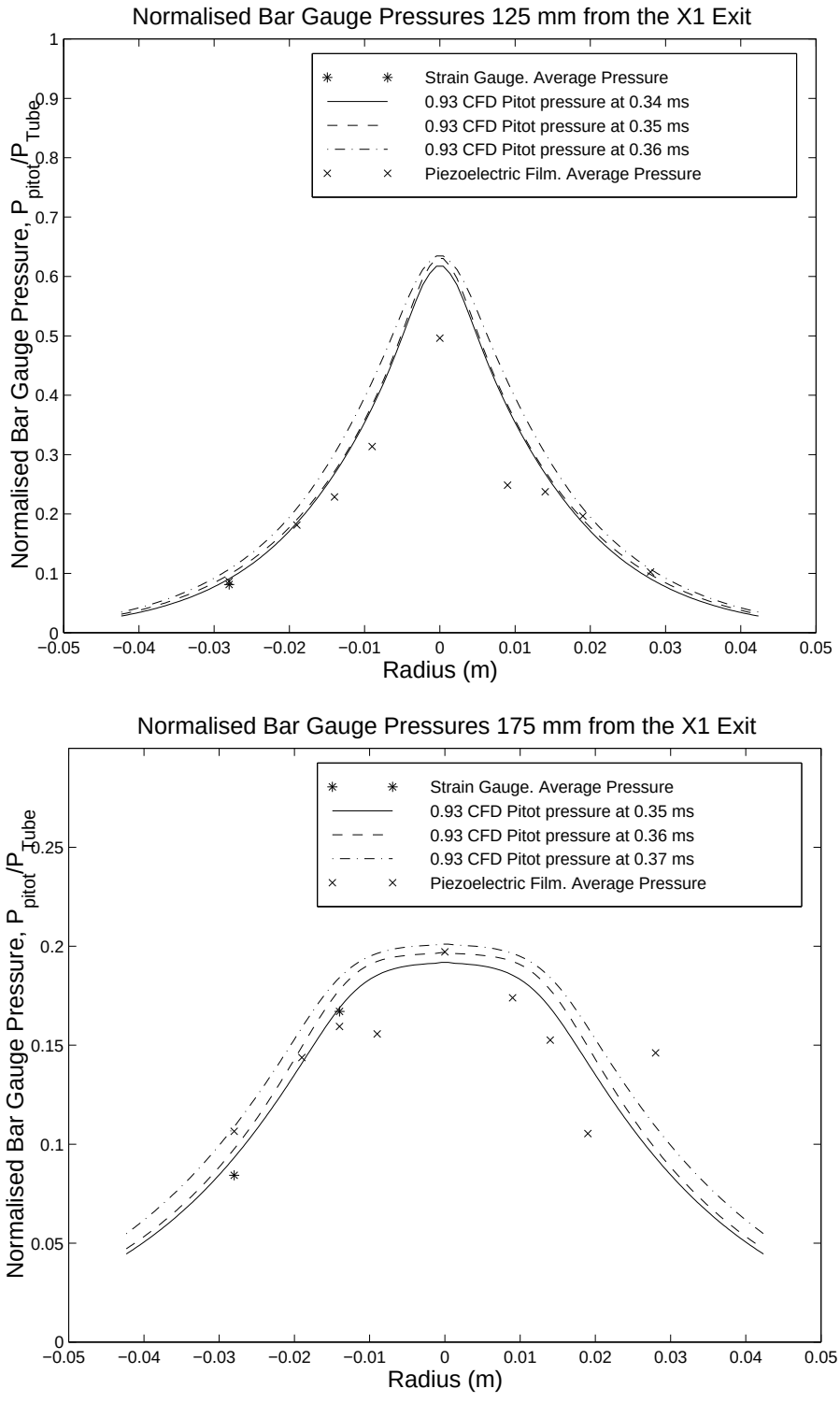

Figure 5.25: Normalised bar gauge pressure profiles in the X1 dump tank at 125 and 175 mm from acceleration tube exit during the passage of the test gas. Computed values are from *x1rn2srhr*.

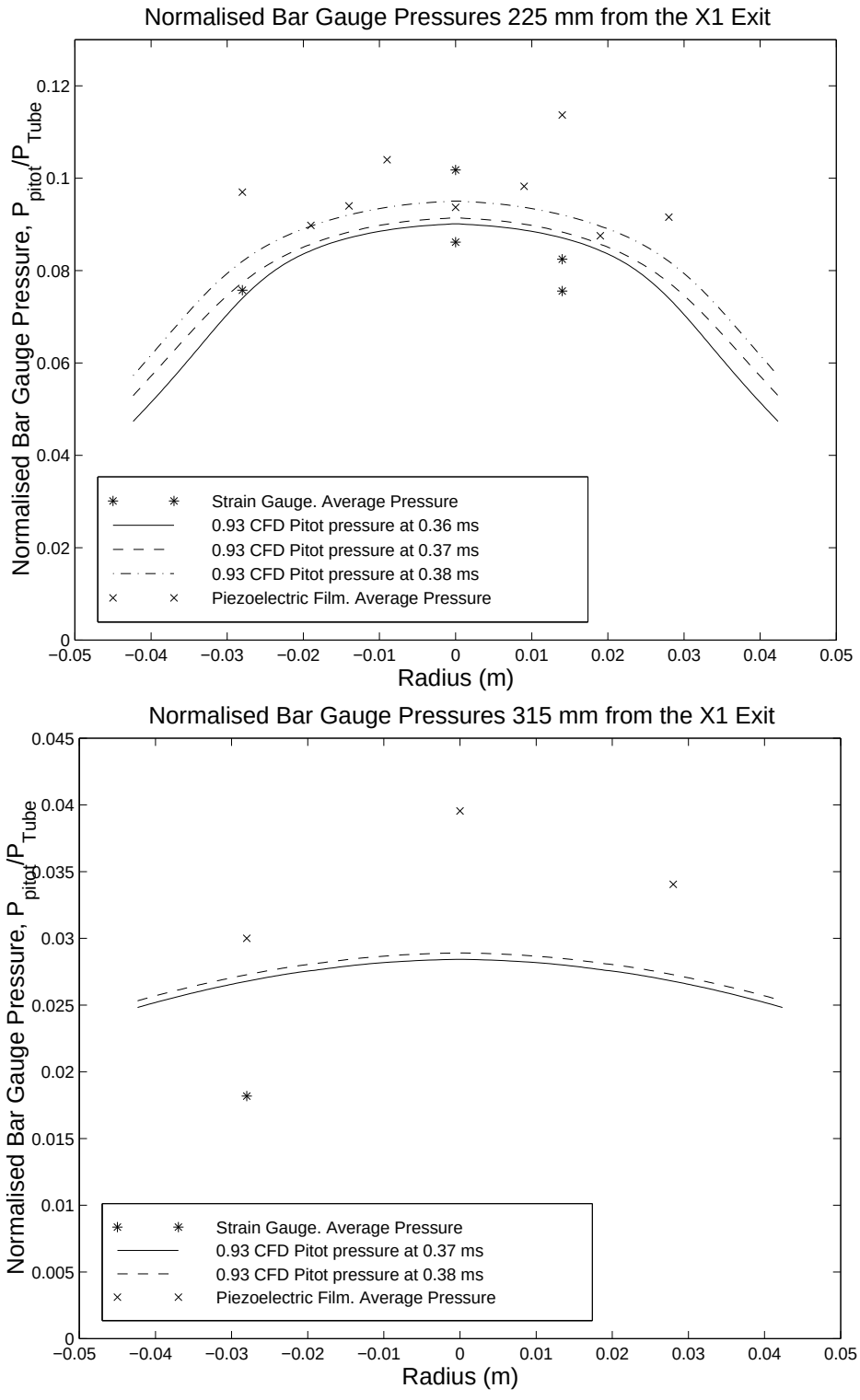

Figure 5.26: Normalised bar gauge pressure profiles in the X1 dump tank at 225 and 340 mm from acceleration tube exit during the passage of the test gas. Computed values are from *x1rn2srhr*.

Figures 5.24 to 5.26 show a comparison of the full set of experimental bar gauge pressure profiles in the dump tank and the results of the simulation, *x1rn2srhr*, during the passage of the test gas. The agreement between both the shape and magnitude of the computed and experimental profiles is much better than for the simulations presented in the previous sections. This confirms that it is important to include the effects of non-ideal secondary diaphragm rupture in a computational model of the facility. From the profiles at 75 and 125 mm from the acceleration tube exit, it can be seen that the computed Pitot pressures near the centerline are slightly overestimated due to the secondary shock speed being overestimated by 8.1%. At $x = 175$ mm, the divergence of the test flow has caused the core of high Pitot pressure flow to be spread across the dump tank such that the agreement between the computed and experimental bar gauge pressure profiles appears to be improved. At the nominal test location, $x = 225$ mm, the Pitot pressure is reasonably uniform near the centerline, indicating that it would be suitable for experiments. The agreement between the computed and experimental profiles is quite good considering the amount of scatter in the experimental data. The experimental values at $x = 340$ mm are considerably higher than the computational results. It is believed that this is due to the high degree of rarefaction at axial locations so far into the dump tank.

Having established that the results from the simulation including the holding time model are in reasonable agreement with the experimental data of reference [49], the estimated test conditions from this simulation will now be presented for the benefit of researchers conducting experiments in X1. The profiles of some important flow properties at the nominal test location, $x = 225$ mm, are shown in Figure 5.27. The profiles shown are from $t = 370\,\mu$s, at this time the test flow is nominally steady. It is believed that the most significant errors in the estimated conditions are those in the flow speed, and hence the Pitot pressure and Mach number. It appears that the other quantities have been estimated more accurately for the following reasons: the error of around 17% in Pitot pressure near the centerline at $x = 75$ mm is approximately what is expected for an 8% error in flow speed, which indicates that the estimate of density must be fairly accurate; the static pressure traces from near the exit of the accelation tube indicated that the static pressure of the flow has been estimated with reasonable accuracy. From Figure 5.27 it can be seen that the axial velocity is fairly constant across the test flow. The variation in Pitot pressure seen in Figure 5.26 is due to the variation in density across the test flow.

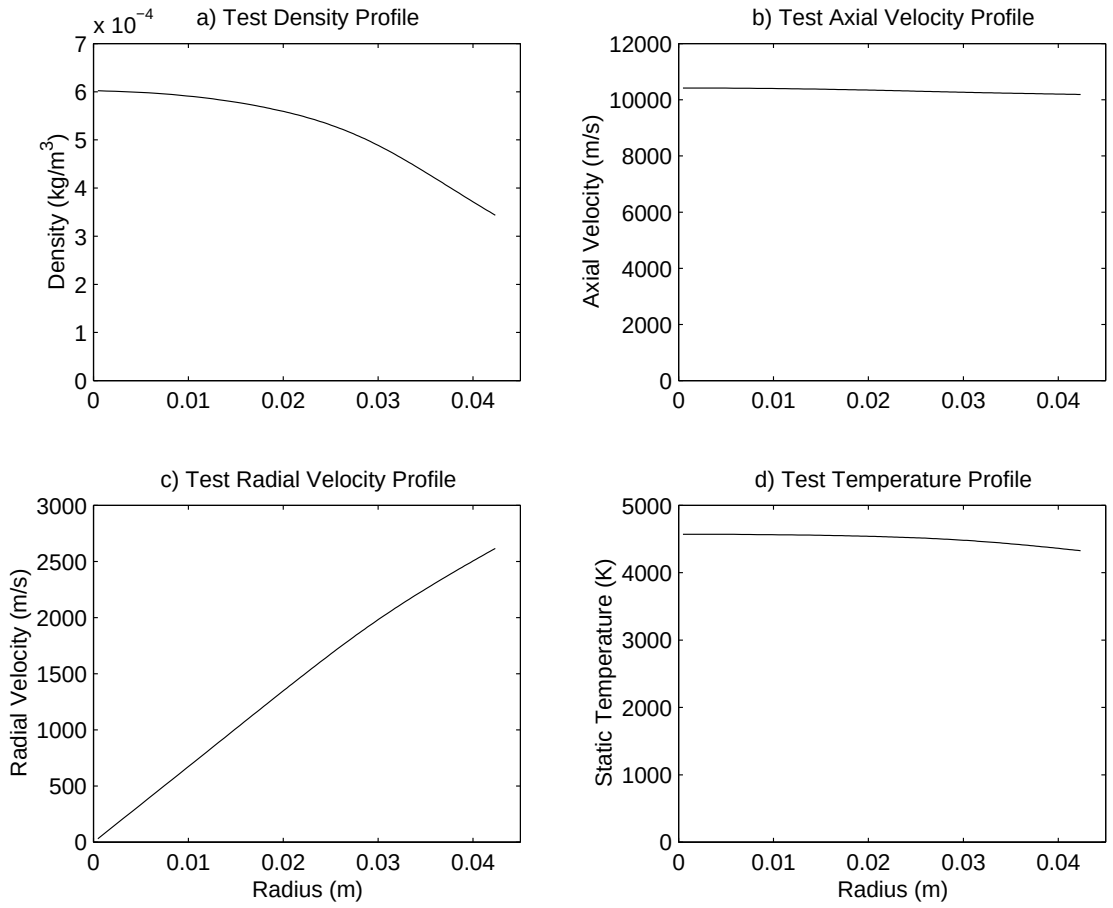

Figure 5.27: Computed profiles of density, axial velocity, radial velocity and static temperature at the nominal test location in X1, 225 mm from acceleration tube exit. Profiles are from $t = 370\,\mu$s.

The profile of radial velocity shows that the flow angularity becomes very high as radius increases. This may pose a problem for researchers who wish to test models with large widths.

Figure 5.28 shows the variation of rarefaction parameters, axial velocity and density along the centerline in the dump tank at $t = 370\,\mu$s, which is during the test time at $x = 225$ mm. From the axial profile of the breakdown parameter based on an object size of 10 mm, it can be seen that at the nominal test location $P_D \approx 0.1$, so we would expect strong non-continuum effects in the flow over a model of this size. The large axial gradient of density seen in Figure 5.28 is problematic for testing models with large axial lengths. The computational data presented in Figures 5.27 and 5.28 indicates that the test flow produced during low-density operation of X1 is well suited to testing relatively compact models, such as blunt bodies, at rarefied hypervelocity conditions. The test flow speed generated in X1 is of the same order as that encountered during an aerobraking maneuver, which will allow computational techniques such as DSMC to be experimentally calibrated

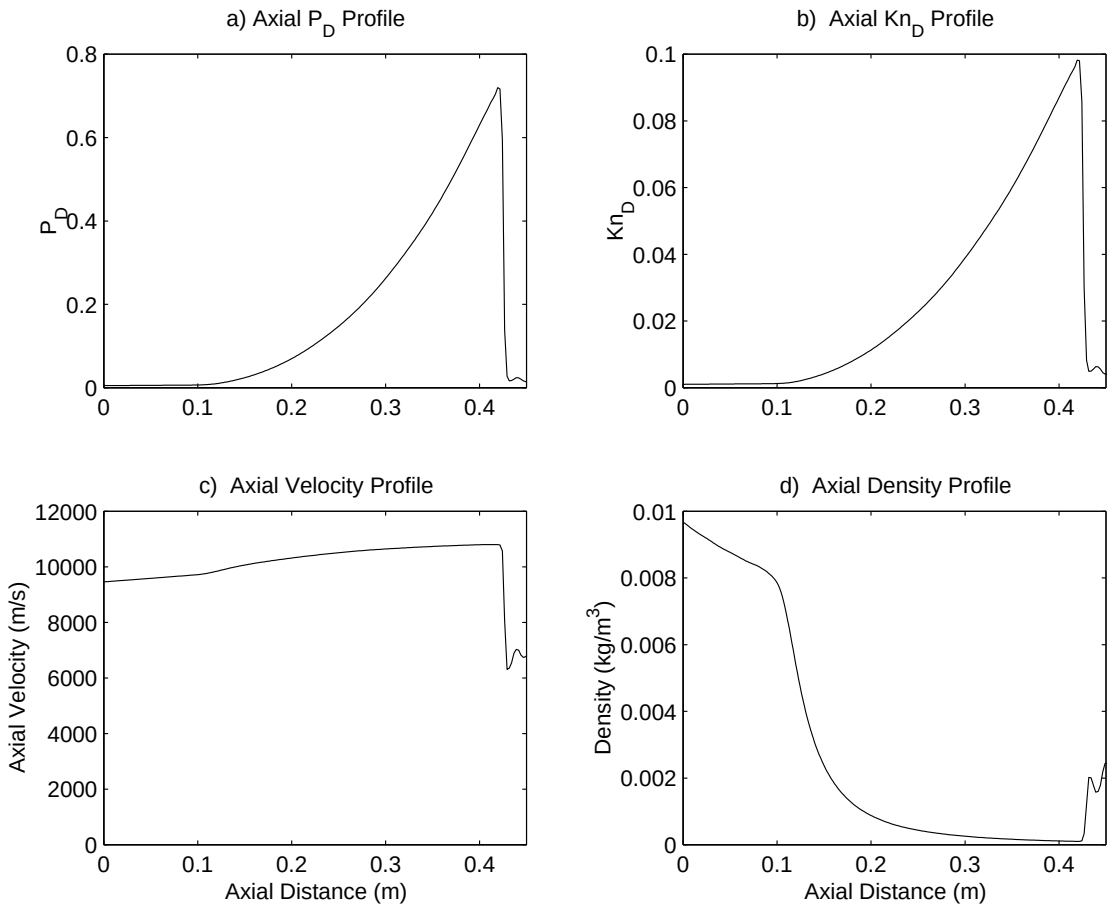

Figure 5.28: Computed profiles of breakdown parameter, P_D, Knudsen number, Kn_D (based on $D = 10\,\text{mm}$), axial velocity and density along the centerline in the dump tank. Profiles are from $t = 370\,\mu\text{s}$ when the secondary contact surface is located at $x \approx 425\,\text{mm}$.

for the conditions encountered during this important application.

5.6 Conclusion: Required Simulation Features

In this chapter, the results of a number of simulations have been presented and compared with experimental data. In each consecutive CFD model, the modelling of the flow through X1 was varied. This allows some conclusions to be drawn on the degree of model complexity that is required to produce reliable estimates of the real conditions.

To estimate the width of the high Pitot pressure core flow in the dump tank with reasonable accuracy, it was necessary to resolve the boundary layer along the acceleration tube wall. This requires the computational model to include viscous effects and at least some of the length of the acceleration tube.

To establish what chemistry model is most appropriate for the flow in X1, axisymmetric simulations of the facility were run with both equilibrium and frozen chemistry. The secondary shock speed was overestimated by 4.5% in the simulation with equilibrium chemistry while it was underestimated by 6.2% in the simulation with frozen chemistry. The simulation with frozen chemistry overestimated the Pitot pressures in the facility by a much greater margin than the equilibrium simulation, indicating that the equilibrium model more accurately represents the actual flow chemistry. This conclusion was supported by the results of one-dimensional simulations of the facility with both equilibrium and finite-rate chemistry.

The effects of non-ideal diaphragm rupture were modelled in the final axisymmetric simulation of X1 via the inclusion of the holding time model for light diaphragm rupture. The error in the secondary shock speed increased to 8.1% in this simulation. However, the inclusion of the holding time model significantly improved the agreement between the computed and experimental bar gauge pressures in the dump tank and also brought the computed static pressures near the secondary diaphragm into closer agreement with those measured experimentally. This indicates that it is important to include the effects of non-ideal diaphagm rupture to accurately simulate the flow in X1 when operated at low densities.

CHAPTER 6

Conclusions

This thesis was concerned with the development and application of computational models of the flow though hypersonic impulse facilities when the facilities are operated at conditions designed to produce a rarefied test flow. The overall objective was to take a step towards the provision of a rarefied hypervelocity test flow in a wind tunnel facility, which could then be used to experimentally assess computational methods such as DSMC. Computational models of two impulse facilities, the Small Shock Tunnel (SST) and the X1 expansion tube, were developed during the course of this thesis. The final chapter of this thesis is concerned with the conclusions that can be drawn from the development of these models and the results that were obtained from them. Recommendations are made regarding how the SST should be operated, what flow processes must be modelled to successfully simulate the flow in impulse facilities, and what further computational and experimental work should be undertaken on the topic of this thesis.

6.1 Modelling of the SST

The SST is incapable of producing a hypervelocity test flow due to its limited stagnation temperature. Instead, it was proposed to use this facility to generate a high Mach number, rarefied non-reacting reference flow for computational and experimental techniques to be applied in X1. To assess the feasibility of this proposal, a joint analytical and computational approach was taken. First, analytical calculations of the operating conditions required to produce a target level of test flow rarefaction were carried out. Computational models of the facility were then formulated to investigate two dimensional effects such as boundary layers and the nozzle starting process, which were neglected in the analytical calculations.

Axisymmetric simulations of the flow though the SST's Mach 7 contoured nozzle and test section revealed that, in order for the nozzle to start properly during low-density operation, the backpressure in the test section must be reduced such that the test flow is significantly underexpanded. When this was done, a reasonably uniform test flow was generated despite the nozzle being operated at pressures an order of magnitude lower than it was designed for. The simulations also revealed that the thick boundary layer at the nozzle exit, which forms along the nozzle wall during low-density operation, causes the test flow to expand less than was anticipated in the analytical calculations. This results in the test flow failing to meet the target level of rarefaction when the SST is operated at the analytically determined conditions.

Axisymmetric simulations of the flow though the SST's Mach 7 conical nozzle and test section revealed that the conical nozzle will start properly with a backpressure four times larger than that for which the contoured nozzle will start. The reasons for this are the shorter length of the conical nozzle and the stronger, favourable pressure gradients present along its entire length. Further simulations were run in which the pressures in the facility were reduced below those calculated analytically. Through an iterative process a new set of operating conditions were determined that are predicted to generate a reasonably uniform test flow with the target level of rarefaction.

Evaluating different rarefaction parameters thoughout the flow field in the SST revealed that while rarefaction effects should be present on a small model placed in the test flow, the flow field itself can be adequately simulated using a continuum CFD code. From a simulation of the entire SST, it was determined that a useful rarefied test flow still results when the variations in nozzle supply pressure are taken into account. Finally, through a review of rarefaction effects that have been presented in the literature, an experiment was devised in which measurable rarefaction effects should be present if the experiment is conducted at the new test flow conditions.

The overall conclusion from the study of low-density flow in the SST is that the facility is capable of producing a high Mach number rarefied test flow if it is operated as specified in this thesis. Hence, the proposal to use the SST to produce a non-reacting reference flow for computational and experimental techniques to be applied in X1 is feasible.

6.2 Modelling of X1

Since 1998, an experimental investigation into producing a rarefied hypervelocity test flow in X1 has been undertaken at the University of Queensland [87, 49]. To complement this study, an investigation into the computational modelling of low-density hypervelocity flow in an expansion tube was carried out as part of this thesis. The results of a number of simulations of low-density flow though X1 were presented in Chapter 5 and compared with the experimental data of reference [49]. In each of the simulations, some aspect of the computational modelling was altered. This allows some conclusions to be drawn on the degree of model complexity that is required to produce reliable estimates of the real conditions.

To estimate the width of the high Pitot pressure core flow in the dump tank with reasonable accuracy, it was necessary to resolve the boundary layer along the acceleration tube wall. This requires the computational model to include viscous effects and at least some of the length of the acceleration tube.

To evaluate whether it was valid to use a continuum CFD code to simulate the low-density flow through X1, the Bird's breakdown parameter [10] was evaluated thoughout the facility at one instant. Non-continuum effects were found to be limited to the interior of shocks and the flow that has expanded around the corner at the acceleration tube exit. It is expected that the flow in this region will not greatly affect the properties of the test flow near the centerline.

To establish what chemistry model is most appropriate for the flow in X1, axisymmetric simulations of the facility were run with both equilibrium and frozen chemistry. The secondary shock speed was overestimated by 4.5% in the simulation with equilibrium chemistry while it was underestimated by 6.2% in the simulation with frozen chemistry. The simulation with frozen chemistry overestimated the Pitot pressures in the facility by a much greater margin than the equilibrium simulation, indicating that the equilibrium model more accurately represents the actual flow chemistry. This conclusion was supported by the results of a number of Lagrangian one-dimensional simulations of the facility with both equilibrium and finite-rate chemistry. These simulations were primarily used to investigate the effects of two non-ideal diaphragm rupture models, the "holding time" and "diaphragm inertia" models, on the flow in the acceleration tube. It was found

that the use of the holding time model along with finite-rate chemistry results in a higher dissociation level of the initial portion of the expanded test gas than for the more realistic diaphragm inertia model. It was also determined that the departure from equilibrium of the test flow is much greater when the holding time model is used. At least one new conclusion that can be drawn from the results presented in this thesis; for the low density operating conditions presently used in X1, the flow conditions towards the end of the tube predicted using the holding time model with equilibrium chemistry are in reasonable agreement with those computed using the diaphragm inertia model with either finite-rate or equilibrium chemistry.

The effects of non-ideal diaphragm rupture were modelled in the final axisymmetric simulation of X1 via the inclusion of the holding time model for light diaphragm rupture. The error in the secondary shock speed increased to 8.1% in this simulation. However, the inclusion of the holding time model significantly improved the agreement between the computed and experimental bar gauge pressures in the dump tank and also brought the computed static pressures near the secondary diaphragm into closer agreement with those measured experimentally. This indicates that it is important to include the effects of non-ideal diaphagm rupture to accurately simulate the flow in X1 when operated at low densities.

Having established that the results from the simulation including the holding time model were in reasonable agreement with the experimental data of reference [49], the esimated test conditions from this simulation were presented for the benefit of researchers conducting experiments in X1. The computational data presented in Figures 5.27 and 5.28 indicates that the test flow produced during low-density operation of X1 is well suited to testing relatively compact models, such as blunt bodies, at rarefied hypervelocity conditions. The test flow speed generated in X1 is of the same order as that encountered during an aerobraking maneuver, which will allow computational techniques such as DSMC to be experimentally calibrated for the conditions encountered during this important application.

6.3 Recommendations

A new set of operating conditions for the SST with the Mach 7 conical nozzle installed are presented in Table 3.7. These conditions have been predicted to produce a uniform Mach 6.5 test flow with a breakdown parameter of 0.04 (based on a model size of 10 mm). Before attempts are made to use these new operating conditions for experimental research, a Pitot pressure survey of the test flow should be carried out to verifiy the accuracy of the simulations presented in this thesis. Once this has been completed, it is recommended that a spherically blunted cone with a nose radius of 3 mm be tested in the SST when operated at the conditions given in Table 3.7. During these tests, it is recommended that the stagnation point heat flux be measured with one of the thin film gauges currently in use at UQ. It is hoped that the rarefaction of the test flow will cause the stagnation point heat flux to measurably deviate from its continuum value by more than 10%.

The results presented in this thesis indicate that to produce accurate estimates of the flow field in X1 when operated at low-densities, the minimum set of flow processes that must be modelled are: the boundary layer in the acceleration tube; the equilibrium chemistry of the flow; the effects of non-ideal secondary diaphragm ruputure. As the flow in some regions of the dump tank is non-continuum, a DSMC simulation of the free jet into the dump tank should be carried out to more thoroughly assess the accuracy of the continuum estimations made in this thesis. It is recommended that computational techniques listed above be used to calculate the state of the gas exiting the acceleration tube, which can then be used as an inflow boundary condition in the DSMC simulation. Other aspects of the computational modelling of X1 that require further investigation are the gradual opening of the primary diaphragm, which may account for the gradual pressure rise behind the primary shock, and the effect of non-equilibrium chemistry on the results of an axisymmetric simulation. Also, the simulations presented in this thesis should be re-run on a more refined computational grid to better capture features such as the boundary in the acceleration tube.

Bibliography

[1] Allegre, J., "The SR3 low density wind-tunnel: facility capabilities and research development," AIAA Paper 92-3972, July 1992.

[2] Amann, H. O., "Experimental Study of the Starting Process in a Reflection Nozzle." *The Physics of Fluids Supplement*, Vol. I, 1969, pp. I–150–I–153.

[3] Anderson, J. D., *Hypersonic and High Temperature Gas Dynamics*, McGraw-Hill, New York, 1989, pp. 453.

[4] Anderson, J. D., *Hypersonics and High Temperature Gas Dymanics*, McGraw-Hill, New York, 1989, pp. 20-23.

[5] Anderson, J. D., *Modern Compressible Flow: with Historical Perspective*, McGraw-Hill, New York, 2nd ed., 1990.

[6] Attwood, J., "Characterisating a Mach seven contoured nozzle for a shock tunnel," Undergraduate Thesis, University of Queensland, 1997.

[7] Austin, J. M., Jacobs, P. A., Kong, M. C., Barker, P., Littleton, B. N., and Gammie, R., "The small shock tunnel facility at UQ," Tech. Rep. 2/97, Department of Mechanical Engineering, The University of Queensland, July 1997.

[8] Bakos, R. J., *An Investigation of Test Flow Nonequilibrium Effects on Scramjet Combustion*, Ph.D. thesis, University of Queensland, 1994.

[9] Bakos, R. J. and Morgan, R. G., "Chemical recombination in an expansion tube," *AIAA Journal*, Vol. 32, No. 6, June 1994, pp. 1316–1319.

[10] Bird, G. A., *Rarefied Gas Dynamics and the Direct Simulation of Gas Flows*, Claredon Press, Oxford, 1994.

[11] Borque, B., "Development of a hypervelocity wind tunnel for rarefied flow," Undergraduate Thesis, University of Queensland, 1999.

[12] Boyd, I. D. and Gokcen, T., "Computation of axisymmetric and ionized hypersonic flows using particle and continuum methods," *AIAA Journal*, Vol. 32, No. 9, September 1994, pp. 1828–1835.

[13] Cercignani, C. and Tironi, G., "Some applications to the transition regime of a new set of boundary conditions for Navier-Stokes equations," *Proceedings of the 6th International Symposium on Rarefied Gas Dynamics, vol. 1*, 1970.

[14] Chase, M. W., *JANAF Thermochemical Tables*, American Institute of Physics, New York, N.Y., 1985.

[15] Cheng, H. K., CAL Report No. AF-1285-A-7, 1961.

[16] Cheng, H. K. and Emanuel, G., "Perspective on hypersonic nonequilibrium flow," *AIAA Journal*, Vol. 33, No. 3, March 1995, pp. 385–400.

[17] Chiu, H. H., "Development of a test facility for hypervelocity rarefied flows," Departmental Report 2000/09, Department of Mechanical Engineering, University of Queensland, September 2000.

[18] Chrusciel, G. T., Lewis, C. H., and Sugimura, T., "Slip effects in hypersonic rarefied flow," *Proceedings of the 12th International Symposium on Rarefied Gas Dynamics, Vol. 2*, Charlottesville, Va., 1980, pp. 1040–1054.

[19] Craddock, C. S., *Computational Optimization of Scramjets and Shock Tunnel Nozzles*, Ph.D. thesis, University of Queensland, 1999.

[20] Craddock, C. S., Jacobs, P. A., and Gammie, R., "Operating instructions for the small shock tunnel at UQ," Tech. Rep. 8/98, Department of Mechanical Engineering, The University of Queensland, July 1998.

[21] Dankert, C., "DLR Göttingen hypersonic vacuum wind tunnels V1G and V2G and high vacuum wind tunnel V3G," Brochure, DLR, SM-SK-ATD, Bunsenstrasse 10, D-37073 Göttingen, Germany, November 1996.

[22] Davies, L. and Wilson, J., "Influence of Reflected Shock and Boundary-Layer Interaction on Shock-Tube Flows," *The Physics of Fluids Supplement*, Vol. 1, 1969, pp. I–37–I–43.

[23] Doolan, C. J., *A Two-Stage Free-Piston Driver for Hypervelocity Expansion Tubes*, Ph.D. thesis, University of Queensland, 1997.

[24] Fox, R. W. and McDonald, A. T., *Introduction to Fluid Mechanics*, John Wiley and Sons, New York, 4th ed., 1994, pp. 394-395.

[25] Gottlieb, J. J. and Groth, C. P. T., "Assessment of Riemann solvers for unsteady one-dimensional inviscid flows of perfect gases," *Journal of Computational Physics*, Vol. 78, 1988, pp. 437–458.

[26] Gregorenko, V., Naumov, A., and Hvostor, N., "Influence of Non-Stationary Flow Effects on Test Time of a Hypersonic Shock Tunnel," *Scientific Notes of the Central Hydrodynamic Institute*, Vol. 15, No. 5, 1984.

[27] Grossman, B. and Cinnella, P., "Flux-split Algorithms for Flows with Non-equilibrium Chemistry and Vibrational Relaxation," *Journal of Computational Physics*, Vol. 88, No. 1, 1990, pp. 131.

[28] Gupta, R. N., "Viscous shock-layer study of thermochemical nonequilibrium," *Journal of Thermophysics and Heat Transfer*, Vol. 10, No. 2, 1996, pp. 257–266.

[29] Gupta, R. N., Moss, J. N., and Price, J. M., "Assessment of Thermochemical Nonequilibrium and Slip Effects for Orbital Re-Entry Experiment," *Journal of Thermophysics and Heat Transfer*, Vol. 11, No. 4, October-December 1997, pp. 562–569.

[30] Gupta, R. N., Yos, J. M., Thompson, R. A., and Lee, K. P., "A review of reaction rates and thermodynamic and transport properties for an 11-species air model for chemical and thermal nonequilibrium calculations to 30000 K," NASA Reference Publication 1232, NASA Office of Management, Scientific and Technical Information Division, 1990.

[31] Hendricks, W. L., "A Simularity solution of the Navier-Stokes Equations with Wall Catalysis and Slip for Hypersonic, Low Reynolds Number Flow Over Spheres," AIAA Paper No. 75-675, May 1975.

[32] Ivanov, M. S. and Gimelshein, S. F., "Computational Hypersonic Rarefied Flows," *Annual Review of Fluid Mechanics*, Vol. 30, 1998, pp. 469–505.

[33] Jacobs, P., "L1D: A Computer Program for the Simulation of Transient-flow Facilities," Department of Mechanical Engineering Report 1/99, The University of Queensland, Brisbane, Australia, January 1999.

[34] Jacobs, P. A., "Transient, Hypervelocity Flow in an Axisymmetric Nozzle," AIAA Paper 91-0295, 1991.

[35] Jacobs, P. A., "L1d: A computer code for the quasi-one-dimensional modelling of transient flow facilities." WBM Internal Report, 1992.

[36] Jacobs, P. A., " Quasi-One-Dimensional Modelling of a Free-Piston Shock Tunnel," *AIAA Journal*, Vol. 32, No. 1, 1994, pp. 137–145.

[37] Jacobs, P. A., "Numerical simulation of transient hypervelocity flow in an expansion tube," *Computers Fluids*, Vol. 23, No. 1, 1994, pp. 77–101.

[38] Jacobs, P. A., "MB_CNS: A computer program for the simulation of transient compressible flows," Tech. Rep. 10/96, Department of Mechanical Engineering, The University of Queensland, December 1996.

[39] Jacobs, P. A., "L1d: A computer code for the quasi-one-dimensional modelling of transient-flow facilities," Tech. Rep. 1/99, Department of Mechanical Engineering, The University of Queensland, 1999.

[40] Jacobs, P. A., Morgan, R. G., Stalker, R. J., and Mee, D. J., "Use of Argon-Helium Driver-Gas Mixtures in the T4 Shock Tunnel," *19th International Symposium on Shock Waves, Marseille, France.*, Springer-Verlag, 1993.

[41] Jain, A. C. and Adimurthy, V., "Hypersonic Merged Stagnation Shock Layers Part II: Cold Wall Case," *AIAA Journal*, Vol. 12, No. 3, March 1974, pp. 348–354.

[42] Jones, J. J., "Some performance characteristics of the LRC 3 3/4 - inch pilot tube using and unheated hydrogen driver," *4th Hypervelocity Techniques Symposium*, 1965.

[43] Kendall, M. A., *A Study of High-Enthalpy, Entropy Raising Drivers for Impulse Facilities*, Ph.D. thesis, University of Queensland, 1998.

[44] Koshmarov, Y. A., "Heat transfer of a sharp cone in a supersonic rarefied gas flow," *International Journal of Heat and Mass Transfer*, Vol. 9, No. 1, 1966, pp. 951–957.

[45] Lees, L., *Jet Propulsion*, Vol. 26, 1956, pp. 259–269.

[46] Lengrand, J. C., Allegre, J., Chpoun, A., and Raffin, M., "Rarefied hypersonic flow over a sharp flat plate: Numerical and experimental results," *Progress in Astronautics and Aeronautics vol. 160, RGD: Space Science and Engineering*, 1992, pp. 276–284.

[47] Lin, S. C., "Low density shock tube studies of reaction rates related to the high altitude hypersonic flight problem," *Proceedings of the Second International Symposium on Rarefied Gas Dynamics*, 1960, pp. 623–642.

[48] Lord, R. G., "Direct simulation of rarefied flow over a sharp 45^0 cone with incomplete surface accommadation," *Proceedings of the 19th International Symposium on Rarefied Gas Dynamics, Vol. 2*, New York, 1995, pp. 1243–1249.

[49] Macrossan, M. M., Chiu, H. H., and Mee, D. J., "A test facility for hypervelocity rarefied flow," *Proceedings of the 22nd International Symposium on Rarefied Gas Dynamics*, Sydney, July 10-14 2000.

[50] Macrossan, M. N., "Some developments of the equilibrium particle simulation method for the direct simulation of compressible flows," ICASE Interim Report 27, (NASA CR 198175), June 1995.

[51] McBride, B., Gordon, S., and Reno, M., "Thermodynamic Data for Fifty Reference Elements," NASA Technical Paper 3287, 1993.

[52] McIntyre, T., "Private communication," Physics Department, University of Queensland, August 2000.

[53] Miller, C. G., "Shock Shapes on Blunt Bodies in Hypersonic-Hypervelocity Helium, Air and CO_2 Flows, and Calibration Results in the Langley 6-inch Expansion Tube," NASA TN D-7800, 1975.

[54] Mirels, H., "Test time in low pressure shock tubes," *Physics of Fluids*, Vol. 6, No. 9, 1963, pp. 1201.

[55] Morgan, R. G., "A review of the use of expansion tubes for creating superorbital flows," AIAA Paper 97-0279, 1997.

[56] Morgan, R. G. and Stalker, R. J., "Double diaphragm driven free piston expansion tube," *Proceedings 18th International Symposium on Shock Tubes and Waves*, 1992.

[57] Moss, J. N., "Rarefied hypersonic flows: Simulation, experiments and applications," *Proceedings of the 19th International Symposium on Rarefied Gas Dynamics*, New York, 1995.

[58] Moss, J. N., Cuda, V., and Simmonds, A. L., "Nonequilibrium effects for hypersonic transitional flows," AIAA Paper 87-0404, 1987.

[59] Muntz, E. P., "Rarefied Gas Dynamics," *Annual Review of Fluid Mechanics*, Vol. 21, 1989, pp. 387–417.

[60] Neely, A. J., *Experimental and Analytical Study of a Pilot Superorbital Expansion Tube for Aerothermodynamic Testing to 13 km/s in Air*, Ph.D. thesis, University of Queensland, 1995.

[61] Owen, A., "Magnetic suspension and rarefied flows," First year report, Oxford University, June 1992.

[62] Palmer, R. A., *Measurement of Heat Transfer in Superorbital Flows*, Ph.D. thesis, University of Queensland, 1999.

[63] Park, C., "Assessment of a two-temperature kinetic model for dissociating and weakly ionizing nitrogen," *Journal of Thermophysics and Heat Transfer*, Vol. 2, No. 1, January 1988, pp. 8–16.

[64] Park, C., *Nonequilibrium Hypersonic Aerothermodynamics*, John Wiley & Sons, Inc., New York, 1989.

[65] Park, C., "A review of reaction rates in high temperature air," AIAA Paper 89-1740, 1989.

[66] Paull, A., Stalker, R. J., and Stringer, I. A., "Experiments on an expansion tube with a free piston driver," *AIAA 15th Aero. Testing Conference*, San Diego, California 1988.

[67] Petrie-Repar, P., *Numerical Simulation of Diaphragm Rupture*, Ph.D. thesis, University of Queensland, 1998.

[68] Petrie-Repar, P. J. and Jacobs, P. A., "A computational study of shock speeds in high-performance shock tubes," *International Journal on Shock Waves, Detonations and Explosions*, Vol. 8, No. 2, April 1998, pp. 79–91.

[69] Prabhu, R. K. and Erickson, W. D., "A rapid method for the computation of equilibrium chemical compostion of air to 15000 k," NASA-2792, 1999.

[70] Quirk, J. J., "An alternative to unstructured grids for computing gas dynamic flows around arbitrarily complex two-dimensional bodies." *Computers and Fluids*, Vol. 23, No. 1, 1993, pp. 125–142.

[71] Rizkalla, O., "Eqstate - a system of high temperature equilibrium chemistry subroutines," Technical Report, GASL, New York, 1991.

[72] Roberts, G. T., Kendall, M. A., and Morgan, R. G., "Shock-diaphragm interaction in expansion tubes," *21st International Symposium on Shock Waves*, Great Keppel Island, Australia, July 20-25 1997.

[73] Shidlovskiy, V. P., *Introduction to the Dynamics of Rarefied Gases*, American Elsevier Publishing, New York, 1967.

[74] Shimada, T., "Comparison of numerical solutions of transition regime flows: direct simulation Monte Carlo and Navier-Stokes computation," *Progress in Astronautics and Aeronautics vol. 159, RGD: Theory and Simulation*, 1992, pp. 256–267.

[75] Shinn, J. L. and Miller, C. G., "Experimental perfect-gas study of expansion tube flow characteristics," NASA-TP-1317, 1978.

[76] Smith, A. L. and Mee, D. J., "Dynamic strain measurement using piezoelectric polymer film," *Journal of Strain Analysis*, Vol. 31, No. 6, 1996, pp. 463–465.

[77] Smith, C. E., "The Starting Process in a Hypersonic Nozzle," *Journal of Fluid Mechanics*, Vol. 24, 1966, pp. 625–640.

[78] Srinivasan, S., Tannehill, J. C., and Weilmuenster, K. J., "Simplified Curve Fits for the Thermodynamic Properties of Equilibrium Air," NASA Reference Publication 1181, 1987.

[79] Stalder, J. R., "The use of low-density wind tunnels in aerodynamic research," *Proceedings of the First International Symposium on Rarefied Gas Dynamics*, 1958, pp. 1–20.

[80] Stalker, R. and Crane, K., "Driver Gas Contamination in a High Enthalpy Reflected Shock Tunnel," *AIAA Journal*, Vol. 16, No. 3, 1978, pp. 277–279.

[81] Sutcliffe, M., *The Use of an Expansion Tube to Generate Carbon Dioxide Flows Applicable to Martian Atmospheric Entry Simulation*, Ph.D. thesis, University of Queensland, 2000.

[82] Touryan, K. J. and Drake, R. M., "Flow investigations in Delavel supersonic nozzles at very low pressures," *Proceedings of the Third International Symposium on Rarefied Gas Dynamics*, 1962, pp. 402–.

[83] Trimpi, R. L., "A preliminary theoretical study of expansion tube, a new device for producing high-enthalpy short-duration hypersonic gas flows," NASA TR R-133, 1962.

[84] Vidal, R. J. and Bartz, J. A., "Hypersonic low density studies of blunt and slender bodies," *Advances in Applied Mechanicas, Rarefied Gas Dynamics Supplement 3, Vol. 1*, 1964.

[85] Vidal, R. J. and Wittliff, C. E., "Hypersonic low density studies of blunt and slender bodies," *Proceedings of the Third International Symposium on Rarefied Gas Dynamics*, 1962, pp. 343–378.

[86] Vogenitz, F. W. and Takata, G. Y., "Monte-Carlo study of blunt body hypersonic viscous shock layers," *Proceedings of the 7th International Symposium on Rarefied Gas Dynamics*, 1970.

[87] Wendt, M., Macrossan, M., Jacobs, P. A., and Mee, D. J., "Pilot study for a rarefied hypervelocity test facility," *13th Australasian Fluid Mechanics Conference*, December 13-18 1998.

[88] Wilson, G. J., "Time dependent quasi-one dimensional simulations of high enthalpy pulse facilites," *AIAA 4th International Aerospace Planes Conference*, December 1992.

[89] Wittliff, C. E. and Wilson, M. R., "Low density research in the hypersonic shock tunnel," *Proceedings of the Second International Symposium on Rarefied Gas Dynamics*, 1960, pp. 579–591.

[90] Wittliff, C. E., Wilson, M. R., and Hertzberg, A., "The tailored-interface hypersonic shock tunnel," *Journal of Aero/Space Sciences*, Vol. 26, No. 4, 1959, pp. 219–228.

APPENDIX A

Implementing a Finite-Rate Chemistry Model in a Lagrangian 1D Code

The initial simulations of the flow through X1 were run for the limiting situations of equilibrium gas composition and frozen gas composition through the expansion. This approach has been used previously by Miller [53], however Sutcliffe [81] indicated that finite-rate effects are important. The question needs to be further explored and a flow solver incorporating finite-rate chemistry modelling can be used to determine whether one of these extreme flow chemistry models is appropriate, or if an accurate flow field solution can only be obtained if the finite-rate at which chemical reactions proceed is included in the gas dynamic modelling.

Jacobs' one-dimensional code, L1D [39], is extremely useful for modelling expansion tubes because its Lagrangian nature enables it to conveniently simulate piston and diaphragm motion together with the motions of the gases. The implementation of finite-rate chemistry modelling in L1D is simpler than in a flow solver based on a control volume formulation because there are no fluxes of species between L1D's Lagrangian cells (control masses). Using L1D with finite-rate chemistry modelling, the flow chemistry in X1 resulting from the diaphragm inertia model of light diaphragm rupture (described in Chapter 5) can be investigated by modelling the diaphragm as a light piston. The effect of the holding time model on the flow composition can also be assessed using L1D, allowing the two diaphragm rupture models to be explored, along with with the effects of finite-rate chemistry.

This section describes the implementation of finite-rate chemistry modelling in L1D. It begins with a presentation of the equations governing the rates of production of reacting chemical species, and a description of the 5-species nitrogen model used for the expansion

tube modelling. The governing equations and numerical methods used in the modified version of L1D are then discussed. This section concludes with a presentation of two test cases designed to verify that the finite-rate chemistry model was correctly implemented in L1D.

A.1 Finite-Rate Chemistry Model

In 1990, Gupta, Yos, Thompson and Lee [30] published a review of reaction rates and thermodynamic and transport properties for an 11-species air model for chemical and thermal nonequilibrium calculations up to 30,000 K. The purpose of this report was to provide the thermochemical models required to successfully simulate the nonequilibrium flow environment surrounding hypersonic vehicles. These conditions are very similar to those present in an expansion tube operating at low pressures. However, to simplify the analysis of the test flows, X1 is presently operated using nitrogen not air. A finite-rate chemistry model for nitrogen can be extracted from the 11-species air model of Gupta, Yos, Thompson and Lee [30] by including reactions that only involve the various species of nitrogen and electrons. The result is 5-species nitrogen model that includes 5 reactions between the species. The 5 species included in the model are,

$$N_2,\ N,\ N_2^+,\ N^+ \text{ and } e^-.$$

The reactions included in the model are shown in Table A.1. In the first reaction, "M_2" is a third body which in our case is a nitrogen molecule. 5-species nitrogen models that include the reactions listed in Table A.1 have been presented by a number of authors [63, 64, 65, 12]. In some of these models, such as those devised by Park [63, 64], the general third body M_2 in reaction 1 is replaced with N_2, the actual compound that M_2 represents. As a result of this, the equations governing the species reaction rates that were presented in reference [30] incorporate features that are not present in the equations presented by some of the other authors. In the interest of generality, the equations governing the net rate of production of each of the species are presented as in reference [30].

For any multicompontent gas with NS reacting chemical species and NR possible reactions between them, the stoichiometric relations governing the reactions, such as those

Reaction Number, r	Reaction	Third body, M
1	$N_2 + M_2 \rightleftharpoons 2N + M_2$	N_2
2	$N_2 + N \rightleftharpoons 2N + N$	
3	$N + e^- \rightleftharpoons N^+ + 2e^-$	
4	$N_2 + N^+ \rightleftharpoons N + N_2^+$	
5	$N + N \rightleftharpoons N_2^+ + e^-$	

Table A.1: Reactions included in the 5-species nitrogen model.

listed above, can be written as,

$$\sum_{i=1}^{NJ} \alpha_{i,r} X_i \underset{k_{b,r}}{\overset{k_{f,r}}{\rightleftharpoons}} \sum_{i=1}^{NJ} \beta_{i,r} X_i \tag{A.1}$$

where r = 1, 2, ... , NR. NJ is the number of reacting species, NS, plus the number of catalytic bodies. $\alpha_{i,r}$ and $\beta_{i,r}$ are the stoichiometric coefficients for the reactants and products respectively. X_i is the concentration of the i'th species or catalytic body in moles per unit volume. The catalytic bodies can be reacting chemical species or linear combinations of non-reacting species.

The net rate of production of species i in mass per unit volume per unit time is given by,

$$\dot{\omega}_i = M_i \sum_{r=1}^{NR} \left(\frac{dX_i}{dt} \right)_r \tag{A.2}$$

or,

$$\dot{\omega}_i = M_i \sum_{r=1}^{NR} \left(\beta_{i,r} - \alpha_{i,r} \right) \left(R_{f,r} - R_{b,r} \right) \tag{A.3}$$

where M_i is the molecular weight of species i in g/mole and,

$$\begin{aligned} R_{f,r} &= k_{f,r} \prod_{j=1}^{NJ} \left(\gamma_j \rho \right)^{\alpha_{i,r}} \\ R_{b,r} &= k_{b,r} \prod_{j=1}^{NJ} \left(\gamma_j \rho \right)^{\beta_{i,r}} \end{aligned} \tag{A.4}$$

Here $k_{f,r}$ and $k_{b,r}$ are the forward and backward rate coefficients for the r'th reaction and γ_j is the mole number, which is defined as,

$$\gamma_j = \begin{cases} \frac{X_i}{\rho} = \frac{f_i}{M_i} & (j = 1, 2, ..., NS) \\ \sum_{i=1}^{NS} \left(Z_{j-NS,i} \, \gamma_i \right) & (j = NS+1, ..., NJ) \end{cases} \tag{A.5}$$

where ρ is the density in g/cm^3, f_i is the mass fraction of species i and X_i has units of moles/cm^3. The constants $Z_{j-NS,i}$ are functions of the catalytic efficiencies of the NS species and determined from the linear dependence of the catalytic bodies on the NS species [30]. The values of the constants for the 11-species air model are given in Table A.6 in Section A.4. In the 5-species nitrogen models where N_2 is used explicitly instead of the general third body, M_2, there are no catalytic bodies defined and hence values of $Z_{j-NS,i}$ are not required.

The rate coefficients $k_{f,r}$ and $k_{b,r}$ are expressed in the modified Arrhenius form as,

$$k_{f,r} = A_{f,r} T^{B_{f,r}} e^{-T_{D_{f,r}}/T}$$

$$k_{b,r} = A_{b,r} T^{B_{b,r}} e^{-T_{D_{b,r}}/T}$$

where $T_{D_{f,r}}$ and $T_{D_{b,r}}$ are the characteristic temperatures for the forward and backward reactions, respectively. Values of the rate coefficients for the five reactions in the nitrogen model extracted from reference [30] are shown in Table A.2.

Reaction Number, r	Forward Rate Coefficient, $k_{f,r}$ (cm^3/mole.sec)	Backward rate coefficient, $k_{b,r}$ (cm^3/mole.sec)
1	$1.92 \times 10^{17} T^{-0.5}\ e^{-1.131\times10^5/T}$	$1.09 \times 10^{16}\ T^{-0.5}$
2	$4.15 \times 10^{22} T^{-1.5}\ e^{-1.131\times10^5/T}$	$2.32 \times 10^{21}\ T^{-1.5}$
3	$(1.1 \pm 0.4) \times 10^{32} T^{-3.14}\ e^{-1.69\times10^5/T}$	$(2.2 \pm 0.7) \times 10^{40}\ T^{-4.5}$
4	$2.02 \times 10^{11} T^{0.81}\ e^{-1.3\times10^4/T}$	$7.8 \times 10^{11}\ T^{0.5}$
5	$(1.4 \pm 0.3) \times 10^{13}\ e^{-6.78\times10^4/T}$	$(1.5 \pm 0.5) \times 10^{22}\ T^{-1.5}$

Table A.2: Forward and backward rate coefficients for 5-species nitrogen model extracted from [30].

The values given in Table A.2 are only appropriate for flow velocities up to about 8 km/s. For higher flow velocities, such as those present in X1, the backward rate coefficients can be obtained from the forward rate coefficients using,

$$k_{b,r} = \frac{k_{f,r}}{K_{eq,r}}. \tag{A.6}$$

This method of calculating the backward rate coefficients is used for all flow conditions in the other 5-species nitrogen models surveyed [63, 64, 65]. The equilibrium constants $K_{eq,r}$ were obtained at a set of discrete temperatures using the atomic partition functions

and molecular partition functions provided in reference [64]. The computed values of $K_{eq,r}$ were then curve fitted in reference [30] using the least squares curve-fit method to obtain the following expression for $K_{eq,r}$ as a function of temperature:

$$ln\left(K_{eq,r}\right) = A_{K_{eq,r}} Z^5 + B_{K_{eq,r}} Z^4 + C_{K_{eq,r}} Z^3 + D_{K_{eq,r}} Z^2 + E_{K_{eq,r}} Z + F_{K_{eq,r}} \quad \text{(A.7)}$$

where,

$$Z = ln\left(10^4/T\right).$$

Since the electronic partition functions of atomic species are significantly affected at high temperatures and low densities, the curve fit coefficients of reference [30] are given for 6 different values of total number density. These curve fit coefficients are used in preference to those of Park [64] as Park's coefficients were obtained by using only five discrete temperatures (2000, 4000, 6000, 8000 and 10,000 K) and as a result of this they are in disagreement with the exact values at higher temperatures [30]. The curve fit coefficients in equation A.7 are listed in Table A.7 in Section A.4.

For implementation of the 5-species finite-rate chemistry model of nitrogen in L1D, the forward rate coefficients of references [30], [63] and [64] were initially included. Attempts to solve the test cases described in Section A.3 revealed that there are numerical problems associated with using the forward rates coefficients of references [30] and [63] in L1D: There was difficulty in maintaining the stability of the scheme at the beginning of each simulation, and the allowable time step monatomically decreased for the entire simulation time. For this reason the forward rate coefficients of reference [64] alone were finally adopted. These are listed in Table A.3. Note that, in reality, the rate coefficients of reaction 3 are functions of the electron temperature while the rate coefficients of reactions 1, 2 are governed by the geometric average of the vibrational temperature and the translational-rotational temperature [63]. As L1D is a one-temperature code, all rate coefficients and flow properties are determined from the thermodynamic temperature. This assumes that the vibrational-electron-electronic temperature is the same as the heavy particle translational-rotational temperature, which introduces inaccuracies into the model. The rate coefficient parameters for reaction 4 were taken from reference [63] as they were not listed in reference [64]. This should not be a problem as the parameters for the charge-exchange reaction are inconsequential; the reaction rate is so fast that the process is most

likely in local equilibrium, in which case the ratio of the mass fractions of the two ions becomes a function of temperature and not the rate coefficient [63].

r	$A_{f,r}$ (cm^3/mole.sec)	$B_{f,r}$	$T_{D_{f,r}}$ K
1	7.0×10^{21}	-1.6	113,200
2	3.0×10^{22}	-1.6	113,200
3	2.5×10^{33}	-3.82	168,600
4	9.85×10^{12}	-0.18	12,100
5	2.0×10^{13}	0.0	67,500

Table A.3: Parameters for determination of the forward rate coefficients for dissociating and weakly ionizing nitrogen from reference [64] (parameters for reaction 4 are from reference [63]).

The set of equations presented in this section, along with the rate coefficients given in Table A.3 and the equilibrium constant curve fits in Table A.7, can be used to calculate the rate of production of each species in a reacting multicomponent gas. In the next section, a description of L1D with this finite-rate chemistry modelling incorporated into it is presented. Verification that the finite-rate chemistry model for nitrogen has been correctly implemented is presented in Section A.3.

A.2 Implementation of Finite Rate Chemistry Modelling in L1D

L1D is a computer program for the simulation of transient-flow facilities such as light-gas launchers and free-piston driven shock tunnels. The original code was written by Jacobs [35] and has been added to by the author. This section describes the numerical modelling behind L1D with a focus on the finite-rate chemistry modelling added by the author.

The principal features of L1D are:

- A quasi-one-dimensional formulation of the equations governing the gas dynamics. The axial distance along the facility is the only spatial coordinate however, the effects of a gradual variation of the cross-stream area are modelled.
- A facility is modelled using several components which can be slugs of gas, pistons/projectiles or diaphragms. The slugs of gas may be independent or interact

with neighbouring components. The motion of the pistons/projectiles and the behaviour of the diaphragms are coupled to the gas dynamics via the boundary (end) conditions of the gas slugs.

- The discretisation of the gas slugs is Lagrangian. Each gas slug is divided into a set of control-masses (or gas particles) and their positions are followed.

- A robust shock capturing scheme that allows the same set of equations to be used to compute the motion of the gas whether a shock is present or not. The scheme results in shocks being smeared over a couple of computational cells. In practice, this is not a problem as any smeared shocks can be sharpened by increasing the resolution of the discretisation.

- Nominal second-order accuracy in both time and space.

- Viscous effects are included using the standard engineering correlations for friction and heat transfer in pipe flow. These correlations were derived for steady incompressible flow however, they seem to perform adequately in simulations even though the flows are predominantly unsteady and are very compressible [39].

- Several different gas types are modelled through the inclusion of suitable equations of state and viscosity curve-fits. While each gas slug can contain only one gas type, it may be a homogeneous mixture of other gases.

- Finite-rate chemistry is simulated by applying the conservation equation to the species mass fractions within each cell. The reaction rates are explicitly calculated from the species mass fractions, temperature and density in a cell. (This is the new feature/capability.)

To simulate a specific facility, a model of the facility is assembled from a number of components, which may be pistons, diaphragms or gas slugs, which are contained within a duct with a specified area profile. The description of each component is formulated separately and components interact via their boundary conditions. The core of L1D is a time-stepping loop that first applies the specified boundary conditions and then advances the state of the entire system forward in time by a small increment known as a time step. The following subsections describe the governing differential equations for the gas

dynamics, the equations of state, and the time-stepping scheme implemented in L1D. Jacobs' report [39] should be referred to for details of the other aspects of L1D, which have not been altered.

A.2.1 Gas Dynamics

In L1D each gas slug is modelled from a Lagrangian perspective, where each slug is divided into a number of control masses (referred to as cells) that move in a variable-area duct. Flow in only one dimension is considered and any area changes in the tube area are assumed to be gradual. While the one-dimensional formulation of the gas-dynamic equations cannot properly model the boundary layer along the tube wall, some of the boundary layer's effects are modelled through the addition of wall shear stress terms into the momentum equation and heat transfer terms in the energy equation. These approximations are arguably the most troublesome part of the modelling process as they cannot be fixed later by simply increasing the resolution of the simulation [39].

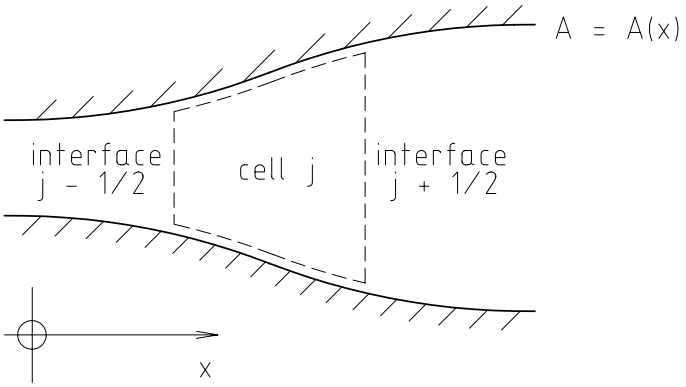

Figure A.1: A typical control-mass or Lagrangian cell.

A typical control-mass cell (labelled j) is shown in Figure A.1. Its interfaces with adjacent cells are labelled $j - \frac{1}{2}$ and $j + \frac{1}{2}$. In the Lagrangian description, the velocity of the cell interfaces equates to the local fluid velocity;

$$\frac{dx_{j\pm\frac{1}{2}}}{dt} = u_{j\pm\frac{1}{2}} \,, \tag{A.8}$$

where x is the position of the cell interface and u is the local gas velocity computed with a Riemann solver described in reference [39].

The average density within the cell is given by,

$$\overline{\rho_j} = \frac{m_j}{\overline{A_j}\left(x_{j+\frac{1}{2}} - x_{j-\frac{1}{2}}\right)} \ , \tag{A.9}$$

where $\overline{(\cdot)}$ represents an average value in a cell, m_j is the constant mass of gas in cell j, and A is the area of the duct.

The net mass rate of production of species i in cell j per unit volume per unit time, $\dot{\omega}_{i,j}$, is calculated using equations A.3 to A.7 and the curve fits presented in Tables A.3 and A.7. The time derivative of the species mass fraction, $\dot{f}_{i,j}$, is then found using,

$$\dot{f}_{i,j} = \frac{1000}{\overline{\rho_j}}\dot{\omega}_{i,j} \ , \tag{A.10}$$

Note that using this equation to calculate $\dot{f}_{i,j}$ neglects the binary diffusion of species between cells, which has been assumed to be negligible by other authors (e.g. [19]). The routines for calculating the reaction rates for the 5-species nitrogen model are included in the file n2fr.c and are called by the function L_reaction_rates within L1D.

Pressure forces acting on the cell interfaces and viscous forces acting at the duct wall govern the rate of change of momentum in a cell, which is given by,

$$\frac{d}{dt}m_j\overline{u_j} = \left[p_{j-\frac{1}{2}}A_{j-\frac{1}{2}} - p_{j+\frac{1}{2}}A_{j+\frac{1}{2}} + \overline{p_j}\left(A_{j+\frac{1}{2}} - A_{j-\frac{1}{2}}\right) - \overline{F_{wall}} - \overline{F_{loss}}\right] \ , \tag{A.11}$$

where F_{wall} is the shear friction force at the wall and F_{loss} is an effective body-force due to pipe-fitting losses, for example. The calculation of these loss terms from standard engineering correlations is described in detail in reference [39].

The work done at the cell interfaces and heat transfer from the duct wall cause the rate of change of energy within a cell, which is given by,

$$\frac{d}{dt}m_j\overline{E_j} = \left[p_{j-\frac{1}{2}}A_{j-\frac{1}{2}}u_{j-\frac{1}{2}} - p_{j+\frac{1}{2}}A_{j+\frac{1}{2}}u_{j+\frac{1}{2}} + \overline{q_j}\right] \ , \tag{A.12}$$

where,

$$E = e + \sum_{i=1}^{N_S} 1000\frac{(\Delta H_f^o)_{T_R,i}}{M_i}f_i + \frac{1}{2}u^2$$

is the total specific energy of the gas, e is the sensible internal energy of the gas mixture,

q is the rate of heat transfer into the cell and $(\Delta H_f^o)_{T_R,i}$ is the molar heat of formation of species i at the reference temperature $T_R = 0$ K. This term provides the mechanism for energy absorption and release due to chemical reactions. Evaluation of q using standard engineering correlations for heat transfer in pipe flow is described in detail in [39]. Note that there is no shear stress term in the energy conservation equation. The reason for this is that the kinetic energy lost due to the action of the wall shear stress adds to the internal energy of the gas near the wall and, as there is no mass transfer between cells, the total energy of the cell is not altered by this mechanism.

A.2.2 Equations of State

The governing differential equations for the gas dynamics (equations A.8, A.10, A.11 and A.12) are supplemented by specifying an equation of state that relates the thermodynamic properties of the gas. For a perfect gas, the equation of state is,

$$P = \rho \, R \, T \, , \tag{A.13}$$

where R is the gas constant. If the gas is considered to be calorically perfect, the specific internal energy is given by,

$$e = C_v \, T \, , \tag{A.14}$$

where C_v is the specific heat capacity of the gas at constant volume. The equation of state for a calorically perfect gas may then be written as,

$$P = \rho \, (\gamma - 1) \, e \, , \tag{A.15}$$

The speed of sound in the gas, a, is given by,

$$a = \sqrt{\gamma \, R \, T} = \sqrt{\gamma \, \frac{P}{\rho}} = \sqrt{\gamma \, (\gamma - 1) \, e} \, . \tag{A.16}$$

The thermodynamic properties of a number of ideal gases are given in Table A.4. For mixtures of perfect gases (e.g. helium-argon mix), the perfect gas relations are used along

with the effective thermodynamic properties,

$$C_p = \sum_i^{NSP} f_i(C_p)_i \ , \ \ C_v = \sum_i^{NSP} f_i(C_v)_i \ , \ \ R = \sum_i^{NSP} f_i R_i \ , \ \ \gamma = \frac{C_p}{C_v} \ . \tag{A.17}$$

Gas	MW (kg/kg-mole)	R (J/kg.K)	γ	C_p (J/kg.K)	C_v (J/kg.K)
Air	28.97	287.0	1.400	1004.5	717.5
Hydrogen	2.016	4124	1.409	14207	10083
Helium	4.006	2077	1.667	5191	3114
Argon	39.948	208.1	1.667	520.1	312
Nitrogen	28.013	296.8	1.400	1038	742
Oxygen	32.0	259.8	1.393	920.9	661.1
He, Ar mix	7.595	1094	1.667	2735	1641

Table A.4: Thermodynamic properties for some ideal gases. The He, Ar mix is 90% He and 10% Ar by volume.

For high temperature flows of nitrogen and air, the dissociation and recombination of chemical bonds within molecules as well as the excitation of vibrational energy modes in individual species can be important.

The sensible energy (energy based on statistical mechanics [3]) can be derived as a function of static temperature for single species and non-reacting gas mixtures in vibrational equilibrium. Solutions of these functions have been tabulated for various species in the form of molar thermodynamic properties listed against temperature [14, 51]. For computational applications it is common to fit a polynomial equation to the tabulated specific heat data. The molar thermodynamic quantities H^o and S^o are then found by integrating this equation. For nitrogen, the polynomial curve fits of reference [71] are used in L1D.

The polynomial used for the molar C_p^o is expressed as,

$$C_p^o/R^o = a_1 + a_2 T + a_3 T_2 + a_4 T_3 + a_5 T^4 \ . \tag{A.18}$$

A different set of polynomial coefficients, $a_1 ... a_7$, are used for each species. Integration of the expression for C_p^o yields the following polynomial for the molar enthalpy at

temperature T,

$$H^o/R^o = a_1T + a_2T^2/2 + a_3T^3/3 + a_4T^4/4 + a_5T^5/5 + a_6 \ . \tag{A.19}$$

The curve fits of reference [71] are referenced to a temperature of 298.15 K. This requires the integration constant a_6R^o in Eq. (A.19) to set the molar enthalpy at 298.15 K to be equal to the heat of formation at that standard reference temperature. This poses a problem computationally since we require the sensible energy of the gas to maintain a positive value for all temperatures. To facilitate this, the expression for enthalpy was referenced to 0 K by deducting the heat of formation at 298.15 K and adding the difference in enthalpy between 0 K and 298.15 K. The enthalpy of formation at 0 K is not added to the integration constant since it is accounted for in the energy conservation equation (equation A.12).

If the expression for C_p^o in Eq. (A.18) is divided by T and then integrated, the resulting polynomial function for molar entropy is,

$$S^o/R^o = a_1lnT + a_2T + a_3T^2/2 + a_4T^3/3 + a_5T^4/4 + a_7 \ . \tag{A.20}$$

The Gibbs free energy,

$$G^o = H^o - TS^o \ , \tag{A.21}$$

is used by the equilibrium chemistry models in L1D to calculate the equilibrium constant for a particular reaction.

The molar internal energy, E^o, for each species can also be calculated from H^o using,

$$E^o = H^o - R^oT \ . \tag{A.22}$$

For a gas mixture, the specific sensible internal energy in $\mathrm{J/kg}$ can be computed from the individual species molar values at a given temperature using the equation,

$$e = \sum_{i=1}^{N_S} 1000\, f_i \frac{E_i^o}{M_i} \ , \tag{A.23}$$

L1D includes a model of nitrogen in chemical equilibrium. This model iteratively calculates the species mass fractions, temperature and pressure in a cell given the density

and specific internal energy (including enthalpy of formation) using the fast equilibrium method of reference [69] that utilises equations A.18 to A.23. The 5-species finite-rate chemistry model for nitrogen uses this equilibrium model to initialise the composition of the gas slugs at the beginning of a simulation. From then on the composition is determined through integration of the species conservation equation (equation A.10).

Once the temperature and composition of the gas mixture have been determined by either the equilibrium or finite-rate chemistry model, the remaining non-conservative properties can be calculated. First, the gas constant of the mixture, R_{mix}, is calculated using,

$$R_{mix} = \sum_{i=1}^{N_S} f_i R_i \ . \tag{A.24}$$

The pressure is given by Dalton's law of partial pressures, which can be expressed as,

$$p = \rho R_{mix} T \ . \tag{A.25}$$

An effective value of γ is then calculated using,

$$\gamma_{eff} = \frac{h}{e} \ . \tag{A.26}$$

The frozen speed of sound [27] is used for all computations in where chemistry is involved and is defined as,

$$a^2 = \gamma_{eff}(\gamma_{eff} - 1)e \ . \tag{A.27}$$

An equation of state for air in chemical equilibrium is also included in L1D; the curve fits given in [78] are used to obtain P, T, a and γ as functions of ρ and e for temperatures up to $25000\ K$.

A.2.3 Time Stepping

The state quantities for both pistons and gas slugs are advanced from time level n to time level $n+1$ using the following predictor-corrector scheme;

$$\begin{aligned} \Delta U^{(1)} &= \Delta t \, \tfrac{dU^{(n)}}{dt} \, , \\ U^{(1)} &= U^{(n)} + \Delta U^{(1)} \, , \\ \Delta U^{(2)} &= \Delta t \, \tfrac{dU^{(1)}}{dt} \, , \\ U^{(n+1)} &= U^{(1)} + \tfrac{1}{2} \left(\Delta U^{(2)} - \Delta U^{(1)} \right) \, . \end{aligned} \tag{A.28}$$

Here the superscripts (1) and (2) indicate intermediate results and ($\frac{dU}{dt}$) includes the rate of change of interface positions, cell momentum, cell energy, cell species mass fractions, piston velocity and piston position. A first-order scheme can be implemented by only using first stage so $U^{(n+1)} = U^{(1)}$. While first-order time-stepping requires fewer operations than second-order time-stepping, it is also less robust [39].

To maintain stability, the time step is restricted according to the following criteria;

$$\Delta t \leq \Delta t_{allowed} = CFL \text{ minimum} \left(\Delta t_{signal}, \, \Delta t_{chem} \right) \, , \tag{A.29}$$

where $\Delta t_{allowed}$ is the smallest value for all cells in the computational domain and CFL is the specified Courant-Friedrichs-Lewy number, which is normally restricted to values less than or equal to 0.5. For each cell, the inviscid signal time is approximated as,

$$\Delta t_{signal} = \frac{\Delta x}{|u| + a} \, . \tag{A.30}$$

The chemistry time step, Δt_{chem}, is selected so that no change in species concentration, C_i, is greater than 3.5×10^{-3} moles/m^3 in a single time step. For each cell, Δt_{chem} is calculated using

$$\Delta t_{chem} = min_i \left(\frac{3.5 \times 10^{-6} M_i}{\rho \dot{f}_i} \right) \, . \tag{A.31}$$

The criterion was developed from that of Craddock [19] who permitted a maximum change of 10^{-4} kg/m^3 in species density in a single time step in his explicit scheme. The new criteria was adopted because the density of electrons is orders of magnitude less than those of the other species, hence a criteria based on species density does not directly

ensure the stability of reactions involving electrons.

A.3 Test Cases

The Lagrangian one-dimensional code, L1D, was used to solve two test case flow problems where the effects of finite-rate chemistry are significant. The objective of this was to assess whether the finite-rate chemistry modelling was correctly implemented in L1D.

The first test case selected for this purpose was that of a uniform, high temperature slug of nitrogen relaxing from an initial state determined using the fast equilibrium model of reference [69]. The purpose of this test case was to assess whether the equilibrium state calculated using the 5-species finite-rate chemistry model is close to that predicted by the existing equilibrium model used in L1D. The initial temperature and pressure of the gas slug were taken to be 7081.5 K and 37.24 kPa respectively. The test case was run for 0.5 ms to ensure equilibrium was established. Figure A.2 shows the variation of the molecular nitrogen mass fraction, f_0, and sensible internal energy, e, over time. It can be seen from this figure that around 200 μs must elapse before the equilibrium state reached. This is due to the fact that the net reaction rates become very small for small deviations from equilibrium. The overall change in composition between the initial and final (equilibrium) states is indicated by the change in the mass fraction of N_2, which was found to decrease by 1.36%. The change in final composition from the equilibrium state calculated by the fast equilibrium model resulted in a 3.88% drop in the sensible internal energy of the gas slug. Taking into account the fact that the fast equilibrium model used only includes four species (N_2^+ is omitted), these deviations were deemed to be acceptable.

The second test case selected was a shock wave travelling through a constant area duct with a velocity of 6.4 km/s. The quiescent gas downstream of the shock had an initial pressure of 1 torr and an initial temperature of 298 K. Computational results for this test case have been published by Park [63, 64]. For nitrogen, the effects of finite-rate chemistry are significant in a 2 cm long relaxation zone following the shock wave.

The test case was initiated by setting up two uniform slugs of gas; a left slug with its flow state set to the equilibrium conditions behind the shock, and a right slug with its state set to the quiescent conditions. The equilibrium conditions behind the shock were calculated using the computational tool Shock1D described in Section 5.1.1 and are shown

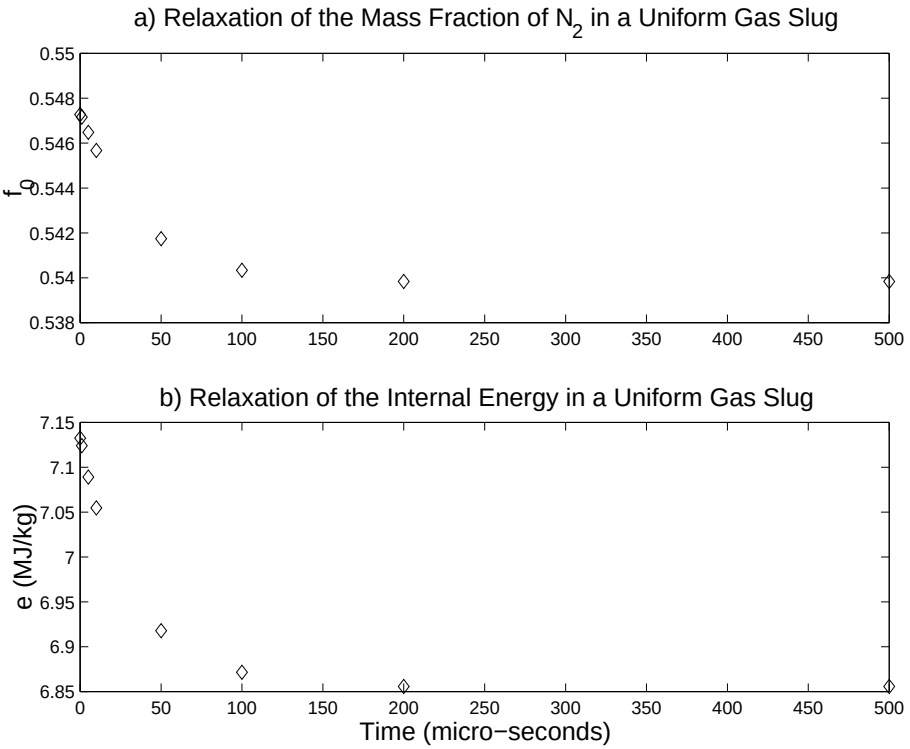

Figure A.2: Relaxation of a) the mass fraction of N_2, f_0, and b) the sensible internal energy, e, in a uniform, high temperature gas slug from the values determined from a fast equilibrium model [69].

in Table A.5. These initial conditions cause a shock with a velocity of approximately 6.4 km/s to propagate into the right slug once the simulation is started. The shock speed deviates slightly from 6.4 km/s because of the chemical nonequilibrium in the relaxation zone. However, it will be shown later that the magnitude of this error is very small.

Quiescent pressure	1 torr
Quiescent temperature	298 K
Shock speed	6.4 km/s
Equilibrium post shock pressure	57.3070 kPa
Equilibrium post shock temperature	6904.90 K
Equilibrium post shock velocity	5942.86 m/s

Table A.5: Initial conditions for the 6.4 km/s shock wave test case.

The nonequilibrium relaxation zone is established as the shock propagates into the quiescent gas. To establish a sufficiently long relaxation zone, the simulation must be run for at least enough time for the shock to propagate 2 cm downstream of the interface between the gas that was originally at the equilibrium post shock conditions, and the gas that has been processed by the shock in nonequilibrium. To minimize any risk that

the chemistry in the relaxation zone was affected by the initial equilibrium conditions, a simulation time was selected such that the interface was 10 cm from the shock at the end of the simulation. Assuming that the interface travels with the equilibrium post shock velocity shown in Table A.5, the required simulation time was found to be 219 μs, which was then rounded to 200 μs.

The simulation was run with CFL numbers of 0.25 and 0.125. There were no visible differences between the results of the two simulations. The species mole fractions in the relaxation zone obtained from the L1D simulation are shown in Figure A.3 along with the results published by Park [63]. From the simulation results, the nonequilibrium shock speed was found to be 6401.05 m/s, which deviates from the values in Park's calculations by only 0.016% and hence should not significantly affect the results. An aberration in the computed mole fractions can be seen approximately 0.012 m from the shock. This is caused by the number density in the cell at this location crossing one of the threshold values at which different curve fits are used to calculate the equilibrium constant. While this causes a small discontinuity in the mole fractions of the ionized species, it does not have a significant effect on the thermodynamic properties of the gas. It can be seen from Figure A.3 that towards the end of the relaxation zone, where the gas state approaches equilibrium, the species mole fractions from the L1D simulation are in agreement with Park's results. It is apparent that the relaxation rates immediately behind the shock are significantly greater than in Park's results. In Park's results the reaction rates were calculated from the geometric average of the heavy-particle translational temperature, T, and the vibrational-electron-electronic temperature, T_v, while in the L1D simulations only T was used. The variation of T and T_v in the relaxation zone are shown in Figure A.4. Due to the gradual increase of T_v in the region immediately behind the shock, the average temperature used by Park is significantly less than T in this region, leading to lower reaction rates than those used in L1D. From these results it can be concluded that the solutions produced by L1D are as expected for a method using a single temperature to calculate the reaction rates; the finite-rate chemistry modelling appears to have been implemented correctly.

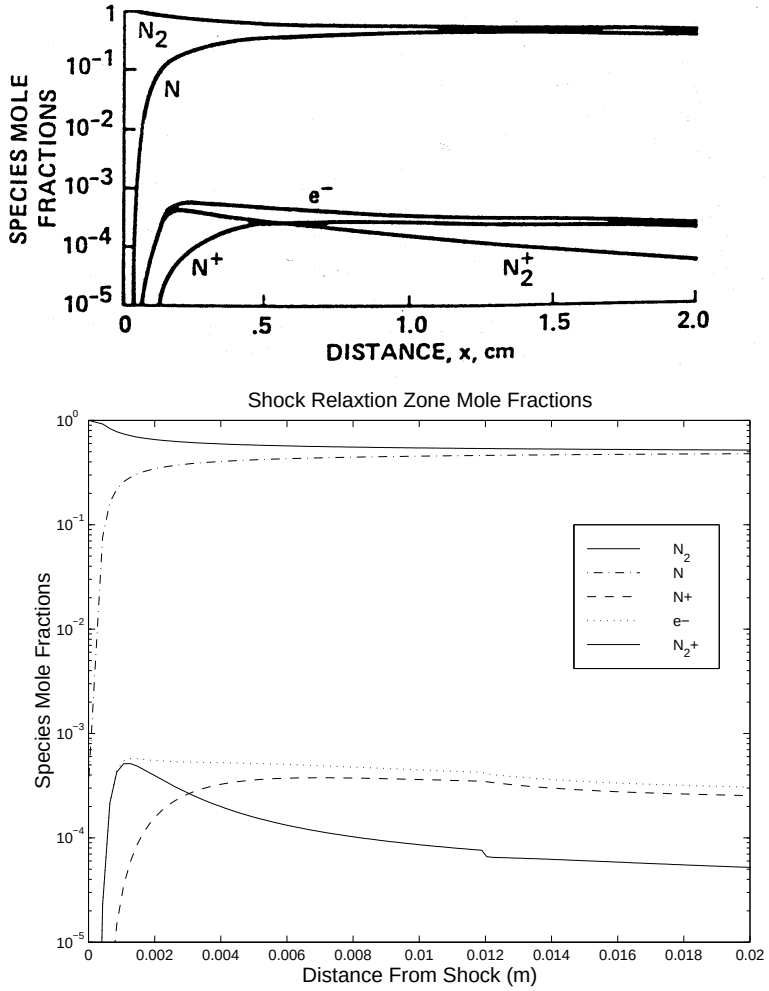

Figure A.3: Post shock relaxation zone species mole fractions from a) Park [63], and b) L1D.

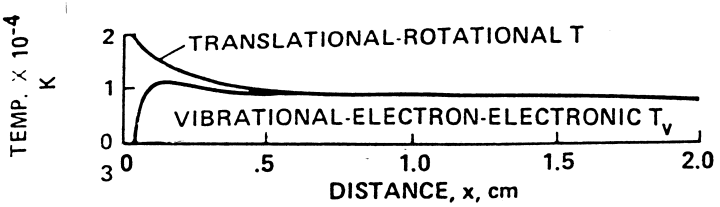

Figure A.4: Post shock relaxation zone heavy-particle translational and vibrational-electron-electronic temperatures from Park [63].

A.4 Curve-Fit Coefficients and Constants for Chemistry Modelling

Catalytic bodies	$Z_{(j-NS),i}$	O_2 (i=1)	N_2 (i=2)	O (i=3)	N (i=4)	NO (i=5)	NO+ (i=6)	O_2^+ (i=7)	N_2^+ (i=8)	O+ (i=9)	N+ (i=10)
M_1	1,i	9	2	25	1	1	0	0	0	0	0
M_2	2,i	1	2.5	1	0	1	0	0	0	0	0
M_3	3,i	1	1	20	20	20	0	0	0	0	0
M_4	3,i	4	1	0	0	0	0	0	0	0	0
M_1	5,i	0	0	0	0	0	1	1	1	1	1

Table A.6: Third body efficiencies relative to argon from reference [30].

n	$A_{K_{eq,r}}$	$B_{K_{eq,r}}$	$C_{K_{eq,r}}$	$D_{K_{eq,r}}$	$E_{K_{eq,r}}$	$F_{K_{eq,r}}$
Reaction 1: $N_2 + M_2 \rightleftharpoons 2N + M_2$						
1e+14	0.000000e+00	0.142518e+01	-0.179191e+01	-0.152245e+00	-0.172635e+02	-0.777060e+01
1e+15	0.000000e+00	-0.131460e+01	-0.211364e+01	-0.655486e+00	-0.156315e+02	-0.831884e+01
1e+16	0.000000e+00	-0.120533e+01	-0.240055e+01	-0.123908e+01	-0.140810e+02	-0.870302e+01
1e+17	0.000000e+00	-0.111597e+01	-0.260376e+01	-0.181730e+01	-0.128199e+02	-0.890679e+01
1e+18	0.000000e+00	-0.104068e+01	-0.273172e+01	-0.246330e+01	-0.116894e+02	-0.898864e+01
1e+19	0.000000e+00	-0.100734e+01	-0.274128e+01	-0.293912e+01	-0.110496e+02	-0.897632e+01
Reaction 2: $N_2 + N \rightleftharpoons 2N + N$						
1e+14	0.000000e+00	-0.142518e+01	-0.179191e+01	-0.152245e+00	-0.172635e+02	-0.777060e+01
1e+15	0.000000e+00	-0.131460e+01	-0.211364e+01	-0.655486e+00	-0.156315e+02	-0.831884e+01
1e+16	0.000000e+00	-0.120533e+01	-0.240055e+01	-0.123908e+01	-0.140810e+02	-0.870302e+01
1e+17	0.000000e+00	-0.111597e+01	-0.260376e+01	-0.181730e+01	-0.128199e+02	-0.890679e+01
1e+18	0.000000e+00	-0.104068e+01	-0.273172e+01	-0.246330e+01	-0.116894e+02	-0.898864e+01
1e+19	0.000000e+00	-0.100734e+01	-0.274128e+01	-0.293912e+01	-0.110496e+02	-0.897632e+01
Reaction 3: $N + e^- \rightleftharpoons N^+ + 2e^-$						
1e+14	-0.474396e+00	0.614580e-02	-0.229468e+01	-0.114334e+02	-0.157101e+02	-0.213937e+02
1e+15	-0.474831e+00	-0.654883e-01	-0.202828e+01	-0.113511e+02	-0.165058e+02	-0.210712e+02
1e+16	-0.453275e+00	-0.204988e+00	-0.185082e+01	-0.109883e+02	-0.172377e+02	-0.208889e+02
1e+17	-0.417456e+00	-0.373700e+00	-0.178585e+01	-0.104515e+02	-0.177927e+02	-0.208436e+02
1e+18	-0.370274e+00	-0.564285e+00	-0.182040e+01	-0.975050e+01	-0.182364e+02	-0.208947e+02
1e+19	-0.337233e+00	-0.682777e+00	-0.190692e+01	-0.923376e+01	-0.184523e+02	-0.209704e+02
Reaction 4: $N_2 + N^+ \rightleftharpoons N + N_2^+$						
1e+14	0.000000e+00	-0.454093e+00	0.710863e+00	0.878489e+00	-0.551525e+01	-0.128042e-01
1e+15	0.000000e+00	-0.381287e+00	0.446289e+00	0.792372e+00	-0.472167e+01	-0.334316e+00
1e+16	0.000000e+00	-0.299935e+00	0.177941e+00	0.619510e+00	-0.388369e+01	-0.565230e+00
1e+17	0.000000e+00	-0.227847e+00	-0.380430e-01	0.398254e+00	-0.315226e+01	-0.691244e+00
1e+18	0.000000e+00	-0.164537e+00	-0.202432e+00	0.112950e+00	-0.247625e+01	-0.746487e+00
1e+19	0.000000e+00	-0.135176e+00	-0.255223e+00	-0.112672e+00	-0.209774e+01	-0.745209e+00
Reaction 5: $N + N \rightleftharpoons N_2^+ + e^-$						
1e+14	-0.412910e+00	0.821758e+00	-0.287790e-01	-0.982394e+01	-0.355555e+01	-0.136596e+02
1e+15	-0.393669e+00	0.659271e+00	0.211819e+00	-0.915117e+01	-0.509279e+01	-0.131548e+02
1e+16	-0.352549e+00	0.439073e+00	0.325352e+00	-0.820528e+01	-0.644087e+01	-0.128633e+02
1e+17	-0.298223e+00	0.203171e+00	0.299515e+00	-0.714841e+01	-0.743445e+01	-0.127819e+02
1e+18	-0.228297e+00	-0.607538e-01	0.132638e+00	-0.588631e+01	-0.822061e+01	-0.128577e+02
1e+19	-0.176536e+00	-0.233712e+00	-0.760369e-01	-0.495445e+01	-0.860561e+01	-0.129867e+02

Table A.7: Coefficients for the curve-fits for $K_{eq,r}$ from reference [30]. n is the total number density in particles/cm^3.

APPENDIX **B**

Simulation Input Parameter Files

B.1 Mb_cns Simulations

B.1.1 m7ndt.sit

```
# m7ndt.sit
# Last nozzle and dump tank of the Drummond shock tube with
# 1. Choke inflow
# 2. M7 contoured nozzle.
# 3. He driving N2
# 4. Conditions to produce rarefied flow
# 5. 50 Pa in the Dump tank

BEGIN_GEOMETRY

   NODE h   0.039000 0.003500
   NODE h0  0.039000 0.000000
   NODE i   0.043000 0.003500
   NODE j   0.048000 0.003500
   NODE k   0.053000 0.004681
   NODE l   0.084000 0.012000
   NODE l0  0.084000 0.000000
   NODE m1  0.109057 0.017648
   NODE m2  0.139165 0.023187
   NODE m3  0.179825 0.029117
   NODE m4  0.219679 0.033567
   NODE m5  0.269094 0.037700
   NODE m6  0.319988 0.040816
   NODE m7  0.369282 0.042884
   NODE m8  0.414000 0.043621
   NODE n0  0.414000 0.000000
   NODE n1  0.414000 0.045600
   NODE n2  0.394000 0.057100
   NODE n3  0.317000 0.057100
   NODE n4  0.317000 0.152000
   NODE n5  0.414000 0.152000
   NODE p0  0.550000 0.000000
   NODE p1  0.550000 0.043621
   NODE p2  0.550000 0.045600
   NODE p3  0.550000 0.152000

   LINE   h0h  h0 h
```

```
   LINE   hi   h i
   BEZIER ik   i j j k
   LINE   kl   k l
   LINE   h0l0 h0 l0
   LINE   l0l  l0 l
   SPLINE lm8  8 l m1 m2 m3 m4 m5 m6 m7 m8
   LINE   l0n0 l0 n0
   LINE   n0m8 n0 m8
   LINE   m8n1 m8 n1
   LINE   n3n2 n3 n2
   LINE   n2n1 n2 n1
   LINE   n3n4 n3 n4
   LINE   n4n5 n4 n5
   LINE   n1n5 n1 n5
   LINE   n0p0 n0 p0
   LINE   m8p1 m8 p1
   LINE   n1p2 n1 p2
   LINE   n5p3 n5 p3
   LINE   p0p1 p0 p1
   LINE   p1p2 p1 p2
   LINE   p2p3 p2 p3


   # Define the boundaries

   POLYLINE west5  1 + h0h
   POLYLINE north5 3 + hi + ik + kl
   POLYLINE south5 1 + h0l0
   POLYLINE east5  1 + l0l

   POLYLINE north6 1 + lm8
   POLYLINE south6 1 + l0n0
   POLYLINE east6  1 + n0m8

   POLYLINE north7 1 + m8p1
   POLYLINE south7 1 + n0p0
   POLYLINE east7  1 + p0p1

   POLYLINE north8 1 + n1p2
   POLYLINE east8  1 + p1p2
   POLYLINE west8  1 + m8n1

   POLYLINE north9 1 + n5p3
   POLYLINE east9  1 + p2p3
   POLYLINE west9  1 + n1n5

   POLYLINE north10 1 + n4n5
   POLYLINE south10 2 + n3n2 + n2n1
   POLYLINE west10  1 + n3n4


END_GEOMETRY

BEGIN_FLOW
   # Gas and flow properties
   GAS_TYPE  perf_n2
   GAS_STATE inflow_n2   1.0566e5 800.37 0.0 1541.67 1.0
   GAS_STATE dumptank_n2 50.000   0.0    0.0 295.65  1.0
```

```
# Set the boundary discretisation before building the blocks
DISCRETISE west5  70  0 0 0.0
DISCRETISE north5 80  0 0 0.0
DISCRETISE east5  70  0 1 1.1
DISCRETISE south5 80  0 0 0.0

DISCRETISE north6 200 1 0 1.2
DISCRETISE east6  70  0 1 1.1
DISCRETISE south6 200 1 0 1.2

DISCRETISE north7 80  1 0 1.2
DISCRETISE east7  70  0 0 0.0
DISCRETISE south7 80  1 0 1.2

DISCRETISE north8 80  1 0 1.2
DISCRETISE east8   5  0 0 0.0
DISCRETISE west8   5  0 0 0.0

DISCRETISE north9 80  1 0 1.2
DISCRETISE east9  60  1 0 1.2
DISCRETISE west9  60  1 0 1.2

DISCRETISE north10 60  0 1 1.2
DISCRETISE south10 60  0 1 1.2
DISCRETISE west10  60  1 0 1.2

BOUNDARY_SPEC west5 SUP_IN inflow_n2
BOUNDARY_SPEC north5 FIXED_T 295.65
BOUNDARY_SPEC north6 FIXED_T 295.65
BOUNDARY_SPEC west8 FIXED_T 295.65
BOUNDARY_SPEC north9 FIXED_T 295.65
BOUNDARY_SPEC north10 FIXED_T 295.65
BOUNDARY_SPEC west10 FIXED_T 295.65
BOUNDARY_SPEC south10 FIXED_T 295.65

BOUNDARY_SPEC east7  SUP_OUT
BOUNDARY_SPEC east8  SUP_OUT
BOUNDARY_SPEC east9  SUP_OUT

BLOCK noz5  + north5 + east5 + south5 + west5
BLOCK noz6  + north6 + east6 + south6 + east5
BLOCK test7 + north7 + east7 + south7 + east6
BLOCK test8 + north8 + east8 + north7 + west8
BLOCK test9 + north9 + east9 + north8 + west9
BLOCK test10 + north10 + west9 + south10 + west10

CONNECT_BLOCKS noz5  east noz6  west
CONNECT_BLOCKS noz6  east test7 west
CONNECT_BLOCKS test7 north test8 south
CONNECT_BLOCKS test8 north test9 south
CONNECT_BLOCKS test9 west  test10 east

# GRID_TYPE tube3 AO
# GRID_TYPE tube4 AO

FILL_BLOCK noz5  dumptank_n2
FILL_BLOCK noz6  dumptank_n2
```

```
   FILL_BLOCK test7 dumptank_n2
   FILL_BLOCK test8 dumptank_n2
   FILL_BLOCK test9 dumptank_n2
   FILL_BLOCK test10 dumptank_n2

END_FLOW

BEGIN_CONTROL
   TITLE FULL Drummond tunnel, M7 nozzle, helium driving N2.
   CASE_ID 0

   AXISYMMETRIC
   VISCOUS

   # TURBULENT tube0
   # TURBULENT tube1
   # TURBULENT tube2
   # TURBULENT tube3
   # TURBULENT noz6
   # TURBULENT tube11
   # TURBULENT tube12
   # TURBULENT tube13
   # TURBULENT tube14
   # TURBULENT tube15
   # TURBULENT tube16

   FLUX_CALC ausmdv
   MAX_TIME  1.0e-3
   MAX_STEP  200000
   TIME_STEP 5.0e-8

   DT_PLOT    200.0e-6
   DT_HISTORY 1.0e-6
   HISTORY_CELL noz5 1 1
   HISTORY_CELL noz5 1 70
   HISTORY_CELL noz6 1 70
   HISTORY_CELL noz6 1 1
END_CONTROL

# Name the output files and build them.
BEZIER_FILE m7ndt.bez
PARAM_FILE m7ndt.p
BUILD

EXIT
```

B.1.2 m7coni_ndt.sit

```
# m7coni_ndt.sit
# nozzle and dump tank of the Drummond shock tube with
# 1. Choked inflow
# 2. M7 conical nozzle.
# 3. He driving N2
# 4. Conditions to produce rarefied flow PRF of 15
# 5. 0.5 torr in dumptank

BEGIN_GEOMETRY
```

```
NODE i0  0.038900 0.000000
NODE i   0.038900 0.003500
NODE j   0.043900 0.003500
NODE k   0.048900 0.004200
NODE l   0.103000 0.011800
NODE l0  0.103000 0.000000

NODE m   0.268350 0.035000
NODE n0  0.268350 0.000000
NODE n1  0.268350 0.037900
NODE n2  0.258350 0.039700
NODE n3  0.158350 0.039700
NODE n4  0.158350 0.152000
NODE n5  0.268350 0.152000
NODE p0  0.443000 0.000000
NODE p1  0.443000 0.035000
NODE p2  0.443000 0.037900
NODE p3  0.443000 0.152000

LINE   i0i  i0 i
BEZIER ik   i j j k
LINE   kl   k l
LINE   i0l0 i0 l0
LINE   l0l  l0 l
LINE   lm  l m
LINE   l0n0 l0 n0
LINE   n0m  n0 m
LINE   mn1  m  n1
LINE   n3n2 n3 n2
LINE   n2n1 n2 n1
LINE   n3n4 n3 n4
LINE   n4n5 n4 n5
LINE   n1n5 n1 n5
LINE   n0p0 n0 p0
LINE   mp1  m  p1
LINE   n1p2 n1 p2
LINE   n5p3 n5 p3
LINE   p0p1 p0 p1
LINE   p1p2 p1 p2
LINE   p2p3 p2 p3


# Define the boundaries

POLYLINE west5  1 + i0i
POLYLINE north5 2 + ik + kl
POLYLINE south5 1 + i0l0
POLYLINE east5  1 + l0l

POLYLINE north6 1 + lm
POLYLINE south6 1 + l0n0
POLYLINE east6  1 + n0m

POLYLINE north7 1 + mp1
POLYLINE south7 1 + n0p0
POLYLINE east7  1 + p0p1
```

```
   POLYLINE north8 1 + n1p2
   POLYLINE east8  1 + p1p2
   POLYLINE west8  1 + mn1

   POLYLINE north9 1 + n5p3
   POLYLINE east9  1 + p2p3
   POLYLINE west9  1 + n1n5

   POLYLINE north10 1 + n4n5
   POLYLINE south10 2 + n3n2 + n2n1
   POLYLINE west10  1 + n3n4


END_GEOMETRY

BEGIN_FLOW
   # Gas and flow properties
   GAS_TYPE  perf_n2
   GAS_STATE inflow_n2   7.044e4  800.37 0.0 1541.67 1.0
   GAS_STATE dumptank_n2 66.64    0.0    0.0 295.65  1.0

   # Set the boundary discretisation before building the blocks
   DISCRETISE west5  70  0 0 0.0
   DISCRETISE north5 110 0 0 0.0
   DISCRETISE east5  70  0 1 1.1
   DISCRETISE south5 110 0 0 0.0

   DISCRETISE north6 150 1 0 1.2
   DISCRETISE east6  70  0 1 1.1
   DISCRETISE south6 150 1 0 1.2

   DISCRETISE north7 80  1 0 1.2
   DISCRETISE east7  70  0 0 0.0
   DISCRETISE south7 80  1 0 1.2

   DISCRETISE north8 80  1 0 1.2
   DISCRETISE east8   5  0 0 0.0
   DISCRETISE west8   5  0 0 0.0

   DISCRETISE north9 80  1 0 1.2
   DISCRETISE east9  60  1 0 1.2
   DISCRETISE west9  60  1 0 1.2

   DISCRETISE north10 60  0 1 1.2
   DISCRETISE south10 60  0 1 1.2
   DISCRETISE west10  60  1 0 1.2

   BOUNDARY_SPEC west5 SUP_IN inflow_n2
   BOUNDARY_SPEC north5 FIXED_T 295.65
   BOUNDARY_SPEC north6 FIXED_T 295.65
   BOUNDARY_SPEC west8 FIXED_T 295.65
   BOUNDARY_SPEC north9 FIXED_T 295.65
   BOUNDARY_SPEC north10 FIXED_T 295.65
   BOUNDARY_SPEC west10 FIXED_T 295.65
   BOUNDARY_SPEC south10 FIXED_T 295.65

   BOUNDARY_SPEC east7  SUP_OUT
   BOUNDARY_SPEC east8  SUP_OUT
```

```
   BOUNDARY_SPEC east9  SUP_OUT

   BLOCK noz5  + north5 + east5 + south5 + west5
   BLOCK noz6  + north6 + east6 + south6 + east5
   BLOCK test7 + north7 + east7 + south7 + east6
   BLOCK test8 + north8 + east8 + north7 + west8
   BLOCK test9 + north9 + east9 + north8 + west9
   BLOCK test10 + north10 + west9 + south10 + west10

   CONNECT_BLOCKS noz5  east noz6  west
   CONNECT_BLOCKS noz6  east test7 west
   CONNECT_BLOCKS test7 north test8 south
   CONNECT_BLOCKS test8 north test9 south
   CONNECT_BLOCKS test9 west  test10 east

   # GRID_TYPE tube3 AO
   # GRID_TYPE tube4 AO

   FILL_BLOCK noz5  dumptank_n2
   FILL_BLOCK noz6  dumptank_n2
   FILL_BLOCK test7 dumptank_n2
   FILL_BLOCK test8 dumptank_n2
   FILL_BLOCK test9 dumptank_n2
   FILL_BLOCK test10 dumptank_n2

END_FLOW

BEGIN_CONTROL
   TITLE FULL Drummond tunnel, M7 nozzle, helium driving N2.
   CASE_ID 0

   AXISYMMETRIC
   VISCOUS

   # TURBULENT tube0
   # TURBULENT tube1
   # TURBULENT tube2
   # TURBULENT tube3
   # TURBULENT noz6
   # TURBULENT tube11
   # TURBULENT tube12
   # TURBULENT tube13
   # TURBULENT tube14
   # TURBULENT tube15
   # TURBULENT tube16

   FLUX_CALC ausmdv
   MAX_TIME  1.0e-3
   MAX_STEP  200000
   TIME_STEP 5.0e-8

   DT_PLOT    200.0e-6
   DT_HISTORY 1.0e-6
   HISTORY_CELL noz5 1 1
   HISTORY_CELL noz5 1 70
   HISTORY_CELL noz6 1 70
   HISTORY_CELL noz6 1 1
END_CONTROL
```

```
# Name the output files and build them.
BEZIER_FILE m7coni_ndt.bez
PARAM_FILE m7coni_ndt.p
BUILD

EXIT
```

B.1.3 m7coni_full.sit

```
# m7coni_full.sit
# The FULL Drummond shock tube with
# 1. M7 conical nozzle.
# 2. Low density flow.

BEGIN_GEOMETRY
   NODE a  -0.500000 0.031000
   NODE a0 -0.500000 0.000000
   NODE b  -0.285000 0.031000
   NODE b0 -0.285000 0.000000
   NODE c  -0.180000 0.031000
   NODE c0 -0.180000 0.000000
   NODE d  -0.068000 0.031000
   NODE d0 -0.068000 0.000000
   NODE e1 -0.013000 0.000000
   NODE e2 -0.013000 0.010000
   NODE e3  0.000000 0.020000
   NODE e4  0.000000 0.031000
   NODE f   0.014450 0.031000
   NODE g   0.014450 0.003500
   NODE h   0.028900 0.003500
   NODE i   0.035900 0.003500
   NODE i0  0.035900 0.000000
   NODE j   0.040900 0.003500
   NODE k   0.045900 0.004200
   NODE l   0.100000 0.011800
   NODE l0  0.100000 0.000000
   NODE m   0.265350 0.035000
   NODE n0  0.265350 0.000000
   NODE n1  0.265350 0.037900
   NODE n2  0.255350 0.039700
   NODE n3  0.155350 0.039700
   NODE n4  0.155350 0.152000
   NODE n5  0.265350 0.152000
   NODE p0  0.380000 0.000000
   NODE p1  0.380000 0.035000
   NODE p2  0.380000 0.037900
   NODE p3  0.380000 0.152000
   NODE q   -1.0     0.031
   NODE q0  -1.0     0.0
   NODE r   -1.5     0.031
   NODE r0  -1.5     0.0
   NODE s   -2.0     0.031
   NODE s0  -2.0     0.0
   NODE t   -2.5     0.031
   NODE t0  -2.5     0.0
```

```
NODE u6  -2.990   0.031
NODE u5  -3.0     0.031
NODE u4  -3.0     0.0295
NODE u3  -3.013   0.0295
NODE u2  -3.0     0.020
NODE u1  -3.0     0.010
NODE u0  -3.0     0.0
NODE v   -3.783   0.0295
NODE v0  -3.783   0.0

LINE   ab   a b
LINE   a0a  a0 a
LINE   a0b0 a0 b0
LINE   b0b  b0 b
LINE   bc   b c
LINE   b0c0 b0 c0
LINE   c0c  c0 c
LINE   c0d0 c0 d0
LINE   cd   c d
LINE   d0d  d0 d
LINE   d0e1 d0 e1
LINE   de4  d e4
BEZIER e1e4 e1 e2 e3 e4
BEZIER e4h  e4 f g h
LINE   hi   h i
LINE   e1i0 e1 i0
LINE   i0i  i0 i
BEZIER ik   i j j k
LINE   kl   k l
LINE   i0l0 i0 l0
LINE   l0l  l0 l
LINE   lm  l m
LINE   l0n0 l0 n0
LINE   n0m  n0 m
LINE   mn1  m  n1
LINE   n3n2 n3 n2
LINE   n2n1 n2 n1
LINE   n3n4 n3 n4
LINE   n4n5 n4 n5
LINE   n1n5 n1 n5
LINE   n0p0 n0 p0
LINE   mp1  m  p1
LINE   n1p2 n1 p2
LINE   n5p3 n5 p3
LINE   p0p1 p0 p1
LINE   p1p2 p1 p2
LINE   p2p3 p2 p3

LINE   q0a0 q0 a0
LINE   qa   q  a
LINE   q0q  q0 q
LINE   r0q0 r0 q0
LINE   rq   r  q
LINE   r0r  r0 r
LINE   s0r0 s0 r0
LINE   sr   s  r
LINE   s0s  s0 s
LINE   t0s0 t0 s0
```

```
LINE   ts   t  s
LINE   t0t  t0 t
LINE   u0t0 u0 t0
LINE   u6t  u6 t
BEZIER u3u6 u3 u4 u5 u6
BEZIER u0u3 u0 u1 u2 u3
LINE   v0u0 v0 u0
LINE   vu3  v u3
LINE   v0v  v0 v

# Define the boundaries
POLYLINE north0 1 + ab
POLYLINE west0  1 + a0a
POLYLINE south0 1 + a0b0
POLYLINE east0  1 + b0b

POLYLINE north1 1 + bc
POLYLINE south1 1 + b0c0
POLYLINE east1  1 + c0c

POLYLINE north2 1 + cd
POLYLINE south2 1 + c0d0
POLYLINE east2  1 + d0d

POLYLINE north3 1 + de4
POLYLINE south3 1 + d0e1
POLYLINE east3  1 + e1e4

POLYLINE north4 2 + e4h + hi
POLYLINE south4 1 + e1i0
POLYLINE east4  1 + i0i

POLYLINE north5 2 + ik + kl
POLYLINE south5 1 + i0l0
POLYLINE east5  1 + l0l

POLYLINE north6 1 + lm
POLYLINE south6 1 + l0n0
POLYLINE east6  1 + n0m

POLYLINE north7 1 + mp1
POLYLINE south7 1 + n0p0
POLYLINE east7  1 + p0p1

POLYLINE north8 1 + n1p2
POLYLINE east8  1 + p1p2
POLYLINE west8  1 + mn1

POLYLINE north9 1 + n5p3
POLYLINE east9  1 + p2p3
POLYLINE west9  1 + n1n5

POLYLINE north10 1 + n4n5
POLYLINE south10 2 + n3n2 + n2n1
POLYLINE west10  1 + n3n4

POLYLINE north11 1 + qa
POLYLINE south11 1 + q0a0
```

```
   POLYLINE west11  1 + q0q

   POLYLINE north12 1 + rq
   POLYLINE south12 1 + r0q0
   POLYLINE west12  1 + r0r

   POLYLINE north13 1 + sr
   POLYLINE south13 1 + s0r0
   POLYLINE west13  1 + s0s

   POLYLINE north14 1 + ts
   POLYLINE south14 1 + t0s0
   POLYLINE west14  1 + t0t

   POLYLINE north15 2 + u3u6 + u6t
   POLYLINE south15 1 + u0t0
   POLYLINE west15  1 + u0u3

   POLYLINE north16 1 + vu3
   POLYLINE south16 1 + v0u0
   POLYLINE west16  1 + v0v
END_GEOMETRY

BEGIN_FLOW
   # Gas and flow properties
   GAS_TYPE  perf_he_n2
   GAS_STATE dumptank_n2   65.79     0.0   0.0 295.65 1.0 0.0
   GAS_STATE initial_n2  1100.00     0.0   0.0 295.65 1.0 0.0
   GAS_STATE initial_he   216.667e3  0.0   0.0 295.65 0.0 1.0

   # Set the boundary discretisation before building the blocks
   DISCRETISE north0 90  0 0 0.0
   DISCRETISE east0  70  0 1 1.1
   DISCRETISE south0 90  0 0 0.0
   DISCRETISE west0  70  0 1 1.1

   DISCRETISE north1 60  0 0 0.0
   DISCRETISE east1  70  0 1 1.1
   DISCRETISE south1 60  0 0 0.0

   DISCRETISE north2 100 0 1 1.2
   DISCRETISE east2  70  0 1 1.1
   DISCRETISE south2 100 0 1 1.2

   DISCRETISE north3 150 0 0 0.0
   DISCRETISE east3  70  0 1 1.1
   DISCRETISE south3 150 0 0 0.0

   DISCRETISE north4 100 0 0 0.0
   DISCRETISE east4  70  0 0 0.0
   DISCRETISE south4 100 0 0 0.0

   DISCRETISE north5 80  0 0 0.0
   DISCRETISE east5  70  0 1 1.1
   DISCRETISE south5 80  0 0 0.0

   DISCRETISE north6 200 1 0 1.2
   DISCRETISE east6  70  0 1 1.1
```

```
DISCRETISE south6 200 1 0 1.2

DISCRETISE north7 80  1 0 1.2
DISCRETISE east7  70  0 0 0.0
DISCRETISE south7 80  1 0 1.2

DISCRETISE north8 80  1 0 1.2
DISCRETISE east8   5  0 0 0.0
DISCRETISE west8   5  0 0 0.0

DISCRETISE north9 80  1 0 1.2
DISCRETISE east9  60  1 0 1.2
DISCRETISE west9  60  1 0 1.2

DISCRETISE north10 60  0 1 1.2
DISCRETISE south10 60  0 1 1.2
DISCRETISE west10  60  1 0 1.2

DISCRETISE north11 180  0 0 0.0
DISCRETISE south11 180  0 0 0.0
DISCRETISE west11  70   0 1 1.1

DISCRETISE north12 180  0 0 0.0
DISCRETISE south12 180  0 0 0.0
DISCRETISE west12  70   0 1 1.1

DISCRETISE north13 180  0 0 0.0
DISCRETISE south13 180  0 0 0.0
DISCRETISE west13  70   0 1 1.1

DISCRETISE north14 180  0 0 0.0
DISCRETISE south14 180  0 0 0.0
DISCRETISE west14  70   0 1 1.1

DISCRETISE north15 180  0 0 0.0
DISCRETISE south15 180  0 0 0.0
DISCRETISE west15  70   0 1 1.1

DISCRETISE north16 180  0 0 0.0
DISCRETISE south16 180  0 0 0.0
DISCRETISE west16  70   0 1 1.1

BOUNDARY_SPEC north0 FIXED_T 295.65
BOUNDARY_SPEC north1 FIXED_T 295.65
BOUNDARY_SPEC north2 FIXED_T 295.65
BOUNDARY_SPEC north3 FIXED_T 295.65
BOUNDARY_SPEC north4 FIXED_T 295.65
BOUNDARY_SPEC north5 FIXED_T 295.65
BOUNDARY_SPEC north6 FIXED_T 295.65

BOUNDARY_SPEC north11 FIXED_T 295.65
BOUNDARY_SPEC north12 FIXED_T 295.65
BOUNDARY_SPEC north13 FIXED_T 295.65
BOUNDARY_SPEC north14 FIXED_T 295.65
BOUNDARY_SPEC north15 FIXED_T 295.65
BOUNDARY_SPEC north16 FIXED_T 295.65
BOUNDARY_SPEC west16 FIXED_T 295.65
```

```
BOUNDARY_SPEC east7  SUP_OUT
BOUNDARY_SPEC east8  SUP_OUT
BOUNDARY_SPEC east9  SUP_OUT

BLOCK tube0 + north0 + east0 + south0 + west0
BLOCK tube1 + north1 + east1 + south1 + east0
BLOCK tube2 + north2 + east2 + south2 + east1
BLOCK tube3 + north3 + east3 + south3 + east2
BLOCK tube4 + north4 + east4 + south4 + east3
BLOCK noz5  + north5 + east5 + south5 + east4
BLOCK noz6  + north6 + east6 + south6 + east5
BLOCK test7 + north7 + east7 + south7 + east6
BLOCK test8 + north8 + east8 + north7 + west8
BLOCK test9 + north9 + east9 + north8 + west9
BLOCK test10 + north10 + west9 + south10 + west10

BLOCK tube11 + north11 + west0 + south11 + west11
BLOCK tube12 + north12 + west11 + south12 + west12
BLOCK tube13 + north13 + west12 + south13 + west13
BLOCK tube14 + north14 + west13 + south14 + west14
BLOCK tube15 + north15 + west14 + south15 + west15
BLOCK tube16 + north16 + west15 + south16 + west16

CONNECT_BLOCKS tube0 east tube1 west
CONNECT_BLOCKS tube1 east tube2 west
CONNECT_BLOCKS tube2 east tube3 west
CONNECT_BLOCKS tube3 east tube4 west
CONNECT_BLOCKS tube4 east noz5  west
CONNECT_BLOCKS noz5  east noz6  west
CONNECT_BLOCKS noz6  east test7 west
CONNECT_BLOCKS test7 north test8 south
CONNECT_BLOCKS test8 north test9 south
CONNECT_BLOCKS test9 west  test10 east

CONNECT_BLOCKS tube11 east tube0 west
CONNECT_BLOCKS tube12 east tube11 west
CONNECT_BLOCKS tube13 east tube12 west
CONNECT_BLOCKS tube14 east tube13 west
CONNECT_BLOCKS tube15 east tube14 west
CONNECT_BLOCKS tube16 east tube15 west

# GRID_TYPE tube3 AO
# GRID_TYPE tube4 AO

FILL_BLOCK tube0 initial_n2
FILL_BLOCK tube1 initial_n2
FILL_BLOCK tube2 initial_n2
FILL_BLOCK tube3 initial_n2
FILL_BLOCK tube4 initial_n2

# Later, these need to be filled with dumptank_n2
FILL_BLOCK noz5  dumptank_n2
FILL_BLOCK noz6  dumptank_n2
FILL_BLOCK test7 dumptank_n2
FILL_BLOCK test8 dumptank_n2
FILL_BLOCK test9 dumptank_n2
FILL_BLOCK test10 dumptank_n2
```

```
   # Driver and upstream-part of the shock tube
   FILL_BLOCK tube11 initial_n2
   FILL_BLOCK tube12 initial_n2
   FILL_BLOCK tube13 initial_n2
   FILL_BLOCK tube14 initial_n2
   FILL_BLOCK tube15 initial_n2
   FILL_BLOCK tube16 initial_he
END_FLOW

BEGIN_CONTROL
   TITLE FULL Drummond tunnel, M7 nozzle, helium driving N2, PRF 15.
   CASE_ID 0

   AXISYMMETRIC
   VISCOUS

#   TURBULENT tube0
#   TURBULENT tube1
#   TURBULENT tube2
#   TURBULENT tube3
#   TURBULENT noz6
#   TURBULENT tube11
#   TURBULENT tube12
#   TURBULENT tube13
#   TURBULENT tube14
#   TURBULENT tube15
#   TURBULENT tube16

   FLUX_CALC efm
   MAX_TIME  2.0e-3
   MAX_STEP  800000
   TIME_STEP 0.2e-8

   DT_PLOT    0.5e-3
   DT_HISTORY 1.0e-6
   HISTORY_CELL tube4 1 1
   HISTORY_CELL tube3 1 70
   HISTORY_CELL tube2 1 70
   HISTORY_CELL test7 1 1
END_CONTROL

# Name the output files and build them.
BEZIER_FILE m7coni_full.bez
PARAM_FILE m7coni_full.p
BUILD

EXIT
```

B.1.4 x1rn2eq.sit

```
# x1rn2eq.sit
# X1 expansion tunnel with freejet.
# Notes:
# 1. Rarefied flow in dumptank
# 2. He driving N2 test gas
# 3. Model downstream of secondary diaphragm
# 4. N2 accelerator gas
```

```
# 5. Equilibrium inflow conditions
# 6. Equilibrium flow in acceleration tube
# 7. Good x-resolution

BEGIN_GEOMETRY
   NODE a   0.0     0.01905
   NODE a0  0.0     0.0
   NODE b   0.0     0.0425
   NODE c  -0.038   0.0425
   NODE d  -0.038   0.1475
   NODE e   0.0     0.1475
   NODE f   0.5285  0.1475
   NODE g   0.5285  0.0425
   NODE j   0.5285  0.01905
   NODE j0  0.5285  0.0
   NODE k  -0.1200  0.01905
   NODE k0 -0.1200  0.0
   NODE l  -0.3760  0.01905
   NODE l0 -0.3760  0.0
   NODE m  -0.7760  0.01905
   NODE m0 -0.7760  0.0
   NODE n  -1.299   0.01905
   NODE n0 -1.299   0.0
   NODE o  -2.018   0.01905
   NODE o0 -2.018   0.0
   NODE p  -2.718   0.01905
   NODE p0 -2.718   0.0
   NODE q  -2.910   0.01905
   NODE q0 -2.910   0.0

   LINE a0a a0 a
   LINE ab a b
   LINE cb c b
   LINE cd c d
   LINE de d e
   LINE ef e f
   LINE gf g f
   LINE jg j g
   LINE j0j j0 j
   LINE a0j0 a0 j0
   LINE aj a j
   LINE bg b g
   LINE be b e
   LINE ka k a
   LINE k0a0 k0 a0
   LINE k0k k0 k
   LINE lk l k
   LINE l0k0 l0 k0
   LINE l0l l0 l
   LINE ml m l
   LINE m0l0 m0 l0
   LINE m0m m0 m
   LINE nm n m
   LINE n0m0 n0 m0
   LINE n0n n0 n
   LINE on o n
   LINE o0n0 o0 n0
   LINE o0o o0 o
```

```
   LINE po p o
   LINE p0o0 p0 o0
   LINE p0p p0 p
   LINE qp q p
   LINE q0p0 q0 p0
   LINE q0q q0 q

   # Define the boundaries
   POLYLINE north0  1 + ka
   POLYLINE east0   1 + a0a
   POLYLINE south0  1 + k0a0
   POLYLINE west0   1 + k0k
   POLYLINE north1  1 + aj
   POLYLINE east1   1 + j0j
   POLYLINE south1  1 + a0j0
   POLYLINE north2  1 + bg
   POLYLINE east2   1 + jg
   POLYLINE west2   1 + ab
   POLYLINE north3  1 + ef
   POLYLINE east3   1 + gf
   POLYLINE west3   1 + be
   POLYLINE north4  1 + de
   POLYLINE south4  1 + cb
   POLYLINE west4   1 + cd
   POLYLINE north5  1 + lk
   POLYLINE south5  1 + l0k0
   POLYLINE west5   1 + l0l
   POLYLINE north6  1 + ml
   POLYLINE south6  1 + m0l0
   POLYLINE west6   1 + m0m
   POLYLINE north7  1 + nm
   POLYLINE south7  1 + n0m0
   POLYLINE west7   1 + n0n
   POLYLINE north8  1 + on
   POLYLINE south8  1 + o0n0
   POLYLINE west8   1 + o0o
   POLYLINE north9  1 + po
   POLYLINE south9  1 + p0o0
   POLYLINE west9   1 + p0p
   POLYLINE north10 1 + qp
   POLYLINE south10 1 + q0p0
   POLYLINE west10  1 + q0q
END_GEOMETRY

 BEGIN_FLOW
   # Gas and flow properties
   GAS_TYPE eq_n2
   GAS_STATE initial_n2  15.0        0.0      0.0 296      1.0
   GAS_STATE inflow_n2   0.5581978e6 4787.283 0.0 7044.259 1.0

   # Set the boundary discretisation before building the blocks
   DISCRETISE north0  180  0 0 0.0
   DISCRETISE east0   30  0 1 1.2
   DISCRETISE south0  180  0 0 0.0
   DISCRETISE west0   30  0 1 1.2
   DISCRETISE north1  300 1 0 1.2
   DISCRETISE east1   30  0 1 1.2
   DISCRETISE south1  300 1 0 1.2
```

```
DISCRETISE north2  300 1 0 1.2
DISCRETISE east2   80  0 0 0.0
DISCRETISE west2   80  0 0 0.0
DISCRETISE north3  300 1 0 1.2
DISCRETISE east3   100 1 0 1.1
DISCRETISE west3   100 1 0 1.1
DISCRETISE north4  40  0 0 0.0
DISCRETISE south4  40  0 0 0.0
DISCRETISE west4   100 1 0 1.1
DISCRETISE north5  360 0 0 0.0
DISCRETISE south5  360 0 0 0.0
DISCRETISE west5   30  0 1 1.2
DISCRETISE north6  520 0 0 0.0
DISCRETISE south6  520 0 0 0.0
DISCRETISE west6   30  0 1 1.2
DISCRETISE north7  700 0 0 0.0
DISCRETISE south7  700 0 0 0.0
DISCRETISE west7   30  0 1 1.2
DISCRETISE north8  960 0 0 0.0
DISCRETISE south8  960 0 0 0.0
DISCRETISE west8   30  0 1 1.2
DISCRETISE north9  920 0 0 0.0
DISCRETISE south9  920 0 0 0.0
DISCRETISE west9   30  0 1 1.2
DISCRETISE north10 260 0 0 0.0
DISCRETISE south10 260 0 0 0.0
DISCRETISE west10  30  0 1 1.2

BOUNDARY_SPEC north0  FIXED_T 298.0
BOUNDARY_SPEC north3  FIXED_T 298.0
BOUNDARY_SPEC north4  FIXED_T 298.0
BOUNDARY_SPEC north5  FIXED_T 298.0
BOUNDARY_SPEC north6  FIXED_T 298.0
BOUNDARY_SPEC north7  FIXED_T 298.0
BOUNDARY_SPEC north8  FIXED_T 298.0
BOUNDARY_SPEC north9  FIXED_T 298.0
BOUNDARY_SPEC north10 FIXED_T 298.0
BOUNDARY_SPEC west2   FIXED_T 298.0
BOUNDARY_SPEC south4  FIXED_T 298.0
BOUNDARY_SPEC west4   FIXED_T 298.0
BOUNDARY_SPEC west10  SUP_IN  inflow_n2
BOUNDARY_SPEC east1   SUP_OUT
BOUNDARY_SPEC east2   SUP_OUT
BOUNDARY_SPEC east3   SUP_OUT

BLOCK b0 + north0 + east0 + south0 + west0
BLOCK b1 + north1 + east1 + south1 + east0
BLOCK b2 + north2 + east2 + north1 + west2
BLOCK b3 + north3 + east3 + north2 + west3
BLOCK b4 + north4 + west3 + south4 + west4
BLOCK b5 + north5 + west0 + south5 + west5
BLOCK b6 + north6 + west5 + south6 + west6
BLOCK b7 + north7 + west6 + south7 + west7
BLOCK b8 + north8 + west7 + south8 + west8
BLOCK b9 + north9 + west8 + south9 + west9
BLOCK b10 + north10 + west9 + south10 + west10

FILL_BLOCK b0 initial_n2
```

```
   FILL_BLOCK b1 initial_n2
   FILL_BLOCK b2 initial_n2
   FILL_BLOCK b3 initial_n2
   FILL_BLOCK b4 initial_n2
   FILL_BLOCK b5 initial_n2
   FILL_BLOCK b6 initial_n2
   FILL_BLOCK b7 initial_n2
   FILL_BLOCK b8 initial_n2
   FILL_BLOCK b9 initial_n2
   FILL_BLOCK b10 initial_n2

   CONNECT_BLOCKS b0 east b1 west
   CONNECT_BLOCKS b1 north b2 south
   CONNECT_BLOCKS b2 north b3 south
   CONNECT_BLOCKS b3 west b4 east
   CONNECT_BLOCKS b0 west b5 east
   CONNECT_BLOCKS b5 west b6 east
   CONNECT_BLOCKS b6 west b7 east
   CONNECT_BLOCKS b7 west b8 east
   CONNECT_BLOCKS b8 west b9 east
   CONNECT_BLOCKS b9 west b10 east
END_FLOW

BEGIN_CONTROL
   TITLE X1 expansion tube with free jet
   CASE_ID 0

   AXISYMMETRIC
   VISCOUS
   FLUX_CALC ausmdv
   MAX_TIME  350.0e-6
   MAX_STEP  10000000
   TIME_STEP 1.0e-8

   DT_PLOT    50.0e-6
   DT_HISTORY 1.0e-6

   HISTORY_CELL b0 1 30      # at8.    cell 0

   # BLOCK 1 HISTORY CELLS
   # Acceleration tube exit
   HISTORY_CELL b1 1  1      # r=0mm.  cell 1

   # x=0mm before recoil
   HISTORY_CELL b1 30  1     # r=0mm.  cell 2
   HISTORY_CELL b1 30  12    # r=10mm. cell 3
   HISTORY_CELL b1 30  18    # r=14mm. cell 4

   # x=50mm before recoil
   HISTORY_CELL b1 76  1     # r=0mm.  cell 5
   HISTORY_CELL b1 76  6     # r=5mm.  cell 6
   HISTORY_CELL b1 76  18    # r=14mm. cell 7

   # x=100mm before recoil
   HISTORY_CELL b1 112  1    # r=0mm.  cell 8
   HISTORY_CELL b1 112  6    # r=5mm.  cell 9
   HISTORY_CELL b1 112  18   # r=14mm. cell 10
```

```
   # x=150mm before recoil
   HISTORY_CELL b1 143  1    # r=0mm.  cell 11
   HISTORY_CELL b1 143  6    # r=5mm.  cell 12
   HISTORY_CELL b1 143  18   # r=14mm. cell 13

   # x=200mm before recoil
   HISTORY_CELL b1 170  1    # r=0mm.  cell 14
   HISTORY_CELL b1 170  6    # r=5mm.  cell 15
   HISTORY_CELL b1 170  18   # r=14mm. cell 16

   # x=315mm before recoil
   HISTORY_CELL b1 224 1     # r=0mm.  cell 17
   HISTORY_CELL b1 224 6     # r=5mm.  cell 18
   HISTORY_CELL b1 224 18    # r=14mm. cell 19

   # BLOCK 2 HISTORY CELLS
   # x=50mm before recoil
   HISTORY_CELL b2 76  31    # r=28mm. cell 20

   # x=100mm before recoil
   HISTORY_CELL b2 112 31    # r=28mm. cell 21

   # x=150mm before recoil
   HISTORY_CELL b2 143 31    # r=28mm. cell 22

   # x=200mm before recoil
   HISTORY_CELL b2 170 31    # r=28mm. cell 23

   # x=315mm before recoil
   HISTORY_CELL b2 224 31    # r=28mm. cell 24

   # Static Pressure Transducers
   HISTORY_CELL b5 1 30      # cell 25
   HISTORY_CELL b6 1 30      # cell 26
   HISTORY_CELL b7 1 30      # cell 27
   HISTORY_CELL b8 1 30      # cell 28
   HISTORY_CELL b9 1 30      # cell 29
END_CONTROL

# Name the output files and build them.
BEZIER_FILE x1rn2eq.bez
PARAM_FILE x1rn2eq.p
BUILD

EXIT
```

B.1.5 x1rn2srhr.sit

```
# x1rn2srhr.sit
# X1 expansion tunnel with freejet.
# Notes:
# 1. Rarefied flow in dumptank
# 2. He driving N2 test gas
# 3. Model downstream of secondary diaphragm
# 4. N2 accelerator gas
# 5. Equilibrium inflow conditions
# 6. Gas processed by reflected shock included
```

```
# 7. Equilibrium flow in acceleration tube
# 8. Double x-resolution of x1rn2sr

BEGIN_GEOMETRY
   NODE a   0.0     0.01905
   NODE a0  0.0     0.0
   NODE b   0.0     0.0425
   NODE c  -0.038   0.0425
   NODE d  -0.038   0.1475
   NODE e   0.0     0.1475
   NODE f   0.5285  0.1475
   NODE g   0.5285  0.0425
   NODE j   0.5285  0.01905
   NODE j0  0.5285  0.0
   NODE k  -0.1200  0.01905
   NODE k0 -0.1200  0.0
   NODE l  -0.3760  0.01905
   NODE l0 -0.3760  0.0
   NODE m  -0.7760  0.01905
   NODE m0 -0.7760  0.0
   NODE n  -1.299   0.01905
   NODE n0 -1.299   0.0
   NODE o  -2.018   0.01905
   NODE o0 -2.018   0.0
   NODE p  -2.718   0.01905
   NODE p0 -2.718   0.0
   NODE q  -2.910   0.01905
   NODE q0 -2.910   0.0
   NODE r  -2.91845 0.01905
   NODE r0 -2.91845 0.0
   NODE s  -3.110   0.01905
   NODE s0 -3.110   0.0

   LINE a0a a0 a
   LINE ab a b
   LINE cb c b
   LINE cd c d
   LINE de d e
   LINE ef e f
   LINE gf g f
   LINE jg j g
   LINE j0j j0 j
   LINE a0j0 a0 j0
   LINE aj a j
   LINE bg b g
   LINE be b e
   LINE ka k a
   LINE k0a0 k0 a0
   LINE k0k k0 k
   LINE lk l k
   LINE l0k0 l0 k0
   LINE l0l l0 l
   LINE ml m l
   LINE m0l0 m0 l0
   LINE m0m m0 m
   LINE nm n m
   LINE n0m0 n0 m0
   LINE n0n n0 n
```

```
   LINE on o n
   LINE o0n0 o0 n0
   LINE o0o o0 o
   LINE po p o
   LINE p0o0 p0 o0
   LINE p0p p0 p
   LINE qp q p
   LINE q0p0 q0 p0
   LINE q0q q0 q
   LINE rq r q
   LINE r0r r0 r
   LINE r0q0 r0 q0
   LINE sr s r
   LINE s0s s0 s
   LINE s0r0 s0 r0

   # Define the boundaries
   POLYLINE north0  1 + ka
   POLYLINE east0   1 + a0a
   POLYLINE south0  1 + k0a0
   POLYLINE west0   1 + k0k
   POLYLINE north1  1 + aj
   POLYLINE east1   1 + j0j
   POLYLINE south1  1 + a0j0
   POLYLINE north2  1 + bg
   POLYLINE east2   1 + jg
   POLYLINE west2   1 + ab
   POLYLINE north3  1 + ef
   POLYLINE east3   1 + gf
   POLYLINE west3   1 + be
   POLYLINE north4  1 + de
   POLYLINE south4  1 + cb
   POLYLINE west4   1 + cd
   POLYLINE north5  1 + lk
   POLYLINE south5  1 + l0k0
   POLYLINE west5   1 + l0l
   POLYLINE north6  1 + ml
   POLYLINE south6  1 + m0l0
   POLYLINE west6   1 + m0m
   POLYLINE north7  1 + nm
   POLYLINE south7  1 + n0m0
   POLYLINE west7   1 + n0n
   POLYLINE north8  1 + on
   POLYLINE south8  1 + o0n0
   POLYLINE west8   1 + o0o
   POLYLINE north9  1 + po
   POLYLINE south9  1 + p0o0
   POLYLINE west9   1 + p0p
   POLYLINE north10 1 + qp
   POLYLINE south10 1 + q0p0
   POLYLINE west10  1 + q0q
   POLYLINE north11 1 + rq
   POLYLINE south11 1 + r0q0
   POLYLINE west11  1 + r0r
   POLYLINE north12 1 + sr
   POLYLINE south12 1 + s0r0
   POLYLINE west12  1 + s0s
END_GEOMETRY
```

```
BEGIN_FLOW
  # Gas and flow properties
  GAS_TYPE eq_n2
  GAS_STATE initial_n2  15.0        0.0      0.0 296      1.0
  GAS_STATE inflow_n2   0.5581978e6 4787.283 0.0 7044.259 1.0
  GAS_STATE shocked_n2  6.826364e6  0.0      0.0 10284    1.0

  # Set the boundary discretisation before building the blocks
  DISCRETISE north0  180  0 0 0.0
  DISCRETISE east0   30  0 1 1.2
  DISCRETISE south0  180  0 0 0.0
  DISCRETISE west0   30  0 1 1.2
  DISCRETISE north1  300 1 0 1.2
  DISCRETISE east1   30  0 1 1.2
  DISCRETISE south1  300 1 0 1.2
  DISCRETISE north2  300 1 0 1.2
  DISCRETISE east2   80  0 0 0.0
  DISCRETISE west2   80  0 0 0.0
  DISCRETISE north3  300 1 0 1.2
  DISCRETISE east3   100 1 0 1.1
  DISCRETISE west3   100 1 0 1.1
  DISCRETISE north4  40  0 0 0.0
  DISCRETISE south4  40  0 0 0.0
  DISCRETISE west4   100 1 0 1.1
  DISCRETISE north5  360 0 0 0.0
  DISCRETISE south5  360 0 0 0.0
  DISCRETISE west5   30  0 1 1.2
  DISCRETISE north6  520 0 0 0.0
  DISCRETISE south6  520 0 0 0.0
  DISCRETISE west6   30  0 1 1.2
  DISCRETISE north7  700 0 0 0.0
  DISCRETISE south7  700 0 0 0.0
  DISCRETISE west7   30  0 1 1.2
  DISCRETISE north8  960 0 0 0.0
  DISCRETISE south8  960 0 0 0.0
  DISCRETISE west8   30  0 1 1.2
  DISCRETISE north9  920 0 0 0.0
  DISCRETISE south9  920 0 0 0.0
  DISCRETISE west9   30  0 1 1.2
  DISCRETISE north10 260 0 0 0.0
  DISCRETISE south10 260 0 0 0.0
  DISCRETISE west10  30  0 1 1.2
  DISCRETISE north11 15  0 0 0.0
  DISCRETISE south11 15  0 0 0.0
  DISCRETISE west11  30  0 1 1.2
  DISCRETISE north12 340 0 0 0.0
  DISCRETISE south12 340 0 0 0.0
  DISCRETISE west12  30  0 1 1.2

  BOUNDARY_SPEC north0  FIXED_T 298.0
  BOUNDARY_SPEC north3  FIXED_T 298.0
  BOUNDARY_SPEC north4  FIXED_T 298.0
  BOUNDARY_SPEC north5  FIXED_T 298.0
  BOUNDARY_SPEC north6  FIXED_T 298.0
  BOUNDARY_SPEC north7  FIXED_T 298.0
  BOUNDARY_SPEC north8  FIXED_T 298.0
  BOUNDARY_SPEC north9  FIXED_T 298.0
```

```
   BOUNDARY_SPEC north10 FIXED_T 298.0
   BOUNDARY_SPEC west2   FIXED_T 298.0
   BOUNDARY_SPEC south4  FIXED_T 298.0
   BOUNDARY_SPEC west4   FIXED_T 298.0
   BOUNDARY_SPEC north11  FIXED_T 298.0
   BOUNDARY_SPEC north12  FIXED_T 298.0
   BOUNDARY_SPEC west12  SUP_IN  inflow_n2
   BOUNDARY_SPEC east1   SUP_OUT
   BOUNDARY_SPEC east2   SUP_OUT
   BOUNDARY_SPEC east3   SUP_OUT

   BLOCK b0 + north0 + east0 + south0 + west0
   BLOCK b1 + north1 + east1 + south1 + east0
   BLOCK b2 + north2 + east2 + north1 + west2
   BLOCK b3 + north3 + east3 + north2 + west3
   BLOCK b4 + north4 + west3 + south4 + west4
   BLOCK b5 + north5 + west0 + south5 + west5
   BLOCK b6 + north6 + west5 + south6 + west6
   BLOCK b7 + north7 + west6 + south7 + west7
   BLOCK b8 + north8 + west7 + south8 + west8
   BLOCK b9 + north9 + west8 + south9 + west9
   BLOCK b10 + north10 + west9 + south10 + west10
   BLOCK b11 + north11 + west10 + south11 + west11
   BLOCK b12 + north12 + west11 + south12 + west12

   FILL_BLOCK b0 initial_n2
   FILL_BLOCK b1 initial_n2
   FILL_BLOCK b2 initial_n2
   FILL_BLOCK b3 initial_n2
   FILL_BLOCK b4 initial_n2
   FILL_BLOCK b5 initial_n2
   FILL_BLOCK b6 initial_n2
   FILL_BLOCK b7 initial_n2
   FILL_BLOCK b8 initial_n2
   FILL_BLOCK b9 initial_n2
   FILL_BLOCK b10 initial_n2
   FILL_BLOCK b11 shocked_n2
   FILL_BLOCK b12 inflow_n2

   CONNECT_BLOCKS b0 east b1 west
   CONNECT_BLOCKS b1 north b2 south
   CONNECT_BLOCKS b2 north b3 south
   CONNECT_BLOCKS b3 west b4 east
   CONNECT_BLOCKS b0 west b5 east
   CONNECT_BLOCKS b5 west b6 east
   CONNECT_BLOCKS b6 west b7 east
   CONNECT_BLOCKS b7 west b8 east
   CONNECT_BLOCKS b8 west b9 east
   CONNECT_BLOCKS b9 west b10 east
   CONNECT_BLOCKS b11 east b10 west
   CONNECT_BLOCKS b12 east b11 west
END_FLOW

BEGIN_CONTROL
   TITLE X1 expansion tube with free jet
   CASE_ID 0

   AXISYMMETRIC
```

```
VISCOUS
FLUX_CALC ausmdv
MAX_TIME  320.0e-6
MAX_STEP  10000000
TIME_STEP 1.0e-8

DT_PLOT    80.0e-6
DT_HISTORY 1.0e-6

HISTORY_CELL b0 1 30      # cell 0

# BLOCK 1 HISTORY CELLS
# Acceleration tube exit
HISTORY_CELL b1 1  1      # cell 1
HISTORY_CELL b1 1  6      # cell 2

# x=0mm before recoil
HISTORY_CELL b1 30  1     # cell 3
HISTORY_CELL b1 30  6     # cell 4

# x=50mm before recoil
HISTORY_CELL b1 76  1     # cell 5
HISTORY_CELL b1 76  6     # cell 6
HISTORY_CELL b1 76  18    # cell 7

# x=100mm before recoil
HISTORY_CELL b1 112  1    # cell 8
HISTORY_CELL b1 112  6    # cell 9
HISTORY_CELL b1 112  18   # cell 10

# x=150mm before recoil
HISTORY_CELL b1 143  1    # cell 11
HISTORY_CELL b1 143  6    # cell 12
HISTORY_CELL b1 143  18   # cell 13

# x=200mm before recoil
HISTORY_CELL b1 170  1    # cell 14
HISTORY_CELL b1 170  6    # cell 15
HISTORY_CELL b1 170  18   # cell 16

# x=315mm before recoil
HISTORY_CELL b1 224 1     # cell 17
HISTORY_CELL b1 224 6     # cell 18
HISTORY_CELL b1 224 18    # cell 19

# BLOCK 2 HISTORY CELLS
# x=50mm before recoil
HISTORY_CELL b2 76  8     # cell 20

# x=100mm before recoil
HISTORY_CELL b2 112 8     # cell 21

# x=150mm before recoil
HISTORY_CELL b2 143 8     # cell 22

# x=200mm before recoil
HISTORY_CELL b2 170 8     # cell 23
```

```
   # x=315mm before recoil
   HISTORY_CELL b2 224 8     # cell 24

   # Static Pressure Transducers
   HISTORY_CELL b5 1 30      # cell 25
   HISTORY_CELL b6 1 30      # cell 26
   HISTORY_CELL b7 1 30      # cell 27
   HISTORY_CELL b8 1 30      # cell 28
   HISTORY_CELL b9 1 30      # cell 29
END_CONTROL

# Name the output files and build them.
BEZIER_FILE x1rn2srhr.bez
PARAM_FILE x1rn2srhr.p
BUILD

EXIT
```

B.2 L1D Simulations

B.2.1 x1inert_dia.Lp

```
X1inertial diaphragm model, frc. 15-March-00
0                   test_case, Mach 4 nozzle attached
2 1 0               nslug, npiston, ndiaphragm
25.0e-6   1000000   max_time, max_steps
1.0e-8   0.25       dt_init, CFL
2 2                 Xorder, Torder
0.25e-6  1.0e-7      dt_plot, dt_his
2                                 hnloc
-2.718                            hxloc[0]:  at1
-2.018                            hxloc[1]:  at3
tube definition follows:
1  1                n, nseg
-4.000  0.0381 1    xb[0], Diamb[0], linear[0]
-1.000  0.0381 1
0                   nKL
296.0  0            Tnominal, nT
Piston definition of light diaphragm
0  type of piston
2.36e-5 0.0381 9.0e-6 mass, diam, length
0 0                    p_restrain, is_restrain
1.0 0                  x_buffer, hit_buffer
0 0                    with_brakes, brakes_on
0 1                    left_slug_id, left_slug_end_id
1 0                    right_slug_id, right_slug_end_id
4.5e-6 0.0             x0, v0
slug 0: N2 test gas
500  0 1 1.01       nnx, to_end_1, to_end_2, strength
0 1                 viscous, adiabatic
V  4787.283         left boundary : velocity (fixed wall)
P 0                 right boundary: piston_id
1                   hn_cell
498                 hx_cell
-4.00 -2.910 13 5.582e5 4787.283 7044.26 Initial: x1, x2, gas, p, u, T
```

```
slug 1: N2 accelerator gas
500 0 0 0.0         nnx, to_end_1, to_end_2, strength
0 1                 viscous, adiabatic
P 0                 left boundary : neighbour_slug_id, end
F                   right boundary: neighbour_slug_id, end, diaphragm_id
0                   hn_cell
-2.910 -1.000 13 15.0 0.0 296.0 Initial: x1, x2, gas, p, u, T
```

B.2.2 x1ht.Lp

```
Static X1 Acceleration Tube with Reflected Shock, f.r.c., inviscid. 30-06-2000
0                                   test case
3 0 0                               nslug, npiston, ndiaphragm
400.0e-6 500000                     max_time, max_step
1.0e-8 0.25                         dt_init, CFL
2 2                                 Xorder, Torder
5.0e-6 1.0e-6                      dt_plot, dt_his
6                                   hnloc
-2.718                              hxloc[0]:  at1
-2.018                              hxloc[1]:  at3
-1.299                              hxloc[2]:  at45
-0.776                              hxloc[3]:  at6
-0.376                              hxloc[4]:  at7
-0.120                              hxloc[5]:  at8
tube definition follows:
200   1                             n, nseg
-5.0 0.0381 1                       xb[i], Diamb[i], linear[i]
-0.0 0.0381 1
0                                   nKL
296.0 0                             T_nominal, nT
Slug[0]: Nitrogen behind the primary shock
250 0 0 0.0                         nnx, to_end_1, to_end_2, strength
0 1                                 viscous_effects, adiabatic
V 4787.28                           left boundary: solid wall, velocity
S 1 0                               right boundary: gas_slug_id, gas_slug_end_id
0                                   hncell
-5.000 -2.91845 13 558.1978e3 4787.28 7044.259   x1, x2, gas, p, u, T
Slug[1]: Nitrogen behind reflected shock
250 0 0 0.0                         nnx, to_end_1, to_end_2, strength
0 1                                 viscous_effects, adiabatic
S 0 1                               left boundary: gas_slug_id, gas_slug_end_id
S 2 0                               right boundary: solid wall, velocity
0                                   hncell
-2.91845 -2.910 13 6.826364e6 0.0 10284.0   x1, x2, gas, p, u, T
Slug[2]: Nitrogen fill gas in the acceleration tube
250 0 0 0.0                         nnx, to_end_1, to_end_2, strength
0 1                                 viscous_effects, adiabatic
S 1 1                               left boundary: gas_slug_id, gas_slug_end_id
F                                   right boundary: solid wall, velocity
0                                   hncell
-2.910 0.0 13 15.0 0.0 296.0        x1, x2, gas, p, u, T
```